The Role of Glutamine Synthetase in Vascular Health and Disease

Claire Hermine Ozber

Submitted in accordance with the requirements for
Doctor of Philosophy

The University of Leeds

Leeds Institute of Cardiovascular and Metabolic Medicine,
School of Medicine

April 2021

The candidate confirms that the work submitted is her own and that appropriate credit has been given where reference has been made to the work of others.

Acknowledgements

Firstly, I would like to thank my supervisors - I am absolutely biased but I have genuinely had the dream team in Dr Richard Cubbon, Dr Nadira Yuldasheva and Professor Mark Kearney.

To Dr Richard Cubbon – thank you so much for the opportunity to do this project, and just as I'd started to give up hope of doing a PhD! Your support, guidance and understanding over the last 3 years, and particularly in this past year with the Covid19 pandemic, has been phenomenal. I cannot thank you enough.

To Dr Nadira Yuldasheva – thank you so much for everything you have done for me throughout this project, from teaching me a whole host of new skills to encouraging me to persevere with them and helping me produce work I am proud of.

To Professor Mark Kearney – thank you for welcoming me into the broader Kearney group, for supporting my research endeavours, and for encouraging me along the way.

I would also like to thank all of the Cubbon and Kearney group as it has been an absolute pleasure working with you all – I've gained so much experience and knowledge and confidence. Thanks so much for letting me be a lab-hours/bench hog in the last few months so I can get this done and dusted – I have really appreciated it!

Particular thanks go to:

- Natallia Makava and Anna Skromna – your endless support throughout this project is genuinely so appreciated, thank you for teaching me new techniques and for letting me ask you a thousand questions along the way and for quite literally being my eyes when looking at aortic valve leaflets on the microscopes!
- Asjad Visnagri and Thomas Slater – the organ bath may well be affectionately known as the paper machine but let's be honest, it was also the bane of my life – thank you so much for all your help and training and support whilst I mastered it!
- Natalie North – thank you for providing me with so many protocols and letting me borrow reagents and generally being an immense help! Thank you so much for being understanding of my needing to balance this PhD project with my technician work – it really is genuinely appreciated
- Alex Bruns and Jane Brown – for helping me in my frantic last couple of weeks in the lab, particularly with the BCA assays and Western Blotting, and for general support and training throughout the project
- Hema Viswambharan and Simon Futers – Hema, thank you for teaching me the eNOS assay, and Simon for helping me with the general radioactive lab duties

- Mel Reay, Andy Horner, Scott Fawcett, and everyone in the CBS team for your help with colony maintenance, skills training, and general help and guidance – I've learnt so much from all of you and become confident in my skills thanks to you
- Fiona Platt, and the FBS bioimaging team – Sally Boxall and Ruth Hughes – thank you so much for your help with all of the immunofluorescent work, absolute pain to get it to work but so pretty when it does!!
- Professor Wouter H Lamers (Amsterdam, Netherlands) - thanks for providing the $GS^{+/LacZ}$ mouse model to the Cubbon group, without which this project would not be possible

I would also like to thank my PGT John Huntriss for your general support, chats, problem solving, and for never doubting me when I've said I want to get this done early, I really appreciated your confidence in me!

Thanks also go to Kay White and the SOT team, Alan, Julie, David, Val, Jason, and Ping – the absolute backbone of LICAMM! Thanks for answering my incessant questions, helping me fix things, putting up with the fact that I never ever remembered to sign-off my orders (Sorry Val and Julie!), and generally being incredibly helpful and supportive, especially with my return to work after lockdown in September!

To all the friends I've made in LICAMM – and I've really made a lot (you all know who you are and I'm not going to list you all as it would honestly take up another page!) - thanks so much for being so welcoming and for all your moral support, chats, cakes, and general morale boosting throughout this project! Looking forward to when Covid is over and we can actually socialise together again! I've really missed that this last year!

I'd also like to thank my family and my friends outside of LICAMM – even when we are apart, thanks to the power of the internet, you've all been cheering me on and asking me when I'll finish and encouraging me to get on with it!

Finally, last but most certainly not least… This thesis is dedicated to my parents – thank you for everything and for loving and supporting me throughout. Thank you for encouraging me to pursue this as a career from all the way back in high school, for putting up with my never-ending moaning when I've had a bad day, for helping me celebrate when experiments are going well or I make a breakthrough in learning something new, and for boring you to death whilst you listen to me constantly blabbing on about everything and nothing, including trying to explain my experiments to you! This last year has been insanely hard with the pandemic, and shielding only made it worse, so thank you for encouraging me to stick with this and to get back on campus and into the lab to finish up this work. Thank you really for generally putting up with me– no mean feat! It's really been a joint effort and I couldn't have achieved it without you.

Abstract

Atherosclerosis is a complex multifactorial disease. Much work has been undertaken to understand its pathogenesis, including events relating to atherosclerotic plaque rupture; which causes myocardial infarction and stroke; one marker of plaque instability is increased glutamine synthetase (GS) expression. GS, which synthesises glutamine from ammonia and glutamic acid, is expressed in multiple cell lineages of the plaque, and amongst endothelial cells (ECs) is enriched in the arterial subset. Recently, a novel role of GS has been found in ECs, by which it regulates cytoskeletal remodelling via RhoJ palmitoylation; this could be relevant for other facets of endothelial biology. As such, this thesis examines the role of GS in arterial function and atherosclerosis.

Mice with global GS haploinsufficiency, $GS^{+/LacZ}$, were compared to littermate controls with normal GS expression. *Ex vivo* aortic vasodilation was assessed using acetylcholine and sodium nitroprusside, and vasoconstriction with phenylephrine (PE), both before and after endothelial nitric oxide synthase (eNOS) inhibition with L-NMMA. Aortic eNOS activity was inferred via conversion of radiolabelled L-arginine to L-citrulline. $GS^{+/LacZ}$ were crossed with $ApoE^{-/-}$ and fed a Western Diet before atherosclerotic plaques were examined histologically.

PE-induced vasoconstriction was significantly impaired in $GS^{+/LacZ}$; pre-incubation with L-NMMA abrogated this, suggesting increased basal nitric oxide (NO) bioavailability, and increased eNOS activity was corroborated in an activity assay. $GS^{+/LacZ}ApoE^{-/-}$ mice showed reduced atherosclerotic burden in the whole aorta. Aortic root histology corroborated this, along with smaller plaques exhibiting multiple hallmarks of plaque instability, including proportionally larger necrotic cores, altered plaque collagen staining, and a striking pattern of lipid deposition within the caps.

In summary, global GS haploinsufficiency increases arterial NO bioavailability and reduces atherosclerotic plaque volume, but with multiple histologic features of plaque instability. Further studies are needed to define the underpinning mechanisms in the hope of elucidating new strategies for managing cardiovascular risk.

Table of Contents

List of Figures

List of Tables

Abbreviations

^{14}C	Carbon-14
3Rs	"Replacement, Reduction, and Refinement"; principles of humane animal research
α-SMA	Alpha smooth muscle actin
β cell	Beta cells (insulin secreting pancreatic cells)
µm	Micrometre/micron
µCi	Microcurie
µl	Microlitre
ACh	Acetylcholine
ACTB	Gene encoding beta-actin
AF488	Alexa Fluor 488 fluorophore
AF647	Alexa Fluor 647 fluorophore
AGEs	Advanced glycolysis endproducts
ANOVA	Analysis of variance
$ApoE^{-/-}$	Mouse genotype: knockout of the gene encoding Apolipoprotein-E
ATP	Adenosine triphosphate
AUC	Area under curve analysis
BCA	Bicinchoninic acid
BCP	1-Bromo-3-chloropropane
BH_4	Tetrahydrobiopterin
BLAST	Basic local alignment search tool (used for sequence alignment)
BSA	Bovine serum albumin
C57BL/6	C57 Black 6 (background mouse strain)
Ca^{2+}	Calcium signalling
CaM	Calmodulin
Cav1	Caveolin-1
cDNA	Complementary DNA (single strand, produced by reverse transcription of mrna)

CEB	Cell extraction buffer
cGMP	Cyclic guanosine-3' 5-monophosphate
CHD	Coronary heart disease
CO_2	Carbon dioxide
COL1A2	Collagen type I alpha 2 chain
COL3A1	Collagen type III alpha 1 chain
CVD	Cardiovascular disease
DAPI	4′,6-diamidino-2-phenylindole; blue fluorescent DNA stain
dH_2O	Distilled water
DM	Diabetes mellitus
DNA	Deoxyribonucleic acid
dNTPs	Deoxyribonucleotide triphosphates
DPM	Disintegrations per minute
DPX	Mountant containing Distyrene, a Plasticizer, and Xylene
EC	Endothelial cell
ECM	Extracellular matrix
EDTA	Ethylenediaminetetraacetic acid
E_{max}	Maximum effect (of a drug)
eNOS	Endothelial nitric oxide synthase
FAM	6-Carboxyfluorescein fluorophore
g	Gram
GLUL	Gene encoding Glutamine synthetase
$GLUL^{KD}$	Knockdown of glutamine synthetase gene
GS	Glutamine synthetase
$GS^{+/+}$	Mouse genotype: wild-type expression of glutamine synthetase
$GS^{+/+}ApoE^{-/-}$	Mouse genotype: wild-type glutamine synthetase, crossed with knockout of Apolipoprotein E
$GS^{+/LacZ}$	Mouse genotype: single allelic replacement of glutamine synthetase with the β-galactosidase gene

$GS^{+/LacZ}ApoE^{-/-}$	Mouse genotype: single allelic replacement of glutamine synthetase with *lacz*, crossed with knockout of Apolipoprotein-E
GS^{ECKO}	Mouse genotype: endothelial cell specific knockout of glutamine synthetase
GTP	Guanosine triphosphate
GTPase	Guanosine triphosphate hydrolysing enzyme
GTT	Glucose tolerance test
GWAS	Genome-wide association study/studies
H_2O	Water
HCl	Hydrochloric acid
HDL	High-density lipoprotein
HEPES	4-(2-hydroxyethyl)-1-piperazineethanesulfonic acid; a buffering agent
HPRT	Gene encoding hypoxanthine-guanine phosphoribosyltransferase
HRP	Horseradish peroxidase
HSB	Hue Saturation Brightness colour space
HUVEC	Human umbilical vein endothelial cell
Hz	Hertz
IB4	Isolectin B4
ID	Identification (number)
IFN-y	Interferon gamma
IL-1B	Interleukin-1b protein
IL1B	Gene encoding Interleukin-1b
iNOS	Inducible nitric oxide synthase
ITT	Insulin tolerance test
IU	International units
KCl	Potassium chloride
$KMnO_4$	Potassium permanganate
L	Litre

L-NMMA	L-N^G-monomethyl arginine citrate; nitric oxide synthase (NOS) inhibitor
LacZ	Gene encoding β-galactosidase
LDL	Low-density lipoprotein
M0	Quiescent macrophages
M1	Macrophage activation state 1; pro-inflammatory
M2	Macrophage activation state 2; repair
MCE	Major cardiovascular event (e.g. Stroke, myocardial infarction)
mg	Milligram
mL	Millilitre
mm	Millimetre
mmol	Millimoles
mRNA	Messenger ribonucleic acid
MSO	Methionine sulfoximine (Glutamine synthetase inhibitor)
n.s.	Not (statistically) significant
NaN_3	Sodium azide
NaNP	Sodium nitroprusside
NaOH	Sodium hydroxide
NCBI	National Center for Biotechnology Information (USA)
nmol	Nanomoles
nNOS	Neuronal nitric oxide synthase
NO	Nitric oxide
NOS	Nitric oxide synthase
O_2	Oxygen
OCT	Optimum cutting temperature compound (for cryopreservation)
PBS	Phosphate buffered saline
PCR	Polymerase chain reaction
PE	Phenylephrine
PFA	Paraformaldehyde

PGI_2	Prostacyclin
phospho-eNOS	Phosphorylated endothelial nitric oxide synthase
phospho-eNOS (S1177)	Endothelial nitric oxide synthase phosphorylated at the Serine-1177 residue
PI3K-Akt	Phosphatidylinositol-3 kinase and protein kinase B signalling
PTB buffer	PBS/Triton™ X-100/Bovine serum albumin buffer
PVDF	Polyvinylidene difluoride (membrane)
qPCR	Quantitative polymerase chain reaction
RGB	Red Green Blue colour space
RHO	Ras homolog family
RHOJ	Ras homolog gene family, member J
RHOJ	Gene encoding Ras homolog gene family, member J
$RHOJ^{KD}$	Knockdown of *RHOJ* gene
RNA	Ribonucleic acid
ROI	Region of interest
ROS	Reactive oxygen species
rpm	Revolutions per minute
rs10911021	Single nucleotide polymorphism associated with increased cardiovascular risk in people with Type 2 Diabetes Mellitus
RT	Reverse transcription
RT-qPCR	Real-time quantitative polymerase chain reaction
S1177	Serine-1177 residue (of enos)
scRNA-seq	Single-cell RNA sequencing
SDS-PAGE	Sodium dodecyl sulphate–polyacrylamide gel electrophoresis
shRNA	Short hairpin RNA
SNP	Single nucleotide polymorphism
STZ	Streptozotocin
T1DM	Type 1 diabetes mellitus
T2DM	Type 2 diabetes mellitus

TBS	Tris-buffered saline
TESPA	(3-aminopropyl)triethoxysilane
TNFs	Tumour necrosis factors
TREM2	Gene encoding Triggered receptor expressed on myeloid cells 2
TXA_2	Thromboxane-A2
UK	United Kingdom
USA	United States of America
v/v	Volume by volume
VSMC	Vascular smooth muscle cell
w/v	Weight by volume
WT	Wild-type
ZNF648	Gene encoding Zinc finger protein 648

Chapter 1 Introduction

1.1 Overview of cardiovascular disease

According to the World Health Organisation, cardiovascular disease (CVD) is now the leading cause of mortality globally, accounting for 31% of deaths worldwide. Globally, approximately 17.9 million people die annually of CVD[1]. Here in the United Kingdom (UK), cardiovascular and circulatory diseases account for approximately 27% of all-cause mortality, accounting for 167,000 deaths annually, of which 44,000 are premature deaths occurring before the age of 75. Although in the U.K. the mortality rate has halved over the last 50 years, approximately 7.4 million people are currently living with heart and circulatory diseases. Additionally, it has been indicated that the cost of healthcare relating to CVD is approximately £9 billion per annum and the total cost to the economy is approximately £19 billion per annum, including premature deaths and disability and other informal costs[2].

CVDs encompass many diseases of the heart and circulatory system including thrombotic, acquired, and congenital disorders. Despite this, the majority of deaths – 85 % globally - are attributable to two specific conditions, coronary heart disease (CHD) and stroke[1]. In the UK, 23,000 premature deaths annually are directly due to coronary heart disease (CHD), and stroke remains the biggest cause of severe disability[2]. These conditions are most often due to the development of atherosclerosis within the vasculature which ultimately can occlude the vessel. This can happen either directly due to the plaque volume or indirectly through the plaque rupturing leading to thrombosis that results in a major cardiovascular event[3].

Multiple factors have been found to confer increased risk of developing atherosclerosis and an increased risk of a major cardiovascular event such as a myocardial infarction or stroke thereafter. These factors include obesity[4], type 2 diabetes mellitus (T2DM)[5,6], age[7], hypertension[8], genetics[9], sex, and environmental risk factors such as poverty, smoking, and air pollution[1,2]. Frequently, people with CHD and stroke have multiple risk factors and co-morbidities that contribute to vascular dysfunction and subsequent atherogenesis[1,2,8,10].

1.2 Vascular biology

1.2.1 Gross morphology of the vasculature

The vasculature consists of a network of specialised blood vessels including arteries, veins and capillaries, amongst others. Large blood vessels consist of three main layers, the innermost tunica intima, the central tunica media, and the outermost tunica adventitia. The adventitia predominantly consists of collagen, elastin and fibroblasts along with some vascular smooth muscle cells (VSMCs) and ensures the vessel maintains its tensile strength and compliance to blood flow. The tunica media predominantly consists of VSMCs and the constriction and relaxation of these cells that alters their tone. The tunica media is then separated from the innermost layer, the intima, by internal elastic lamina[11]. Finally, the tunica intima consists of a basal lamina lined with and supporting an epithelial monolayer of cells known as the endothelium[11–13].

1.2.2 Endothelial cell specialisation

Endothelial cells (ECs) were once believed to be a simple barrier between the blood flowing within the lumen and the rest of the body[11,12]. Multiple studies have since indicated that these endothelial cells (ECs) possess substantial functional and molecular specialisation adapted to their local environment and physiological role[11–15].

As vascular pressure and tone is considerably increased in arteries compared to veins and vascular pressure is at its lowest in the capillaries, it therefore follows that EC morphology also differs. For example, capillaries can be divided into three main types: continuous barrier, fenestrated, and sinusoidal and the differentiation of ECs into these types is regulated in an organotypic manner specific to their function. Continuous barrier capillaries are linked together with tight junctions and are also adhered to a basal lamina. These capillaries are widely found in most organs and transport molecules from the blood through the ECs in a controlled manner and into the VSMCs and beyond, such as in the blood-brain barrier interface. By contrast, sinusoidal capillaries allow for the free movement of materials due to their large intercellular gaps. Fenestrated capillaries are the intermediary, allowing for some movement of small molecules across their intracellular membranous pores[14]. Additionally, ECs have been shown to differ phenotypically on a cytoskeletal level between arteries and veins in their use of ß-Actin fibres known as F-actin. The specific organisation of these fibres and their adhesion to the focal adhesion points and therefore the extracellular matrix (ECM) has been shown to be a defining feature present only in adult arterial ECs and not within venous ECs[13,16].

Although some of the pathways involved in this specialisation had been elucidated, the advent of single-cell RNA sequencing (scRNA-seq) has enabled us to examine the heterogeneity of a population of cells through probing the unique transcriptome of every individual cell sequenced. The first major project to apply this to the whole organism was the "*Tabula Muris*" project in 2018, which utilised the house mouse, *Mus musculus*, as a model to produce a cell transcriptome atlas. This project isolated and individually RNA sequenced over 100,000 cells from 20 different organs and tissues from the mouse model. A particular focus of the project was to enable "controlled comparison of gene expression in cell types that are shared between tissues, such as T lymphocytes and endothelial cells from different anatomical locations"[17]. A subsequent study from 2020 by Kalucka *et al.* takes this a stage further by focussing purely on 32,000 ECs from 11 different tissues[18].

In the case of both data sets, these studies have further confirmed that ECs are transcriptomically distinguishable from other cell types. Additionally, these studies have also confirmed that although there must be transcriptomic similarity in order to be an EC, anatomically separate populations are also transcriptomically heterogeneous. Furthermore, these anatomical groupings of cells are not homogenous with subsets identified within these populations, including the ability to differentiate between arterial and venous ECs based on specific gene expression[17,18]. These findings have since been further validated through independent analysis of the EC data of the *Tabula Muris* study[19] and are additionally supported by the work of Kalluri *et al* which determined the normal mouse aorta to have specialised EC subsets with disease-relevant functions[20].

In 2020 this technology has been applied to human tissues to attempt to create a human cell atlas. The Human Cell Landscape study performed scRNA-seq on cells from multiple adult and foetal donated tissues and organs including replicates from multiple donors. Encompassing analysis of 702,868 cells including 7140 ECs, again the clustering indicated that whilst some transcriptional elements must be similar to define a cell type, there are again organotypic subsets and functional subsets. This study also gained new insights on EC function through the identification of immune-active clusters[21]. Additionally, another 2020 study analysed 84,363 cells spanning 15 tissues and organs from a single male adult donor and also identified immune-active clusters and found similar patterns of similarity and heterogeneity within ECs[22].

Interestingly, the Human Cell Landscape study also opted to compare their human cell data to publicly available murine scRNA-seq data, including ECs, to examine both similarity and heterogeneity of cell types between species. This analysis also confirmed that where orthologous gene expression is conserved, cell types tend to also be conserved with similar gene expression patterns, further confirming the suitability of the

mouse as a suitable model organism, including for specialist studies such as those focussed on EC function[21]

Together these studies suggest that far from being a simplistic barrier, subsets of ECs have specialist roles, even within the localised environment of a single tissue, and regardless of species-specific differences. Furthermore, the elucidation of new clusters with unexpected gene expression patterns also suggests that there are still multiple functions of the endothelium yet to be elucidated.

1.2.3 Endothelial function: Regulation of vascular tone

In addition to roles in controlled transportation of compounds from the blood to the surrounding tissues and participation in the immune system, amongst others, the endothelium plays a critical role in the regulation of vascular tone. ECs produce a variety of vasoactive compounds. These compounds modulate calcium (Ca^{2+}) signalling within the vascular smooth muscle cells (VSMCs), in turn causing either vasoconstriction or vasodilation accordingly[12,13,23].

These endothelium-derived vasoactive compounds include the synergistic prostanoids prostacyclin (PGI_2) and thromboxane A2 (TXA_2) which have opposing effects. PGI_2 binds to a VSMC receptor to induce synthesis of cyclic guanosine-3' 5-monophosphate (cGMP). The downstream effects cGMP synthesis is both a reduction in Ca^{2+} being released from and an increased restoration of Ca^{2+} within the sarcoplasmic reticulum, both of which serve to decrease intracellular Ca^{2+} levels. Together this results in a decrease in a decrease in myosin light chain kinase activity resulting in decreased VSMC tension and subsequent vasorelaxation. By contrast, TXA_2 binds to thromboxane-prostanoid receptors on VSMCs and induces an increase in intracellular Ca^{2+} levels resulting in vasoconstriction[12,23].

Another well documented endothelium-derived vasoactive compound is nitric oxide, NO, a potent vasodilator[13,23,24]. NO is formed by conversion of the amino acid L-arginine to L-citrulline and NO by nitric oxide synthases[25]. NO then diffuses from the endothelium into the underlying smooth muscle where it binds to the enzyme soluble guanylyl cyclase. This bound and now activated enzyme converts guanosine triphosphate (GTP) to cGMP, again inducing a change in Ca^{2+} flux within the cytoplasmic reticulum resulting in vasorelaxation as seen for PGI_2[12,23].

1.2.4 Endothelial nitric oxide synthase (eNOS)

Endothelial nitric oxide synthase (eNOS) is one of three nitric oxide synthase (NOS) isoforms, each of which serve to produce NO. The others are iNOS - named for being inducible by cytokines and nNOS – named for being discovered in neurons. Although all three are present in blood vessels, it is eNOS which is the primary source of NO in the endothelium[25]. Like the inducible isoform iNOS, eNOS has been previously shown to be constitutively active and continuously produces a basal level of NO[24]. Although eNOS is constitutively active, the amount of activity is also able to be both up- and down-regulated[12,23,26].

1.2.4.1 Regulation of eNOS activity

It is well established that eNOS activity is dependent on its interactions with other proteins such as caveolin-1 (Cav1) and calmodulin (CaM)[23,24,27]. Cav1 is located in the caveolae, small invaginations of the cell membrane capable of being endocytosed. Cav1 binds to eNOS through the Cav1-binding domain and consequently sequesters eNOS in the caveolae[27]. This binding of eNOS to Cav1 also sterically inhibits the binding of eNOS to CaM, and CaM binding is necessary for NO production. Therefore, Cav1 could be considered a negative regulator of eNOS activity[23,24,27].

As such, in order for eNOS to produce NO, it must therefore be released from Cav1 and bind to CaM instead. This CaM-eNOS complex formation can be induced by two different types of pathways, described as either calcium Ca^{2+}-dependent or Ca^{2+}-independent[23,24,26].

In Ca^{2+}-dependent pathways, agonists either bind to their specific receptors or act to open ion channels in the EC membrane. This results in an influx of Ca^{2+} through these channels and/or Ca^{2+} being released from the endoplasmic reticulum, increasing the intracellular concentration of Ca^{2+}. Increased Ca^{2+} concentration promotes dissociation of eNOS from Cav1. Rising Ca^{2+} concentrations also alter the conformation of CaM and eNOS, enabling the association of CaM with the CaM-binding domain of eNOS, activating eNOS. An example of an agonist capable of inducing this pathway is acetylcholine (ACh)[23,24,26].

In Ca^{2+}-independent pathways directly activate eNOS through post-translational phosphorylation[28]. One of the most well described of these is the insulin signalling pathway[29]. Insulin binds to its receptor on the surface of ECs, activating the phosphatidylinositol-3 kinase and protein kinase B (PI3K-Akt) signalling. This stimulates the phosphorylation of eNOS at serine-1177, altering the protein conformation and exposing the CaM binding domain. As eNOS has a higher binding

affinity to CaM than it does to Cav1, eNOS preferentially binds CaM rather than Cav1, then translocates into the cytosol enabling NO production[23,24,28,29].

By contrast, whilst phosphorylation at serine-1177 up-regulates eNOS activity, phosphorylation at threonine-495 downregulates eNOS activity[28]. As with activating phosphorylation, agonists bind to their specific G-protein coupled receptors in the EC membrane. These G-proteins then activate Rho-kinase, which then phosphorylates eNOS at threonine-495, altering the enzyme conformation, preventing CaM binding and therefore stopping NO production. One such agonist capable of inducing this effect is TXA_2. The subsequent reduction in NO produces an additive effect in terms of TXA_2. inducing vasoconstriction[12,23,28].

1.2.4.2 eNOS uncoupling and endothelial dysfunction

eNOS is synthesised as a monomer and in order to produce NO must not only bind CaM, and the substrate L-arginine but also co-factors such as tetrahydrobiopterin (BH_4) to form eNOS dimers. It is these dimers which enable an electron flux in order to convert L-arginine to L-citrulline and NO via the eNOS oxygenase domain. BH_4 and L-arginine are both essential for eNOS dimer formation, known as eNOS coupling. Where there are insufficient quantities of either one or both of these compounds, these dimers do not form, and this is known as eNOS uncoupling. Uncoupled eNOS still has the oxygenase domains exposed but rather than producing NO, superoxide free radicals are produced instead[23,24,30]

When these superoxides are produced, they can induce a wide range of effects described as oxidative stress, including lipid and protein oxidisation[27], and DNA damage[31]. Additionally, the bioavailability of NO itself is further reduced due to it reacting with superoxide to generate peroxynitrite[32], itself another damaging oxidant. Ultimately, these reactive compounds promote inflammation, hypertension and vascular remodelling[31,33]. As such, it is necessary for eNOS activity to be tightly regulated to prevent these effects[23,26]. Recently, it has been shown that one such regulatory molecule is the cytoskeletal component protein ß-actin[30,34].

As discussed previously, in ECs, ß-actin is organised at the plasma membrane in fibres known as F-actin[16] and it has been shown that eNOS co-localises with these fibres where its oxygenase domain interacts with ß-actin. This interaction increases production of NO and reduces production of superoxides by eNOS. As yet, the specific mechanism by which this shift from superoxide production to NO production occurs is unknown. However, it is thought that ß-actin binding may alter eNOS conformation, thus enabling electron transfer[30,35].

1.3 Atherosclerosis

1.3.1 Endothelial dysfunction and initiation of atherogenesis

Endothelial dysfunction characterised by reduced eNOS activity and/or eNOS uncoupling, has been shown to play a key role in the development of atherosclerosis[36]. Evidence suggests that this dysfunction precedes plaque formation[37], with production of superoxides and reactive oxygen species (ROS) causing oxidative damage to both ECs and VSMCs[31,38]. Although the exact mechanism is as yet unknown, it is believed that this oxidative damage may lead to endothelial injury which results in increased endothelial permeability[23] and lipids accumulating in the arterial sub-endothelial space[3,33,39].

This sub-endothelial accumulation of lipids and lipoproteins, particularly low-density lipoproteins (LDLs) that undergo local oxidation, may in turn cause a self-perpetuating feedback loop whereby they reduce the uptake of L-arginine[33], driving eNOS uncoupling and superoxide production and increasing oxidative stress[40–42]. This link between lipids and vascular function is further indicated by the finding that hypercholesterolemia is associated with reduced endothelium-dependent vasodilation[24,33].

1.3.2 Inflammation and immune cell involvement in the developing atherosclerotic plaque

As the plaque progresses from a fatty streak to fibro-atheroma, the accumulating lipoproteins are oxidised by both enzymes within the arterial intima and by ROS produced as a result of eNOS dysfunction. In response to both the increasing bioavailability of ROS and the presence of oxidised lipids, ECs and VSMCs augment inflammatory processes, expressing leukocyte adhesion molecules, and secreting proteoglycans and chemokines. This attracts a variety of immune cells to the developing plaque including T-lymphocytes, mast cells, monocytes, and platelets. Again, eNOS dysfunction further accelerates this process since NO has been shown to reduce the activation and adhesion of platelets and leukocytes to the endothelium, reduce cytokine signalling and also reduce monocyte recruitment, thereby retarding plaque development[3,39].

Upon infiltration of the sub-endothelium, these monocytes both proliferate and transform into macrophages in response to signalling factors secreted by ECs. As some macrophages express scavenger receptors, they are able to absorb the oxidised lipoproteins. As these receptors are not downregulated by increasing intracellular lipid levels, these macrophages are therefore capable of continuously accumulating lipids.

These macrophages eventually develop into lipid-laden foam cells, features of which include storing some of the acquired cholesterol as crystals[3,39,43].

1.3.3 The roles of macrophage subtypes

Previously, macrophages were divided into three sub-classes, the quiescent M0, and the activated pro-inflammatory M1 and repairing M2 phenotypes[44]. These were identified by cell- markers such as the pro-inflammatory Tumour necrosis factors (TNFs) for M1 and the anti-inflammatory Interleukin-4 and Interleukin-10 cytokines for M2. It was also believed that M1 macrophages contained more lipids compared to M2 cells[39,43,45]. However, it has since been recognised that macrophages have high plasticity and recent scRNA-seq studies have shown that, as with ECs, these populations do not segregate as once believed. Additionally, the transcriptomics insights from these studies are redefining macrophage phenotypes[46–48].

Firstly, one such study examined murine aortic cell populations taken from both animals which had developed atherosclerosis having been fed a high-fat diet for 11 weeks and non-diseased aortas from animals fed a regular chow diet and identified three distinct macrophage populations. These three groups comprise of a resident population, a pro-inflammatory population with enhanced Interleukin-1b (*IL1B*) expression, and third distinct group found to express *TREM2* (triggered receptor expressed on myeloid cells 2). Interestingly, this study was also able to determine that whilst the resident population is present in both diseased and non-diseased aortas, the *IL1B*- and *TREM2*-enhanced populations were unique to the plaque microenvironment. Furthermore, whilst it was previously believed that the pro-inflammatory “M1” populations were involved in lipid metabolism, it was also noted that specialist lipid function genes were predominantly expressed by *TREM2*-expressing macrophages, rather than the pro-inflammatory *IL1B*-expressing population[46].

This finding is confirmed by another murine aortic atherosclerosis study which focussed on the gene expression patterns of foamy versus non-foamy macrophages. Unsurprisingly, foamy macrophages were found to have a distinct gene expression pattern related to lipid-processing. However, interestingly it was also found that the majority of macrophages expressing the pro-inflammatory marker *IL1B* were non-foamy[47]. These findings have been similarly replicated in a study on human atherosclerotic plaques obtained by carotid endarterectomy. Again, multiple distinct macrophage populations were identified, including one transcriptionally similar to those described as M1 previously insofar as expressing TNF and other pro-inflammatory mediators. Additionally, the two populations previously described as unique to atherosclerotic plaques, the *IL1B*-enhanced pro-inflammatory and *TREM2*-enhanced foamy populations were also observed in this study[48].

1.3.4 Advanced plaque architecture

Foam cells have limited migration and therefore remain in the lipid-rich core. As the number of foam cells and other activated cells increases within this microenvironment, inflammation increases, provoking the death of macrophages and VSMCs. This increasing cell death further increases inflammation due to the continuous release of pro-inflammatory cytokines, thus perpetuating the cycle and accelerating plaque development. As the plaque progresses, this self-perpetuating inflammatory cycle results in the formation of a necrotic core consisting of cellular debris and pooling lipids previously sequestered within cells, including cholesterol crystals. This necrotic core further promotes inflammation, particularly the release of the IL1B protein, inducing further cell death, and therefore a pro-inflammatory loop[3,39,49].

In response to increasing inflammation, both VSMCs and macrophages differentiate and proliferate before producing collagen and elastin proteins. These immature collagen and elastin proteins mature into cross-linked fibres with a higher tensile strength, and these fibres are assembled into a fibrous cap over the necrotic core[43,50–53]. This fibrous cap preserves lumenal blood flow and prevents thrombus formation by sequestering the core from the bloodstream[3,39].

As the plaque progresses, calcium deposition takes place in the subintimal space, initially developing in the lipid core. Although the exact mechanisms are not yet known, it has been suggested that increasing inflammation and subsequent apoptosis is a trigger point, with apoptotic cells acting as nucleating foci for the calcification to develop from[54]. Where a plaque has a fully calcified plate, the structure of the cap is strengthened, providing stability to the plaque structure and preventing rupture, as seen in patients with stable angina. It is worth noting that such plaques are often asymptomatic. However, these plaques may still trigger myocardial infarction or stroke should the plaque grow large enough to occlude the vessel[3,39,54].

1.3.5 Plaque rupture

Unchecked inflammation may lead to enhanced proteolytic activity which can weaken and thin the fibrous cap through inflammatory cytokines such as Interferon-gamma (IFN-y) inhibiting VSMC proliferation and subsequent production and maturation of collagen, and the activation of matrix metalloproteinases which degrade the collagen and elastin fibres. These plaques are then vulnerable to rupture through breakdown of the cap or endothelial erosion[3,39,52,55].

Cap breakdown typically occurs in the shoulder region of the plaque due to the cap being thinnest at this point and therefore vulnerable to the pulsatile stresses of blood pressure[52,56]. Although cap breakdown most often results in thrombotic occlusion and

major cardiovascular events, some unstable plaques may remain asymptomatic. This is due to the fissures in the cap being thin and superficial, therefore being overlaid with a new layer of fibrous cap without triggering acute thrombosis. As this process can occur multiple times at a single site, a small subset of these so-called rupture-and-repair plaques may remain asymptomatic unless progressing toward significant vessel occlusion[3,39].

Another subset of plaques rupture through localised endothelial cell apoptosis and subsequent denudation of the endothelium which leads to thrombosis formation on account of EC damage rather than fulminant cap rupture and these events account for the majority of the remaining 30% of cardiovascular thrombotic events. As such, regardless of the mechanism of plaque rupture or plaque size, should thrombosis occur and it extend into the arterial lumen occluding it, it may be life-threatening[3,39].

1.3.6 Physical factors of plaque stability

As plaques may be stable, asymptomatically maintain a cycle of rupture, repair and repeat, or instead undergo sudden life-threatening thrombotic rupture, several studies have been undertaken to understand what makes a plaque stable or vulnerable.

Physical factors identified include fibrous cap thickness with thinner caps being more prone to rupture. Plaque ulceration is indicative of previous fissures, which may then be protected again with a new layer of fibrous cap. This new cap may be thinner than the previously ruptured layer due to the collagen having not fully matured or simply being thinner due to exposure to the same inflammatory proteolytic processes[3,39,50]. This may make them particularly prone to further rupture regardless of whether the plaque is currently symptomatic or asymptomatic. Similarly, intraplaque haemorrhage may be indicative of a previous fissure that whilst resulting in thrombosis, did not result in total vascular occlusion. Similarly, the tensile strength of caps is also an important factor as a cap may be weaker due to collagen and/or elastin incompletely maturing or fragmenting[3,50,52,55].

Calcium deposition is also a key factor in plaque stability. Although large plate calcifications may provide stability to the plaque structure, so-called “spotty” calcifications, which are small nodules, are associated with an increased risk of major cardiovascular events due to plaque rupture. This is particularly the case with those at the shoulder of the plaque, as they increase the friability of the cap[3,51,54].

Unsurprisingly, the volume of both the whole plaque and the lipid core have also been associated with plaque rupture risk. Larger necrotic cores are associated with greater inflammation and therefore a greater risk of rupture through either cap thinning or endothelial erosion. Typically, larger plaques will have larger lipid cores and therefore

be subject to increased plaque stresses such as inflammation, thinning of the cap, and calcium deposition[3,39].

1.3.7 Molecular markers of plaque stability

In addition to studies identifying morphological and histological markers of plaque instability, several studies aimed to elucidate differential gene expression of asymptomatic and symptomatic plaques to identify novel pathways that may alter plaque stability.

Whilst necrosis and apoptosis of foam cells can result in increased inflammation and accelerated plaque development, in both of the scRNA-seq studies identifying *TREM2*-expressing foam cells as uniquely present in atherosclerosis, these cells were described as exerting influence on plaque architecture, suggesting a specialised role for these cells. In the murine healthy versus diseased aortic populations study, it was suggested that *TREM2* cells were potentially involved in calcification owing to their "osteoclast-like" gene expression patterns[46]. Similarly, in the human carotid endarterectomy study, these cells were described as having a "fibrosis-promoting" phenotype[48]. Within this study, a number of differentially expressed genes were identified as markers of this TREM2-expressing foam cell-like macrophage population. One such gene was the gene encoding glutamine synthetase (GS), *GLUL*, which was strongly reduced in these cells in direct contrast to the other specialised macrophage populations which all express GS equally[48]. Together, these studies suggest that cells expressing *TREM2* may be associated with alterations in plaque stability, although this remains speculative[46,48].

Another study looking to correlate gene expression with plaque stability used a combination approach of both molecular biology and histology. This work began with a microarray comparison of carotid plaque tissue from a small number of stroke patients and asymptomatic patients with similar risk factor profiles to identify potential candidate genes. The genes identified in this screen were then validated using qPCR of samples from an extended patient group. From this approach, 10 genes were confirmed as having significantly different expression between the two groups. These genes were then evaluated for their correlation with plaque features such as markers of cell death and proliferation, plaque ulceration, intra-plaque haemorrhage, and the degree of carotid artery stenosis. This study found the expression of most candidate genes correlated to at least one of these parameters with increased expression of one gene, *GLUL*, correlating to multiple markers, despite having not been previously identified as a marker of plaque stability[57].

Another study aiming to correlate gene expression patterns utilised bioinformatics methods to reanalyse microarray data generated previously from the macrophage-rich regions of human atherosclerotic plaques. These samples were originally obtained by carotid endarterectomy and consisted of six stable and five ruptured human atherosclerotic plaques. From this analysis, a total of 268 genes were identified as having differential expression between the two groups, with 68 being upregulated and 204 downregulated in ruptured plaques compared to the stable group. Unsurprisingly, a number of the genes downregulated in ruptured plaque are directly associated with plaque architecture, such as the extracellular matrix and collagen fibril genes *COL3A1* (collagen type III alpha 1 chain) and *COL1A2* (collagen type I alpha 2 chain). This suggests these plaques had a weaker cap phenotype. Again unsurprisingly, inflammatory marker genes were found to have been upregulated, including members of the TNF family. Interestingly, another gene found to be upregulated within ruptured plaques was again *GLUL*, thereby confirming the findings of the previous microarray study comparing stable to unstable plaques[58].

Together, these studies suggest there is a clear difference in gene expression patterns between stable and unstable or ruptured plaques as identified by physical markers. From these studies, a number of genes have been identified as influencing plaque stability, including the collagen genes *COL3A1* and *COL1A2*, and inflammatory markers in the TNF gene family. Additionally, novel markers have been identified such as increased *TREM2* expression being unique to macrophages in the atherosclerotic microenvironment and associated with these macrophages having specialist architectural roles. Additionally, these studies have also identified the gene *GLUL*, encoding the enzyme glutamine synthetase (GS), as a potential novel marker of plaque instability.

1.3.8 Increased GS as a marker of plaque instability

GLUL was first identified as a potential marker of plaque vulnerability in the combination approach study on human carotid plaques discussed before. Whilst most candidate genes correlated with at least one instability marker, *GLUL*, was found to have a 2.2-fold increased expression and shown to correlate with multiple features. These features included not only physical indicators of plaque instability including the degree of carotid artery stenosis, plaque ulceration, intraplaque haemorrhage, and calcification, but also all three markers of cell death and proliferation tested within this study. Furthermore, this study also utilised immunohistochemical techniques to validate these findings and determine patterns of protein expression within the plaques through staining. This analysis showed the product of *GLUL*, glutamine synthetase (GS), to be

most expressed in macrophages and smooth muscle cells and strong staining was seen around the necrotic lipid core and at the shoulder of the plaque[57].

Similarly, in one microarray study on human carotid plaques, plaques were classified by whether patients were symptomatic or asymptomatic, with 40 asymptomatic and 87 symptomatic plaques assayed respectively. *GLUL* was found to be upregulated in symptomatic plaques, with symptomatic plaques having a 1.3-fold increase compared to asymptomatic samples[59].

These findings that *GLUL* is expressed in macrophages and may be a marker of plaque stability have both been further indicated by a recent study analysing macrophage-rich regions also taken from human carotid plaques. In this study, although they focussed on genes associated with either inflammation or the production of extracellular matrix proteins such as collagen, *GLUL* was also measured on that chip and found to be significantly increased, with a 1.1-fold increase in ruptured plaques when compared to stable plaques[58].

1.4 Glutamine synthetase

1.4.1 The role of glutamine synthetase

As discussed previously, various studies have been undertaken with the aim of correlating gene expression to markers of atherosclerotic plaque stability or instability, of which a number of studies have identified *GLUL*, as a candidate gene[57–59].

GLUL encodes the enzyme glutamine synthetase (GS), the primary role of which is well characterised insofar as it is the only enzyme capable of *de novo* synthesis of glutamine. GS produces glutamine from the precursors glutamate and ammonia in an ATP-dependent reaction. The reverse process is possible through the glutaminase enzymes, allowing these compounds to be recycled and reused[60].

Studies have shown that both the expression of GS and metabolism of glutamine are cell- and tissue- dependent. For example, GS expression is known to be high in the brain due to the essential requirement for ammonia and glutamate disposal in the brain[61]. GS is also highly expressed within the kidneys as it is involved in ammonia detoxification, processing excess ammonia unable to be converted into urea and, in doing so, providing hydrogen ions for use in subsequent ammonia production from waste amino acids[60]. Within the liver, GS expression is again linked to ammonia homeostasis, with *GLUL* deficient mice experiencing hyperammonemia. Interestingly, GS is expressed zonally within liver lobules, with only the hepatocytes closest to the hepatic portal having a high expression of GS[62,63].

Whilst this primary role of GS is well described, *de novo* glutamine synthesis is arguably not critical within ECs as glutamine is present in high levels within the blood and able to be both transported into and consumed by the ECs[64,65].

Studies have also indicated that within ECs, GS and glutamine are associated with homeostasis of other amino acids such as arginine[66] and asparagine[67], hinting at other roles. Furthermore, a recent study has indicated that GS is not only involved in the synthesis and homeostasis of glutamine, but is also involved in DNA damage repair through influencing nucleotide metabolism[68].

This suggestion that GS expression varies between organs and even between cells within these organs has been further extended by recent scRNA-seq studies demonstrating that not only is *GLUL* expressed in an organotypic manner, but it is also expressed in a cell specific manner too, with only certain subsets of cells strongly expressing *GLUL*.

1.4.2 Insights into *GLUL* expression from single-cell RNA sequencing

As discussed previously, the advent of scRNA-seq technology has enabled us to investigate cellular heterogeneity and in differential gene expression between cell clusters. In addition to these insights, it enables us to understand the expression patterns of specific genes of interest beyond those previously identified as enriched population markers.

The *Tabula Muris* project was the first project to attempt to create a whole organism atlas and in doing so isolated and individually RNA sequenced over 100,000 cells from 20 different organs and tissues from the mouse model, including both adult and foetal specimens[17]. This has since been replicated using human donor organs and tissues to produce the Human Cell Landscape[21]. Additionally, the Murine EC Atlas study has focussed specifically on the clustering of EC subsets by functional analysis of the gene expression patterns[18]. In the case of all three of these studies, the data has been made freely available to download online and applications have also been published online for the data to be custom visualised. Tools enabling this custom visualisation include being able to select cells from all or specific tissues and to be able to search for specific genes of interest.

On searching these sets, the heterogeneity of *GLUL* becomes apparent as, across all three studies, almost all clusters contain some *GLUL*-expressing cells, but only certain clusters have a comparatively high percentage of cells expressing GLUL at varying levels, and only certain cell types express relatively high levels of *GLUL*. For example, one cluster in each study can be identified as being similar to one another despite being different studies across two species, as these clusters are all brain-derived and have a high-percentage of *GLUL*-expressing cells with overall high expression levels[17,18,21]. This finding concurs with previously published data that GS is essential in the brain for ammonia detoxification[61] and similarly, the authors have each noted other gene expression patterns and markers have been corroborated with previously published work[17,18,21].

Together these insights further confirm that *GLUL* expression is not uniform and may even suggest that *GLUL* expression may be indicative of specialist roles for subsets of cells. However, they fail to give us an insight into *GLUL* expression patterns and mechanistic interactions linked to disease development.

1.4.3 The associates of reduced *GLUL* expression

1.4.3.1 Reduced *GLUL* expression associated with increased Coronary Heart Disease (CHD) risk

Prior to scRNA-seq studies elucidating cellular gene expression patterns associated with disease, genome-wide association studies (GWAS) provided insight about single nucleotide polymorphisms (SNPs), and therefore putative genes, linked to disease. One such study examining the significantly increased risk of atherosclerosis related major cardiovascular events in patients with type 2 diabetes mellitus (T2DM) implicated *GLUL*[9].

This study used a genome-wide single nucleotide polymorphism (SNP) array to identify genetic loci associated with coronary heart disease (CHD) in patients with T2DM. Of the 2543016 SNPs tested, only 1 SNP, rs10911021 (T>C), showed significant association with CHD across all five patient cohorts included within this study. From this it was also determined that each risk allele confers a 36% increased risk of major cardiovascular events within these patients. This study went on to assess expression of a number of local genes, including the two closest located genes - *ZNF648* and *GLUL* in human umbilical vein endothelial cells (HUVECs) taken from a randomly selected cohort of non-diabetic controls. Whilst *ZNF648* was found to not be expressed in HUVECs and other genes had no correlation with rs10911021 status, *GLUL* expression significantly correlated to the SNP. Compared to homozygotes for the protective allele (T/T), homozygotes for the risk allele (C/C) were found to have a 32% reduction in *GLUL* expression and heterozygotes found to have intermediate expression levels[9]. These findings have since been independently validated on a separate cohort[69]. Strikingly, these studies have also shown that this SNP, rs10911021, conferred no additional risk to non-diabetics suggesting a direct relationship between this SNP and the significantly increased risk of CVD in T2DM[9,69].

1.4.3.2 Reduced *GLUL* expression and high-density lipoprotein cholesterol levels

A further study conducted independently examined whether the SNP rs10911021 is associated with increased CHD risk in a cohort of participants with and without T2DM. This confirmed that presence of the C risk allele of the SNP is associated with CHD risk, and again this was only apparent in the T2DM patients[70].

They also went on to establish whether or not there was a relationship between SNP genotype and serum glutamine concentrations and found there is no association. This study also opted to examine the relationship between the SNP and any of the nine

amino acids which may be transported into the cell via the γ-glutamyl cycle (see later) and determined that, as with glutamine, there is no relationship between genotype and serum concentrations of these amino acids[70].

This study then noted that this SNP is located close to another CHD-associated SNP, rs1689800 (A>G). The SNP rs1689800 is associated with lowered high-density lipoprotein-cholesterol (HDL-C) levels[70], an established marker of increased CHD mortality[71]. As such, this study opted to see whether there was also a relationship between rs10911021 and serum concentrations of HDL-C in both diabetic and non-diabetic partipants[70].

From this investigation, it was determined that whilst the risk allele is associated with a lower mean plasma level of HDL-C in participants without T2DM, unexpectedly it is associated with an increased level of HDL-C in participants with T2DM when compared to matched participants homozygous for the protective allele. This finding suggests a complex relationship between this SNP, T2DM and CHD risk[70].

1.4.3.3 Reduced *GLUL* expression alters the γ-glutamyl cycle

Within the original study of Qi *et al* identifying association between the SNP rs10911021 and CHD risk in people with T2DM, a cohort of 100 T2DM patients were then examined for an association between the SNP and concentrations of either glutamate or glutamine in the blood plasma as these are the substrate and product of GS, respectively. Whilst it was found that there is no correlation between SNP status and either of these measures, they identified that there was a decreased ratio of pyroglutamic acid to glutamate in homozygotes for the risk allele (C/C) when compared to homozygotes for the protective allele(T/T). Furthermore, it was also found that when separating these patients by whether or not they had developed CHD, the pyroglutamic acid to glutamate ratio was also significantly reduced in the CHD patient group compared to the patient group. As both pyroglutamic acid and glutamate are intermediate compounds in the γ-glutamyl cycle, it was suggested that this may at least partially explain the association between rs10911021 and CHD in people with T2DM[9].

The γ-glutamyl cycle is involved in both amino acid metabolism and importantly in the homeostasis of glutathione. Glutathione is an antioxidant compound which serves to protect cells from oxidative stress induced by excessive ROS concentrations. Alterations in glutathione homeostasis may therefore lead to cellular damage and injury and subsequently inflammation, promoting progression of atherosclerosis[9,72]. As such, the influence and association of this SNP with the γ-glutamyl cycle was then further investigated in a separate study by the same investigators[72].

In this study, HUVECs were derived from 62 donors. The association between rs10911021 genotype and *GLUL* expression was measured after quantification of GS protein expression. As expected, homozygotes for the risk allele (C/C) were found to have a 36% reduction in GS expression compared to homozygotes for the protective allele (T/T), and heterozygotes found to have intermediate expression levels[72], further confirming the findings of the initial study[9].

Next, the relationship between SNP genotype and intracellular glutamate or glutamine concentration was examined, although no association was observed. Whilst it was found that there was also no link between SNP genotype and intracellular glutathione concentrations, the ratio between glutathione and glutamate inversely correlated to SNP status with an 18% decrease in homozygotes for the risk allele (C/C) when compared to homozygotes for the protective allele (T/T), and an intermediate 9% decrease in heterozygotes, suggesting a gene dosage effect[72].

The cellular metabolome was then quantified and a panel of 35 metabolites was selected for analysis, all of which were linked to either glutamate metabolism, the γ-glutamyl cycle or glutathione metabolism. Of these, nine were shown to be significantly associated with SNP status, with the majority showing a positive correlation with the risk allele. For these metabolites, concentrations were increased in heterozygotes for the risk allele when compared to homozygotes for the protective allele and were further increased in homozygotes for the risk allele. Notably, only one metabolite, S-lactoyl-glutathione, showed the inverse – a negative correlation between C allele dosage and intracellular metabolite concentrations[72].

S-lactoyl-glutathione is a product of the detoxification of the reactive compound methylglyoxal, a precursor of various advanced glycolysis endproducts (AGEs)[72]. As increased serum concentrations of these methylglyoxal-derived AGEs has been linked to increased cardiovascular disease mortality in both diabetic and non-diabetic patients[73,74], this led to the hypothesis that decreased S-lactoyl-glutathione levels may be linked to defective methylglyoxal detoxification and may therefore play a part in the increased cardiovascular risk seen in patients carrying the risk allele[72].

Further metabolomic analysis confirmed that HUVECs homozygous for the risk allele (C/C) had over 2-fold greater methylglyoxal levels when compared to those homozygous for the protective allele (T/T), and an intermediate increase was also measured in cells heterozygous for the risk allele. In order to confirm that decreased *GLUL* expression was directly responsible for the increase in intracellular methylglyoxal, HUVECs from 14 unique donors were transfected with either an shRNA (short hairpin RNA) designed to downregulate *GLUL* expression or a scrambled control

shRNA. Transduction with the *GLUL*-specific decreased GS protein by 40% and led to a concurrent 40% increase in methylglyoxal concentrations[72].

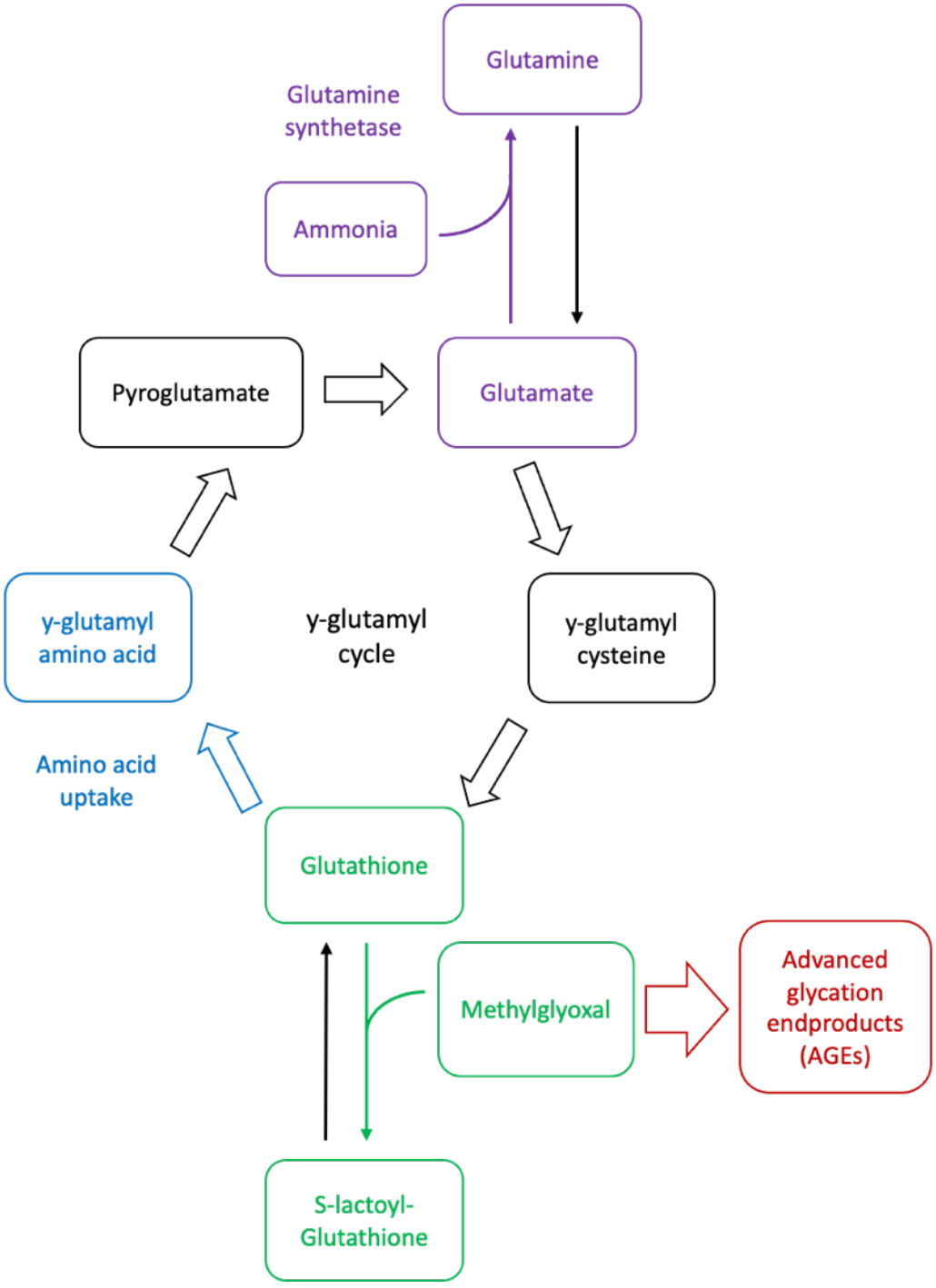

Figure 1: Simplified schematic representation of the γ-glutamyl cycle
Detoxification of methylglyoxal by glutathione (**green**) prevents the production of advanced glycation endproducts (AGEs) associated with increased CVD mortality in both diabetic and non-diabetic patients (**red**). The relationship of glutamine synthetase (*GLUL*) to the γ-glutamyl cycle is highlighted in **purple**, alongside the role of this cycle in amino acid metabolism (**blue**). Adapted from the work of Pipino *et al* [72]

1.4.3.4 Reduced *GLUL* expression reduces angiogenesis and increases inflammation

In addition to studies focusing specifically on the rs10911021 SNP, other studies have also directly investigated the effect of reduced GS expression. One such study in macrophages utilised both genetic knockout and the drug methionine sulfoximine (MSO) that inhibits the enzymatic function of GS. This study first used MSO *in vitro* on M0 quiescent macrophages and found it to skew the ratio of macrophages from the "repair" state to a "pro-inflammatory" state. The *in vivo* phase of this study then looked at the effects of genetic knockout of *GLUL* in macrophages on inflammation and vascularity within the context of tumours. This found that reduced GS expression promoted vessel pruning, reduced endothelial cell branching, and increased inflammation[44].

This role of endothelial GS expression in angiogenesis has also been investigated by Eelen *et al*. using an inducible genetic knockout approach, with a focus on angiogenesis[64]. Unexpectedly, Eelen *et al*. found that whilst endothelial GS is capable of producing glutamine, and will do so in response to severely reduced extracellular glutamine availability, this function is actually a minor role for GS in ECs and instead they described a previously undiscovered role of GS[64].

In this study, the effect of EC-specific *GLUL*-knockout (GS^{ECKO}) on angiogenesis was examined through comparing retinal vascular plexus branching versus wild-type (WT) controls. GS^{ECKO} animals had reduced retinal vascular branching and reduced radial expansion compared to their WT controls. To examine this further, HUVECs were then transfected with a *GLUL*-specific shRNA, reducing GS expression by >80%, and *in vitro* sprouting assays conducted with these *GLUL*-knockdown cells ($GLUL^{KD}$). Again, reduced GS resulted in reduced sprouting and further investigation determined that, at least at physiological concentrations of glutamine, this was not due to reduced EC viability, altered proliferation, increased oxidative stress or changes in either glutathione levels or glutamine oxidation. Cell migration and motility assays were also conducted with these $GLUL^{KD}$ HUVECs, revealing impairment of both[64].

It was also observed that angiogenic sprouts in GS^{ECKO} animals had fewer filopodia, F-actin rich structures which guide EC migration. $GLUL^{KD}$ HUVECs also had reduced lamellipodial area, again indicating impaired membrane F-actin remodelling. Together these, and other, findings suggested that reducing GS negatively affects the remodelling of the actin cytoskeleton required for successful cell migration. Furthermore, $GLUL^{KD}$ HUVECs had increased F-actin levels, predominantly organised into stress-fibre bundles[64].

Murine models of pathological angiogenesis were also treated with MSO in order to inhibit GS activity to see whether this would produce the same outcome as genetically reducing *GLUL* expression. As expected, MSO reduced vessel sprouting in these models. This was explored further through treatment of *GLUL*^{KD} HUVECs with MSO and again, reduced sprouting, reduced motility and decreased lamellipodia were observed alongside increased F-actin levels. As the GS^{ECKO} phenotype is able to be recapitulated by MSO treatment, the results of these experiments not only further confirmed that GS is directly involved in regulating angiogenesis, but that it does so through modulating actin cytoskeleton remodelling and that the catalytic site of the enzyme plays a crucial role in this process[64].

As the RHO (Ras homolog) family of GTPase enzymes are known to mediate actin cytoskeletal remodelling[75], this led to the hypothesis that one of these proteins may be downstream of GS. Within the RHO family, one particular member, RHOJ (Ras homolog family member J), is restricted to ECs[76] and involved in the remodelling of actin within filopodia[77] and therefore this was investigated as a downstream target of GS. From these experiments, it was determined that not only was the decreased motility of *GLUL*^{KD} ECs phenocopied in *RHOJ*^{KD} ECs, but that *GLUL*^{KD} ECs had reduced RHOJ. The direct interaction between GS and RHOJ was then confirmed by a variety of assays including co-precipitation. From these assays, it was also determined that GS and RHOJ proteins predominantly co-localise and interact within the membrane. As membrane localisation and activation of a protein commonly requires palmitoylation, further experimentation determined that GS undergoes autopalmitoylation and directly palmitoylates RHOJ in order to membrane localise it, therefore modulating actin cytoskeleton remodelling[64].

This study by Eelen *et al* therefore represents an entirely new role for GS, independent of its classical roles within ammonia detoxification and the γ-glutamyl cycle[64]. However, sprouting angiogenesis is a capillary and venular restricted phenomenon[78,79] and whilst GS expression within these subsets of ECs is further supported by the findings of the Murine EC Atlas study by Kalucka *et al*, this study also indicated that *GLUL* expression is enriched within the arterial subset[18]. Despite this, the role of GS within arteries has not yet been established and further work would be required to confirm that the mechanism described by Eelen *et al* is also active within the arterial EC subset.

1.5 Summary of the literature

1.5.1 Cardiovascular disease and atherosclerosis

Cardiovascular disease is now a leading cause of severe disability and the leading cause of mortality globally, accounting for approximately one third of all deaths, including here in the UK. Many of these deaths are premature, occurring before the age of 75. The majority of these deaths are caused by strokes and myocardial infarctions and the unifying underlying pathology of these major cardiovascular events (MCEs) is atherosclerosis. Atherosclerosis is a complex multifactorial disease and much work has been undertaken to better understand the factors influencing both the risk of developing atherosclerosis, and of events relating to plaque rupture. Earlier work focussed on this has identified environmental factors such as smoking, pollution and poverty, co-morbid disorders such as obesity, T2DM and hypertension, and irreversible personal risk factors such as sex and age. More recently, work has focussed on the mechanisms underlying atherosclerosis and endothelial dysfunction due to reduced eNOS activity and/or eNOS uncoupling has been shown to play a key role in the development of atherosclerosis and may precede plaque formation through localised cellular oxidative damage and increased inflammation.

In addition to mechanistic studies elucidating the underpinning processes of atherogenesis, plaque architecture has also been examined to identify physical features increasing the risk of MCEs. Whilst plaque volume is linked with MCEs, small non-obstructive plaques may still be unstable and rupture leading to vessel occlusion through thrombosis. These unstable plaques have been shown to have larger necrotic lipid-filled cores and thinner fibrous caps which may also have disordered collagen and elastin due to inflammation leading to proteolytic processes degrading the cap, and/or production of immature collagen from repeated rupture and repair cycles. These weaker caps may lead to multiple fissures and intraplaque haemorrhages and these factors are therefore also indicative of plaque instability. More recently, work has been undertaken to link these properties to molecular factors influencing plaque stability. From these studies, a number of genes have been identified as influencing plaque stability, including the collagen genes *COL3A1* and *COL1A2*, inflammatory markers in the TNF gene family, and novel markers such as macrophage expression of *GLUL*. However, very little is known about the role of *GLUL* in atherogenesis and plaque stability.

1.5.2 GS and cardiovascular risk

Increased expression of the gene *GLUL* has been identified as a novel marker of plaque instability. However, by contrast, lower *GLUL* expression or activity induces a pro-inflammatory skewing in macrophages and may therefore be expected to adversely impact on plaque stability. Additionally, decreased *GLUL* expression related to the SNP rs10911021 has been linked to an increased risk of CHD in T2DM and it has been suggested that this may be due to perturbed levels of γ-glutamyl cycle intermediates resulting in increased oxidative damage. Notably, scRNA-seq studies have shown that *GLUL* expression is enriched in arterial endothelial cells (i.e. a higher percentage of these cells express *GLUL* when compared to other populations of cells), yet we have very little knowledge of the role GS plays in arterial function or disease. The current literature indicates *GLUL* has an important role in arterial biology and that its increased expression in vulnerable plaques could plausibly be an adaptive response, but this requires formal proof. Moreover, the novel role of GS identified by Eelen *et al*. is a reminder that we should not assume the association between *GLUL* and cardiovascular risk in T2DM relates solely to metabolic perturbation and could instead be contributed to be altered actin remodelling, or other undefined factors.

1.5.3 Conclusions

Despite strides forward in our understanding of cardiovascular disease, atherosclerosis remains a leading cause of mortality and disability globally and much work is yet to be done. Despite a wealth of new evidence that GS may play a role in vascular health and disease including a variety of scRNA-seq studies looking at a broad range of cells, the role of GS within the vasculature and the potential influence of GS on atherosclerosis has not yet been fully explored.

Two separate studies have independently identified increased GS expression as a novel marker of plaque instability, and this directly contrasts with the finding that reduced GS expression increases CHD risk in patients with T2DM through altered γ-glutamyl cycle metabolism and the finding that reduced GS expression skews macrophages to a more pro-inflammatory phenotype. Together these studies suggest that GS may have a role in multiple cell types involved in atherosclerosis and further work is required to not only characterise the impact of reduced GS expression on atherogenesis and plaque stability but also to explore whether GS expression does indeed increase in certain cell populations within the developing plaque.

Furthermore, the recent findings that GS has a role within the endothelium beyond *de novo* glutamine synthesis insofar as actin modulation via RhoJ raises further questions

around the function of the healthy vasculature. As such, further work is required to explore this pathway and examine whether eNOS activity may be altered through its interaction with F-actin fibres being altered by the reduced expression of GS, and its subsequent effect on vascular tone, particularly as the relationship between vascular tone and atherogenesis is well described within the literature.

1.6 Hypotheses, Aims and Objectives

Main Objective: This project aims to define the role of GS in atherosclerosis and vascular function

Aim 1: Characterise the role of GS in the development of atherosclerosis

Hypothesis: Reduced GS expression alters the development of atherosclerosis.

Null hypothesis: There is no significant difference in the development of atherosclerosis when GS expression is reduced

Aim 2: Characterise the role of GS in vascular function in health

Hypothesis: Reduced GS expression alters eNOS activity, affecting endothelial function and therefore alters vascular tone.

Null hypothesis: There is no significant difference in eNOS activity and endothelial function and therefore there is no difference in vascular tone when GS expression is reduced

Chapter 2 Materials

2.1 Animal work

Table 1: Experimental mice

Strain	Source
C57BL6/J	Charles River, Belgium
$ApoE^{-/-}$	Charles River, Belgium
$GS^{+/LacZ}$	Non-commercial – University of Amsterdam, Netherlands [80]
$GS^{+/LacZ}ApoE^{-/-}$	Non-commercial – University of Leeds, UK

Table 2: *In vivo* experimental resources

Item	Supplier	Product code
Actrapid® human recombinant insulin, 100 international units/ml	Novo-Nordisk, Denmark	N/A - Prescription only medicine (POM)
D-(+)-glucose	Sigma-Aldrich, USA	G8270
Gibco™ Dulbecco's phosphate buffered saline (PBS)	Thermo Fisher Scientific, USA	14190144
Accu-Chek® Aviva disposable glucose testing strips	Roche Diagnostics, Switzerland	N/A
Accu-Chek® Aviva portable glucometer	Roche Diagnostics, Switzerland	N/A
Disposable surgical scalpel with No.10 blade	Swann-Morton Limited, UK	0501
Millex® Sterile syringe 33mm diameter filter unit, 0.22µm	Merck-Millipore Ltd, Ireland	SLGP033RS
BD Micro-Fine™ Insulin Syringe	BD Biosciences, USA	324892

Table 3: Harvesting equipment and resources

Item	Supplier	Product code
IsoFlo® isoflurane (inhalational anaesthetic)	Zoetis, UK	N/A – Prescription only veterinary medicine
Dumont #55 straight forceps	World Precision Instruments, USA	14099
Vannas student curved spring scissors	Fine Science Tools, Canada	91501-09
Vannas spring scissors – 2.5mm cutting edge	Fine Science Tools, Canada	15000-08
Straight scissors	Fine Science Tools, Canada	91460-11
Phosphate buffered saline (PBS) tablets	Sigma-Aldrich, USA	P4417
Formaldehyde 4% stabilised, buffered (pH 7.0 ±0.2)	VWR International, USA	9713.5000

Table 4: Murine Diets including dietary composition

		Chow Diet	Western Diet
Supplier		B&K Universal Ltd, UK	Special Diet Services, UK
Product name		Beekay Rat and Mouse Diet No 1	Western RD
Product code		#BK001E	#829100
Dietary composition		**% of calories**	
Fats	**Total**	4.73	21.4
	Cholesterol	0	0.2
Carbohydrates		59.73	50%
Protein		18.68	1%

2.2 Gene expression studies

Table 5: Equipment and consumables for molecular biology work

Item	Supplier	Product code
TissueLyser II	QIAgen, Germany	85300
6mm metal cone balls	Retsch Ltd, UK	RS.22.455.0003C
SafeSeal 2mL round-bottom microcentrifuge tubes	Sarstedt, Germany	72.695.500
1.5mL microcentrifuge tubes	Sarstedt, Germany	72.690.001
Heraeus Fresco™ 17 temperature-controlled centrifuge	Thermo Fisher Scientific, USA	75002420
DS-11 FX+ spectrophotometer / fluorometer	DeNovix, USA	N/A
0.2mL thin-walled microcentrifuge PCR tubes 8 tube strips with individual flat-caps	STARLAB Ltd, UK	A1402-3700
MyFuge™ Mini centrifuge with clear lid	Benchmark Scientific, USA	C1008-C
Applied Biosystems® Veriti™ 96 well thermal cycler	Thermo Fisher Scientific, USA	4375786
LightCycler® 480 II	Roche Life Sciences, Germany	05015278001
96 well BrightWhite qPCR plates for Roche LightCycler® 480	PrimerDesign, UK	BW-96480
Optical adhesive seal for BrightWhite 96/384 well plates	PrimerDesign UK	BW-ADVSEAL
Compact centrifuge with microplate rotors	Eppendorf, Germany	5430

Table 6: Molecular biology kits and reagents

Item	Supplier	Product code
TRI reagent solution	Thermo Fisher Scientific, USA	AM9738
1-Bromo-3-Chloropropane	Sigma-Aldrich, USA	B9673-200ML
Ethanol, absolute (200 proof), molecular grade (Fisher Bioreagents™)	Thermo Fisher Scientific, USA	BP2818-500
High-Capacity cDNA Reverse Transcription kit	Thermo Fisher Scientfic, USA	4368814
Invitrogen UltraPure DNase/RNase-Free Distilled Water	Thermo Fisher Scientific, USA	10977015
PrecisionPLUS qPCR Master Mix including SYBR® Green dye	PrimerDesign, UK	PPLUS-CL
Primers for quantitative PCR (qPCR)	Integrated DNA Technologies, USA	See Table 7
PrecisionPLUS qPCR Master Mix for hydrolysis probe quantification	PrimerDesign, UK	PPLUS-CL
TaqMan™ Gene expression assay probe for Mouse *ACTB* (ß-Actin), FAM conjugated	Thermo Fisher Scientific, USA	Mm02619580_g1
TaqMan™ Gene expression assay probe for Mouse *GLUL,* FAM conjugated	Thermo Fisher Scientific, USA	Mm00725701_s1

Table 7: SYBR® green qPCR primer information

Gene target	Primer name	Primer Sequence 5'→3'	Melting temperature (Tm) (°C)	Product length
Mouse *GLUL*	mGSaF	CGGAAACCTGCAGAGACCAA	60.25	120
	mGSaR	GTGGCCGTCTGTTCCCATAA	60.04	
Mouse *HPRT*	HPRT F	GTTGGGCTTACCTCACTGCT	59.96	125
	HPRT R	TAATCACGACGCTGGGACTG	59.83	
	M18S_R	AGAAAAGAGCGGAGGTTCGG	60.04	

2.3 Atherosclerosis studies

2.3.1 General histology

Table 8: Slide preparation reagents and consumables

Item	Supplier	Product code
Uncoated glass slides	Thermo Fisher Scientific, USA	10149870
(3-Aminopropyl)triethoxysilane (APTES)	Sigma-Aldrich, USA	A3648
Acetone	Thermo Fisher Scientific, USA	A1600/PC17
Hydrochloric acid	Sigma-Aldrich, USA	320331
Ethanol	Thermo Fisher Scientific, USA	10680993

Table 9: General histological reagents and consumables

Item	Supplier	Product code
Phosphate buffered saline (PBS) tablets	Sigma-Aldrich, USA	P4417
Formaldehyde 4% stabilised, buffered (pH 7.0 ±0.2)	VWR International, USA	9713.5000
Isopropanol	Thermo Fisher Scientific, USA	11358461
Paraffin wax embedding medium, Solidification point: 55 - 58 °C, in pastille form, Gurr™	VWR International, USA	8002-74-2
Ethanol	Thermo Fisher Scientific, USA	10680993
Xylene	VWR International, USA	28973.328
Potassium permanganate ($KMnO_4$)	Sigma-Aldrich, USA	31404
Oxalic acid	Sigma-Aldrich, USA	75688

Miller's elastin stain	CellPath, Ltd., UK	RHS-235-500ML
Van Gieson solution (0.05% acid fuchsin in saturated picric acid)	Sigma-Aldrich, USA	HT254
Sirius red (Direct Red 80)	Sigma-Aldrich, USA	365548-5G
Oil red O	Sigma-Aldrich, USA	O0625
Picric acid solution, saturated	Sigma-Aldrich, USA	P6744
Acetic acid, glacial	Sigma-Aldrich, USA	A6283
DPX mounting medium	Sigma-Aldrich, USA	06522
DAPI (4′,6-diamidino-2-phenylindole) Fluoromount-G® mounting medium	Southern Biotech, USA	0100-20
Glass coverslips, 22x50mm	Thermo Fisher Scientific, USA	12342118
S35 microtome blades, Fine	Feather, Japan	S35 "Fine"

2.3.2 Immunofluorescent work

Table 10: General equipment and consumables for immunofluorescent work

Item	**Supplier**	**Product code**
CM3050 S Research cryostat microtome	Leica Biosystems, Germany	14903050S01
Low-profile disposable blades 819	Leica Biosystems, Germany	14035838925
Optimum Cutting Temperature (OCT) compound	VWR International, USA	361603E
SuperFrost Plus™ Adhesion glass slides	Thermo Fisher Scientific, USA	10149870
Glass coverslips, 22x50mm	Thermo Fisher Scientific, USA	12342118

Table 11: Immunofluorescent staining antibodies

Target	Species	Supplier	Product code	Dilution
Anti-β-galactosidase	Rabbit	Thermo Fisher Scientific, USA	A11132	1:100
Anti-glutamine synthetase	Rabbit	Abcam, UK	Ab176562	1:100
Anti-α-smooth muscle actin	Mouse	Abcam, UK	ab7817	1:100
Anti-Rabbit Alexa Fluor 647	Goat	Thermo Fisher Scientific, USA	A21246	1:200
Anti-Mouse DyLight 549	Donkey	Novus Biologicals, USA	NBP1-72933	1:100

Table 12: Other reagents for immunofluorescent staining

Item	Supplier	Product code
M.O.M.® (mouse on mouse) blocking reagent	Vector Laboratories, USA	MKB-2213
Dako® Goat serum	Agilent Technologies, USA	X0907
Donkey serum, 10mL	Sigma-Aldrich, USA	D9663-10ML
Isolectin-B4 conjugated to Alexa Fluor 488; 1:100	Thermo Fisher Scientific, USA	I21411
HCS LipidTOX™ Green Neutral Lipid Stain, for cellular imaging - conjugated to Alexa Fluor 488; 1:100	Thermo Fisher Scientific, USA	H34475
DAPI (4′,6-diamidino-2-phenylindole) Fluoromount-G® mounting medium	Southern Biotech, USA	0100-20

Table 13: Immunofluorescent staining buffer

Reagent	Supplier	Product code
Phosphate buffered saline (PBS) tablets	Sigma-Aldrich, USA	P4417
Triton™ X-100	Sigma-Aldrich, USA	X100
Bovine serum albumin (BSA)	Sigma-Aldrich, USA	A9647

Table 14: Confocal microscopy imaging equipment

Item	Supplier
LSM 880 + Airyscan upright confocal microscope*	Carl Zeiss, Germany
Zen Black software	
EC Plan-Neofluor 10x/0.30	
Plan-Apochromat 20x/0.8	
Plan-Apochromat 40x/1.4 Oil DIC	

*Further information on this imaging setup including lasers, filters, and the Airyscan module is available at: https://biologicalsciences.leeds.ac.uk/facilities/doc/bio-imaging-equipment/page/6

2.4 Vascular function studies

Table 15: Krebs-Henseleit buffer – reagents and composition

Reagent	Formula	Supplier	Product code	mmol/l
Sodium chloride	NaCl	Thermo Fisher Scientfic, USA	S/1360/63	119
Sodium hydrogen carbonate	$NaHCO_3$	Thermo Fisher Scientific, USA	S/4240/60	25
D-(+)-glucose	$C_6H_{12}O_6$	Sigma-Aldrich, USA	G8270	11
Potassium chloride	KCl	Thermo Fisher Scientific, USA	P/4280/60	4.7
Calcium chloride dihydrate	$CaCl_2.2H_2O$	Thermo Fisher Scientific, USA	F.W.147.02	2.5
Magnesium sulphate heptahydrate	$MgSO4.7H_2O$	Thermo Fisher Scientific, USA	M/1000/60	1.19
Potassium phosphate monobasic	KH_2PO_4	Sigma-Aldrich, USA	795488	1.18

2.4.1 Aortic vasomotion

Table 16: Organ Bath equipment and software

Item	Supplier	Product code
SZ61 Binocular stereo dissecting microscope	Olympus Corporation, Japan	SZ61BR
8 chamber automatic organ bath	Panlab, USA	LE01086
25ml organ chambers	Panlab, USA	LE0125
Thermostatic power pack	ADInstruments, UK	LE13206
0-20g Isometric force transducers	ADInstruments, UK	MLT0420
Octal bridge amp	ADInstruments, UK	FE228
Powerlab 8/35	ADInstruments, UK	PL3508

Table 17: Drugs used in vasomotion study

Name	Abbreviation	Supplier	Product code
Potassium chloride	KCl	Thermo Fisher Scientific, USA	P/4280/60
(R)-(-)-Phenylephrine hydrochloride	PE	Sigma-Aldrich, USA	P6126
Acetylcholine	ACh	Sigma-Aldrich, USA	A6625
L-N^G-monomethyl Arginine citrate	LNMMA	Calbiochem®, Merck, USA	475886
Sodium nitroprusside, Fluka™	NaNP	Honeywell, Romania	71778

2.4.2 eNOS activity assay

Table 18: eNOS assay equipment

Item	Supplier	Product code
SZ61 Binocular stereo dissecting microscope	Olympus Corporation, Japan	SZ61BR
Precision series balance	Thermo Fisher Scientific, USA	PPS413
Savant™ SpeedVac™ all-in-one vacuum concentrator	Thermo Fisher Scientific, USA	SPD111V
Heraeus Fresco™ 17 temperature-controlled centrifuge	Thermo Fisher Scientific, USA	75002420
TriCarb® 2800 liquid scintillation analyser	Perkin Elmer, USA	2800TR

Table 19: Ion-exchange column preparation

DOWEX® 50WX8 hydrogen form resin	Sigma-Aldrich, USA	1002812228
Sodium hydroxide (NaOH)	Sigma-Aldrich, USA	S8045
Hydrochloric acid (HCl)	Thermo Fisher Scientific, USA	320331
8mL round bottom Falcon® tubes	Corning Incorporated, USA	352027

Table 20: Other eNOS assay consumables and reagents

Item	**Supplier**	**Product code**
Costar™ Flat Bottom 24-well Cell Culture Plates	Corning Incorporated, USA	10380932
1.5mL microcentrifuge tubes	Sarstedt, Germany	72.690.001
Bovine serum albumin	Sigma-Aldrich, USA	A9418
[^{14}C]-L-arginine (50µCi)	Perkin Elmer, USA	NEC267E050UC
Acetylcholine (ACh)	Sigma-Aldrich, USA	A6625
Phosphate buffered saline (PBS) tablets	Sigma-Aldrich, USA	P4417
L-arginine	Sigma-Aldrich, USA	A5006
Ethylenediaminetetraacetic acid (EDTA)	Sigma-Aldrich, USA	E9884
Ethanol	Thermo Fisher Scientific, USA	10680993
Gold Star Multi-purpose liquid scintillation cocktail	Meridian Biotechnologies, UK	GS1
20mL plastic scintillation vials with screw cap	Meridian Biotechnologies, UK	PV1AS

Table 21: 4-(2-hydroxyethyl)-1-piperazineethanesulfonic acid (HEPES) buffer reagents and composition

Reagent	Formula	Supplier	Product code	mmol/l
HEPES	$C_8H_{18}N_2O_4S$	Sigma-Aldrich, USA	H3375	10
Sodium chloride	NaCl	Thermo Fisher Scientfic, USA	S/1360/63	145
Potassium chloride	KCl	Thermo Fisher Scientific, USA	P/4240/53	5
Magnesium sulphate heptahydrate	MgSO4.7H_2O	Thermo Fisher Scientific, USA	M/1000/60	1
D-(+)-glucose	$C_6H_{12}O_6$	Sigma-Aldrich, USA	G8270	10
Calcium chloride dihydrate	$CaCl_2.2H_2O$	Thermo Fisher Scientific, USA	F.W.147.02	1.5

2.5 Protein studies

Table 22: General protein assay equipment

Item	Supplier	Product code
SZ61 Binocular stereo dissecting microscope	Olympus Corporation, Japan	SZ61BR
Heraeus Fresco™ 17 temperature-controlled centrifuge	Thermo Fisher Scientific, USA	75002420
TissueLyser II	QIAgen, Germany	85300
Mini gel tank	Thermo Fisher Scientific, USA	A25977
Trans-Blot® Turbo™ Transfer System	Bio Rad, USA	1704150
G:BOX imaging equipment	Syngene International Ltd., India	N/A

Table 23: Total protein isolation and quantification consumables and reagents

Item	Supplier	Product code
6mm metal cone balls	Retsch Ltd, UK	RS.22.455.0003C
SafeSeal 2mL round-bottom microcentrifuge tubes	Sarstedt, Germany	72.695.500
Cell extraction buffer	Thermo Fisher Scientific, USA	FNN0011
1.5mL microcentrifuge tubes	Sarstedt, Germany	72.690.001
Pierce™ BCA Protein Assay Kit	Thermo Fisher Scientific, USA	23225
96-well flat-bottom clear microplate	Corning incorporated, USA	CLS3628

Table 24: Western blotting consumables and reagents

Item	Supplier	Product code
NuPAGE™ Sample Reducing Agent (10X)	Thermo Fisher Scientific, USA	NP0004
NuPAGE™ LDS Sample Buffer (4X)	Thermo Fisher Scientific, USA	NP0007
NuPAGE™ 4-12% Bis-Tris Protein 1.5mm 15 well mini gels	Thermo Fisher Scientific, USA	NP0336
NuPAGE™ Tris-Glycine SDS Running Buffer (20X)	Thermo Fisher Scientific, USA	NP0002
Color Prestained Protein Standard ladder (10–250 kDa)	New England Biosciences, USA	P7719S
Gel loading tips, 1-200µl	Thermo Fisher Scientific, USA	11927734
Trans-Blot® Turbo™ low fluorescence LF PVDF membrane transfer kit	Bio Rad, USA	1704274
Methanol	Thermo Fisher Scientific, USA	10141720
Ethanol	Thermo Fisher Scientific, USA	10680993
Bovine serum albumin (BSA) powder	Sigma-Aldrich, USA	A7906
Skim milk powder	Sigma-Aldrich, USA	70166
Disposable surgical scalpel with No.10 blade	Swann-Morton Limited, UK	0501
Tween® 20	Sigma-Aldrich, USA	P1379
Tris base	Thermo Fisher Scientific, USA	10370743
Tris-HCl	Thermo Fisher Scientific, USA	10060390
Sodium chloride (NaCl)	Thermo Fisher Scientific, USA	S/1360/63

Sodium azide (NaN_3)	Thermo Fisher Scientific, USA	15835188
Immobilon™ Western Chemiluminescent HRP Substrate Kit	Sigma-Aldrich, USA	WBKLS0050

Table 25: Western blotting antibodies

Target	Species	Supplier	Product code	Dilution
Anti-glutamine synthetase	Rabbit	Abcam, UK	Ab176562	1:1000
B-actin	Mouse	Santa Cruz Biotechnology, USA	SC-4777B	1:5000
eNOS	Mouse	BD Biosciences, USA	610297	1:1000
Phosphorylated-eNOS (S1177)	Rabbit	Cell Signalling Technology, USA	9571S	1:1000
HRP-conjugated anti-mouse	Sheep	Merck Millipore Sigma, USA	NA934-1ML	1:5000
HRP-conjugated anti-rabbit	Donkey	Thermo Fisher Scientific, USA	A27025	1:5000

2.6 Software

Table 26: Software

Name and Version	Supplier
Zen Black	Carl Zeiss, Germany
FIJI ImageJ 2.1.0 (open source)	National Institutes of Health, USA
Image-Pro Plus 6.0	Media Cybernetics, USA
LabChart Pro 8.0	ADInstruments, UK
LightCycler® 480 (proprietary software included with equipment)	Roche Life Sciences, Germany
Excel 2016	Microsoft, USA
Prism 9.0.2	GraphPad Software, USA
W3Schools RGB Calculator	Refsnes Data, Norway
GeneSys	Syngene International Ltd., India

Chapter 3 Methods

3.1 Animal Husbandry

3.1.1 Ethical approval

All animal work was conducted under accepted standards of humane animal care and in accordance with the United Kingdom Animals (Scientific Procedures) Act 1986. All work was conducted at the University of Leeds under Project Licence P144DD0D67 (Project licensee: Professor S Wheatcroft).

3.1.2 Genetically modified mice

GS haploinsufficient mice termed $GS^{+/LacZ}$ were previously developed through single allele replacement of GS with the reporter gene *LacZ* [80]. These mice were backcrossed to the C57BL/6 background for at least 10 generations. Some $GS^{+/LacZ}$ mice on C57BL/6 background were then crossed with C57BL/6 mice homozygous for the deletion of ApoE ($ApoE^{-/-}$) (Charles River, Belgium) to produce a second colony of $GS^{+/LacZ}ApoE^{-/-}$ mice [Table 1].

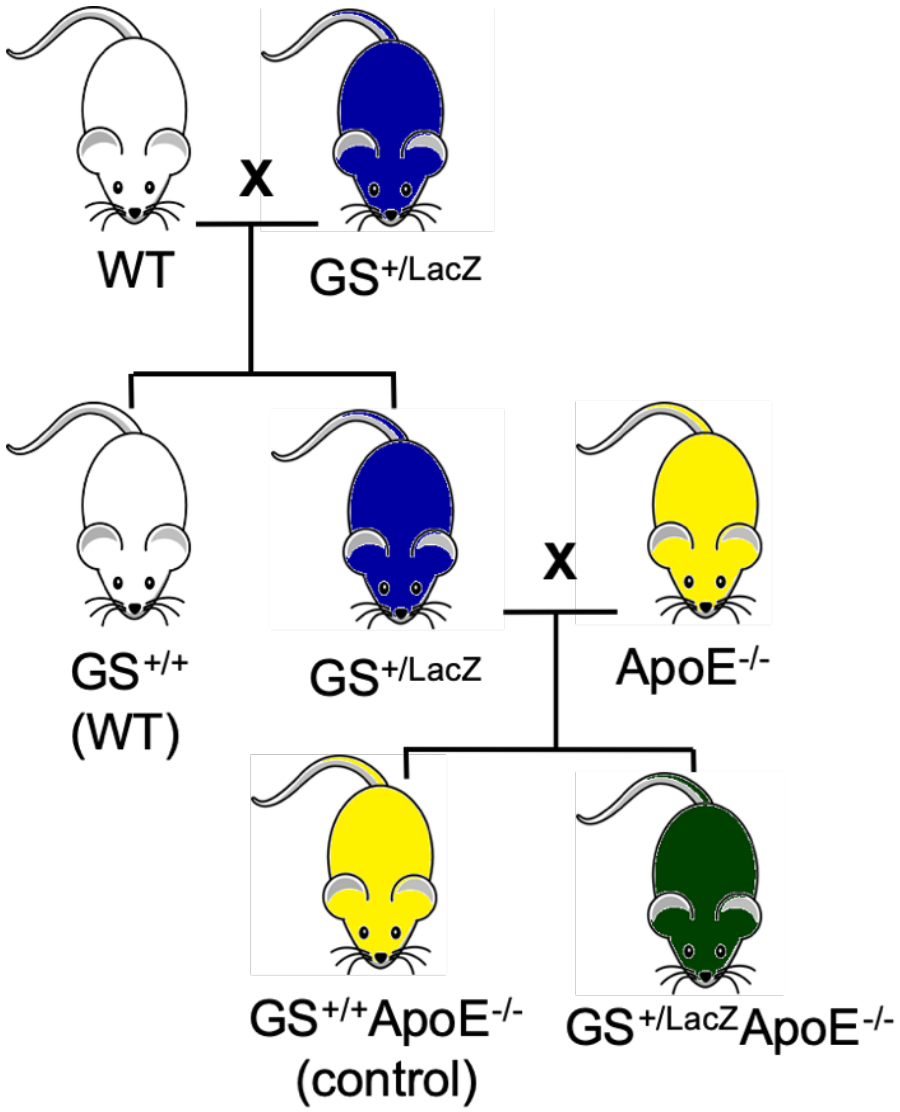

Figure 2: Schematic of genetically modified mouse colonies $GS^{+/LacZ}$ mice with single allele replacement of GS with the reporter gene *LacZ* (**blue**) were backcrossed onto the wild-type C57BL/6 mice with $GS^{+/+}$ genotype (**white**) to produce heterozygous $GS^{+/LacZ}$ mice on a C57BL/6 background with $GS^{+/+}$ littermate controls. Some of these $GS^{+/LacZ}$ mice were then crossed with $ApoE^{-/-}$ C57BL/6 animals with wild-type $GS^{+/+}$ expression (**yellow**) to produce $GS^{+/LacZ}ApoE^{-/-}$ mice (**green**) and $GS^{+/+}ApoE^{-/-}$ littermate controls.

3.1.3 General husbandry

All mice were kept at the University of Leeds central animal facility on a 12-hour light/dark cycle. All animals were housed in individually ventilated cages with controlled temperatures and humidity and appropriate environmental enrichment was also provided within each cage. Animals were housed in either sex-separated groups of ≤5 adult animals or in family groups of parents and pups and, wherever possible, experiments were planned to prevent animals being kept alone in cages.

Pups were weaned at 3-4 weeks post-partum and ear notched to provide a means of identifying individuals. DNA genotyping of mouse strains was performed by TransnetTX® Inc. (USA) using these ear-notch biopsies. Pups were then separated by sex and unless required to establish new breeding cages, females were typically sacrificed shortly after weaning. This is due to cyclical differences in female sex hormones potentially influencing vascular function and/or disease development, and therefore only males were used for experimental purposes, unless stated otherwise.

All animals were weaned onto the standard chow diet and $GS^{+/LacZ}$ colony mice were maintained on this diet for the duration of their lives. $GS^{+/LacZ}ApoE^{-/-}$ colony mice were all fed the chow diet to 8 weeks of age and then experimental males fed a high-cholesterol Western Diet for 6 or 12 weeks thereafter to induce atherosclerosis [Table 4]. Mice were always given *ad libitum* access to water and, unless otherwise specified for experimental purposes, *ad libitum* access to food.

3.1.4 Physiological tests

Male $GS^{+/LacZ}ApoE^{-/-}$ mice and $GS^{+/+}ApoE^{-/-}$ littermate controls were metabolically tested at 7 weeks of age to check for differences in baseline glucose handling and insulin tolerance prior to commencing western diet at 8 weeks old. These tests were repeated at the end of the diet at 19 weeks of age, prior to sacrifice and tissue harvesting at 20 weeks old, to check for any subsequent changes in metabolism induced by the diet. To prevent interference of one test with another, glucose tolerance tests (GTTs) were performed first and insulin tolerance tests (ITTs) 3-5 days later, ensuring restoration of glucose homeostasis.

Additionally, mice were weighed weekly throughout this feeding period from 7 weeks of age until sacrifice.

3.1.4.1 Glucose tolerance test

Mice were fasted overnight with only water for a maximum of 16 hours in a clean cage to prevent consumption of either chow or faeces from the cage floor. Mice were contained in a box with a hole for the tail to protrude from and using a sterile

disposable scalpel a small superficial incision made in the tail sufficient to sample small droplets of tail vein blood. 1-2µl whole blood was sampled using Accu-Chek® test strips and blood glucose concentrations measured using an Accu-Chek® Aviva portable glucometer to provide a fasting blood glucose measurement.

10%/90% w/v D-glucose/dH_2O solution was prepared and sterile-filtered before an appropriate volume injected intraperitoneally to provide a dose of 1mg/g according to mouse weight. After injection, blood was serially sampled via the previous incision every 30 minutes for 2 hours total to provide a total of 5 measurements per mouse.

Throughout the experiment, mice were returned to the cage in between procedures to reduce stress and provide *ad libitum* access to water.

3.1.4.2 Insulin tolerance test (ITT)

Insulin tolerance tests (ITTs) were performed using a similar protocol to GTTs. Mice were fasted for 2 hours with only water in a clean cage and as for GTTs, a superficial tail incision was made for 1-2µl droplets of whole blood to be sampled and measured using the Accu-Chek® Aviva test strips and portable glucometer.

In this protocol, stock 200IU/mL Actrapid® human recombinant insulin was diluted to 0.1IU/mL in phosphate buffered saline (PBS) and, after the initial fasting measurement was made, an appropriate volume of was intraperitoneally injected to provide a dose of 0.75 IU/kg. Blood was then serially sampled at the same time points.

As for GTTs, mice were returned to the cage in between procedures to reduce stress and provide *ad libitum* access to water. Additionally, throughout the experiment, subjects were observed closely and an injection of 10%/90% w/v D-glucose/dH_2O solution was available in the event of hypoglycaemia or compromised recovery.

3.1.5 Euthanasia and harvesting

Mouse euthanasia was conducted using Home Office approved humane techniques.

For one of these techniques, mice were first placed under general anaesthesia using isoflurane delivered via a precision vapouriser connected to an oxygen flow and scavenging system. The oxygen flow system was set to deliver oxygen at a rate of 2L/minute and isoflurane at a concentration of 5% and this was directed to an induction chamber and the animal placed inside. Sufficient anaesthesia was assumed when the mouse was rendered unconscious and the respiratory rate had slowed. The anaesthesia was then diverted to a nose cone and the animal secured to the operating table using surgical tape. The depth of anaesthesia was then tested by observing a change in respiration and checking for a response to both tail-tip and toe pinches. Once satisfied that the mouse was fully anaesthetised, the concentration of isoflurane

being delivered by the nose cone was lowered to 2%. Once anaesthetised, mice were exsanguinated by excision of the vena cava and flushing with PBS solution to prevent blood clotting, followed immediately by perfusion fixation with 4% w/v paraformaldehyde-PBS (PFA-PBS) solution (pH 7.2). This method was typically used to harvest tissue for histological examination [3.3].

Alternatively, mice were placed in a chamber which rendered them unconscious through exposing them to rising concentrations of CO_2 over 12 minutes before euthanasia was confirmed by exsanguination. This technique was typically employed where fixation would be inappropriate, including *ex vivo* work requiring 'live' tissue such as organ bath [3.4.1], and experiments where fresh or frozen tissue would be lysed such as western blotting [3.5.3].

Once sacrificed, tissues were harvested using standard operative techniques and processed as appropriate. Tissues harvested at any time included the heart, aorta, liver and kidneys, and where possible additional tissues not required at the time were harvested and stored appropriately for future use in another protocol. As both euthanasia technique and tissue processing methods were selected according to the experimental protocol, relevant methods below provide specific information.

3.2 Quantification of GS expression

3.2.1 Sample preparation

Mice were humanely euthanised using rising concentrations of CO_2 and exsanguination before the kidneys and the aorta were harvested. These organs were dissected free of surrounding fat and if not used immediately for RNA isolation [3.2.2], snap-frozen using liquid nitrogen before being stored at -80ºC.

3.2.2 RNA isolation

Ribonucleic acid (RNA) was extracted from either kidney or aorta tissue, taking care to prevent either degradation or contamination of the final sample extracted through use of a phase separation method to separate RNA, deoxyribonucleic acid (DNA), and other cellular components including lipids and proteins.

Tissues were placed in 2mL round-bottom microcentrifuge tubes containing a 6mm metal cone ball in each tube. 0.5-1ml cold (~4ºC) TRI Reagent® solution was then added depending on quantity of tissue such that the tissue was sufficiently submerged. Tissues were then mechanically homogenised using a Qiagen TissueLyser II for 1 minute 30 seconds at 30 Hz. Homogenates were transferred to clean 1.7mL microcentrifuge tubes and centrifuged at 4ºC for 10 minutes at 13,000rpm (revolutions per minute) to pellet undigested tissue.

Lysates were again transferred to clean tubes before 50-100µl 1-Bromo-3-chloropropane (BCP) was added, equivalent to 10% of the previously used volume of TRI Reagent solution [A]. Samples were vortexed thoroughly to mix and then incubated at room temperature (approximately 20ºC) for 15 minutes [B]. Samples were then centrifuged for 15 minutes, again at 4ºC and 13,000rpm to complete phase-separation of the cellular components into three distinct layers [C].

The clear aqueous top-layer containing RNA was then transferred to a new tube (approximately 200µl) [C], and an equal volume of cold 100% isopropanol added to each sample. Samples were then vortexed to mix the components and incubated on ice for 10 minutes to precipitate the total RNA. Samples were again centrifuged at 4ºC for 20 minutes at 13,000rpm to pellet the RNA. Supernatants were carefully removed, and the resultant RNA pellets washed in cold 0.5mL 75%/25% v/v ethanol/dH_2O before a final centrifuge step at 4ºC for 2 minutes at 13,000rpm.

Supernatants were again carefully removed, and the tubes left on ice with the lids open for 30 minutes so that the pellets were dry. Pellets were resuspended in 20µl nuclease-free water and the resulting concentrations of RNA (ng/µl) were measured using a DS-11 FX+ spectrophotometer. If not used immediately for reverse transcription [3.2.3], RNA isolates were stored at -80 ºC for future use.

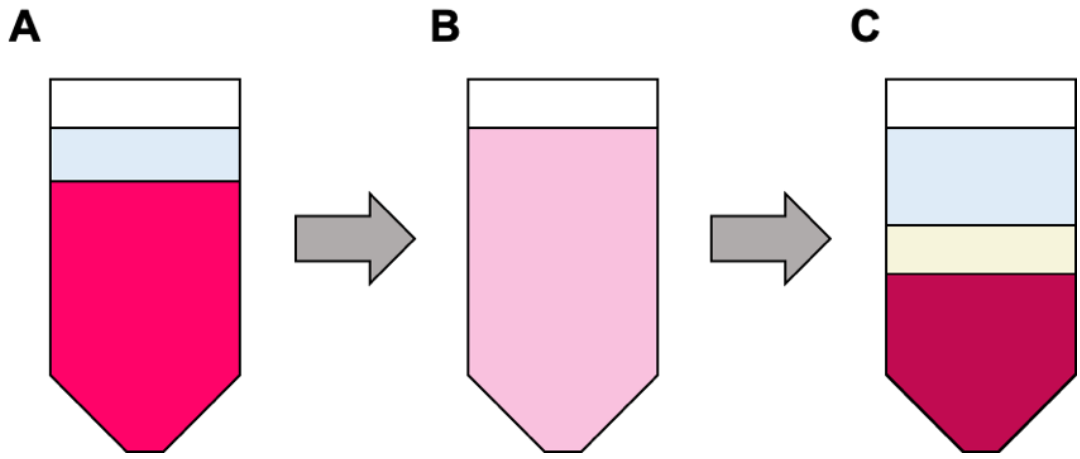

Figure 3: Schematic of RNA isolation by phase-separation BCP (**clear**) was added to lysates in TRI Reagent® solution (**bright pink**) [**A**]. Samples were mixed thoroughly (**milky pink**) [**B**] and then separated into 3 different phases – an aqueous phase (**clear**) containing dissolved RNA, an interphase (**cream**) consisting of precipitated DNA, and an organic phase (**dark pink**) containing other cellular components [**C**]

3.2.3 Reverse transcription (RT)

After isolation of the total RNA, 2000ng per sample was reverse transcribed to single-strand complementary DNA (cDNA) using the High-Capacity cDNA Reverse Transcription kit. This kit contains all the components needed for reverse transcription, including enzymes, primers, and dNTPs (deoxyribonucleotide triphosphates) and is stored at -20ºC.

The RNA isolates and kit components were defrosted before a “master mix” for the total number of reactions required was prepared in a microcentrifuge tube on ice, as per manufacturer’s instructions [Table 27].

Table 27: Reverse transcription master mix protocol

Component	**Volume per reaction (µl)**
Nuclease-free water	4.2
10X RT buffer	2
10X RT Random primers	2
25X dNTP mix (100mM)	0.8
MultiScribe™ Reverse Transcriptase enzyme	1.0
Total "mastermix" volume	**10**

The mastermix was vortexed to mix the contents thoroughly. Then, into 0.2mL thin-walled PCR tubes, 10µl mastermix per reaction was added, plus the volume of RNA required to transcribe 2000ng and finally, a further volume of water added to bring the total reaction volume to 20µl [Table 28].

Table 28: Reverse transcription reaction

Component	**Volume per reaction (µl)**
Mastermix	10
2000ng total RNA	X
Nuclease-free water	Y=(20-(X+10))
Total reaction volume	**20**

Tubes were sealed and then the contents gently mixed by manually inverting the tubes. The tubes were centrifuged for 10 seconds on a single-speed mini-centrifuge to collect all the components at the bottom of the tube. The tubes were then placed in a 96-well thermal cycler with the program set according to the kit manufacturer's recommendations [Table 29].

Table 29: Reverse transcription conditions

Step	Function	Temperature (°C)	Time (minutes)
1	Pre-incubation	25	10
2	Reverse transcription	37	120
3	Reaction enzyme denaturation	85	5
4	Cooling and holding	4	

Assuming 1:1 RNA to cDNA reverse transcription achieved, the final concentration of the cDNA is 100ng/µl. Samples were either used immediately for quantitative polymerase chain reaction (qPCR) [3.2.4] or stored at -20ºC until future use.

3.2.4 qPCR – SYBR® green protocol

GLUL gene expression levels were measured using real-time qPCR. The gene hypoxanthine-guanine phosphoribosyltransferase, *HPRT,* was selected as a housekeeper and mouse specific primers were designed from the NCBI reference sequence NM_013556.2 using the Primer-BLAST tool (NCBI, USA). GS primers were designed the same way using the NCBI *GLUL* reference sequence NM_008131.4 [Table 7].

The cDNA samples and qPCR reaction components were defrosted before two master mixes were prepared In microcentrifuge tubes, one mix per gene of interest, sufficient for the total number of samples and controls required to each be tested in duplicate [Table 30].

Table 30: SYBR® green qPCR master mix

Component	Volume per reaction (µl)
PrecisionPLUS 2X master mix with SYBR® green dye	10
Forward primer	1
Reverse primer	1
Nuclease-free water	7
Total reaction volume	**19**

19µl of master mix was added to each required well of a 96-well qPCR plate. Then 1µl cDNA (100ng, see 3.2.3) was added to the appropriate sample reaction wells and 1µl nuclease-free water was added to the negative control wells. Real-time PCR amplification was achieved using a Roche LightCycler® 480 II instrument; for cycling parameters see Table 31 below.

Table 31: SYBR® green qPCR cycling parameters

Stage	Title	Cycles	Temp (°C)	Time	Acquisition mode
1	Pre-incubation	1	95	10 min	None
2	Amplification	45	95	15 sec	None
			54	1 min	Single
3	Melting curve	1	95 - 37	Pre-set	Continuous, 5/°C
4	Cooling	1	37	Pre-set	None

3.2.5 qPCR – TaqMan™ hydrolysis probe protocol

GLUL gene expression levels were measured using real-time qPCR. The gene ß-actin, *ACTB,* was selected as a housekeeper and mouse specific TaqMan™ gene expression assay mixes were ordered from Thermo Fisher Scientific, each containing forward and reverse primers and gene specific hydrolysis probes conjugated to the FAM fluorophore [Table 6].

The cDNA samples and qPCR reaction components were defrosted before two master mixes were prepared In microcentrifuge tubes, one mix per gene of interest, sufficient for the total number of samples and controls required to each be tested in duplicate.

Table 32: TaqMan™ qPCR master mix

Component	Volume per reaction (µl)
PrecisionPLUS 2X master mix	10
TaqMan™ gene expression assay mix containing primers and probe	1
Nuclease-free water	8
Total reaction volume	**19**

19µl of master mix was added to each required well of a 96-well qPCR plate. Then 1µl cDNA (100ng, see 3.2.3) was added to the appropriate sample reaction wells and 1µl nuclease-free water was added to the negative control wells. Real-time PCR amplification was achieved using a Roche LightCycler® 480 II instrument; for cycling parameters see Table 33 below.

Table 33: TaqMan™ qPCR cycling parameters

Stage	Title	Cycles	Temp (°C)	Time	Acquisition mode
1	Pre-incubation	1	50	2 min	None
		1	95	10 min	None
2	Amplification	45	95	15 sec	None
			60	1 min	Single
3	Cooling	1	37	5 min	None

GS expression levels were confirmed using comparative analysis of the Ct values, which was performed using Excel 2016.

3.3 Histological analyses

$GS^{+/LacZ}ApoE^{-/-}$ mice and $GS^{+/+}ApoE^{-/-}$ littermate controls were fed a high-cholesterol western diet for either 6 or 12 weeks from 8 weeks of age to induce atherosclerosis [3.1.3] before histological methods were used to assess plaque burden and architecture.

3.3.1 Whole aorta

3.3.1.1 Sample preparation

Animals fed a western diet for 12 weeks were terminally anesthetised and perfusion-fixed with 4% PFA-PBS [3.1.5]. The entire aortic tree was dissected and then stored at 4ºC in microcentrifuge tubes containing a sufficient volume of the same PFA-PBS solution to cover the vessel until completely fixed. Once fixed, the aorta was dissected free of fat and other tissue, taking care to not fully dissect the adventitia. The vessel was then split open lengthways and along the outer curvature of the arch to produce a "Y-shape". If not stained immediately, the vessel was then stored in clean PFA-PBS solution at 4ºC for future use.

3.3.1.2 Staining and imaging protocol

Aortas were transferred to microcentrifuge tubes containing 1mL dH_2O and inverted for 1 minute to wash. This was repeated 3 times to fully remove the PFA-PBS solution. The tissues were then transferred to microcentrifuge tubes containing 1mL 60% v/v isopropanol/dH_2O and inverted for 1 minute. This was repeated 3 times to fully remove the dH_2O and prepare the vessel for staining.

Aortas were then transferred to microcentrifuge tubes containing 500µl Oil Red O dye dissolved in 60% isopropanol (saturated solution) and these tubes placed on a rotator for 1hr to ensure even staining. Oil Red O is a red-orange dye capable of staining triglycerides and lipids in order to stain the atherosclerotic plaques. Aortas were then washed again in 1mL 60% isopropanol 3 times to remove the excess Oil Red O dye.

Stained aortas were opened and mounted *en face* using dH_2O between a glass slide and a coverslip before being imaged digitally using an SZ61 dissecting microscope (magnification: 12x) and QICAM Fast 1394 camera.

3.3.1.3 Image analysis

Plaque burden was quantified from these images using Image-Pro Plus 6.0 software. For these analyses, the area of the image which is within the aorta is manually defined and the brachiocephalic artery, the left common carotid artery, and the left subclavian artery excluded from the field of analysis. The plaque areas stained red-orange by the

Oil Red O are then selected for and the software calculates the percentage of the area selected within the analysis field. Finally, to check whether any bias has been introduced in harvesting, the length of the aorta is measured from the top of the arch to the end of the thoracic portion [Figure 4].

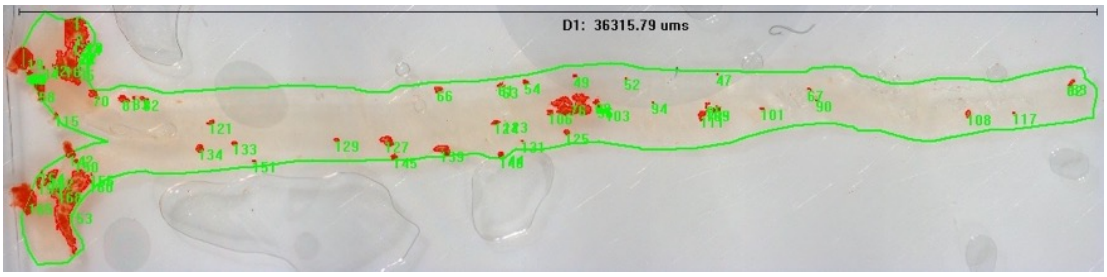

Figure 4: Example analysis of Oil Red O stained aorta The **green line** surrounding the aorta excludes the brachiocephalic, carotid and subclavian arteries, and defines the field of analysis. The **green numbers** indicate the selected Oil Red O stained plaques. The **black line** shows the defined length of the aorta with the length given in microns below

3.3.2 Aortic sinus

3.3.2.1 Slide coating

To ensure adhesion of paraffin-embedded samples to the slides, slides are pre-coated with (3-aminopropyl)triethoxysilane (TESPA) prior to sectioning. Glass slides were placed in histology racks before being cleaned of manufacturing residues and coatings by immersing the rack in 70/30% v/v ethanol/5M hydrochloric acid (HCl) solution for 1 minute. This acid-alcohol solution was then washed by immersion in two washes of dH_2O for 1 minute each. Slides were then washed for 1 minute in 100% ethanol. Racks were placed in a 70ºC histology oven for ~5 minutes until fully dried then left at room temperature for 5 minutes to cool before coating.

Slide racks were agitated in 2%/98% TESPA-acetone solution to evenly coat the slides and the excess then washed by immersing the slides in 100% acetone for 1 minute. As before, this was then washed twice by immersion in dH_2O for 1 minute each before being dried at 70ºC. Dried slides were cooled, boxed and stored at room temperature for future use.

3.3.2.2 Sample preparation

Animals fed a western diet for 12 weeks were sacrificed using either of the methods described in 3.1.5. Hearts were harvested and the apex and majority of the ventricles were removed.

According to the stain to be applied, samples were then prepared for embedding in either paraffin or Optimum Cutting Temperature (OCT) compound. This is because whilst paraffin is suitable for many histological stains, including Miller-van Gieson and Picrosirius red, it is unsuitable for samples to be stained with Oil Red O as this is a lipid specific stain and the paraffin perfusion process replaces lipids with wax rendering them unable to be stained.

Paraffin embedding

For samples to be embedded in paraffin wax, the remaining tissue containing the aortic root was placed in cassettes and stored at 4ºC in 4% w/v PFA-PBS solution to cover the tissue for a minimum of 24 hours. The cassettes were then dehydrated and processed to perfuse the samples with paraffin. Processed samples were then embedded in blocks of paraffin wax before being stored at room temperature (~20ºC).

Prior to cutting, blocks were chilled to 4ºC overnight and maintained on an ice bath throughout sectioning to ensure consistency of sections. Samples were initially trimmed to discard the majority of the tissue until leaflets of the aortic root were visible, at which point they were serial sectioned into ribbons of 5 sections, at a thickness of 5 microns. Ribbons were floated on a 60ºC water bath for ~3 minutes to gently melt the wax and enable adhesion to TESPA-coated slides [3.3.2.1]. Slides were dried on the bench overnight before being stored at room temperature until staining.

Optimum temperature compound embedding

For samples to be cryosectioned, the remaining tissue was placed in microcentrifuge tubes and stored in 1mL 4% w/v PFA-PBS solution at 4ºC to cover the tissue for 24 hours. Samples were embedded in moulds containing optimum cutting temperature (OCT) compound. Moulds were then placed on dry ice to freeze and the resultant blocks stored at -80ºC until cutting.

Prior to cutting, blocks were placed at the cutting temperature of -20ºC for 30 minutes to soften and prevent cracking of the OCT and to prevent tissues from being too brittle. Once on the cryostat microtome, the hearts were trimmed until leaflets of the aortic root were visible, at which point they were serial sectioned at a thickness of 10 microns and adhered to slides. Slides were stored at -80ºC until future use.

3.3.2.3 Miller-van Gieson staining protocol

Slides to be stained were placed in upright racks and then heated in a 70ºC histology oven for 20 minutes to melt the wax. Racks of hot slides were deparaffinised and further dehydrated through 3 washes of 100% xylene for 5 minutes each followed by 3 washes of 100% ethanol for 3 minutes each.

Excess ethanol was rinsed off in dH_2O and the rack dried before the slides were stained as follows: 0.5% $KMnO_4$ for 10 minutes, 2% oxalic acid for 2 minutes, Miller stain for 1 hour 45 minutes. As before, excess ethanol was rinsed off in dH_2O and the rack dried between each of these stages. After incubation in Miller stain, slides were then washed 5 times in 100% ethanol, taking care to not fully wash out the blue stain before excess ethanol was rinsed off and the rack dried. The slides were next transferred to van Gieson for 30 minutes. The rack was then dipped 3 times in dH_2O to remove the excess stain, taking care to not fully wash out the yellow counterstain. The rack was then dried before being placed into the 70ºC oven to completely dry out.

Slides were then placed in clean 100% xylene for 3 minutes three times to clear and restructure the tissue, in place of the previously removed water and paraffin wax. Finally, coverslips were mounted using DPX xylene-based mountant and the slides left to air-dry overnight at room temperature. Slides were protected from sunlight and stored at room temperature until imaging.

3.3.2.4 Picrosirius red staining protocol

Picrosirius acid stain was prepared by dissolving 0.5g Sirius Red dye (also known as Direct Red 80) in 500mL saturated aqueous picric acid solution.

Slides to be stained were placed in upright racks and then heated in a 70ºC histology oven for 20 minutes to melt the wax. Racks of hot slides were deparaffinised and further dehydrated through 3 washes of 100% xylene for 5 minutes each followed by 3 washes of 100% ethanol for 5 minutes each.

Excess ethanol was rinsed off in dH_2O and the rack dried before the slides were placed in Picrosirius red stain for 1 hour. Excess picrosirius red stain was washed off in dH_2O and the rack dried. The slides were then placed in two washes of 0.5% acetic acid for 3 minutes each in order to remove non-specific staining. The rack was then dried before being placed into the 70ºC oven to completely dry out.

Slides were then placed in 3 washes of clean 100% ethanol for 5 minutes each to ensure the tissue was fully dehydrated. To clear and clear and restructure the tissue in place of the previously removed water and paraffin wax, slides were then placed in 100% xylene for 3 minutes three times. Finally, coverslips were mounted using DPX

xylene-based mountant and the slides left to air-dry overnight at room temperature. Slides were protected from sunlight and stored at room temperature until imaging.

3.3.2.5 Oil Red O staining protocol

Fresh Oil Red O stain was prepared by dissolving sufficient Oil Red O dye in 30mL 100% methanol until the solution was saturated. 20mL dH2O was then added and mixed by vortex to produce a 60% isopropanol stain. The excess dye was allowed to precipitate out of the mixture overnight and removed the next day through syringe filtering the stain.

Previously prepared slides were retrieved from the freezer, laid flat, and allowed to air dry at room temperature (~20ºC) for 20 minutes to fully adhere the tissue to the glass. The OCT embedding medium was removed from the now dried slides through 2 washes of 200µl dH_2O for 5 minutes each before the excess was blotted away and the slides allowed to dry for 15 minutes at room temperature. To prepare the tissue for staining, slides were then treated with 200µl 60% isopropanol for 5 minutes before the excess isopropanol was removed by blotting. Slides were then treated with 300µl Oil Red O stain as prepared above, covered in aluminium foil to both prevent light degrading the stain and to prevent evaporation of the stain, and incubated for 1 hour at room temperature. Excess Oil Red O stain was removed by blotting before the slides were then washed with 2 washes of 200µl 60% isopropanol for 5 minutes each, with the excess being blotted away in between washes. The isopropanol was then washed off and the tissue rehydrated through a single wash of 200µl dH_2O for 5 minutes.

Finally, as Oil Red O is solvent soluble, DPX mountant was unsuitable for use and therefore coverslips were mounted to the slides using the aqueous Fluoromount-G® mounting medium typically used in immunofluorescent staining. Slides were then left to air dry at room temperature for 1 hour under an aluminium foil cover and then nail varnish applied to the top and bottom edges of the coverslip as to fully adhere the coverslip to the slide without obscuring the tissue. After 1 hour further drying, slides were placed in holders and wrapped fully in aluminium foil to block the light from degrading the stain and stored at room temperature until imaging.

3.3.2.6 Imaging and analysis

The same section on each slide was imaged digitally using either a BX41 trinocular microscope and QICAM Fast 1394 camera (magnification: 40x) with Image-Pro Plus 6.0 software or alternatively the EVOS™ FL Auto 2 complete microscope and camera imaging system set to brightfield imaging (magnification: 4x). To enable all images to be pooled into the same data set, images were taken of the same micrometre calibration slide on both imaging setups.

For slides stained with Oil Red O, 3 slide images approximately 30-40 microns apart and each 10 microns thick were selected according to the morphology of the aortic root and in particular, the leaflets. For slides stained with either Miller van Gieson or Picrosirius red, four slide images 25-40 microns apart and each 5 microns thick were selected. In both cases, this gave a total span of approximately 90-120 microns.

Images were then opened using ImageJ open-source image analysis software, and the scales of these images were calibrated using the appropriate micrometre calibration slide image before a scale bar was added. For all analyses, the area of the image which is within the aortic sinus was manually defined and then the individual areas of plaque were each individually manually defined, producing multiple regions of interest (ROI).

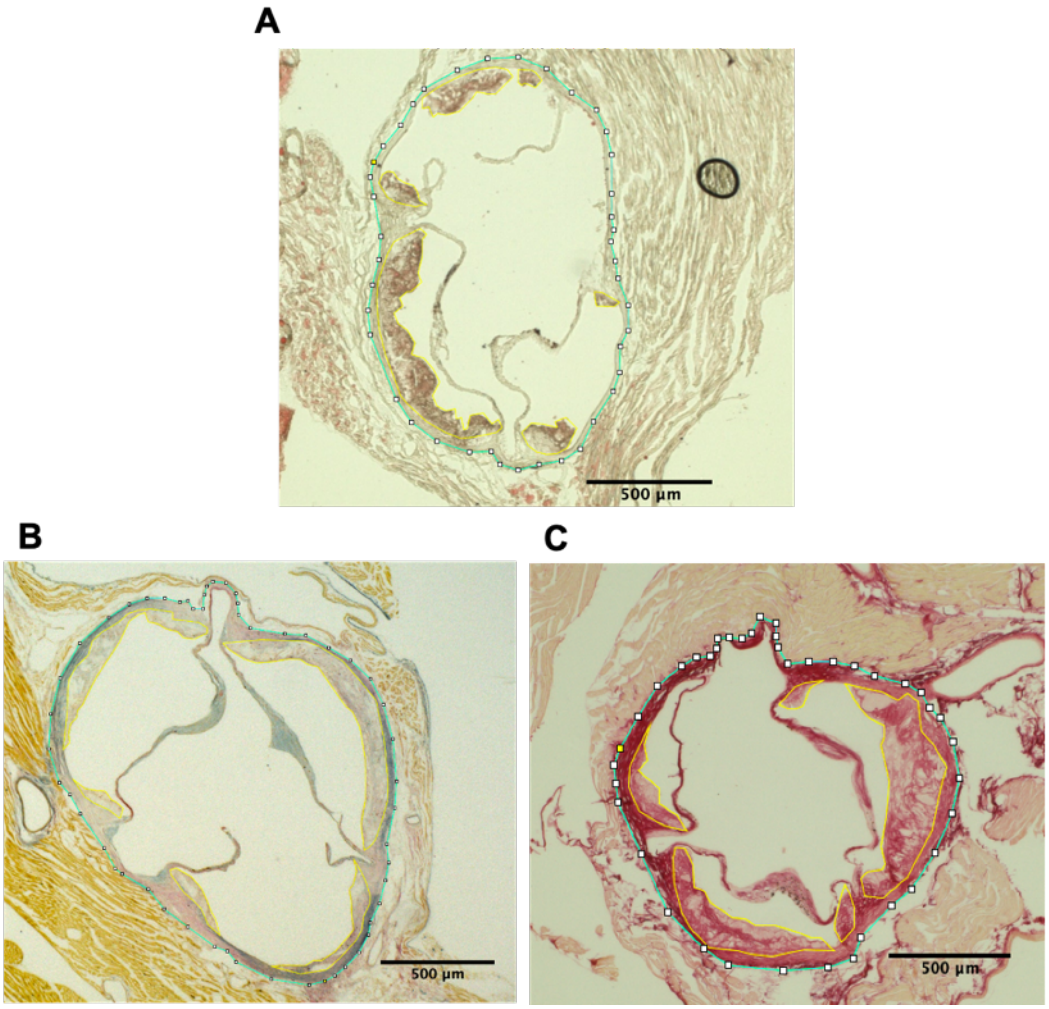

Figure 5: Example analysis of stained aortic root sections The **aqua line** surrounding the aortic sinus denotes the perimeter of the sinus and therefore defines the total field of analysis. The **yellow lines** each surround a single plaque. This method was applied to all images analysed, including cryosections stained with Oil Red O [**A**], and paraffin sections stained with either Miller-van Gieson [**B**], or Picrosirius red [**C**] stained sections

Plaque burden

For quantification of plaque burden, the number of plaques was manually recorded and then the software was used to measure the area of each ROI. Excel 2016 was then used to calculate the percentage of the area within the aortic sinus analysis field defined as plaque, as well as average sinus area, average plaque size and average number of plaques for each genotype [Figure 5].

Lipid deposition

For the lipid deposition analysis, the colour composition of a stained plaque may give an indication of plaque composition. As such, for the largest region of interest within each image as defined previously, a colour histogram was generated, providing information on the overall colour of the plaque.

From this colour histogram [Figure 6], the given mean and mode colour intensities were recorded before Excel 2016 was then used to calculate the average mean and modal intensities for each animal and these were then compared between genotypes.

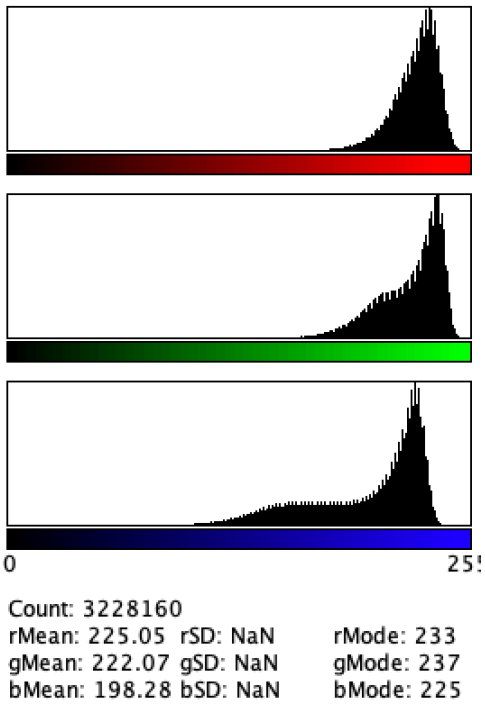

Figure 6: Example colour histogram Below the histograms, supplementary information is provided including the number of pixels counted and the mean and modal intensities for each colour

In addition to RGB colour intensity, colour thresholding was also utilised in order to identify whether there was a spatial difference in fat deposition.

Prior to starting this analysis, the largest plaque region of interest (ROI) was defined and selected for. The Hue Saturation Brightness (HSB) colour space was used to set a colour threshold and therefore filter the image in order to only measure high intensity “true” red staining and in doing so exclude artefacts and background staining [A]. This filtered image was then converted to binary, producing a black and white image [B]. From this binary image, the software was then used to measure the total white space within the defined ROI, and this was provided as a percentage of the area of the ROI. Excel 2016 was then used to calculate the mean area measured for each animal and these were then compared between genotypes.

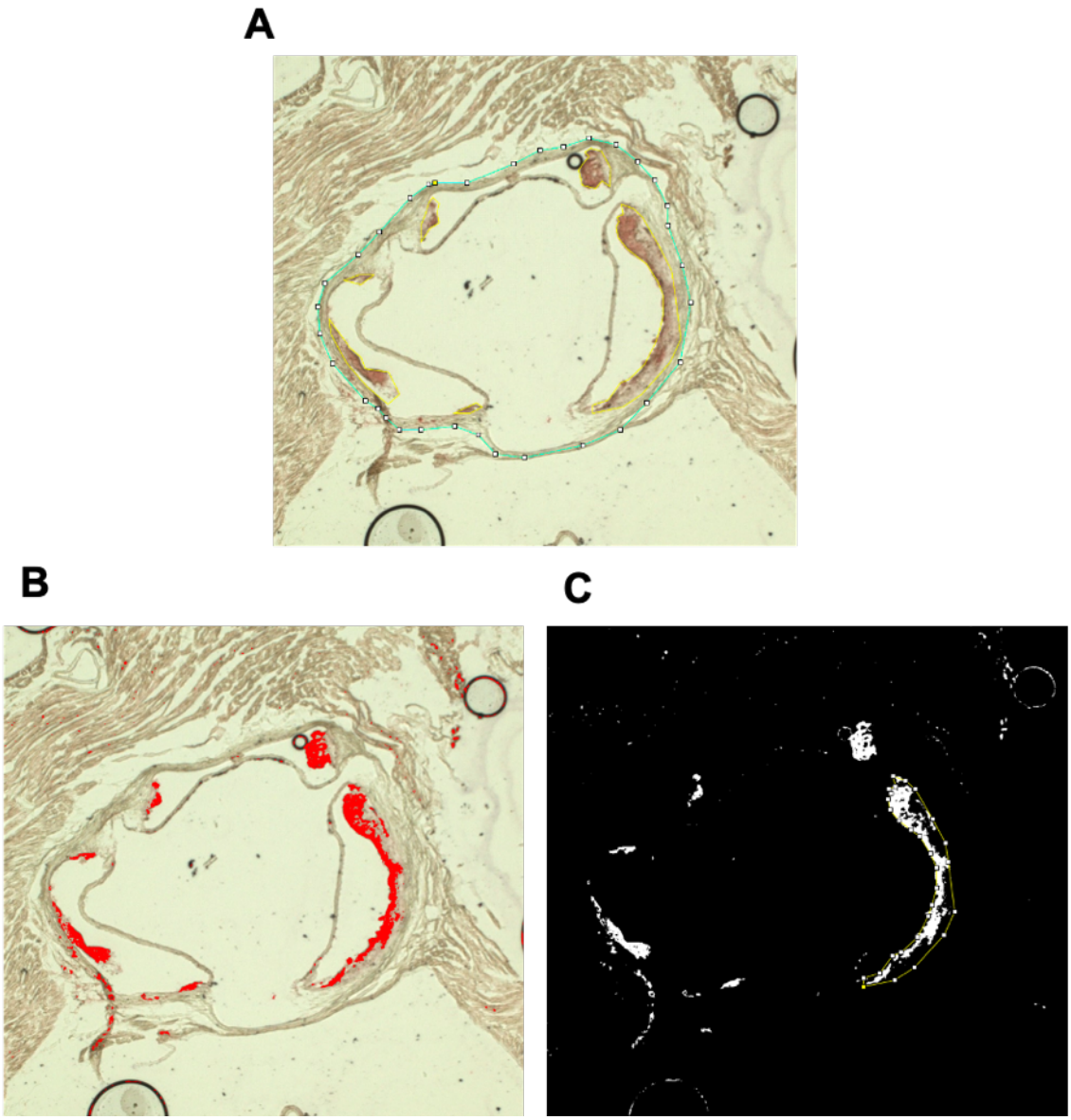

Figure 7: Example lipid deposition analysis using colour thresholding on an Oil Red O stained plaque The perimeter of the sinus and the perimeter of each plaque were each demarcated as regions of interest on the original image of the Oil Red O stained section [**A**]. The Hue Saturation Brightness (HSB) colour space was then used to set a colour threshold and filter the image [**B**]. This filtered image was then converted to binary, producing a black and white image from which the white area of the ROI was provided as a percentage [**C**]

Fibrosis

As for the lipid deposition analysis, the colour composition of a plaque stained for elastin and/or collagen may give an indication of plaque composition.

For both Miller van Gieson and Picrosirius red stained sections, a colour histogram was generated for the largest region of interest [as per Figure 6], and the average mean and modal intensities compared between genotypes. in order to visualise whether there was a difference in overall colour between $GS^{+/LacZ}ApoE^{-/-}$ mice and $GS^{+/+}ApoE^{-/-}$ controls, these mean and modal colour intensity values were then input into a RGB colour viewer online from W3Schools[81].

Additionally, due to the monocoloured nature of the Picrosirius red slides, colour thresholding was utilised in order to identify whether there was a spatial difference in collagen deposition.

As for the Oil Red O stained slides, prior to starting this analysis, the largest plaque region of interest (ROI) was defined and selected for. The Hue Saturation Brightness (HSB) colour space was used to set a colour threshold and therefore filter the image in order to only measure high intensity “true” red and magenta staining and in doing so exclude all other colours and background staining of the extracellular matrix. This filtered image was then converted to a binary black and white image.

Again, the software was then used to measure the percentage of the total area of the ROI taken up by white space and Excel 2016 used to calculate a mean for each mouse before comparing between genotypes.

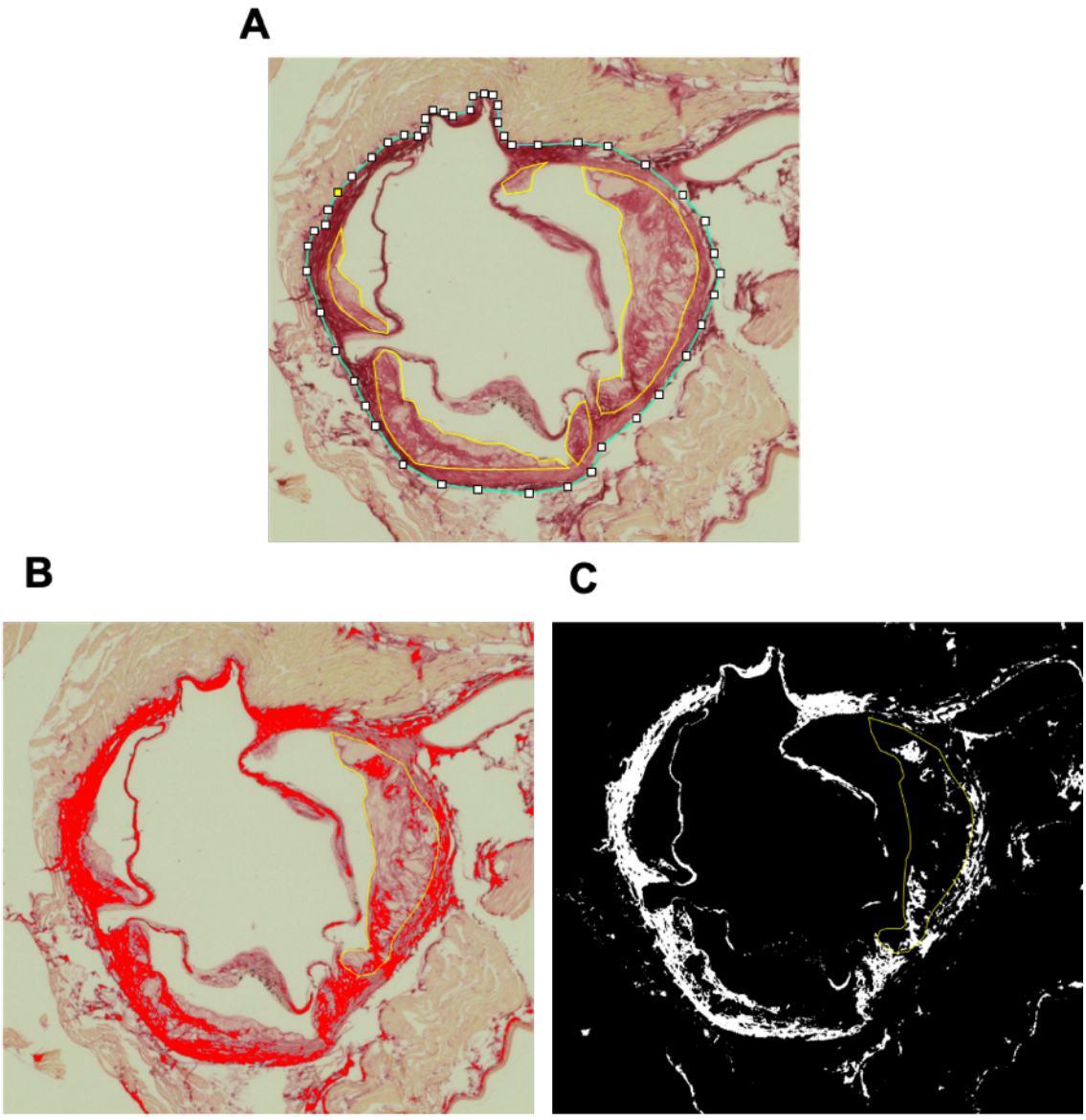

Figure 8: Example collagen deposition analysis using colour thresholding on a Picrosirius red stained plaque The perimeter of the sinus and the perimeter of each plaque were each demarcated as regions of interest on the original image of the Oil Red O stained section [**A**]. The Hue Saturation Brightness (HSB) colour space was then used to set a colour threshold and filter the image [**A**]. This filtered image was then converted to binary, producing a black and white image from which the white area of the ROI was provided as a percentage [**B**]

3.3.3 Immunohistochemistry

3.3.3.1 Sample preparation

Mice fed a western diet for 12 weeks were sacrificed using either of the methods described in 3.1.5 and their heart and liver were harvested. The largest lobe of the liver was retained alongside the upper portion of the heart containing the aortic root, as for Oil Red O staining of aortic sinus sections [3.3.2.2] whilst the rest of the liver and the apex and majority of the ventricles of the heart were discarded. The remaining tissue was placed in microcentrifuge tubes and stored in 1mL 4% w/v PFA-PBS solution at 4ºC to cover the tissue for 24 hours. Samples were embedded in moulds containing OCT compound. Moulds were then placed on dry ice to freeze and the resultant blocks stored at -80ºC until cutting.

Prior to cutting, blocks were placed at the cutting temperature of -20ºC for 30 minutes to soften and prevent cracking of the OCT and to prevent tissues from being too brittle. Once on the cryostat microtome, liver blocks were trimmed until a sufficiently large cross-section of the middle of the lobe was visible, suitable for imaging and staining, whereby they were serial sectioned at a thickness of 20 microns and sections adhered to SuperFrost Plus™ slides. Similarly, heart samples were trimmed until leaflets of the aortic root were visible, at which point they were serial sectioned at a thickness of 10 microns and adhered to slides. Slides were stored at -80ºC until future use.

3.3.3.2 Staining protocol

Blocking and primary antibodies

Prepared slides were retrieved from the freezer and allowed to air dry at room temperature (~20ºC) for 20 minutes to fully adhere the tissue to the glass. Dried slides were placed in immunostaining chambers to facilitate staining. The OCT embedding medium was removed from the slide and the tissue rehydrated through 3 washes of 200µl PBS for 5 minutes each. Slides were then blocked and permeabilised with 200µl PBS/Triton™ X-100/Bovine serum albumin (BSA) buffer (PTB buffer) for 1 hour at 4ºC [Table 13]. After this point, the process diverged according to the choice of stains to be used on the slides.

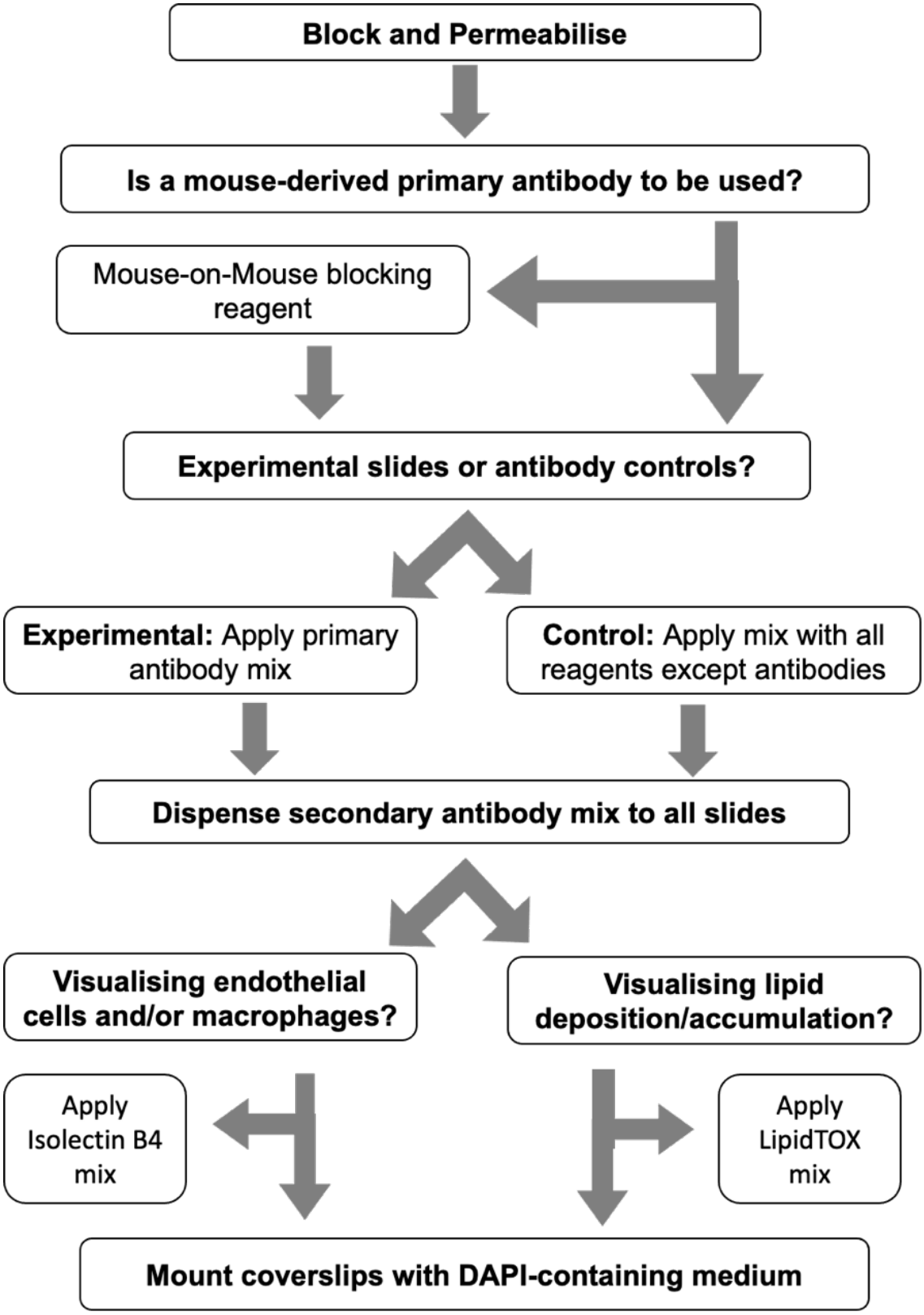

Figure 9: Summary of immunofluorescent staining options The exact process for each slide varies according to the choice of primary antibodies and the optional use of Isolectin B4 or LipidTOX™

M.O.M® (mouse on mouse) blocking reagent was diluted by adding 2 drops of the reagent to 125µl PBS. Slides to be stained with the mouse anti-α-SMA primary antibody were treated with 200µl of this diluted reagent for 1 hour at room temperature to further block the sample, particularly endogenous immunoglobulins, preventing cross-reactivity with the secondary antibody.

During blocking, primary antibody mixes were prepared containing for each slide 1-2µl of each primary antibody chosen and 10µl of appropriate serum according to the secondary antibody to be used later [Table 11]. This was then made up to a final volume of 200µl per slide with PTB buffer [Table 34].

Table 34: Example primary antibody mix

Component	**Volume per slide (µl)**
Goat serum	10
Donkey serum	10
Rabbit anti-ß-galactosidase (1:100)	2
Mouse anti-α-SMA primary antibody (1:100)	2
PTB buffer	176
Total volume	**200**

Matching control mixes were also prepared by omitting the primary antibody/antibodies [Table 35].

Table 35: Example control mix for immunofluorescent staining

Component	**Volume per slide (µl)**
Goat serum	10
Donkey serum	10
PTB buffer	180
Total volume	**200**

Slides were treated with 200µl of either the primary antibody or the control mix as appropriate and incubated overnight at 4ºC.

Secondary antibodies

The next day, excess primary antibody was removed through 3 washes of 200µl PBS for 5 minutes each. During washing, secondary antibody mixes were prepared similarly to primary antibody mixes with each containing 1-2µl of each appropriate secondary antibody chosen and 10µl of appropriate serum(s) and again made up to a final volume of 200µl per slide with PTB buffer [Table 36].

Table 36: Example secondary antibody mix

Component	**Volume per slide (µl)**
Goat serum	10
Donkey serum	10
Goat anti-rabbit conjugated to Alexa Fluor 647 (1:200)	1
Donkey anti-Mouse conjugated to DyLight 549 (1:100)	2
PTB buffer	177
Total volume	**200**

Slides were treated with 200µl of the appropriate secondary antibody mix, covered in aluminium foil to prevent light bleaching the fluorophores, and incubated for 2 hours. Excess secondary antibody was removed through three 200µl PBS washes for 5 minutes each and then the process again diverged according to the choice of stains [Figure 9].

Further application of fluorophores

In order to visualise the endothelial cells and macrophages, some slides were then stained with Isolectin B4 directly conjugated to the Alexa Fluor 488 fluorophore. For each slide to be stained, 2µl Isolectin B4 was diluted in 198µl PTB buffer (1:100; 200µl total volume) and applied to the slide. Slides were again covered with aluminium foil and incubated overnight at 4ºC.

Alternatively, in order to visualise lipid deposition, some slides were then stained with LipidTOX™ also directly conjugated to the Alexa Fluor 488 fluorophore. For each slide to be stained, 1µl LipidTOX™ was diluted in 199µl PTB buffer (1:200; 200µl total volume) and applied to the slide. Slides were again covered with aluminium foil and incubated for 30minutes at room temperature.

Once the appropriate incubation was complete, excess Isolectin B4 or LipidTOX™ was removed through three 200µl PBS washes for 5 minutes each as for the antibody

steps. Slides were removed from the immunostaining chambers and the excess PBS remaining on each slide was drained off onto tissue. For all slides, and coverslips were mounted to the slides using Fluoromount-G® mounting medium containing DAPI (4′,6-diamidino-2-phenylindole), a blue-fluorescent DNA dye which counterstained the nuclei [Figure 9]. Slides were left to air dry at room temperature for 1 hour under an aluminium foil cover and then nail varnish applied to the top and bottom edges of the coverslip as to fully adhere the coverslip to the slide without obscuring the tissue. After 1 hour further drying, slides were placed in holders and wrapped fully in aluminium foil to block the light and stored at 4ºC until imaging.

3.3.3.3 Imaging

Imaging of the sections was performed using a Zeiss LSM880 laser scanning confocal microscope with ZEN Black software [Table 14]. This type of microscopy uses a focussed narrow laser beam to scan the tissue horizontally, blocking out external light to produce a high-resolution high-contrast image.

The Zeiss LSM880 confocal has multiple lasers and filters allowing for different fluorophores with different colours to be imaged simultaneously in the same field of view across multiple channels. Channels were programmed according to the fluorophore combination used on the slides using settings pre-loaded to the ZEN Black software by the manufacturer [Table 37].

Table 37: Fluorophore imaging information

Fluorophore	Absorbance (nm)	Emission (nm)	Colour
AlexaFluor 488	495	519	Green
AlexaFluor 647	650	665	Far red
DyLight 549	556	571	Yellow

Wherever possible, images were taken with no further processing, Occasionally, samples needed to be imaged using Z stacking due to the tissue being in multiple planes (maximum number of images = 5) and then processed within the software to provide a Maximum Intensity Projection.

3.4 Vascular function studies

3.4.1 Aortic vasomotion

Endothelial function was assessed using thoracic aortic rings harvested from 12-14 week old male $GS^{+/LacZ}$ and littermate control $GS^{+/+}$ mice.

3.4.1.1 Experiment preparation

Mice were humanely euthanised using rising concentrations of CO_2 and exsanguination [3.1.5]. The entire aortic tree was harvested into cold (~4°C) Krebs-Henseleit buffering solution [Table 15]. The aorta was dissected free of adherent fat and other tissues before the arch and sub-renal portions of the aorta were removed, leaving only the thoracic (suprarenal) aorta. The thoracic aorta was then divided into rings approximately 3-5mm in length, with each aorta providing 2-4 rings depending on length of suitable undamaged tissue [A]. Two fine triangular wires were then inserted into the open lumen of each aortic ring, taking care to prevent endothelial denudation, before the triangular wires were secured to keep the ring in place [B].

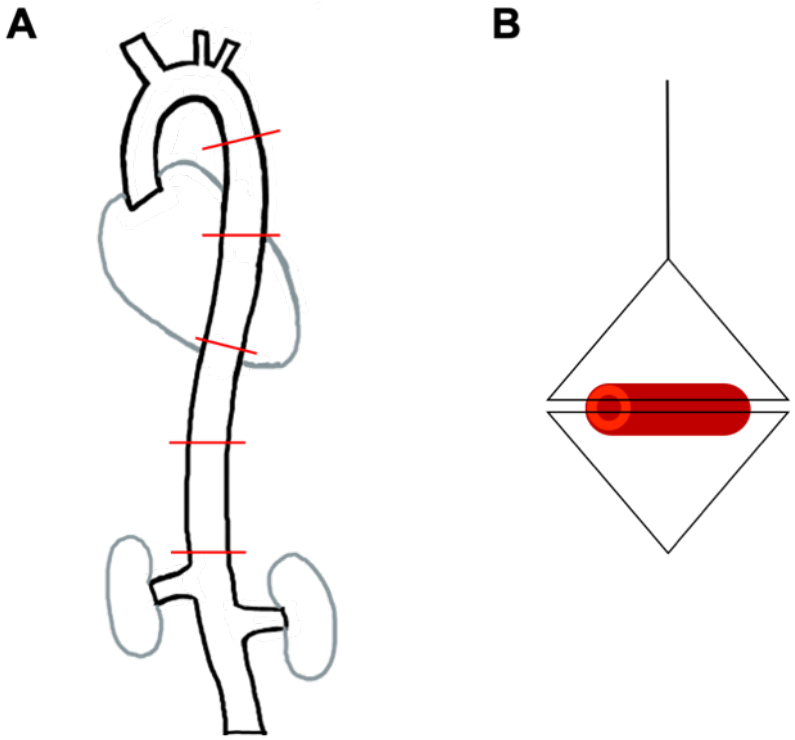

Figure 10: Diagram of aorta and aortic ring mounting The entire aortic tree is harvested from the arch to just below the iliac bifurcation. Once dissected free of fat and other tissues, the thoracic aorta is divided into 2-4 aortic rings [**A**]. The aortic rings are then mounted onto opposing fine wire triangles which are each threaded through the lumen and secured in place [**B**]

These triangular wires were then mounted onto high-sensitivity force transducers and suspended within organ bath chambers [Table 16], each containing ~10mL Krebs buffering solution continuously bubbled with 95%/5% v/v O_2/CO_2 gas and maintained at 37°C [Figure 11].

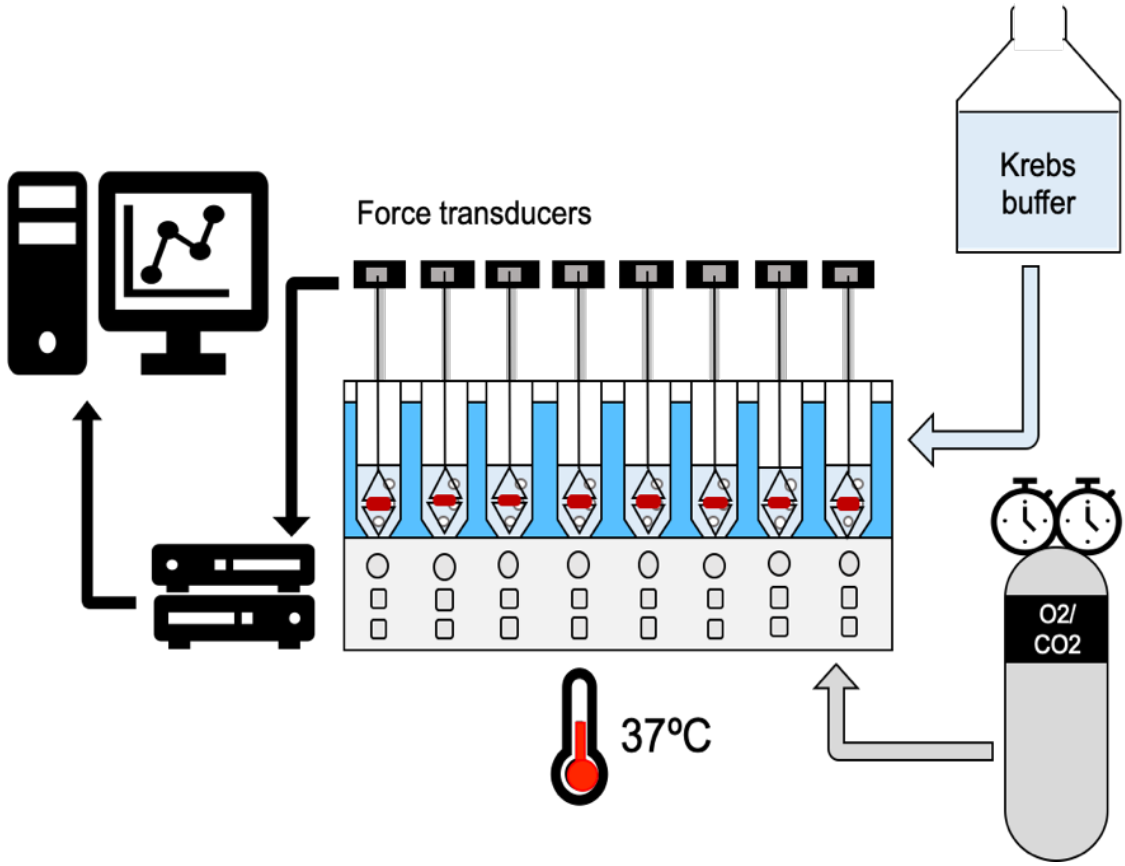

Figure 11: Schematic of Organ bath apparatus The apparatus consists of 8 individually controllable chambers within a water bath heated to 37°C. Each chamber is individually supplied with Krebs buffering solution pre-warmed to 37°C and a mixture of O_2 and CO_2 gases continuously bubbled through. Aortic rings pre-mounted onto triangles are suspended from force transducers affixed to the back of the apparatus, enabling detection of vasorelaxation and vasorelaxation responses. These force signals are passed through an amplifier and displayed on the computer using LabChart 8 software

3.4.1.2 Experimental protocol

The aortic rings were manually stretched over 30 minutes, increasing tension by 0.5g a step, to a final tension of 3g. Rings were rested at this tension to allow equilibration for a further 20 minutes before experiments commenced [Table 17].

Prior to the experimental work commencing, mice were genotyped at 4 weeks old [3.1.3] and then randomly assigned such that for each experiment, one $GS^{+/LacZ}$ and one $GS^{+/+}$ would be harvested approximately 2 months later. Experiments were then conducted blinded to genotype, with only the identification (ID) number available, and genotype information was not linked to the ID number until after initial data analysis was undertaken.

Ring viability and endothelium-independent constriction

The viability of the rings was initially assessed using the endothelium-independent vasoconstrictor potassium chloride (KCl). A single 100µl bolus of 400mM KCl was applied to each chamber containing 10mL Krebs solution, giving a final concentration of 4M and resulting constriction measured. The treatment was washed out thoroughly by replacing the solution with fresh Krebs buffer and rings allowed to relax for a few minutes before the treatment was repeated. At this point, any rings which failed to constrict by >0.25g after two treatments or did not relax back to baseline were discarded. After washing, the rings were re-equilibrated to 3g and allowed to rest for 20 minutes before the next experiment.

Endothelium-dependent vasodilation

After resting and re-equilibrating the tension to 3g as necessary, the rings were treated with the vasoconstrictor phenylephrine (PE) to give a total concentration of 300nM in each chamber and, as with the KCl, the constriction was assessed and any rings which failed to constrict by >0.25g after 3 minutes were discarded. Once rings had fully constricted, the cumulative dose response to the endothelium-dependent vasodilator acetylcholine (ACh) was assessed by addition of incremental doses of ACh from 1nM to 10µM and relaxation measured. Any rings which failed to relax by ~0.3g after accumulative ACh treatment were then discarded. Again, the rings were repeatedly washed by flushing with clean Krebs buffer and re-equilibrated to 3g.

Assessment of PE-induced vasoconstriction

After washing out the ACh from the rings, the cumulative dose response to PE was assessed by addition of incremental doses of PE from 1nM to 10µM and constriction measured before the rings were repeatedly washed by flushing with clean Krebs buffer and re-equilibrated to 3g.

In case of any differences in endothelium-dependent vasoconstriction and to assess any differences in NO bioavailability, the rings were then incubated for 1 hour with the NOS inhibitor L-N^G-monomethyl arginine citrate (L-NMMA). The rings were then re-equilibrated again before the cumulative dose response to PE was re-assessed in the same manner.

Endothelium-independent vasodilation

Finally, to ensure any differences in relaxation exhibited in response to ACh was endothelium mediated and that cells were capable of responding to NO, the cumulative dose response to the endothelium-dependent vasodilator and NO donor sodium nitroprusside (NaNP) was assessed by addition of incremental doses of NaNP from 1nM to 10μM and relaxation measured.

3.4.1.3 Data collection and analysis

Throughout the experiments, tension was recorded in grams using LabChart Pro 7.0 software. The data was then transformed in Excel 2016 such that constriction is expressed as the change in grams, and relaxation as either the change in grams or as the percentage of pre-constricted tension. Dose-response curves were fitted to a non-linear dose-response sigmoidal regression curve using Prism 8.4.1.

3.4.2 eNOS activity assay

Endothelial NOS (eNOS) activity was assessed using the conversion of radiolabelled [^{14}C]- L-arginine to [^{14}C]-L-citrulline by aortic rings harvested from 8-9 week old male $GS^{+/LacZ}$ and littermate control $GS^{+/+}$ mice[23,24].

3.4.2.1 Experimental protocol

500µl pH 7.4 HEPES buffering solution [Table 21] containing 0.25% v/v BSA (HEPES-BSA) was added to wells of a standard 24-well cell culture dish and placed in an incubator to warm to 37°C.

As for aortic vasomotion studies [3.4.1.1], mice were then humanely euthanised using rising concentrations of CO_2 and exsanguination [3.1.5] before the entire aortic tree was harvested into cold (~4°C) Krebs-Henseleit buffering solution [Table 15], dissected free of adherent fat and other tissues, and the arch and descending portions of the aorta removed, leaving only the thoracic aorta. The thoracic aorta was then divided into two approximately equal rings and each ring weighed using a fine weighing balance.

Aortic rings were transferred to separate wells of the pre-warmed HEPES-BSA buffering solution and incubated at 37°C for 40 minutes. Each well was then treated with 5µl of 100µCi/mL [^{14}C]-L-arginine (total dose: 0.5µCi) and the plate incubated for another 5 minutes. One aortic ring from each animal was then treated with the endothelial-dependent vasodilator ACh [3.4.1.2] in order to stimulate eNOS activity. To do this, a single 5µl bolus of 100mM ACh was added to the appropriate wells (final concentration: 100nM), and the plate then incubated for a further 15 minutes.

The radioactive conversion reaction was stopped by transferring the tissue to wells of a standard 24-well plate containing 1mL cold (~4°C) PBS containing 5M unlabelled L-arginine and 4M EDTA in each well. This wash step was repeated again before the aortic rings were then transferred to microcentrifuge tubes containing 100µl 95%/5% v/v ethanol/dH_2O. The tubes were incubated at 4°C overnight to fully stop all reactions and preserve the tissue.

The ethanol was evaporated using a SpeedVac vacuum concentrator set to 35°C for 20 minutes. 100µl 20M pH5.5 HEPES buffer (pH altered with HCl) was added to each tube and the tissues finely minced within this buffer. Samples were then centrifuged for 15 minutes at 13,000rpm to pellet undigested tissue.

100g DOWEX® resin was equilibrated with 100mL 1M sodium hydroxide (NaOH). The resin was then repeatedly washed with dH_2O to remove the excess NaOH until the resin reached a pH ~7.6. The resin was then drained and suspended in a 1:1 ratio in

dH_2O. 2.8mL equilibrated resin suspension was added to 5mL round-bottom tubes to create ion exchange columns [Table 19].

The supernatants containing the cellular components were applied (~100µl) [A] and the tubes mixed thoroughly by vortexing [B]. The resin was then allowed to settle by gravity over 15 minutes at room temperature (~20ºC) in order to separate the [^{14}C]-L-citrulline from any residual [^{14}C]-L-arginine [C].

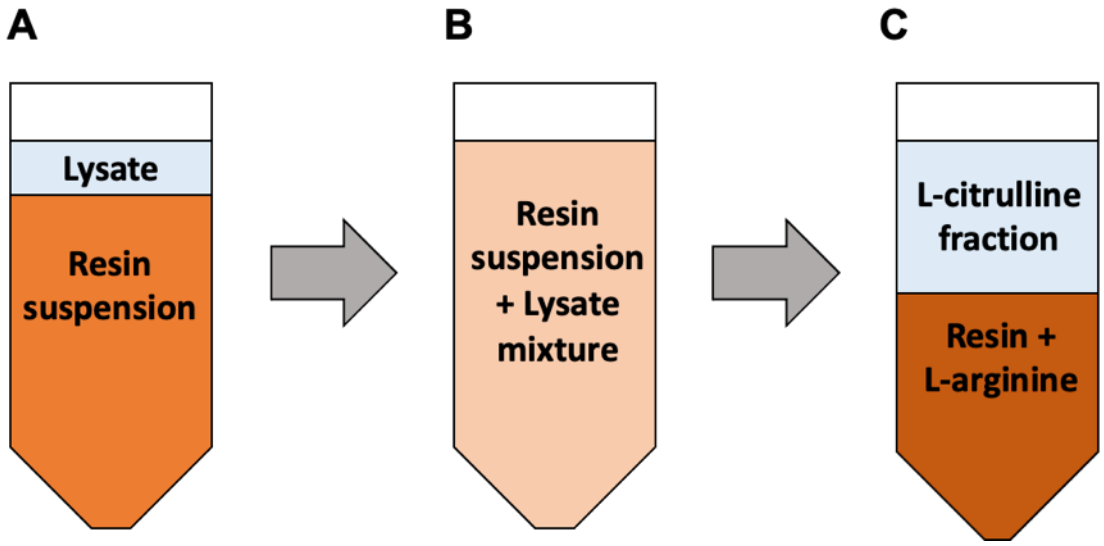

Figure 12: Schematic of ion-exchange column separation of [^{14}C]-L-citrulline from [^{14}C]-L-arginine Aorta lysates (**clear**) were added to equilibrated DOWEX® resin suspension (**orange**) [**A**]. Samples were mixed thoroughly [**B**] and then allowed to separate into two layers – an aqueous layer containing dissolved [^{14}C]-L-citrulline (**clear**), and the resin layer to which residual L-arginine was bound, whether labelled or unlabelled (**dark orange**) [**C**]

For each sample, 10mL scintillation cocktail was dispensed into 20mL plastic scintillation vials before 1mL of the clear aqueous top-layer of the ion-exchange column [C] was added to each tube. The scintillation vials were sealed, and the reaction cocktails mixed by inverting the tubes. Finally, the sample reaction cocktails were analysed for [^{14}C]-L-citrulline content using a Tri-Carb 2800TR liquid scintillation analyser.

3.4.2.2 Data analysis

The scintillation analyser was previously self-calibrated using the control scintillation counting tubes provided by the manufacturer, including a ^{14}C control. The program was set to count the number of disintegrations over 5 minutes and provide an average disintegrations per minute (DPM) value. These mean DPM values were then normalised against the weight of each piece of tissue taken previously to give a final value expressed as DPM/mg.

3.5 Protein analysis

3.5.1 Sample preparation

Adult male and female $GS^{+/LacZ}$ mice and littermate control $GS^{+/+}$ animals were sacrificed using either of the methods described in 3.1.5. The entire aortic tree was harvested from each animal and placed in 2mL round-bottom microcentrifuge tubes before being snap-frozen using liquid nitrogen and then stored at -80ºC.

Tissues were defrosted and 250µl cell extraction buffer (CEB) was added to each tube, such that the tissue was sufficiently submerged. A 6mm metal cone ball was added to each tube before tissues were mechanically homogenised using a Qiagen TissueLyser II for 1 minute at 30 Hz. Homogenates were transferred to clean 1.7mL microcentrifuge tubes and centrifuged at 4ºC for 15 minutes at 13,000rpm (revolutions per minute) to pellet undigested tissue.

Lysates were then transferred to new clean 1.7mL microcentrifuge tubes and kept on ice. The lysates were then vortexed 4 times over 30 minutes to ensure lysed samples were mixed properly. If not used immediately, lysates were then stored at -80ºC.

3.5.2 Total protein quantification

Kidney and aorta lysates were analysed for their total protein concentrations using the Pierce™ Bicinchoninic acid (BCA) Protein Assay Kit. Firstly, standards are prepared by diluting 2mg/mL BSA with CEB to produce final concentrations ranging from 25µg/mL to 2000µg/mL [Table 38], plus a blank.

Table 38: BSA protein standards

Tube	Volume of CEB mix (µl)	Volume and source of BSA (µl)	Final concentration (µg/mL)
A	0	300 of Stock	2000
B	125	375 of Stock	1500
C	325	325 of Stock	1000
D	175	175 of tube B dilution	750
E	325	325 of tube C dilution	500
F	325	325 of tube E dilution	250
G	325	325 of vial F dilution	125
H	400	100 of vial G dilution	25

Lysates were defrosted if not used fresh and then vortexed again 4 times over 30 minutes (once every 10 minutes) to ensure lysed samples were mixed properly. Samples were then diluted with additional cell extraction buffer mix in the ratio of 1:8 (8µl lysate plus 56µl CEB mix) or 1:32 (2µl lysate plus 64µl CEB mix).

25µl of standards and diluted lysates were added to wells of 96-well clear flat-bottomed plates. Kit assay reagents were then mixed at a ratio of 50 parts of “reagent A” to 1 part “reagent B” before 200µl of this reagent mixture is added to each well. Plates were then incubated at 37ºC for 30 minutes in order for the bicinchoninic acid reaction to occur, changing the mixture from a pale green to purple, with the intensity of the colour indicating the concentration of the protein.

Absorbance was then measured at 562 nm (nanometres) using a BioTek™ PowerWave™ plate reader and protein concentration calculated using Excel 2016.

3.5.3 Western blotting

3.5.3.1 Sample preparation

Samples for western blotting were prepared by mixing a volume of aorta lysate equivalent to 40µg, with 2µl NuPAGE™ Sample Reducing Agent (10X), and 5µl NuPAGE™ LDS Sample Buffer (4X), and finally, a volume of water was added to bring the total reaction volume to 20µl [Table 39].

Table 39: Western blotting sample preparation

Component	**Volume per reaction (µl)**
NuPAGE™ Sample Reducing Agent (10X)	2
NuPAGE™ LDS Sample Buffer (4X)	5
40µg total protein lysate	X
Deionised water	Y=(20-(X+7))
Total volume	**20**

This reducing mixture was then heated at 70ºC for 10 minutes to denature the proteins and therefore enable them to be separated by size using gel electrophoresis.

3.5.3.2 Gel electrophoresis and membrane transfer

NuPAGE™ 4-12% polyacrylamide gradient Bis-Tris Protein mini gels with 15 wells (1.5mm) were placed in appropriate mini gel electrophoresis tanks and submerged in 1X NuPAGE™ MES SDS Running Buffer (diluted from 20X using distilled water). 20µl of each pre-prepared protein sample was loaded into the gel wells, alongside 3µl of Color Prestained Protein Standard ladder (10–250 kDa). Electrophoresis was then carried out for 90 minutes at 200V in order to separate the proteins, as indicated by both the separation of the ladder, and by the Coomassie G250 and Phenol Red tracking dyes present within the sample buffer being ran off the bottom of the gel.

The now separated proteins were then transferred from the gels to polyvinylidene difluoride (PVDF) membranes using a Trans-Blot® Turbo™ Transfer System. In order to do this, for each gel, a PVDF membrane was pre-treated with methanol. This methanol-treated membrane and two transfer stacks (consisting of filter pads) were then equilibrated in transfer buffer diluted according to the manufacturer's instructions [Table 40]. These components were then layered in the centre of the base of the transfer cartridge as follows: transfer stack, PVDF membrane, gel, transfer stack. The lid of the cartridge was then fastened on, sandwiching together the components, excess buffer poured out, and the now assembled cartridge placed in the Trans-Blot® Turbo™ Transfer System. The machine was then set to transfer for 15 minutes at 25V (1.3A).

Table 40: Transfer buffer for Trans-Blot® Turbo™ Transfer system

Component	**Volume (mL)**
Trans-Blot® Turbo™ Transfer buffer (5X)	100
100% ethanol	100
Deionised water	300
Total volume	**500**

Once the transfer was completed, adequate protein transfer was confirmed by observing both the complete transfer of the Color Prestained ladder and additionally by observation of the now visible lanes of protein present on the membrane.

3.5.3.3 Immunostaining for Western blotting

Membranes were cut using a disposable scalpel according to the expected molecular weight of the protein of interest, and each cut membrane was blocked for 1 hour at room temperature with 7mL blocking buffer consisting of 5% BSA diluted in 1X Tris-buffered saline (TBS) (diluted from 10X using distilled water) [Table 41] containing 0.02% Tween® 20.

Table 41: 10X Tris-buffered saline (TBS) (pH 7.6)

Component	g/L
Tris base	5.6
Tris-HCl	24
NaCl	88

The primary antibodies were then diluted in this same blocking buffer and 0.02% sodium azide (NaN_3) added to inhibit microbial growth. 7mL primary antibody mixture was applied to each membrane as appropriate and the membranes were then incubated overnight at 4ºC [Table 42].

The next day, excess primary antibody was removed through 5 washes of 7mL 1X TBS-0.02% Tween® 20 buffer for 5 minutes each. During washing, 3% milk solution was prepared by dissolving skimmed milk powder in 1X TBS-0.02% Tween® 20 buffer. In order to visualise the target proteins by chemiluminescence, appropriate secondary antibodies conjugated to the enzyme horseradish peroxidase (HRP) were selected and mixes prepared by diluting these antibodies 1:5000 in the 3% milk solution [Table 42].

Table 42: Immunostaining antibodies for Western blotting

Target protein	Expected molecular weight (kda)	Primary antibody dilution	Secondary antibody	Secondary antibody dilution
B-actin	42	1:5000	HRP-conjugated anti-mouse	1:5000
eNOS	140	1:1000		
Phosphorylated-eNOS (S1177)	140		HRP-conjugated anti-rabbit	
GS	42			

Once washing was complete, 7mL secondary antibody mixture was applied to each membrane as appropriate and the membranes were then incubated for 1 hour at room temperature.

Excess secondary antibody was then removed through 5 washes of 7mL TBS-Tween 20 buffer for 5 minutes each and the membrane kept in clean TBS-Tween 20 buffer until protein visualisation.

3.5.3.4 Protein visualisation and analysis

Target protein visualisation was achieved by treating the washed immunostained membranes with the Immobilon™ Western Chemiluminescent HRP Substrate Kit before imaging the chemiluminescence emitted from the membranes using the Syngene G:BOX equipment and proprietary GeneSys software.

Using ImageJ, the Western blot image was converted to 8-bit greyscale and lanes defined using the rectangle selection tool [A]. The ImageJ gel tool was used to produce lane plots showing the band intensities as peaks. Background membrane staining was deducted by using the line tool to segment the peak, of which the area was measured to provide a densitometry value [B, yellow region]. For ß-actin, these densitometry values were compared between genotypes to assess its suitability as a loading control. For GS, eNOS and phosphorylated eNOS (S1177), densitometry values were normalised to the average ß-actin value for the same genotype and then averaged by genotype for comparison.

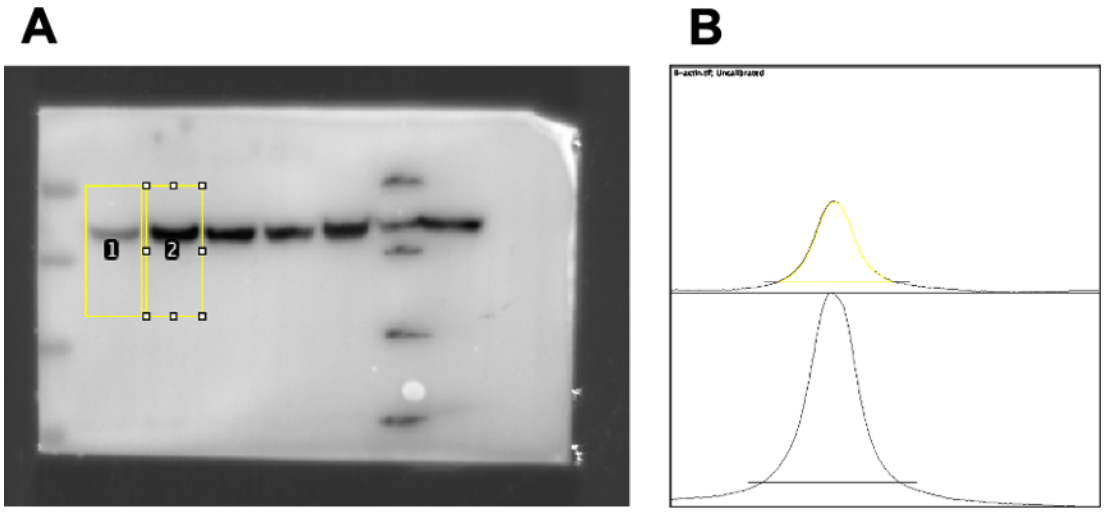

Figure 13: Example Western Blot densitometry analysis using a ß-actin blot
Lanes were defined on the 8-bit ß-actin blot [**A**] and lane plots showing high intensity bands as peaks calculated by the ImageJ software [**B**]. Background membrane staining was deducted by using the line tool to segment the peak and the area of the peak measured to provide a densitometry value [**B, yellow**]

3.6 Statistics

Results are displayed as mean values (± SEM, Standard Error of the mean) for each genotype and, unless otherwise specified, comparisons between groups were made in Prism 8.4.1 using either a Student's t test with Welch's correction or a repeated-measures two-tailed analysis of variance (ANOVA) with Bonferroni corrected multiple comparisons as appropriate. $P<0.05$ was considered statistically significant.

Chapter 4 Results

4.1 Confirmation of GS haploinsufficiency in $GS^{+/LacZ}$ mice

Multiple studies have indicated that GS is differentially expressed throughout the body in a cell- and tissue-dependent manner. It has been documented that some tissues, such as kidneys[60] and liver[62], express high levels of GS. As such, kidneys were utilised as a control tissue to corroborate haploinsufficiency of GS within $GS^{+/LacZ}$ mice. Furthermore, whilst scRNA-seq data does suggest *GLUL* to be enriched in ECs[18], the typical level of GS expression within whole arteries is currently unknown.

Whole kidney and whole aorta tissue were harvested from $GS^{+/LacZ}$ mice and $GS^{+/+}$ controls and total RNA was isolated for each tissue. The RNA was then reverse transcribed to single strand cDNA and the level of GS gene expression was quantified using SYBR Green RT-qPCR [3.2].

When compared to $GS^{+/+}$ controls, GS expression in $GS^{+/LacZ}$ mice was reduced in both kidney [Figure 14A] and aorta [Figure 14B], with a 36.1% (*P*=0.1658; n.s.- not significant) and 68.7% (*P*=0.0467, *) reduction respectively. Additionally, in both $GS^{+/LacZ}$ and $GS^{+/+}$ mice, GS expression was substantially higher in the aorta than in the kidney. Together these data support global haploinsufficiency of GS.

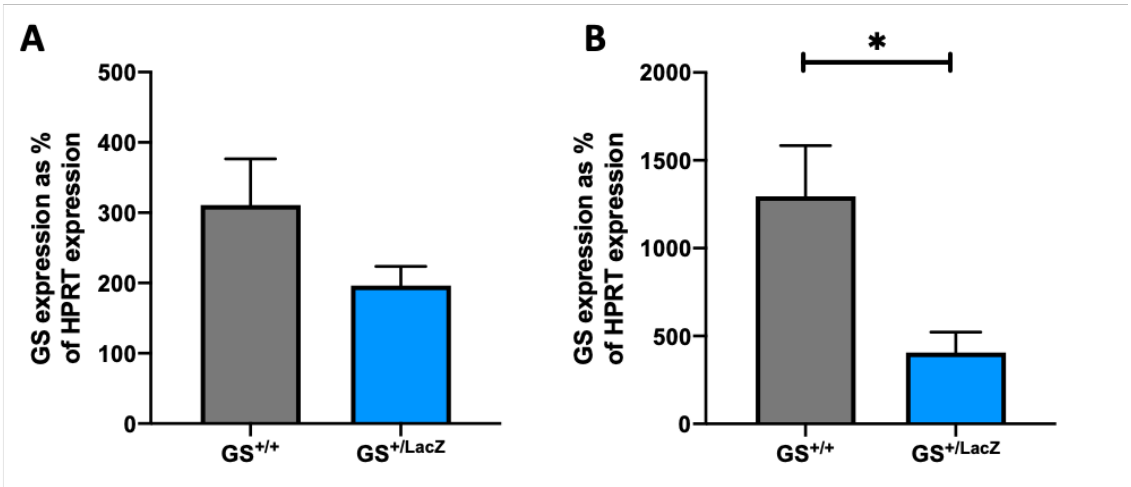

Figure 14: Relative expression of *GLUL* (GS) mRNA in $GS^{+/LacZ}$ mice compared to $GS^{+/+}$ controls GS gene expression in kidney [**A**] and aorta [**B**]. For each group and for each tissue, the expression of *glul* is expressed as a relative percentage of the housekeeper gene, *HPRT* (*n*=4 per genotype)

4.2 Western Diet feeding

$GS^{+/LacZ}$ and $ApoE^{-/-}$ mice were crossed to produce $GS^{+/LacZ}ApoE^{-/-}$ mice and $GS^{+/+}ApoE^{-/-}$ littermate controls. To induce atherosclerosis, male cross-bred progeny were fed a Western diet containing 21.4% fat from 8 weeks of age to up to 20 weeks of age (maximum 12 weeks duration) [3.1].

4.2.1 Time-course comparison of *Glul* expression

As discussed before, GS has been shown to be differentially expressed throughout the body; kidneys have been previously documented as expressing a high level of GS owing to the role of GS in ammonia detoxification [60] and so were used as a control tissue, whilst the GS expression level of the vasculature is currently undocumented although recent scRNA-seq data has indicated ECs to be enriched in *GLUL*[18]. Likewise, despite the previously described link between genetically reduced endothelial GS expression and increased cardiovascular event risk in patients with T2DM[9], the effect of a diet high in cholesterol and fat on GS expression has not been previously investigated.

As such, in order to investigate whether diet influences GS expression, $ApoE^{-/-}$ mice with either wild-type GS expression, $GS^{+/+}ApoE^{-/-}$, or GS haploinsufficiency, $GS^{+/LacZ}ApoE^{-/-}$, were sacrificed at either 8 weeks old having been fed a chow diet (0 weeks Western diet), or at 14 weeks of age having been fed a Western diet for 6 weeks, or at 20 weeks old having been fed a Western diet for the maximum 12 week duration. Whole kidney and whole aorta tissue were harvested from these groups and total RNA was isolated for each tissue. The RNA was then reverse transcribed to single strand cDNA and the level of GS gene expression was quantified using TaqMan™ RT-qPCR [3.2].

As expected, when compared to $GS^{+/+}ApoE^{-/-}$ control mice, GS expression in $GS^{+/LacZ}ApoE^{-/-}$ mice is consistently reduced in both kidney [Figure 15A] and aorta [Figure 15B], irrespective of Western diet feeding duration, although this is not significantly different at any of the time points.

Unexpectedly, this time-course experiment has also indicated that Western diet may alter GS expression in both kidneys and aortas in both $GS^{+/LacZ}ApoE^{-/-}$ mice and $GS^{+/+}ApoE^{-/-}$ controls. Within the kidneys, Western diet feeding decreases GS expression within $GS^{+/LacZ}ApoE^{-/-}$ mice and increases expression within $GS^{+/+}ApoE^{-/-}$ control mice. By contrast, in the aortas, GS expression progressively decreased in $GS^{+/+}ApoE^{-/-}$ controls and in $GS^{+/LacZ}ApoE^{-/-}$ plateaued at a lower than baseline level from 6 weeks to 12 weeks.

Although unexpected, this finding that Western diet may itself reduce aortic GS expression is particularly important as it stresses the need to understand how reduced GS expression influences vascular health and disease, given that diet may independently drive the same processes and as such, warrants further investigation into this phenomenon.

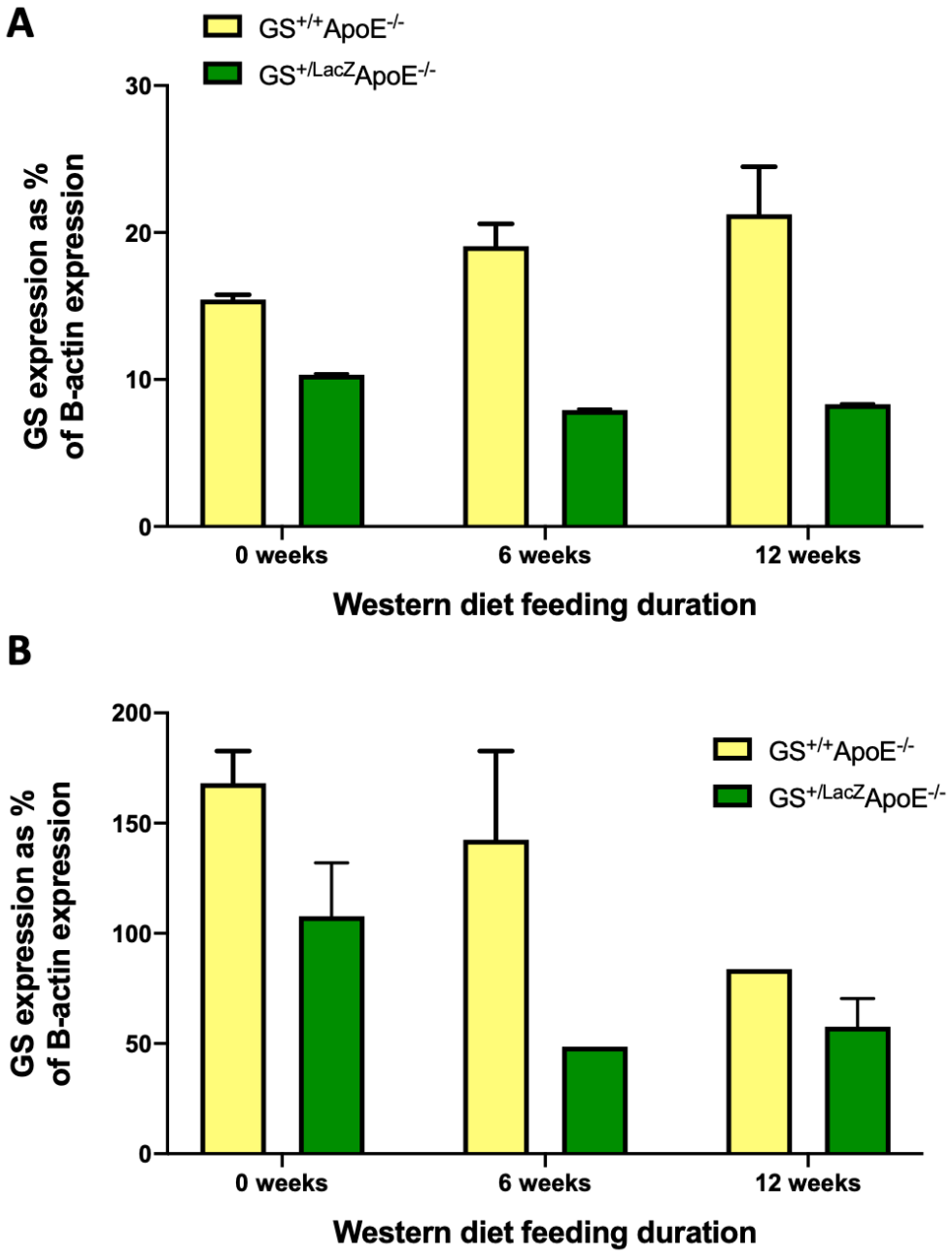

Figure 15: Relative expression of *glul* (GS) mRNA in $GS^{+/LacZ}ApoE^{-/-}$ animals compared to $GS^{+/+}ApoE^{-/-}$ controls GS gene expression in kidney [**A**] and aorta [**B**] harvested from animals aged 8 weeks fed a chow diet (0 weeks western diet) or fed a western diet for either 6 or 12 weeks. For each group and for each tissue, the expression of *glul* is expressed as a relative percentage of the housekeeper gene, ß-actin (*n*=2 per group)

4.2.2 Weight data

Throughout the Western Diet feeding period, mice were weighed weekly [3.1]. There was no significant difference (*P*=0.2818, n.s.) in body mass at any point during the feeding period [Figure 16A] and this was further confirmed by the area under the curve (AUC) analysis also being statistically similar (*P*=0.8634, n.s) [Figure 16B].

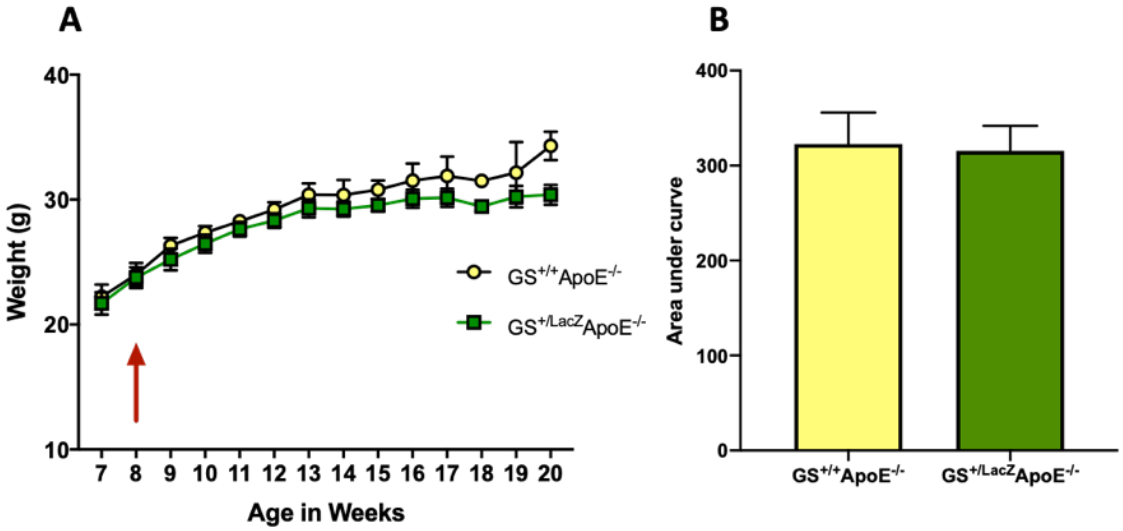

Figure 16: Body mass data Body mass was measured in $GS^{+/LacZ}ApoE^{-/-}$ mice (*n*=8) and $GS^{+/+}ApoE^{-/-}$ controls (*n*=9) from 7 weeks old to 20 weeks old. Western diet feeding commenced at 8 weeks old, as indicated by the **red** arrow, for 12 weeks total [**A**]. An AUC analysis was used to compare the groups [**B**]

4.2.3 Metabolic testing

GTTs and ITTs were performed on the $GS^{+/LacZ}ApoE^{-/-}$ and $GS^{+/+}ApoE^{-/-}$ mice immediately prior to starting the Western diet and again at the end of the diet period [Figure 18].

At baseline (7 weeks old), there was no difference in fasting blood glucose (*P*=0.6293, n.s.) [Figure 17A] or glucose tolerance (*P*=0.6087, n.s.) [B] and this was confirmed by AUC analysis (*P*=0.5981, n.s.) [C]. There was also no difference in insulin tolerance (*P*=0.0921, n.s.) [D] and this was also confirmed by AUC analysis (*P*=0.5918, n.s.) [E].

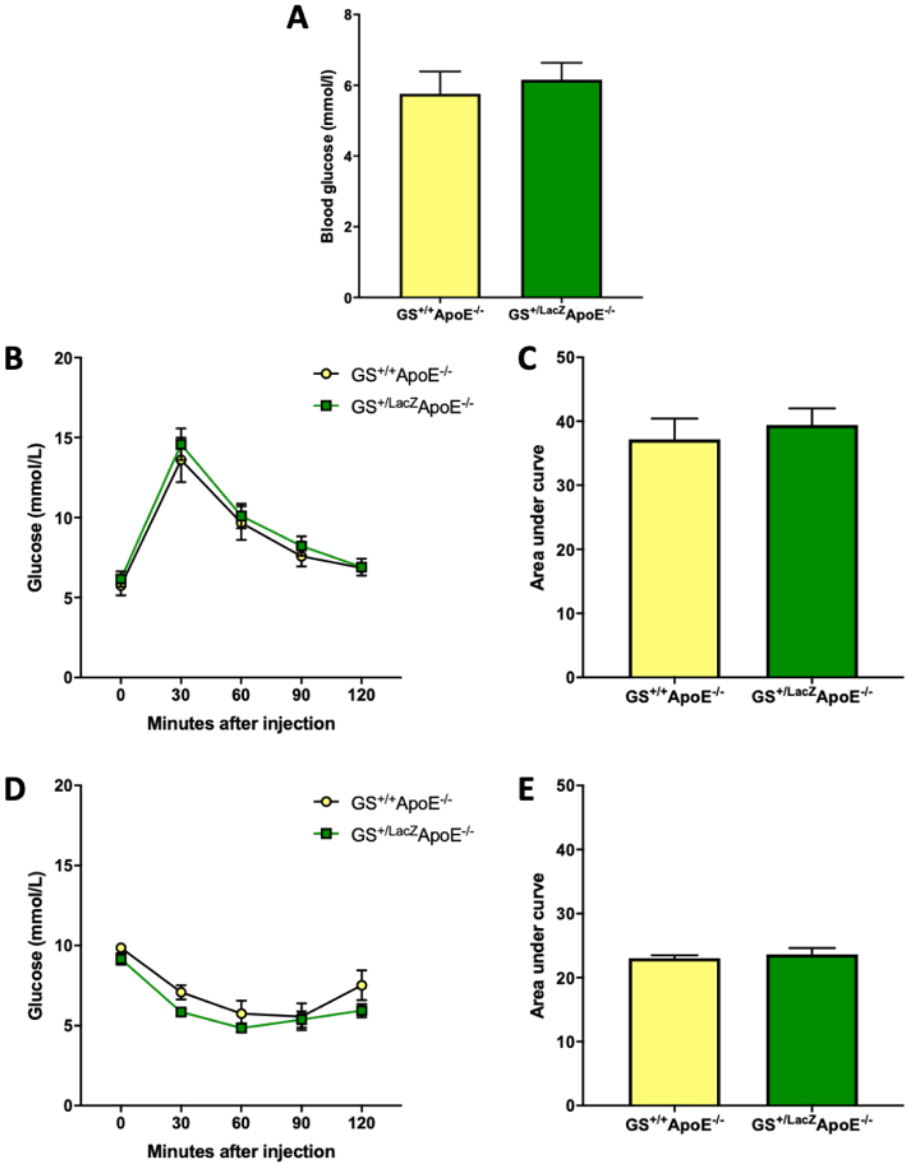

Figure 17: Baseline metabolic data Fasting blood glucose was measured in $GS^{+/LacZ}ApoE^{-/-}$ (*n*=9) and $GS^{+/+}ApoE^{-/-}$ mice (*n*=5) pre-western diet at 8 weeks of age [**A**] prior to GTTs being performed [**B**]. ITTs were also conducted before commencing the western diet [**D**] ($GS^{+/+}ApoE^{-/-}$: *n*=5, $GS^{+/LacZ}ApoE^{-/-}$: *n*=11). AUC analyses were used to compare the groups for both GTT [**C**] and ITT [**E**] respectively

At 20 weeks of age, after 12 weeks of Western diet, whilst there was still no difference in fasting blood glucose (*P*=0.7068, n.s.) [Figure 18A], there is now a significantly improved glucose tolerance in $GS^{+/LacZ}ApoE^{-/-}$ (*P*=0.0212, *) [Figure 18B], confirmed by lower AUC (*P*=0.0197, *) [Figure 18C]. Additionally, there is also a small but statistically insignificant difference in insulin tolerance (*P*=0.1996, n.s.) [Figure 18D], again shown by AUC (*P*=0.3210, n.s.) [Figure 18E].

Together this data suggests that whilst neither genotype develops altered fasting blood glucose, $GS^{+/LacZ}ApoE^{-/-}$ mice are mildly protected from developing diet-induced impairments in both glucose tolerance, and possibly insulin sensitivity, when compared to $GS^{+/+}ApoE^{-/-}$ controls.

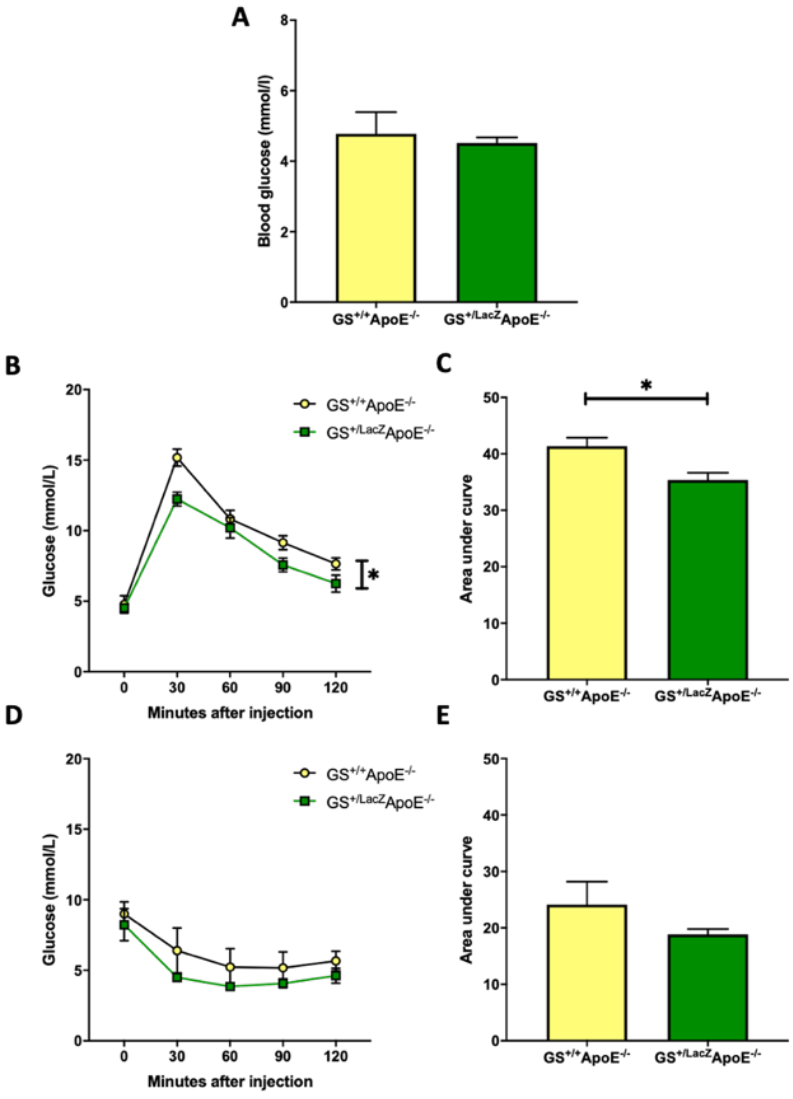

Figure 18: Post-western diet metabolic data Prior to sacrifice, fasting blood glucose was measured in $GS^{+/LacZ}ApoE^{-/-}$ (*n*=7) and $GS^{+/+}ApoE^{-/-}$ (*n*=4) mice at 20 weeks of age after 12 weeks of western diet [**A**] prior to GTTs being conducted [**B**]. ITTs were also conducted before sacrifice [**D**] ($GS^{+/+}ApoE^{-/-}$: *n*=3, $GS^{+/LacZ}ApoE^{-/-}$: *n*=4). AUC analyses were used to compare the groups for both GTT [**C**] and ITT [**E**]

4.3 Histology

Atherosclerosis was induced in both the $GS^{+/LacZ}ApoE^{-/-}$ mice and their $GS^{+/+}ApoE^{-/-}$ littermate controls before animals were anaesthetised, the tissues harvested and the livers, hearts, and/or aortas were harvested and then fixed with PFA-PBS solution for histological examination.

4.3.1 Whole aorta plaque burden

Aortas were harvested and fixed prior to being dissected free of peri-adventitial fat, opened lengthways, and stained with Oil Red O [3.3.1] [Figure 19A-B].The plaque burden and length of each aorta was measured and the mean for each genotype calculated [Figure 19C-D].

There is a significant difference in plaque burden with $GS^{+/LacZ}ApoE^{-/-}$ mice having less than half the amount of plaque of $GS^{+/+}ApoE^{-/-}$ controls (1.92% and 3.98% respectively; P=0.0027, **) [Figure 19C]. There was no significant difference in aortic lengths between genotypes (P=0.3765, n.s.) [Figure 19D].

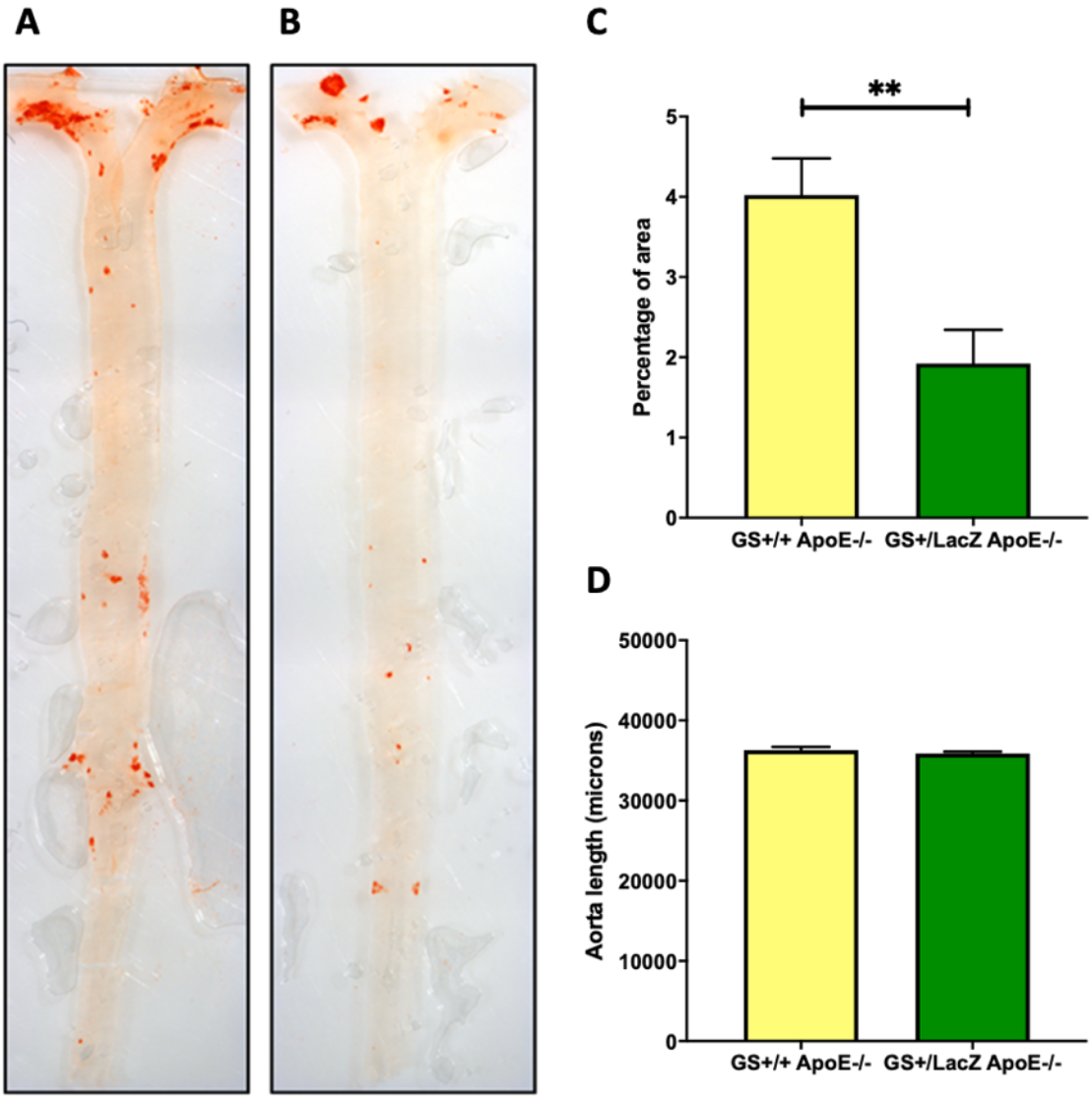

Figure 19: Atherosclerotic plaque burden in whole aorta Aortas were harvested from 20 week old mice after 12 weeks of western diet. Aortas from both $GS^{+/+}ApoE^{-/-}$ controls [**A**] and $GS^{+/LacZ}ApoE^{-/-}$ mice [**B**] were stained with Oil Red O and imaged (representative images showing mean amount of plaque shown; magnification x12). Plaque burden was then quantified [**C**] and the length of the aortas were also quantified [**D**] using Image-Pro Plus 7.0 (*n*=12 per genotype)

4.3.2 Aortic sinus – Lipid deposition

Hearts were fixed using PFA-PBS before being embedded in OCT blocks. Using the cryostat, blocks were trimmed until the aortic valve leaflets were visible. The aortic sinus was then serially sectioned until the leaflets were no longer visible, before being stained with the lipid stain Oil Red O [3.3.2.5] [Figure 20].

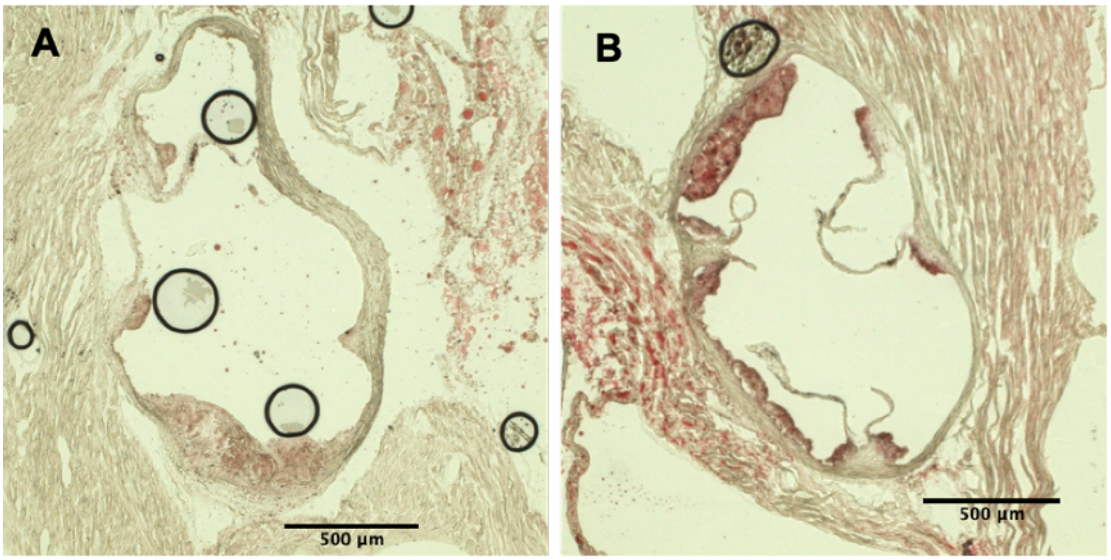

Figure 20: Representative Oil Red O stained aortic root sections Hearts containing the aortic root were harvested from 20 week old animals after 12 weeks of western diet. Aortic sinus regions from both $GS^{+/+}ApoE^{-/-}$ [**A**] control animals and $GS^{+/LacZ}ApoE^{-/-}$ mice [**B**] were stained with Oil Red O and then imaged (magnification: 4x; EVOS imaging system). Black rings shown are artefacts caused by air bubbles within the mounting medium (*n*=3 per genotype)

4.3.2.1 Plaque burden of Oil Red O stained cryosections

The plaque burden (i.e. overall plaque area), the total area of the sinus, the mean plaque area, the mean area of the largest plaque, and the mean number of plaques was measured for each aortic sinus from the images of the Oil Red O stained aortic sinus sections, and the mean value for each of these for each genotype calculated.

There is a significant difference in plaque burden of the aortic sinus, with $GS^{+/+}ApoE^{-/-}$ control mice $GS^{+/LacZ}ApoE^{-/-}$ mice having more approximately 50% more plaque than $GS^{+/LacZ}ApoE^{-/-}$ mice (16.51% and 10.83% respectively; *P*=0.0166, *) [Figure 21A]. This difference in plaque burden is despite there being no significant difference between genotypes in either the total aortic sinus area (*P*=0.4377, n.s.) [Figure 21B], nor in the number of plaques present (*P*=0.2584, n.s.) [Figure 21C]. There is also no significant difference in the mean plaque area (*P*=0.239, n.s) [Figure 21D] nor the mean area of the largest plaque (*P*=0.0625, n.s.) [Figure 21E]. However, qualitative assessment of the images [Figure 20] suggests those of $GS^{+/LacZ}ApoE^{-/-}$ mice to be smaller and this is reflected in the mean area data [Table 43].

Table 43: Mean areas of Oil Red O stained plaques

	Mean plaque area (μm^2)	Mean area of largest plaque (μm^2)
$GS^{+/+}ApoE^{-/-}$	70051	129021
$GS^{+/LacZ}ApoE^{-/-}$	32083	82328

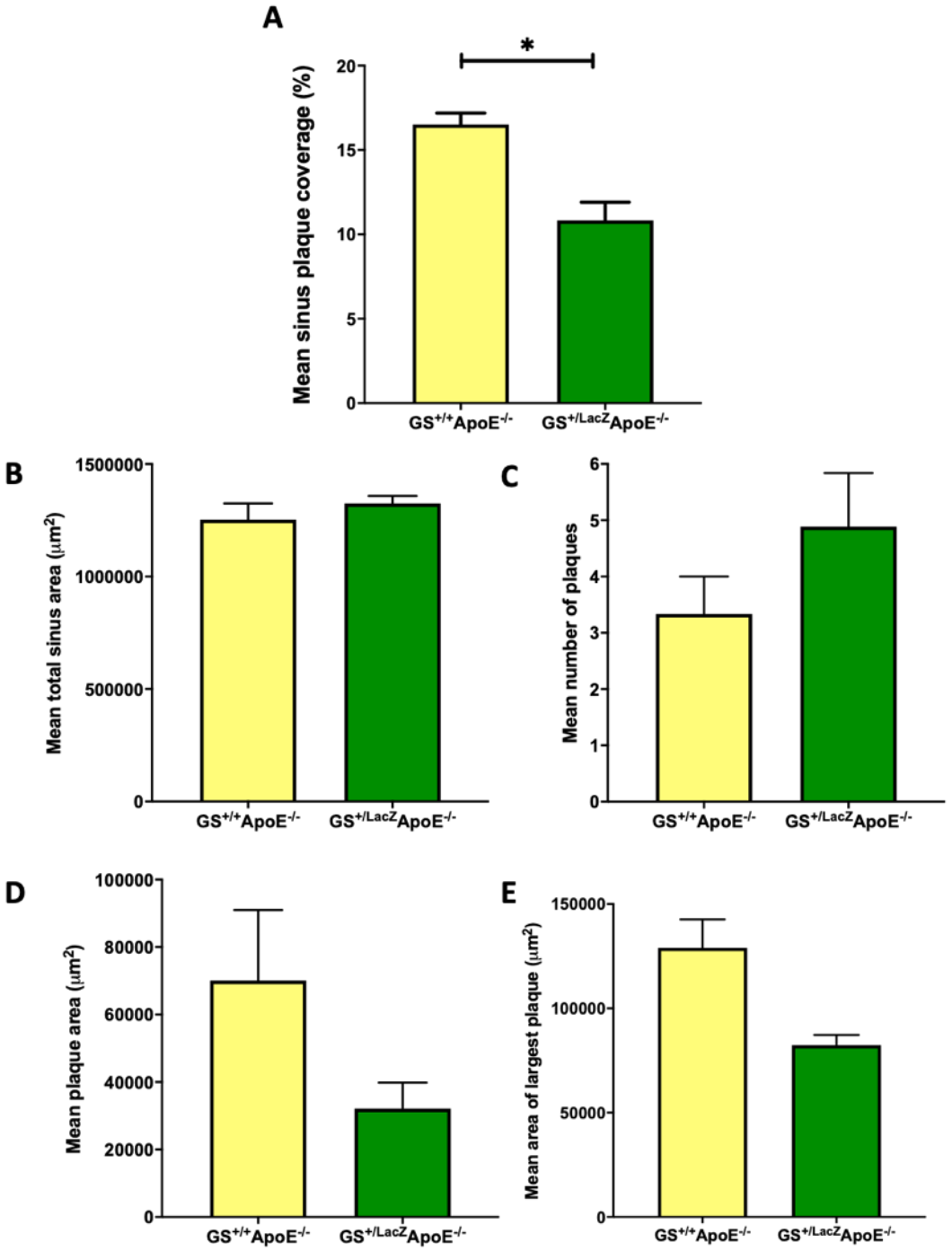

Figure 21: Atherosclerotic plaque burden in the Oil Red O stained aortic sinus
Plaque burden was quantified [**A**] along with the mean area of the sinus [**B**], the mean number of plaques [**C**], the mean plaque area [**D**], and the mean area of the largest plaque [**E]** (*n*=3 per genotype)

4.3.2.2 Lipid deposition

Colour intensity results

In addition to measuring plaque burden, the images of the Oil Red O stained aortic sinus sections were also used to assess plaque composition, since a difference in colour intensity could indicate a difference in lipid deposition. A colour histogram was generated for the largest plaque of each image (as identified in previous plaque burden analyses), producing a mean and mode intensity value for each of the three colours making up the composite image – red, green and blue (RGB). These RGB values were averaged for each animal and these values compared between genotypes.

There are no significant differences in any of the RGB measures, suggesting that the overall colour of the plaques does not differ between genotypes [Figure 22].

Table 44: Colour intensities of Oil Red O stained aortic sinus sections

Colour	Mean / Mode	$GS^{+/+}$ $ApoE^{-/-}$	$GS^{+/LacZ}$ $ApoE^{-/-}$	*P* value and significance	Figure reference
Red	Mean	169.5	170.8	0.8885, n.s.	Figure 22A
	Mode	175.2	166.9	0.4568, n.s.	Figure 22B
Green	Mean	146.4	148.8	0.8459, n.s.	Figure 22C
	Mode	157.2	150.8	0.7224, n.s.	Figure 22D
Blue	Mean	121.9	125.1	0.7569, n.s.	Figure 22E
	Mode	128.7	126.5	0.8817, n.s.	Figure 22F

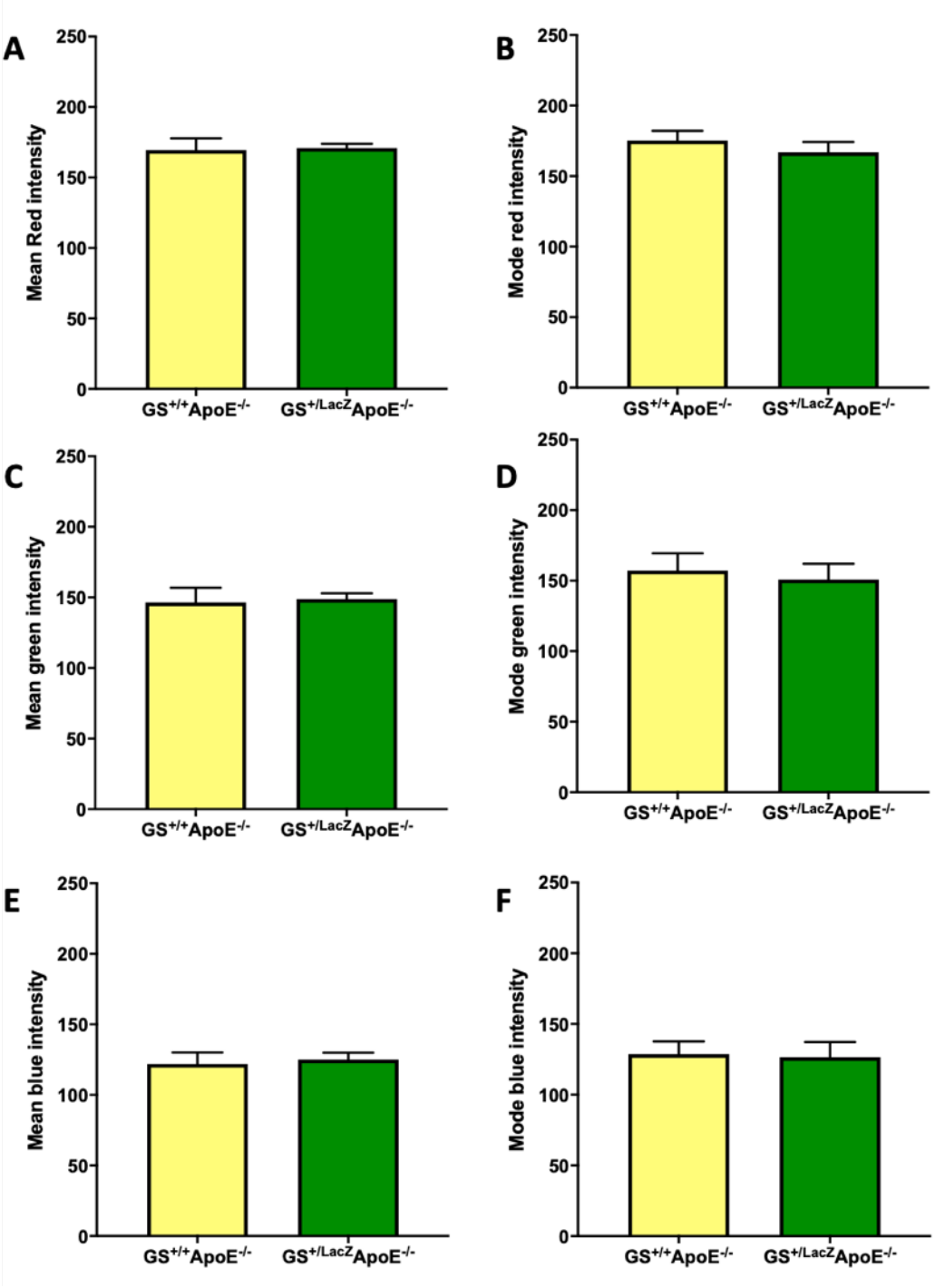

Figure 22: Colour distribution of the largest plaque stained using Oil Red O

ImageJ was used to quantify the mean and modal intensities for Red [**A & B**], Green [**C & D**] and Blue [**E & F**] for the largest plaque of each animal and the average values were then compared between genotypes (*n*=3 per genotype)

Fat distribution analysis by colour thresholding

As qualitative assessment of the Oil Red O stained aortic sinus images [Figure 20] indicated there may be a spatial difference in fat deposition, colour thresholding was also utilised in order to identify whether there was a spatial difference in fat deposition through measuring only high intensity “true” red staining using the Hue Saturation Brightness (HSB) colour space. This was done because the RGB colour intensity values provide a mean value for the whole plaque and is therefore unsuitable for differentiating between plaques with an even staining pattern and those with distinct regions of high and low intensity staining.

There is a significant difference between genotypes in the percentage area of plaque passing the threshold, with $GS^{+/LacZ}ApoE^{-/-}$ mice having more than double the area of red staining when compared with $GS^{+/+}ApoE^{-/-}$ controls (37.45% and 16.35% respectively; *P*=0.0316, *) [Figure 23]. This difference can also be seen in the representative images, where a striking difference in fibrous cap lipid content can also be observed [Figure 20]. This suggests that plaques from $GS^{+/LacZ}ApoE^{-/-}$ animals have a proportionally larger region of concentrated fat deposition and this is predominantly enmeshed within the fibrous cap region of the plaque as opposed to being sequestered in a pool beneath the cap.

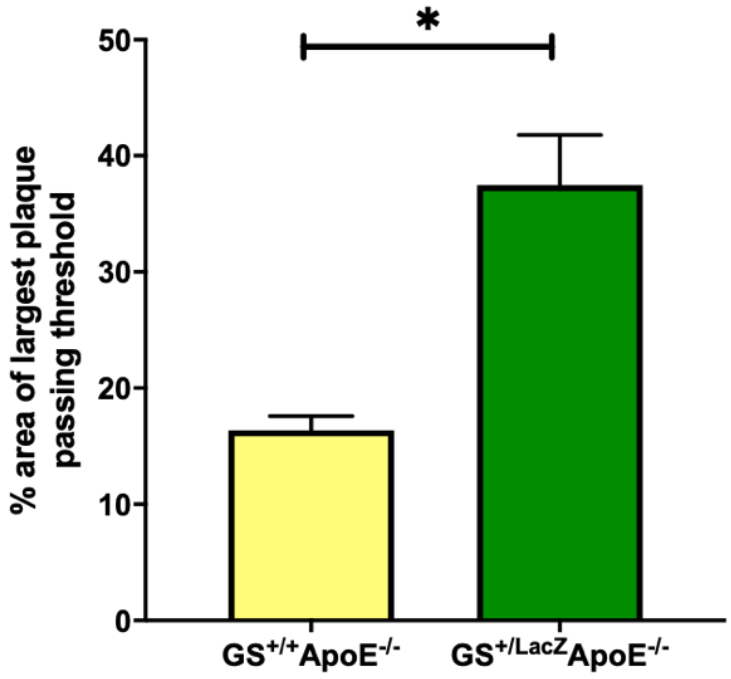

Figure 23: Quantification of fat deposition pattern within the largest plaque stained using Oil Red O ImageJ was used to threshold the Oil Red O staining within the largest plaque of each animal and the mean percentage of area within this plaque passing the colour threshold was then compared between genotypes (*n*=3 per genotype)

4.3.3 Aortic sinus – Fibrosis staining

Hearts were fixed using PFA-PBS before being embedded in paraffin blocks. 5-micron sections were then stained using either the Miller-van Gieson [3.3.2.3] or the Picrosirius red [3.3.2.4] protocols [Figure 24].

The Miller stain specifically stains elastic fibres blue to black whilst the van Gieson stain consists of multiple dyes which together stain collagen magenta to red, and muscle and cytoplasm yellow to orange [Figure 24A-B] and is utilised as a counterstain to the Miller stain[82–84].

By contrast, the Picrosirius red stain consists of the Sirius red dye which specifically stains Type I and Type III collagen fibres red whilst the picric acid acts as a fixative and counterstain, imparting an off-white to pale yellow colour to the cytoplasm [Figure 24C-D] [85,86].

Although each stain enables the visualisation of fibrosis more generally, using both Miller and Picrosirius red stains allows the specific protein content of the fibrous cap to be examined, as differences in cap composition may indicate differences in cap friability[52,55,56].

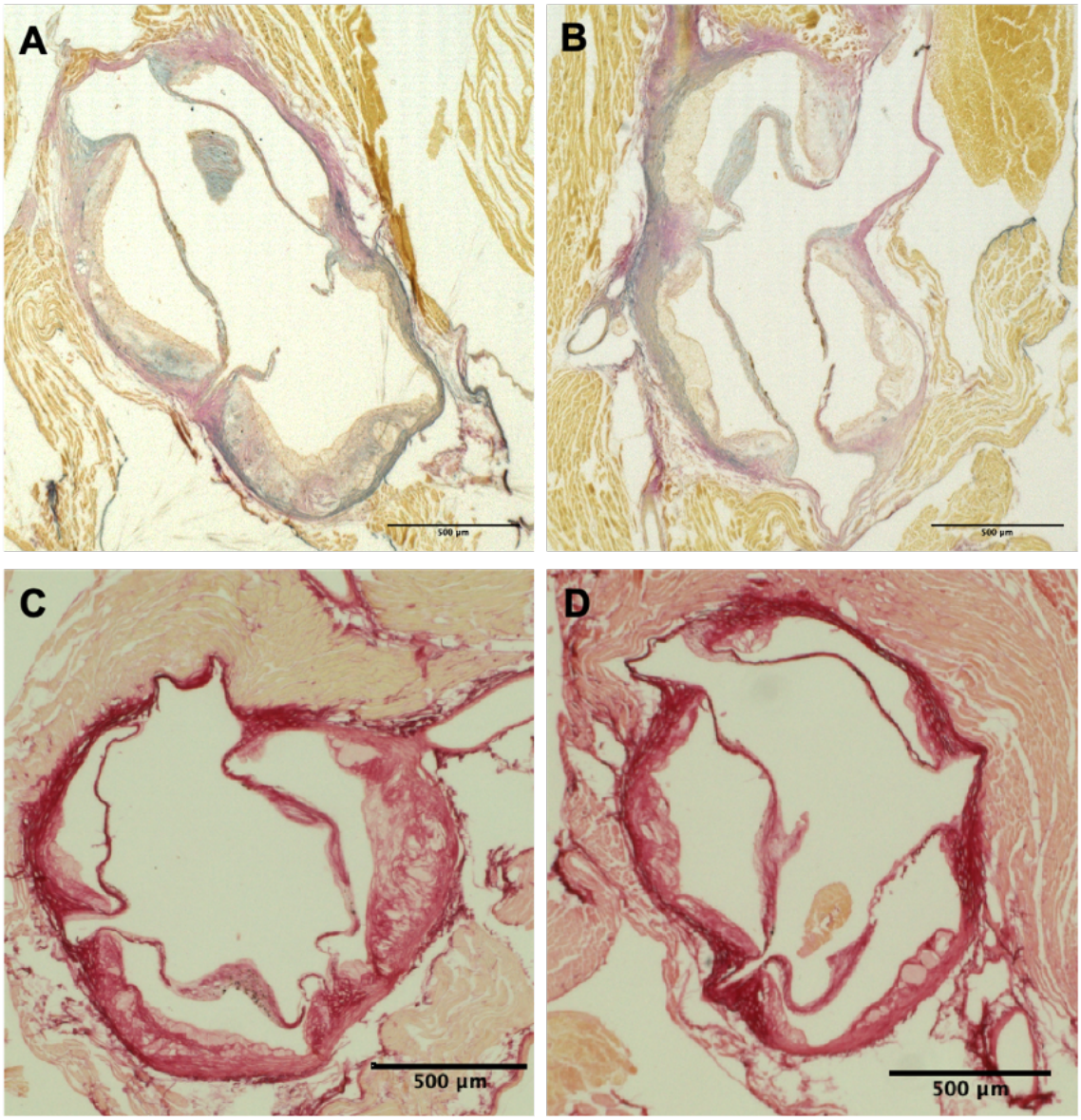

Figure 24: Representative stained aortic root sections depicting fibrous content
Hearts containing the aortic root were harvested from 20 week old mice after 12 weeks of western diet. Aortic sinus regions from both $GS^{+/+}ApoE^{-/-}$ [**A** and **C**] controls and $GS^{+/LacZ}ApoE^{-/-}$ mice [**B** and **D**] were stained with either Miller's Elastin stain and van Gieson counterstain [**A** and **B**] (*n*=7 per genotype) or Picrosirius Red [**C** and **D**] (*n*=7 per genotype) and then imaged (magnification: 4x; EVOS imaging system)

4.3.3.1 Plaque burden

As for the cryosections stained with Oil Red O [4.3.2.1], the plaque burden, the area of the sinus, the mean plaque size, and the mean size of the largest plaque along with the mean number of plaques was measured for each aortic sinus, and the mean value for each of these for each genotype calculated.

Miller van Gieson

Although not significantly different, plaque burden is reduced in the aortic sinus of $GS^{+/LacZ}ApoE^{-/-}$ mice compared to $GS^{+/+}ApoE^{-/-}$ controls (13.06% and 17.39% respectively; *P*=0.1285, n.s.) [Figure 25A], as seen in both whole aortas [Figure 19] and aortic sinus sections stained with Oil Red O [Figure 21]. This difference in plaque burden is despite there being no significant difference between genotypes in either the number of plaques present (*P*=0.1340, n.s.) [Figure 25C] or the aortic sinus area (*P*=0.4495, n.s.) [Figure 25B]. However, there is significantly lower mean plaque area (*P*=0.0261, *) [Figure 25D] and mean area of the largest plaque (*P*=0.0012, **) [Figure 25E] in $GS^{+/LacZ}ApoE^{-/-}$ mice.

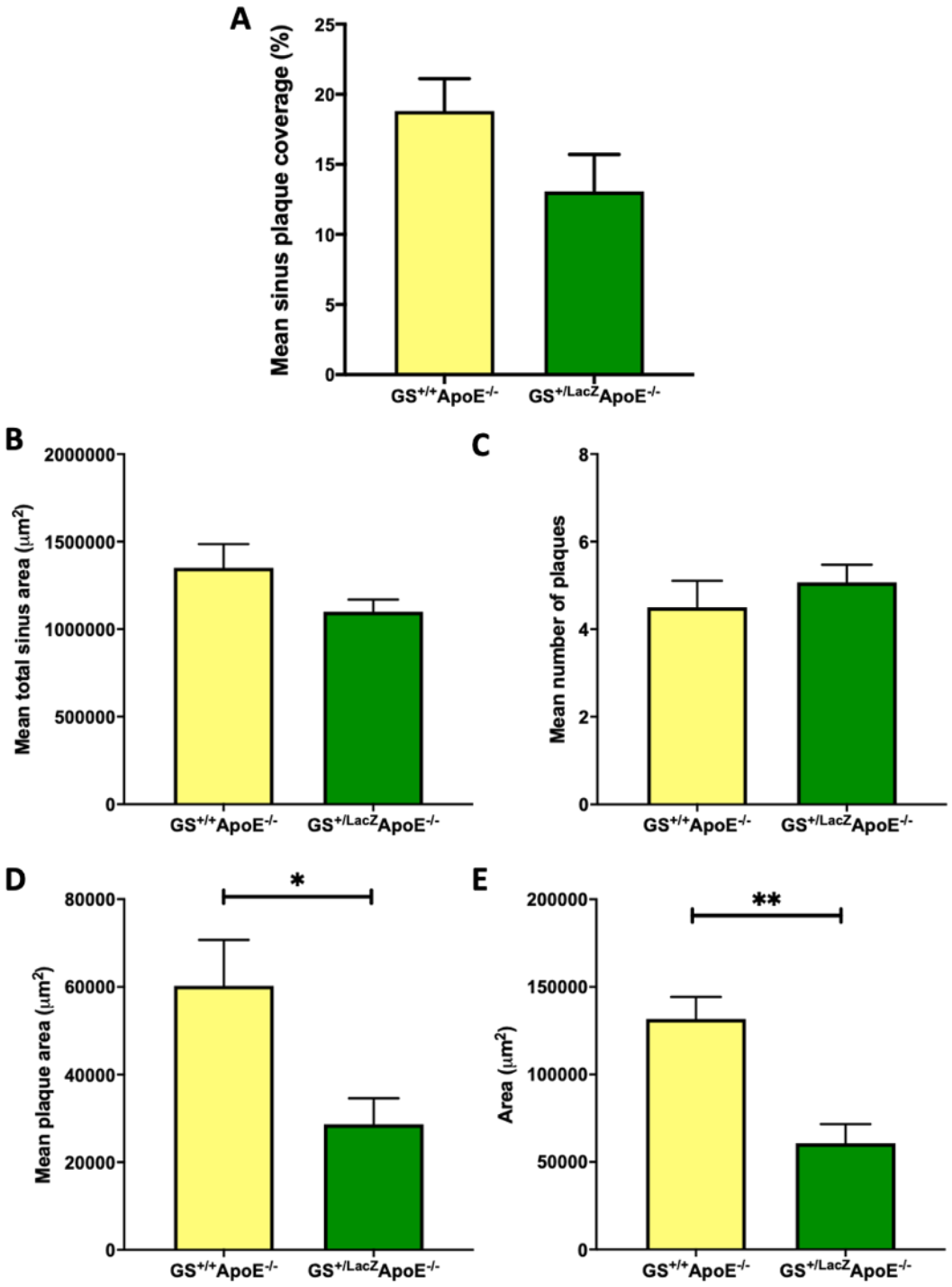

Figure 25: Atherosclerotic plaque burden in the Miller-van Gieson stained aortic sinus Plaque burden was quantified [**A**] along with the mean area of the sinus [**B**], the mean number of plaques [**C**], the mean plaque area [**D**], and the mean area of the largest plaque [**E]** (*n*=7 per genotype)

Picrosirius red

Although not significantly different, plaque burden is reduced in the aortic sinus of $GS^{+/LacZ}ApoE^{-/-}$ mice compared to $GS^{+/+}ApoE^{-/-}$ controls (20.01% and 14.24% respectively; *P*=0.1133, n.s.) [Figure 26A] as seen in sections stained with Miller-van Gieson [Figure 25A]. This difference in plaque burden is despite there being no significant difference between genotypes in either the whole aortic sinus area (*P*=0.1978, n.s.) [Figure 26B] or the number of plaques present (*P*=0.5131, n.s.) [Figure 26C]. However, $GS^{+/LacZ}ApoE^{-/-}$ mice had significantly lower mean plaque area (*P*=0.0252, *) [Figure 26D] and mean area of the largest plaque (*P*=0.0075, **) [Figure 26E].

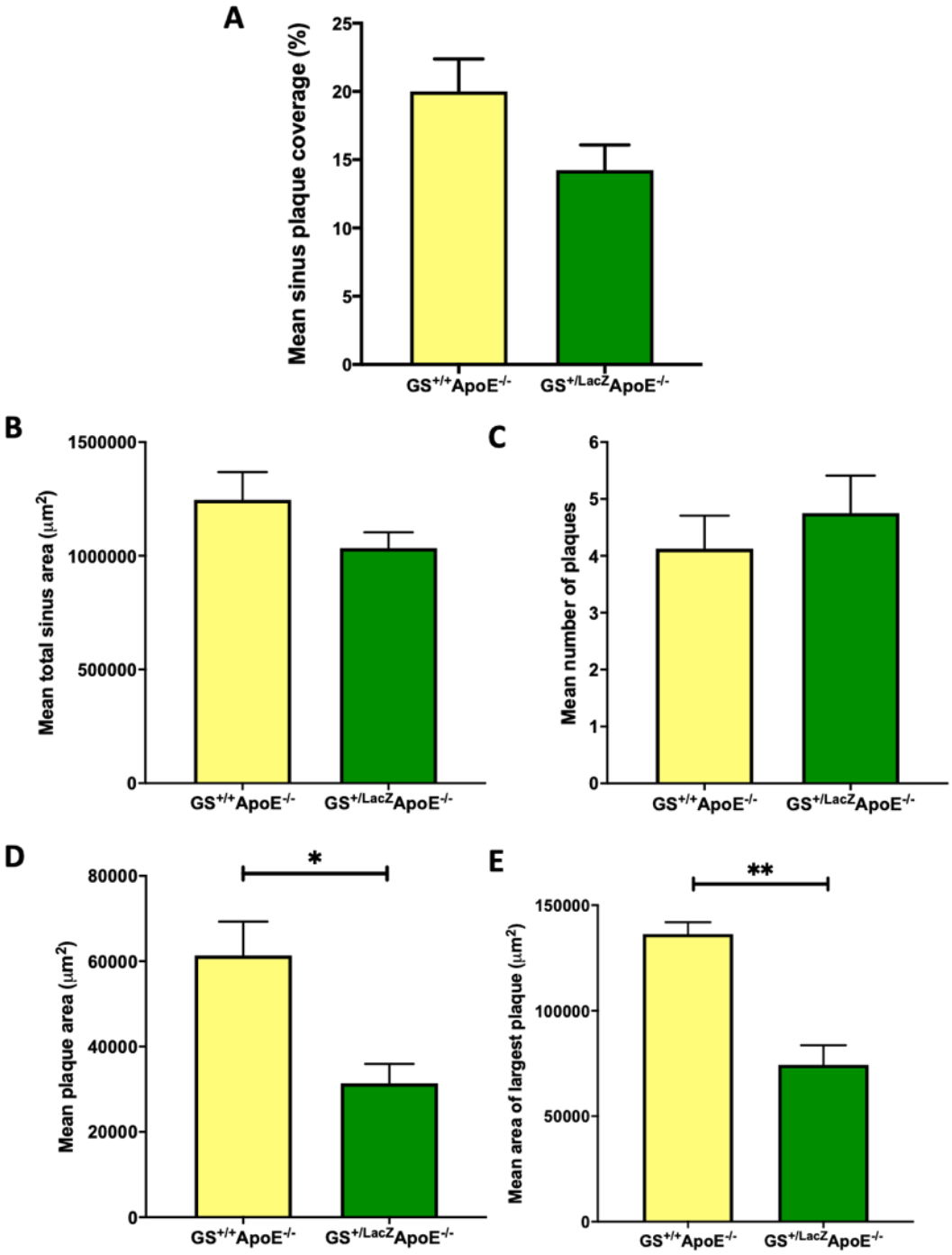

Figure 26: Atherosclerotic plaque burden in the Picrosirius red stained aortic sinus Plaque burden was quantified [**A**] along with the mean area of the sinus [**B**], the mean number of plaques [**C**], the mean plaque area [**D**], and the mean area of the largest plaque [**E]** (*n*=7 per genotype)

4.3.3.2 Plaque architecture

In addition to measuring plaque burden, the images of the stained aortic sinus sections were also used to assess plaque structure as a difference in colour composition could indicate a difference in elastin and/or collagen deposition[82–85].

For both stains, a colour histogram was generated for the largest plaque of each image (as identified in previous plaque burden analyses), producing a mean and mode intensity value for each of the three colours making up the composite image – red, green and blue. These values were averaged for each mouse and these means compared between genotypes. These mean and modal colour intensity values calculated in ImageJ were then input into an online RGB colour viewer in order to visualise any differences, or lack thereof, in overall colour between $GS^{+/LacZ}ApoE^{-/-}$ mice and $GS^{+/+}ApoE^{-/-}$ controls[81].

As slides were stained with either Miller-van Gieson or Picrosirius red, it is expected that the respective groups will have different colour profiles due to different dyes present and therefore these results are unable to be directly compared although the ratios of elastin to collagen can be indirectly inferred with respect to their potential effect on cap friability.

Miller-van Gieson results

Table 45: Colour intensities of Miller-van Gieson stained aortic sinus sections

Colour	Mean / Mode	$GS^{+/+}$ $ApoE^{-/-}$	$GS^{+/LacZ}$ $ApoE^{-/-}$	*P* value and significance	Figure reference
Red	Mean	208.51	219.76	0.1182, n.s.	Figure 27A
	Mode	212.57	229.18	0.0804, n.s.	Figure 27B
Green	Mean	201.02	211.29	0.1896, n.s.	Figure 27C
	Mode	202.46	223.64	0.0389, *	Figure 27D
Blue	Mean	203.60	193.79	0.1453, n.s.	Figure 27E
	Mode	226.79	204.86	0.1300, n.s.	Figure 27F

Whilst there were no significant differences in any of the measures except for the modal green value which is significantly higher in the plaques of $GS^{+/LacZ}ApoE^{-/-}$ mice when compared to those of $GS^{+/+}ApoE^{-/-}$ mice (*P*=0.0389, *) [Figure 27D], the data does suggest that the plaques of $GS^{+/LacZ}ApoE^{-/-}$ mice also have higher mean green intensities [Figure 27C], higher mean and modal red [Figure 27A&B] and lower mean and modal blue intensities [Figure 27E&F] than those of $GS^{+/+}ApoE^{-/-}$ controls, suggesting that these plaques may differ in their overall colour composition and distribution.

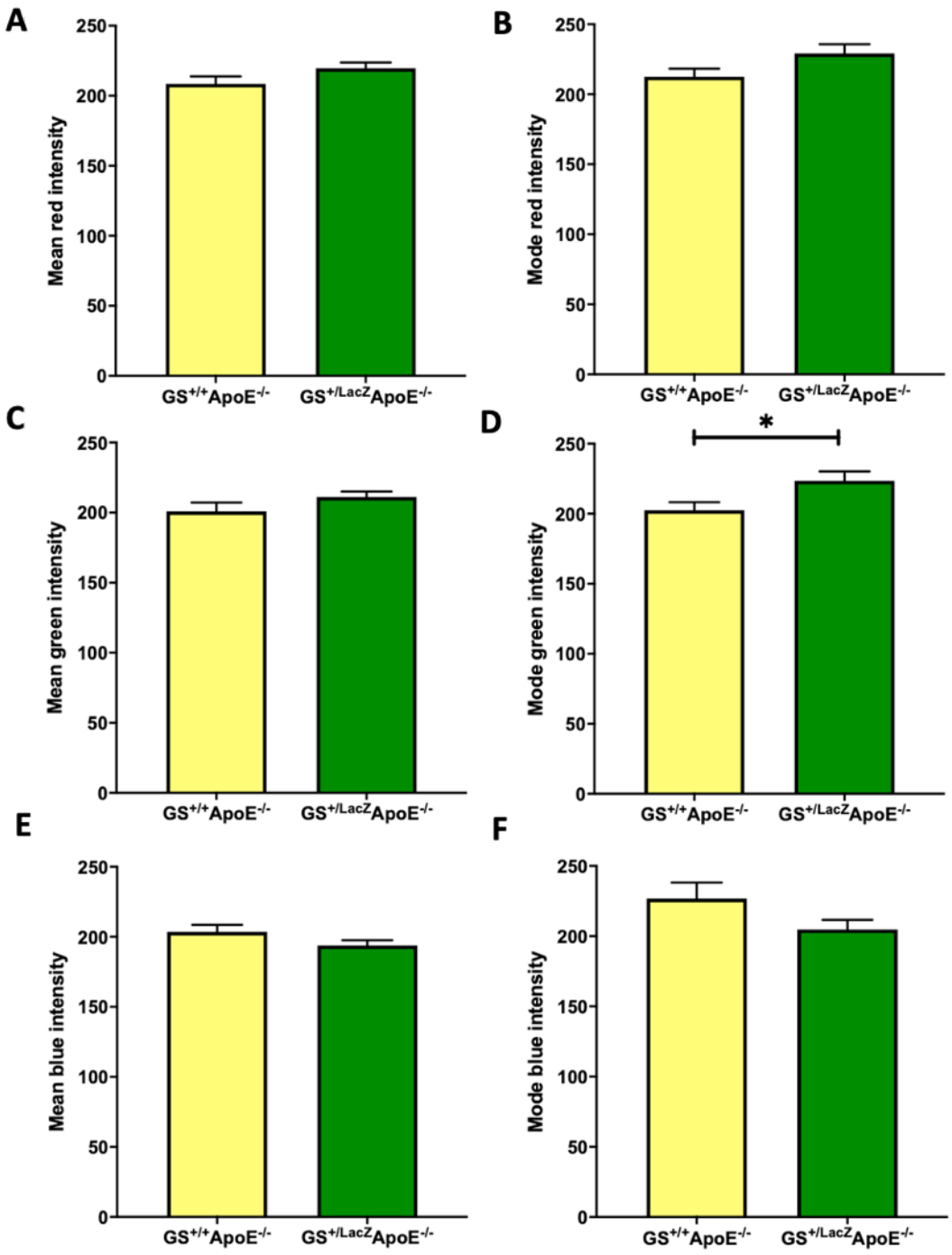

Figure 27: Colour distribution of the largest plaque stained using Miller-van Gieson ImageJ was used to quantify the mean and modal intensities for Red [**A & B**], Green [**C & D**] and Blue [**E & F**] for the largest plaque of each animal and the average values were then compared between genotypes (*n*=7 per genotype)

As qualitative visual assessment of these plaques also suggests there to be a difference in overall colour composition and distribution between the two genotypes, these mean and modal colour intensity values calculated in ImageJ were then visualised using an online RGB colour viewer.

This RGB visualisation indicated that there is a clear visual difference in mean and modal plaque colours between the two genotypes. The plaques of $GS^{+/LacZ}ApoE^{-/-}$ mice have a purple tone, whilst $GS^{+/+}ApoE^{-/-}$ control mice have plaques toned a yellow-beige [Figure 28] and this is also reflected in qualitative analysis of the respective images [Figure 24]. As Miller van Gieson stains fibrous material purple and cytoplasmic and lipid material yellow, this may indicate a difference in plaque composition in so far as the plaques of $GS^{+/LacZ}ApoE^{-/-}$ mice having reduced elastin compared to those of the $GS^{+/+}ApoE^{-/-}$ controls.

Figure 28: Representative schematic of mean and mode colours of Miller van Gieson stained aortic sinus plaques Colours generated by inputting intensity values into the RGB Calculator visualisation tool by W3Schools[81]

Picrosirius red results

Table 46: Colour intensities of Picrosirius red stained aortic sinus sections

Colour	Mean / Mode	$GS^{+/+}$ $ApoE^{-/-}$	$GS^{+/LacZ}$ $ApoE^{-/-}$	*P* value and significance	Figure reference
Red	Mean	211.09	214.19	0.7873, n.s.	Figure 29A
	Mode	251.44	255.00	0.3910, n.s.	Figure 29B
Green	Mean	132.95	109.81	0.2082, n.s.	Figure 29C
	Mode	150.81	89.25	0.2012, n.s.	Figure 29D
Blue	Mean	135.71	109.95	0.1702, n.s.	Figure 29E
	Mode	141.69	104.50	0.2175, n.s.	Figure 29F

There were no significant differences between genotypes in any of the measures [Figure 29] including near identical mean and modal red intensities [Figure 29A&B], which is not unexpected given that this method of collagen staining utilises a red dye. However, the plaques of $GS^{+/LacZ}ApoE^{-/-}$ animals have nominally lower green [Figure 29C&D] and blue [Figure 29E&F] intensities than those of $GS^{+/+}ApoE^{-/-}$ controls, suggesting that these plaques may differ in their overall colour composition and distribution.

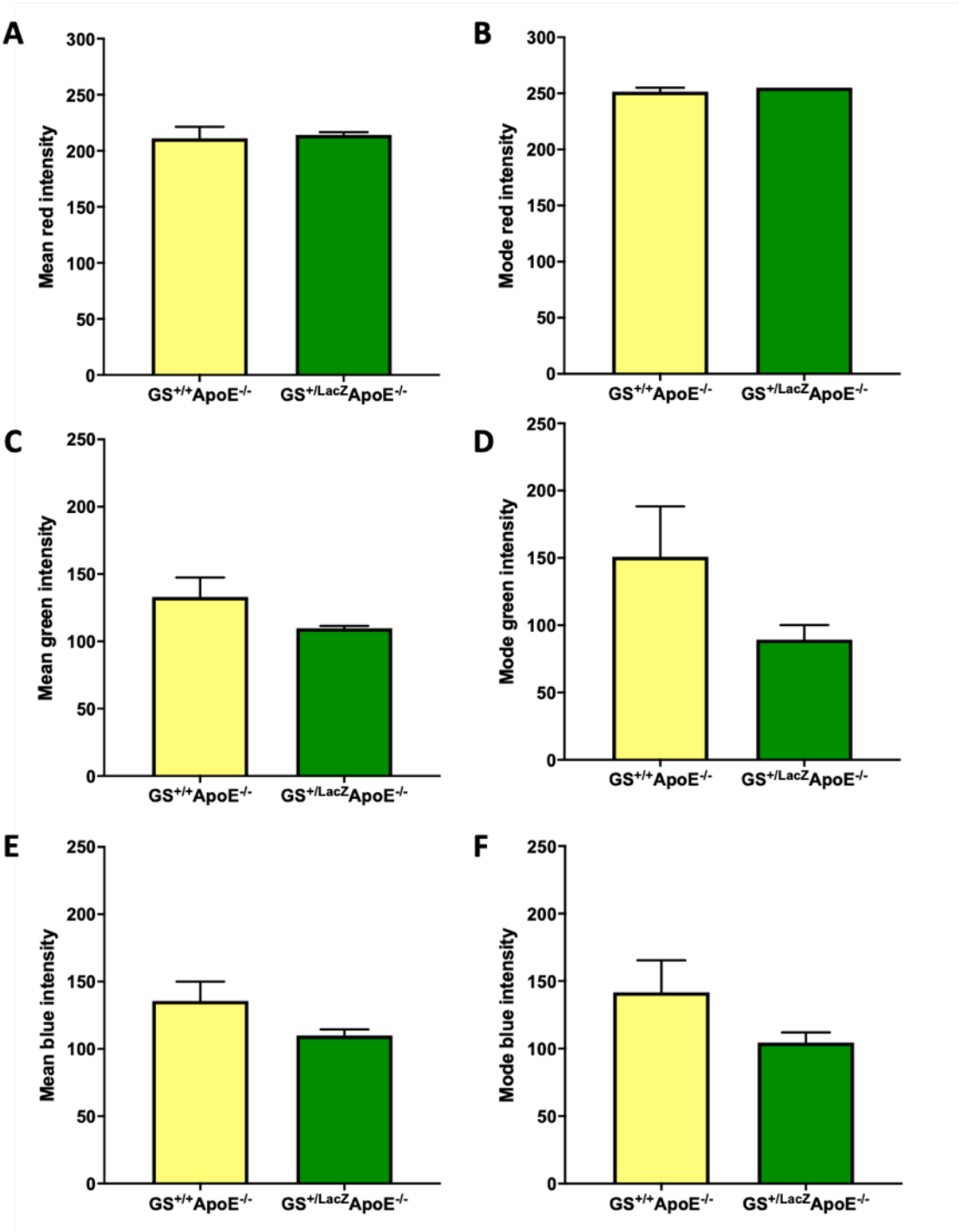

Figure 29: Colour distribution of the largest plaque stained using Picrosirius red
ImageJ was used to quantify the mean and modal intensities for Red [**A & B**], Green [**C & D**] and Blue [**E & F**] for the largest plaque of each mouse and the average values were then compared between genotypes ($GS^{+/+}ApoE^{-/-}$: *n*=4, $GS^{+/LacZ}ApoE^{-/-}$: *n*=3)

Again, the mean and modal colour intensity values calculated in ImageJ were input into an online RGB colour viewer in order to visualise any difference in overall colour between $GS^{+/LacZ}ApoE^{-/-}$ mice and $GS^{+/+}ApoE^{-/-}$ controls. From this, we can see that the plaques of $GS^{+/LacZ}ApoE^{-/-}$ mice are both darker and more intensely red than those of $GS^{+/+}ApoE^{-/-}$ control mice [Figure 30].

As Picrosirius red stains collagen fibres red and cytoplasmic and lipid material cream to yellow, again this may indicate a difference in plaque composition and architecture through differing quantities of collagen present.

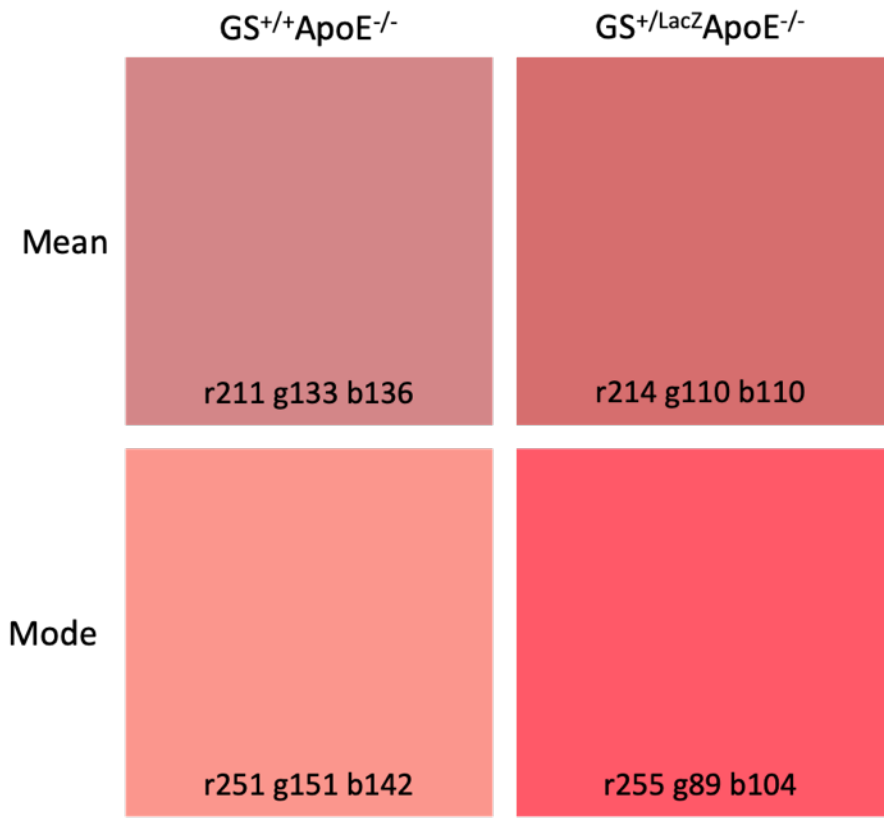

Figure 30: Representative schematic of mean and mode colours of Picrosirius red stained aortic sinus plaques Colours generated by inputting intensity values into the RGB Calculator visualisation tool by W3Schools[81]

Collagen distribution analysis by colour thresholding

As for the slides stained with Oil Red O [4.3.2.2], colour thresholding was utilised to identify whether there was a spatial difference in collagen deposition through using the Hue Saturation Brightness (HSB) colour space and selecting for only high intensity red and magenta staining, and in doing so excluding normal collagen deposition within the extracellular matrix.

Again, this was done because the RGB colour intensity values provide a mean value for the whole plaque and is therefore unsuitable for differentiating between plaques with an even staining pattern and those with distinct regions of high and low intensity staining. However, this also additionally enables exploration of whether or not there is a higher deposition of collagen in the plaques of $GS^{+/LacZ}ApoE^{-/-}$ mice as suggested by previous analyses [Figure 29 & Figure 30].

There is a significant difference between genotypes in the percentage (%) area of plaque passing the threshold, with $GS^{+/+}ApoE^{-/-}$ controls having less than half the amount of collagen staining when compared with $GS^{+/LacZ}ApoE^{-/-}$ mice (11.42% and 23.66% respectively; P=0.0138, *), concurrent with the findings from the previous evaluations.

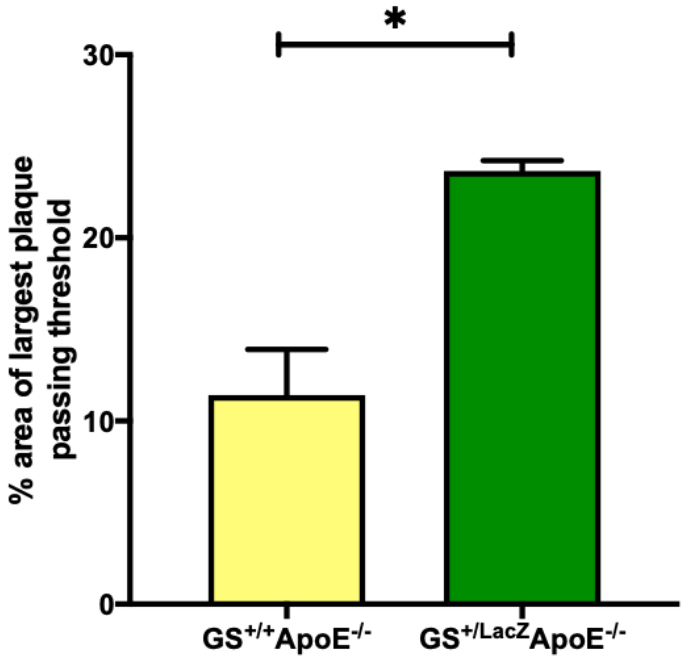

Figure 31: Quantification of collagen deposition pattern within the largest plaque stained using Picrosirius red ImageJ was used to threshold the Picrosirius red staining within the largest plaque of each animal and the mean percentages (%) of area within this plaque passing the colour threshold was then compared between genotypes (n=3)

4.3.4 Summary of histological findings

The use of specific lipid and fibrosis stains has enabled identification of specific features of atherosclerosis associated with plaque stability and instability including plaque burden and plaque size through measuring the area and numbers of plaques present, the plaque architecture and fibrous cap protein content through the use of specific elastin and collagen staining protocols, and the deposition and distribution of lipids.

Together these results suggest that reducing the expression of GS does alter atherogenesis, with $GS^{+/LacZ}ApoE^{-/-}$ mice having a significantly reduced plaque burden which may be at least partially explained by the presence of smaller plaques when compared to $GS^{+/+}ApoE^{-/-}$ controls. These smaller plaques also exhibit an altered phenotype with reduced elastin and increased collagen and a different distribution of lipids [Table 47].

Table 47: Summary of histological findings

	$GS^{+/+}ApoE^{-/-}$ controls	**$GS^{+/LacZ}ApoE^{-/-}$**
Whole aorta plaque burden	3.98% coverage	Reduced: 1.92% coverage
Aortic sinus plaque burden	Increased compared to $GS^{+/LacZ}ApoE^{-/-}$ mice	Decreased compared to controls
Mean plaque area	Increased compared to $GS^{+/LacZ}ApoE^{-/-}$ mice	Decreased compared to controls
Mean area of largest plaque	Increased compared to $GS^{+/LacZ}ApoE^{-/-}$ mice	Decreased compared to controls
Number of plaques	No difference	
Lipid deposition	No difference in overall plaque colour	
Lipid distribution	Evenly distributed throughout plaque; 16.35% of plaque area intensely stained	Concentrated into fibrous cap region; 37.45% of plaque area intensely stained – greater than double that of controls
Elastin deposition	Plaque toned purple due to high deposition of elastin	Plaque toned yellow indicating reduced ratio of elastin to cytoplasm
Collagen deposition	Collagen evenly deposited throughout plaque with reduced area of strong staining	Increased deposition of collagen; concentrated to fibrous cap region

4.3.4 Immunohistochemical analysis of GS expression

As $GS^{+/LacZ}ApoE^{-/-}$ mice contain a single copy of the reporter gene *LacZ*, encoding β-galactosidase, under the control of the GS promotor region of the knocked-out allele, this can be exploited to indicate the pattern and extent of GS expression within tissues from $GS^{+/LacZ}ApoE^{-/-}$ mice[80].

4.3.4.1 Validation of *LacZ* as a reporter of GS

Zonal expression of GS within the lobules of the liver is well documented, showing that GS is expressed within the hepatocytes closest to the hepatic portal veins. This defined zonal expression enables the liver to be used as a control tissue to both check whether the *LacZ* insert is present and active in the $GS^{+/LacZ}ApoE^{-/-}$ mice and additionally to validate the anti-ß-galactosidase antibody as an accurate reporter of GS expression as hepatic GS expression patterns can be compared to those previously published[62,63].

The largest lobe of the liver was harvested from both male $GS^{+/LacZ}ApoE^{-/-}$ mice and $GS^{+/+}ApoE^{-/-}$ controls and fixed using PFA-PBS before being cryoembedded. $GS^{+/LacZ}ApoE^{-/-}$ [Figure 32A-C] and $GS^{+/+}ApoE^{-/-}$ sections [Figure 32D-F] were stained for *LacZ* and a DAPI nuclear counterstain. To check for non-specific staining of the secondary antibody, control sections from $GS^{+/LacZ}ApoE^{-/-}$ mice were stained with only the secondary antibody and DAPI [Figure 32G-I].

$GS^{+/LacZ}ApoE^{-/-}$ sections [Figure 32B-C] clearly show the expected perivenous expression of GS. By contrast, $GS^{+/+}ApoE^{-/-}$ sections [Figure 32E-F] do not show this expression pattern due to the lack of *LacZ* insert as a reporter gene. The control sections [Figure 32H-I] stained only with the secondary antibody also show that the expression pattern seen within the $GS^{+/LacZ}ApoE^{-/-}$ sections is not as a result of non-specific staining. Together, these results indicated that the *LacZ* insert is present and active in the $GS^{+/LacZ}ApoE^{-/-}$ mice and is suitable for use as a reporter of GS in other tissues.

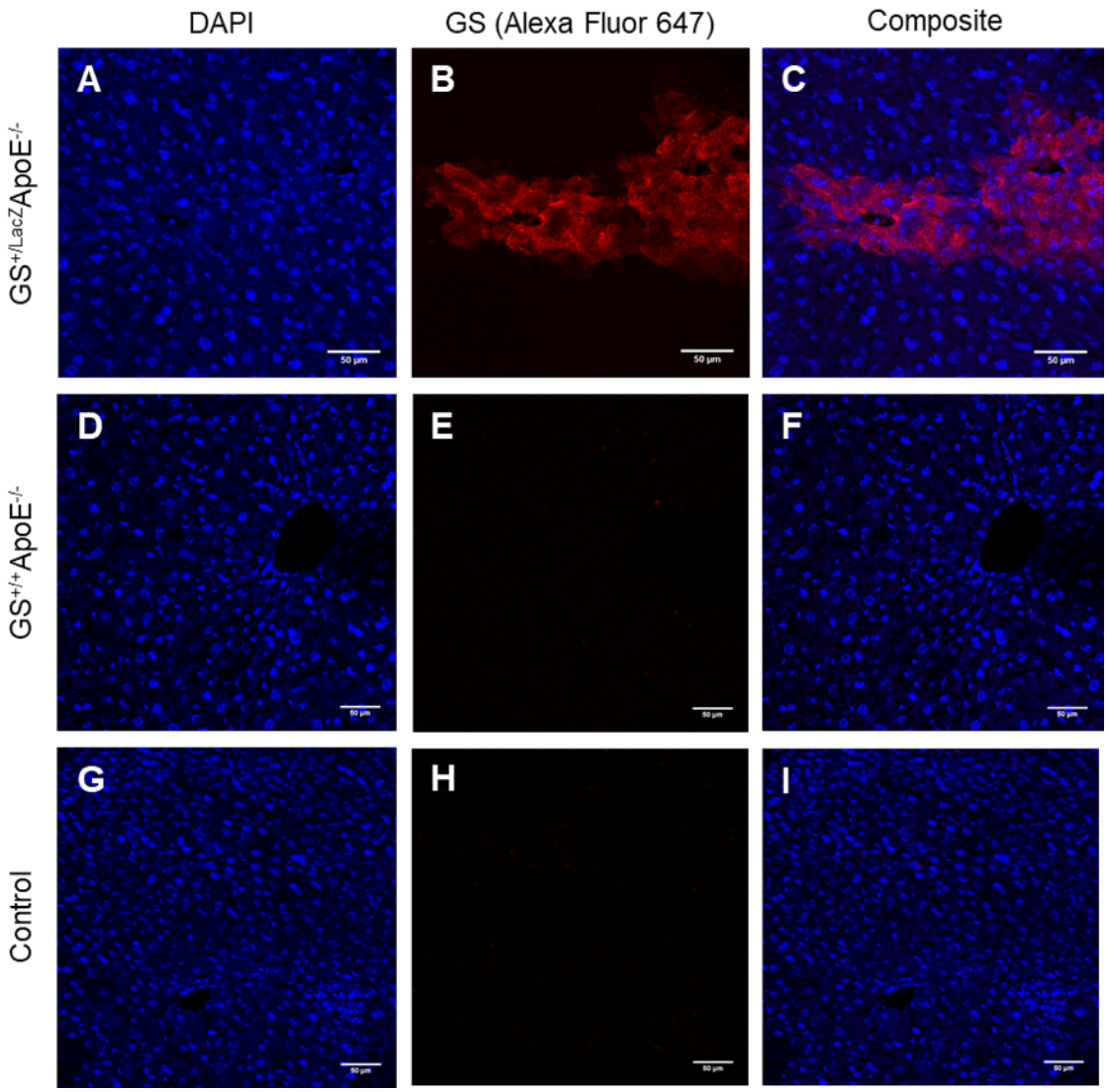

Figure 32: Immunofluorescent co-staining of liver sections Immunofluorescence analyses of cryosectioned liver tissue from $GS^{+/LacZ}ApoE^{-/-}$ mice [**A-C**] and $GS^{+/+}ApoE^{-/-}$ controls [**D-F**] were performed for *LacZ* [**red**] and DAPI [**blue**] (magnification: 20x). Control sections from $GS^{+/LacZ}ApoE^{-/-}$ mice [**G-I**] were stained for comparison with only the secondary antibody [**red**] and DAPI [**blue**] (magnification: 20x)

4.3.4.2 Aortic sinus studies

Based on the confirmation in liver sections that *LacZ* expression could be exploited as a reporter of GS expression [Figure 32], the same staining protocol was then applied to aortic root sections [Figure 33] to investigate whether GS is expressed within atherosclerotic plaques and, if so, where it is most strongly expressed.

Initial exploration of GS expression through the *LacZ* reporter

$GS^{+/LacZ}ApoE^{-/-}$ aortic root sections were stained as described for liver sections. Fully stained $GS^{+/LacZ}ApoE^{-/-}$ sections [Figure 33A-B] suggest that GS is expressed within the atherosclerotic plaque above the aortic valve leaflet, particularly within the lipid core and the shoulder of the plaque. Furthermore, the control sections from the same animal [Figure 33C-D] stained only with the secondary (AF647) antibody confirm that the GS expression seen is not as a result of non-specific staining.

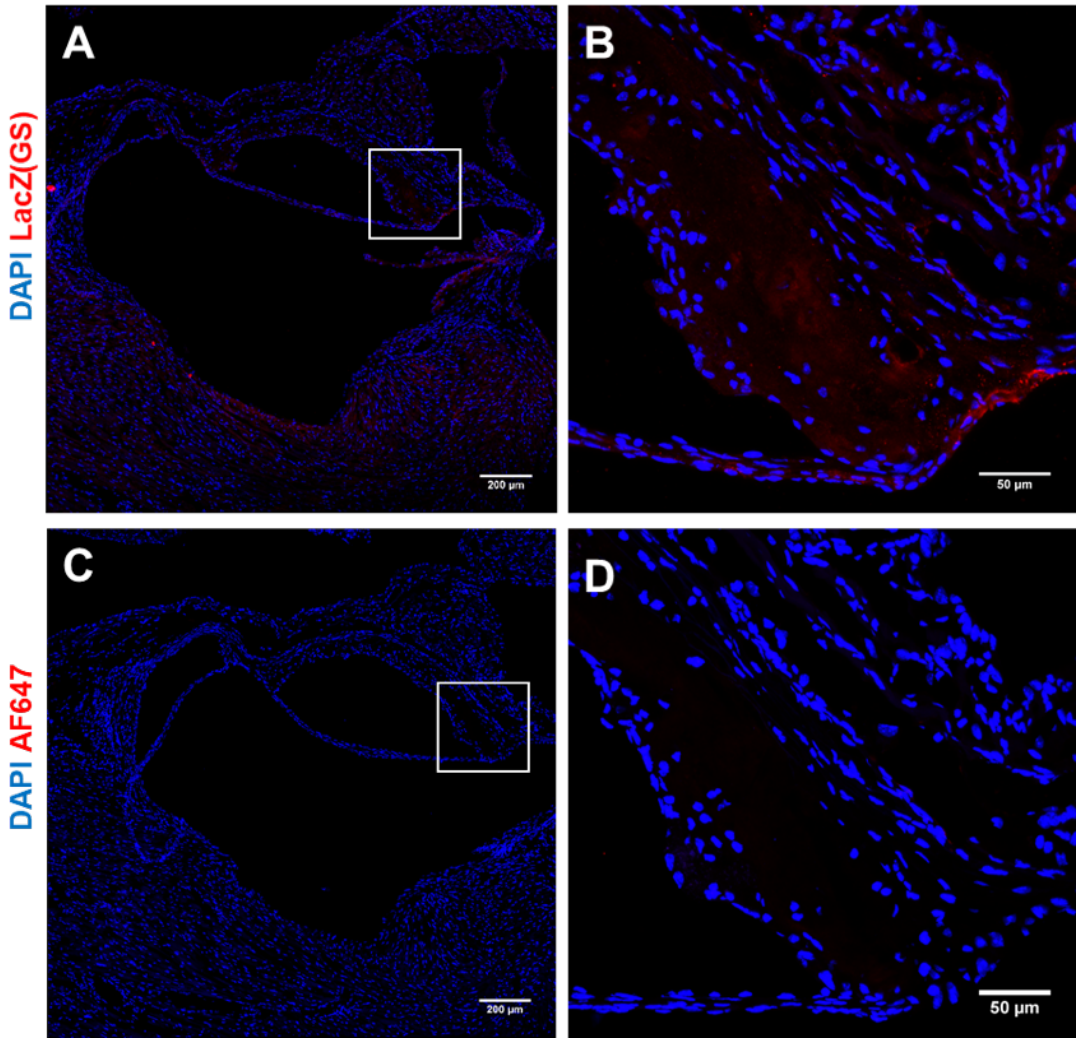

Figure 33: Immunofluorescent anti-*LacZ* staining of aortic root sections
Immunofluorescence analyses of cryosectioned aortic sinus tissue from $GS^{+/LacZ}ApoE^{-/-}$ mice fed a Western Diet for 12 weeks to induce atherosclerosis. Fully stained sections (**top, A & B**) were stained for both *LacZ* (**red**) (as a marker of GS expression) and DAPI (**blue**). Control sections from the same animal (**bottom, C & D**) were stained for comparison with only the AF647 secondary antibody (**red**) and DAPI (**blue**). Images were taken of approximately the same area of the same aortic sinus leaflet and plaque at 10x (l**eft, A & C**) and 40x (**right, B & D**), as marked by the white squares

LacZ reporter expression within different cell types

As the $GS^{+/LacZ}ApoE^{-/-}$ aortic sinus sections stained with an anti-*LacZ* antibody [Figure 33A-B] suggest that GS is expressed most strongly within the core and the shoulder of the atherosclerotic plaque, further co-stains were undertaken to identify the dominant cell types in these areas.

As before, sections from $GS^{+/LacZ}ApoE^{-/-}$ mice were stained with the anti-ß-galactosidase (*LacZ*) primary antibody as a marker of GS expression. Half of these sections were simultaneously co-stained with an anti-α-smooth muscle actin (α-SMA) primary antibody as a marker of vascular smooth muscle cells (VSMCs) [A]. The remaining sections were co-stained with Isolectin B4 (IB4) in order to identify endothelial cells and macrophages [B]. For all slides, nuclei were again counterstained using DAPI.

Sections stained for *LacZ* and α-SMA [A] confirm that GS is particularly strongly expressed within the VSMCs underlying the shoulder of the plaque. Additionally, sections stained for *LacZ* along with IB4 [B] confirm that GS is expressed in macrophages within the core of the plaque. These observations are concurrent with those previously published[57].

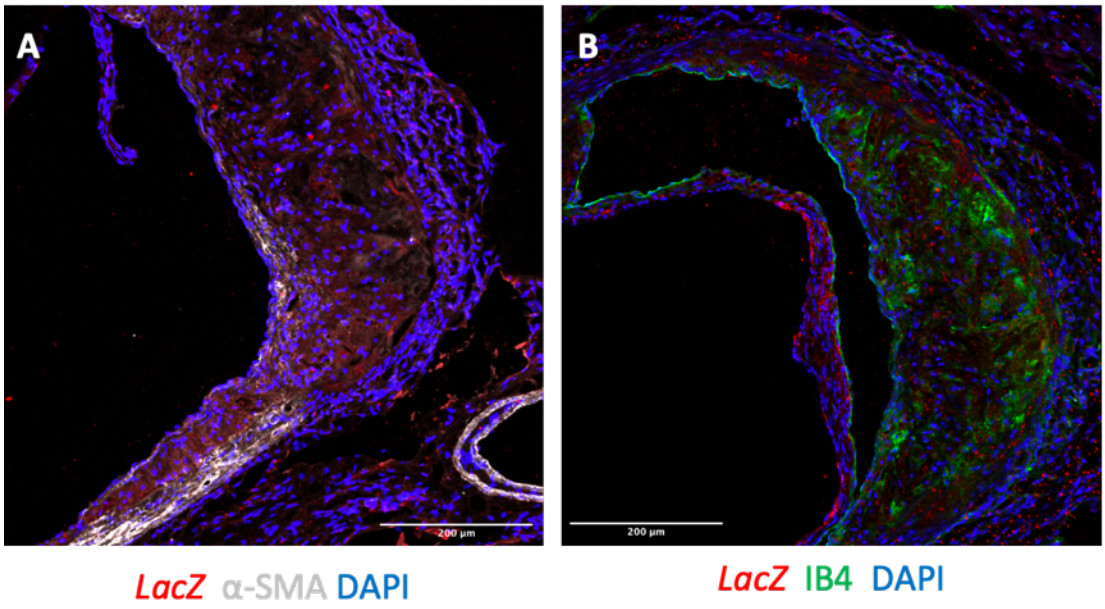

Figure 34: Immunofluorescent co-staining of GS$^{+/LacZ}$ApoE$^{-/-}$ aortic root sections to examine cellular expression of the *LacZ* reporter Immunofluorescence analyses of cryosectioned aortic sinus tissue from GS$^{+/LacZ}$ApoE$^{-/-}$ mice fed a Western Diet for 12 weeks to induce atherosclerosis. All sections were stained for both *LacZ*, as a marker of GS expression [**red**], and DAPI [**blue**]. Sections were also stained for either α-SMA as a marker of VSMCs [**white, A**] or with Isolectin B4 [**green, B**] as a marker of endothelial cells and macrophages (magnification: 20x)

LacZ (GS) expression and markers of plaque stability

As the $GS^{+/LacZ}ApoE^{-/-}$ aortic sinus sections co-stained with an anti-*LacZ* antibody and markers of cell types suggest there may be a difference in plaque structure through different cell composition, further co-stains were undertaken to compare plaque architecture between both $GS^{+/LacZ}ApoE^{-/-}$ mice and $GS^{+/+}ApoE^{-/-}$ controls.

As before, 10-micron thick sections from both $GS^{+/+}ApoE^{-/-}$ and $GS^{+/LacZ}ApoE^{-/-}$ mice were stained with the anti-ß-galactosidase (*LacZ*) primary antibody as a marker of GS expression. These sections were co-stained with the anti-α-smooth muscle actin as a marker of vascular smooth muscle cells (VSMCs) that contribute to fibrous cap stability. Once stained with these antibodies, sections were then stained with LipidTOX™, a lipid soluble stain that visualises lipid distribution, and a DAPI nuclear [Figure 35].

From these slides, the first observation is that, as expected from my earlier data, $GS^{+/+}ApoE^{-/-}$ sections [Figure 35B&C] do not show any GS expression due to the lack of *LacZ* insert as a reporter gene, whilst those taken from $GS^{+/LacZ}ApoE^{-/-}$ mice show *LacZ* reporter within the aortic sinus and throughout the plaque [Figure 35A&D].

In addition to the expected *LacZ* observations, there is also a clear difference in plaque architecture. Firstly, there is a clear difference in plaque size, with $GS^{+/LacZ}ApoE^{-/-}$ sections having smaller plaques [Figure 35B] than those taken from $GS^{+/+}ApoE^{-/-}$ littermate controls [Figure 35A]. There is also a clear difference in cap surface geometry, with $GS^{+/+}ApoE^{-/-}$ plaques exhibiting a smooth, thick, clearly delineated cap [Figure 35C], and $GS^{+/LacZ}ApoE^{-/-}$ plaques exhibiting irregular borders of varying thickness with blebbing [Figure 35D].

Although these composite images allow for assessment of broad gene expression and gross morphology of the plaque, further insights into gene expression and plaque structure can also be gleaned upon examination of the individual fluorescent channels [Figure 36].

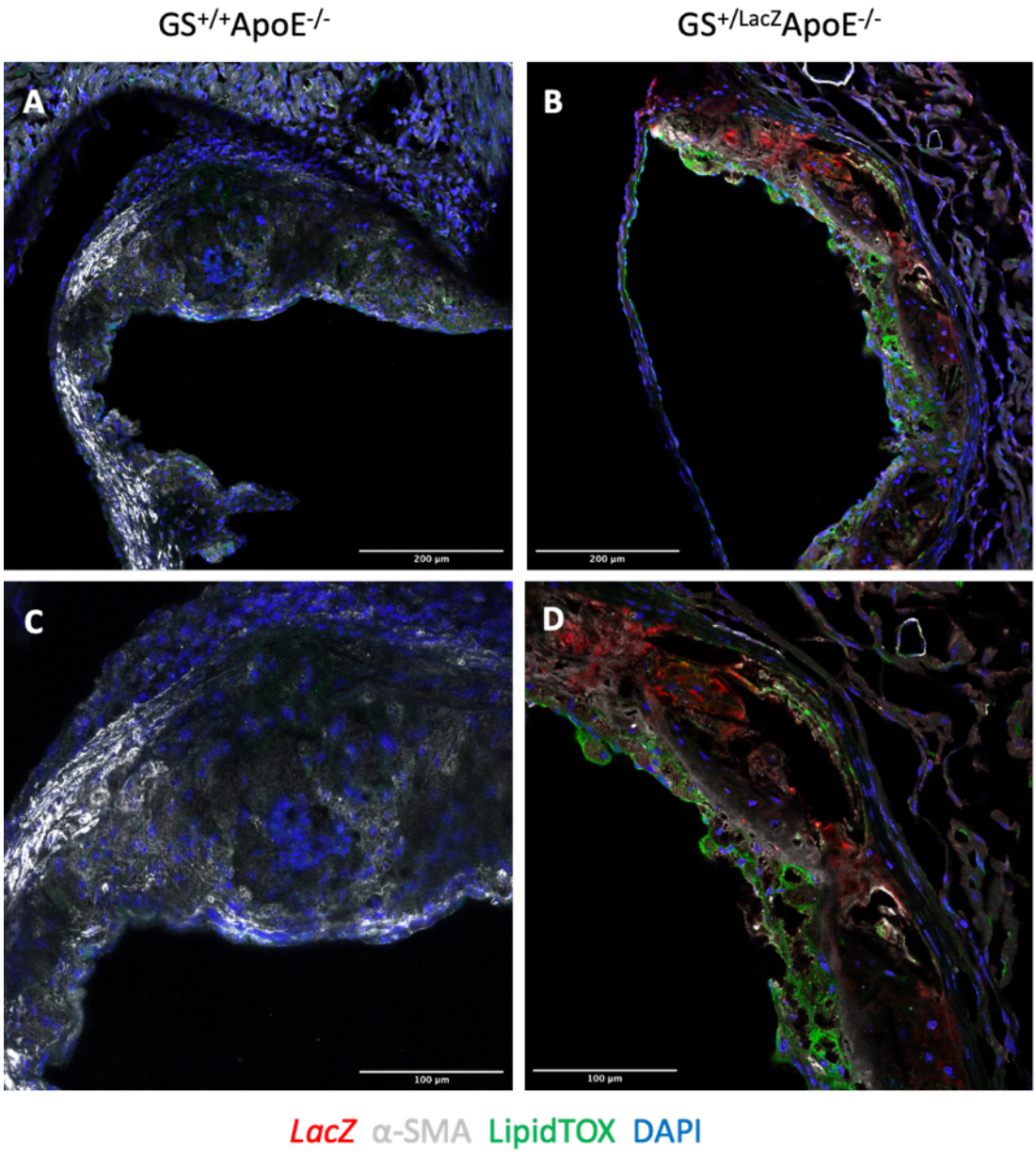

Figure 35: Immunofluorescent co-staining of GS$^{+/LacZ}$ApoE$^{-/-}$ and GS$^{+/+}$ApoE$^{-/-}$ aortic root sections to compare markers of plaque architecture

Immunofluorescence analyses of cryosectioned aortic sinus tissue from both GS$^{+/+}$ApoE$^{-/-}$ [**A & C**] and GS$^{+/LacZ}$ApoE$^{-/-}$ [**B & D**] mice fed a Western Diet for 12 weeks to induce atherosclerosis. All sections were stained for *LacZ*, as a marker of GS expression (**red**), α-SMA (**white**) as a marker of VSMCs, LipidTOX™ (**green**) as a marker of lipid deposition, and DAPI (**blue**). Images were taken of the same area of the leaflet and plaque at 20x (**top, A & B**) and 40x (**bottom, C & D**]

Within the DAPI (blue) channel [Figure 36A&B], gaps in staining are indicative of acellular regions and therefore these unstained areas may indicative of regions of either cell necrosis and/or lipid pooling. When compared to sections taken from $GS^{+/+}ApoE^{-/-}$ controls [Figure 36A], sections taken from $GS^{+/LacZ}ApoE^{-/-}$ mice [Figure 36B] appear to have a larger proportion of plaque depleted of cell nuclei relative to plaque size.

As shown before, $GS^{+/+}ApoE^{-/-}$ sections do not express *LacZ* (red) [Figure 36C]. By contrast, sections taken from $GS^{+/LacZ}ApoE^{-/-}$ mice [Figure 36D] again confirm that GS is expressed throughout the plaque and particularly strongly so within the shoulder of the plaque, concurrent with both previous observations and previously published findings[57].

When examining the α-SMA (white) staining, strong staining possibly indicates regions rich in VSMCs. Overall, the level of staining is decreased in $GS^{+/LacZ}ApoE^{-/-}$ plaques [Figure 36F] when compared to $GS^{+/+}ApoE^{-/-}$ control plaques [Figure 36E]. There is also a different distribution of α-SMA between the genotypes, with $GS^{+/+}ApoE^{-/-}$ sections exhibiting strongest staining in the walls of the aortic root and in the smooth, thick cap, and moderate staining throughout the plaque. By contrast, $GS^{+/LacZ}ApoE^{-/-}$ sections only display strong staining in the shoulder region of the plaque and moderate staining within the plaque clearly delineates smaller, fractured, unstructured caps.

A further difference in plaque architecture is ascertained upon examination of the LipidTOX™ (green) channel as there is a clear difference in both density and distribution of lipids between the genotypes. Firstly, $GS^{+/+}ApoE^{-/-}$ plaques [Figure 36G] have substantially lower staining than $GS^{+/LacZ}ApoE^{-/-}$ plaques [Figure 36H]. Secondly, whilst this staining is diffusely distributed throughout the plaque in $GS^{+/+}ApoE^{-/-}$ sections, within $GS^{+/LacZ}ApoE^{-/-}$ plaques the majority of this staining appears to be integrated into the fragmented cap region of the plaque.

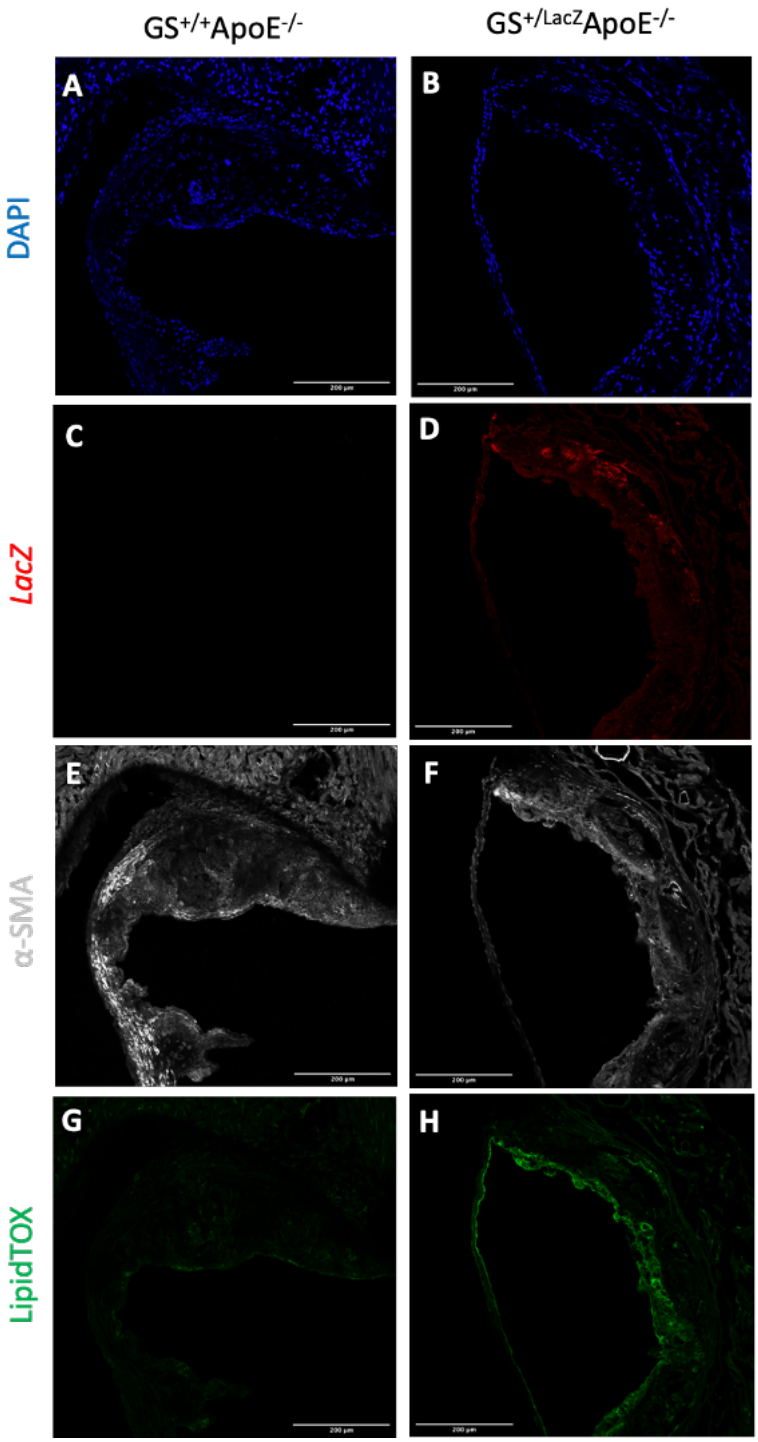

Figure 36: Immunofluorescent staining of aortic root sections to investigate markers of plaque stability Representative immunofluorescence analyses of cryosectioned aortic sinus tissue from both GS$^{+/+}$ApoE$^{-/-}$ [**left**] and GS$^{+/LacZ}$ApoE$^{-/-}$ [**right**] mice fed a Western Diet for 12 weeks to induce atherosclerosis. All sections were stained with DAPI (**blue, A & B**) as a general cell marker, *LacZ* as a marker of GS expression (**red, C & D**), α-SMA (**white, E & F**) as a marker of VSMCs, and LipidTOX™ (**green, G & H**) as a marker of lipid deposition. Slides were imaged using confocal microscopy before ImageJ software was used to separately visualise the different channels within these images for comparison

GS expression and markers of plaque stability

Previously undertaken work has exploited the presence of the *LacZ* reporter gene under the control of the GS promotor region of the knocked-out allele within the $GS^{+/LacZ}ApoE^{-/-}$ mice, enabling both confirmation of haploinsufficiency through use of an anti-*LacZ* antibody and simultaneous assessment of regional GS expression. As such, further co-stains were undertaken to not only compare plaque architecture between both $GS^{+/LacZ}ApoE^{-/-}$ mice and $GS^{+/+}ApoE^{-/-}$ control animals, but to also identify and compare GS expression directly with immunolabelling, rather than using the proxy of LacZ staining.

In a similar method to that utilised previously, 10-micron thick sections from both $GS^{+/+}ApoE^{-/-}$ and $GS^{+/LacZ}ApoE^{-/-}$ animals were stained with the anti-GS primary antibody to directly define GS expression. These sections were co-stained with the anti-α-smooth muscle actin (α-SMA) primary antibody as a marker of vascular smooth muscle cells (VSMCs). Once stained with these antibodies, sections were then stained with LipidTOX to visualise lipid distribution within the plaque. For all slides, nuclei were again counterstained using DAPI [Figure 37].

As seen in the previous staining examining these structural markers in conjunction with *LacZ* reporter expression, again there is a clear difference in plaque size and cap architecture, with $GS^{+/LacZ}ApoE^{-/-}$ sections having smaller, irregular capped plaques [Figure 37B & D], than those of $GS^{+/+}ApoE^{-/-}$ littermate controls [Figure 37A & C]. Again, when examining the stains separately, further insights into GS expression and plaque structure are able to be observed [Figure 38].

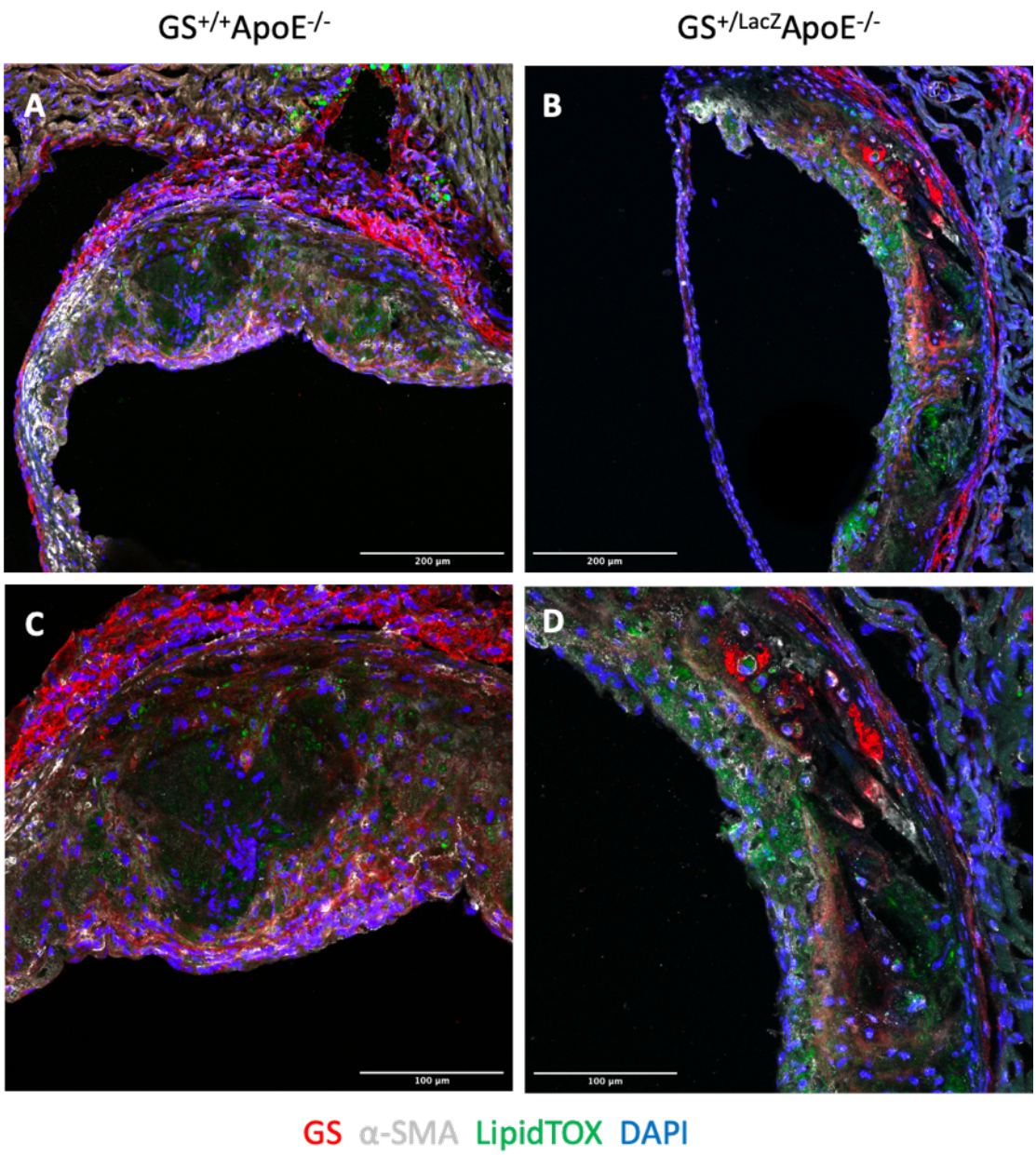

Figure 37: Immunofluorescent co-staining of $GS^{+/LacZ}ApoE^{-/-}$ and $GS^{+/+}ApoE^{-/-}$ aortic root sections to compare markers of plaque architecture

Immunofluorescence analyses of cryosectioned aortic sinus tissue from both $GS^{+/+}ApoE^{-/-}$ [**A & C**] and $GS^{+/LacZ}ApoE^{-/-}$ [**B & D**] mice fed a Western Diet for 12 weeks to induce atherosclerosis. All sections were stained for GS expression (**red**), α-SMA (**white**) as a marker of VSMCs, LipidTOX™ (**green**) as a marker of lipid deposition, and DAPI (**blue**). Images were taken of the same area of the leaflet and plaque at 20x [**top, A & B**] and 40x [**bottom, C & D**]

As seen previously, within the DAPI (blue) channel [Figure 38A&B], plaques from $GS^{+/+}ApoE^{-/-}$ controls [Figure 38A] have fewer, smaller acellular regions indicative of necrosis and/or lipid pooling than those of $GS^{+/LacZ}ApoE^{-/-}$ mice [Figure 38B]. Additionally, the different quantity distribution of α-SMA (white) between the genotypes is maintained, with $GS^{+/LacZ}ApoE^{-/-}$ sections exhibiting strong staining in the shoulder region of the plaque and moderate staining indicating the presence of small, fractured, unstructured caps [Figure 38F], in comparison to $GS^{+/+}ApoE^{-/-}$ controls displaying stronger staining throughout the plaque and particularly strongly in the walls of the sinus and within the thick cap [Figure 38E]. Similarly, the difference in density and distribution of lipids (LipidTOX™, green) between the genotypes is maintained with $GS^{+/LacZ}ApoE^{-/-}$ plaques exhibiting stronger staining and the majority being present within the cap region [Figure 38H], whilst this stain is diffusely distributed throughout the plaque in $GS^{+/+}ApoE^{-/-}$ sections [Figure 38G].

In the case of this experiment, examining the GS (red) channel provides new insights into plaque expression of GS. Interestingly, whilst overall the intensity is expectedly lower in the $GS^{+/LacZ}ApoE^{-/-}$ sections [Figure 38D] than those from their littermate $GS^{+/LacZ}ApoE^{-/-}$ controls [Figure 38C], the distribution of GS is much more even within the $GS^{+/+}ApoE^{-/-}$ than within the $GS^{+/LacZ}ApoE^{-/-}$ sections, whereby certain regions are so intensely stained as to suggest higher GS levels in those regions than even exhibited in the wild-type tissue. Also unexpectedly, only the $GS^{+/LacZ}ApoE^{-/-}$ plaques display the specific increased shoulder staining pattern previously published[57] and may therefore be indicative of a difference in cellular composition, such as a higher accumulation of *GLUL*-enriched cells within the shoulder region of $GS^{+/LacZ}ApoE^{-/-}$ plaques when compared to those from $GS^{+/+}ApoE^{-/-}$ controls.

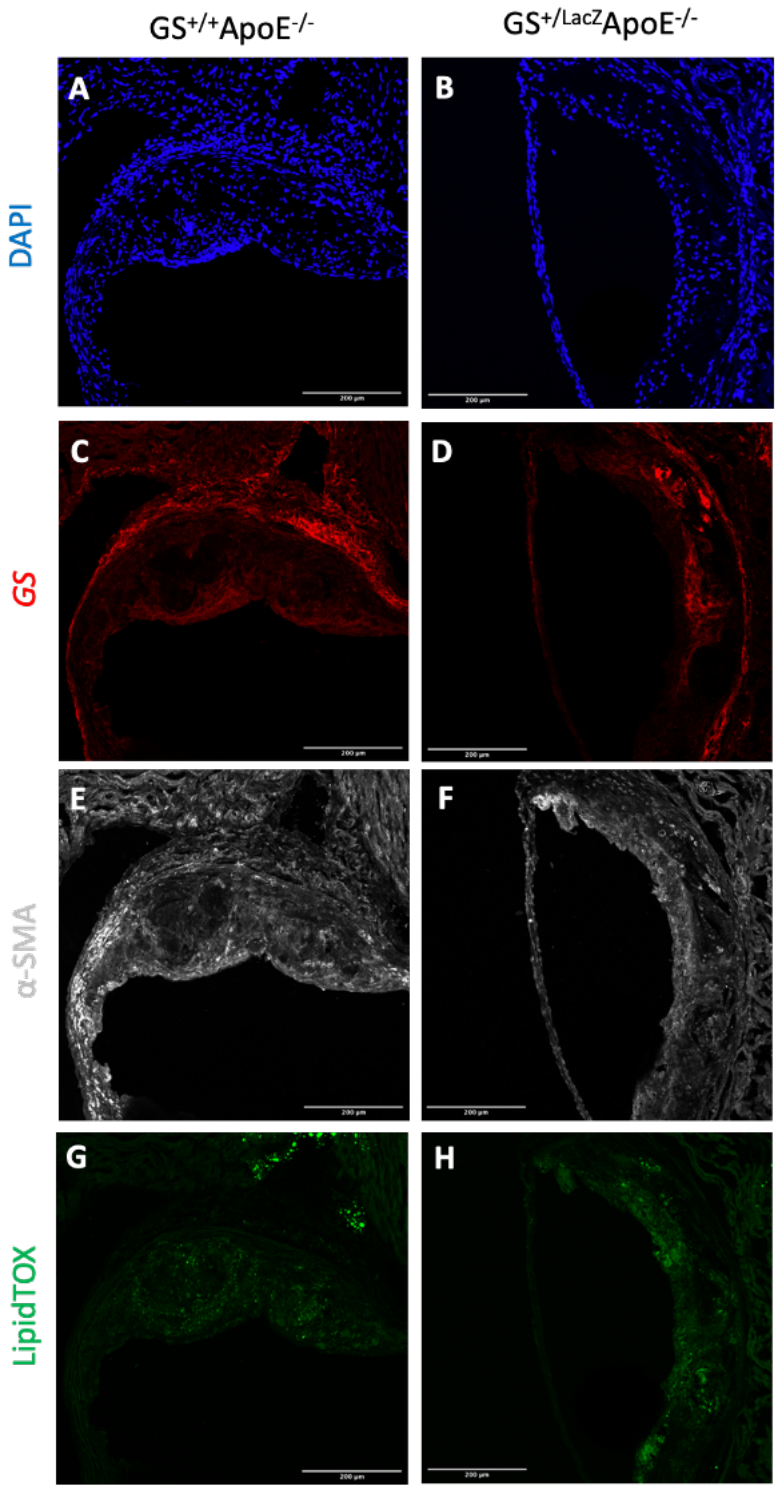

Figure 38: Immunofluorescent staining of aortic root sections to investigate markers of plaque stability Immunofluorescence analyses of cryosectioned aortic sinus tissue from both $GS^{+/+}ApoE^{-/-}$ [**left**] and $GS^{+/LacZ}ApoE^{-/-}$ [**right**] mice fed a Western Diet for 12 weeks to induce atherosclerosis. All sections were stained with DAPI (**blue, A & B**) as a general cell marker, GS (**red, C & D**), α-SMA (**white, E & F**) as a marker of VSMCs, and LipidTOX™ (**green, G & H**) as a marker of lipid deposition. Slides were imaged using confocal microscopy before ImageJ software was used to separately visualise the different channels within these images for comparison

Summary of immunofluorescent staining results

Firstly, use of specific immunofluorescent stains has enabled identification of specific features of plaque architecture associated with plaque stability and instability including, plaque size, surface geometry, cellular vs acellular regions through the use of the nuclear stain DAPI, VSMC-rich areas and cap structure through targeting α-SMA, identification of macrophage-rich areas using Isolectin B4, and lipid density and distribution through the use of LipidTOX™.

Secondly, these results suggest that GS is expressed to an extent in all cell types and is present throughout the entire plaque [Figure 38]. GS expression tends to be most intense in α-SMA rich regions, but regions of higher intensity staining have been observed which correlate to regions which are both rich in DAPI staining and have lower levels of α-SMA [Figure 37]. Co-staining utilising the *LacZ* reporter alongside Isolectin B4 staining possibly indicates these areas are rich in macrophages.

Finally, the specific pattern of increased GS expression at the shoulder region identified using *LacZ* reporter staining has unexpectedly been confirmed as unique to $GS^{+/LacZ}ApoE^{-/-}$ plaques when re-examined using an anti-GS antibody and compared to $GS^{+/+}ApoE^{-/-}$ plaques [Figure 38].

Table 48: Summary of immunofluorescent staining observations

	$GS^{+/+}ApoE^{-/-}$	$GS^{+/LacZ}ApoE^{-/-}$
GS expression: distribution and intensity	GS evenly expressed throughout the plaque with no particularly intense regions; strong expression observed within sinus walls	Overall intensity is expectedly lower; certain regions so intensely stained as to suggest higher GS levels in those regions than in wild-type tissue; localised increase of GS within cap region; strongly increased GS expression at the shoulder region unique to genotype
GS expression: co-localisation	GS is expressed to an extent in all cell types as indicated by co-staining; staining most intense within α-SMA rich regions, suggestive of predominantly VSMCs and some macrophages; some regions of higher intensity staining co-localise with Isolectin B4 staining suggesting macrophage presence	
Isolectin B4	Even distribution throughout plaque	Distributed throughout plaque, strong staining in fibrous cap region
α-SMA staining	Strong staining throughout the plaque, particularly within the walls of the aortic root and within the fibrous caps	Strong staining only within the shoulder region of the plaque; moderate staining delineating smaller unstructured fibrous caps
Fibrous cap structure	Smooth, thick caps covering surface of plaque	Small, thin, fractured, unstructured caps with blebbing and irregular surface geometry
Plaque size	Larger plaques compared to $GS^{+/LacZ}ApoE^{-/-}$	Smaller plaques compared to $GS^{+/+}ApoE^{-/-}$ controls
Acellular regions (lack of DAPI staining)	Fewer regions, smaller in size	Higher number of regions which are proportionally larger
Lipid distribution (LipidTOX™)	Diffuse even distribution throughout plaque	Stronger intensity of staining throughout plaque; very strong staining within fibrous cap region

4.4 Vascular function

Preceding the development of atherosclerosis, endothelial dysfunction involves changes to vascular tone through decreased NO bioavailability[23,24,29,37,40,41]. As such, the impact of reduced GS expression on endothelial function, and more specifically on NO production by eNOS, was examined through the *ex vivo* assessment of vasomotor function using aortic rings in the organ bath [3.4.1].

Aortic rings were harvested from male, 12-14-week-old $GS^{+/LacZ}$ mice and $GS^{+/+}$ littermate controls (n>9) and suspended within the organ bath apparatus. The rings were then treated with the vasodilators acetylcholine (ACh) [Figure 40] and sodium nitroprusside (NaNP) [Figure 42], and the vasoconstrictors potassium chloride (KCl) [Figure 39] and phenylephrine (PE), with the response to PE being tested both before and after incubation with the non-selective NOS inhibitor L-NMMA [Figure 41].

4.4.1 Ring viability and initial assessment of constriction by KCl

Rings were constricted with a single supraphysiological bolus of KCl in order to assess the ability of rings to constrict in response to stimuli, and therefore ring viability. Where rings failed to constrict sufficiently (>0.25g) or were subsequently unable to relax when KCl was washed out, the rings and subsequent data were discarded as either outcome indicates damage to the tissue.

There is no difference in KCl-induced vasoconstriction between genotypes (P=0.5767, n.s.) [Figure 39].

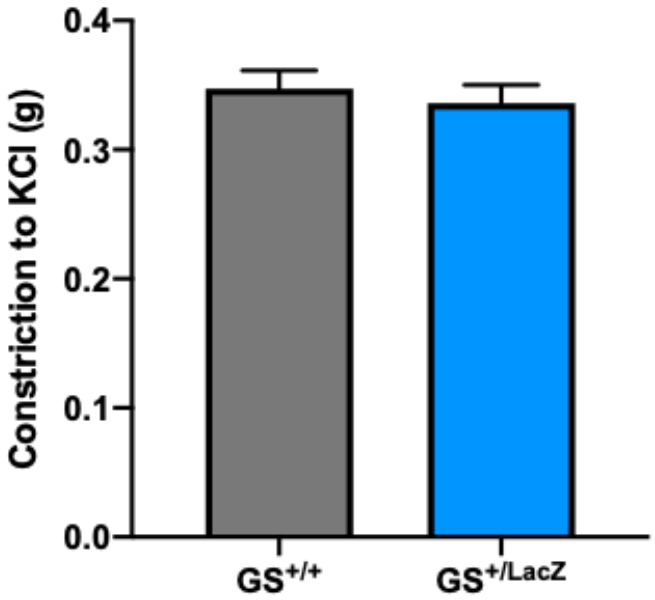

Figure 39: KCl-induced vasoconstriction The mean maximum increase in vasoconstriction induced by KCl was compared between genotypes ($GS^{+/+}$: n=15, $GS^{+/LacZ}$: n=13)

4.4.2 Endothelium-dependent vasodilation

Rings were first constricted with PE before the cumulative dose response to the endothelium-dependent vasodilator ACh [Figure 40].

When vasorelaxation is expressed as a percentage of pre-constricted tension, there is no difference in vasorelaxation between genotypes (*P*=0.2598, n.s.), indicating that the rings of both genotypes relax in a proportionally equivalent way [Figure 40A] and this is also confirmed by AUC analysis (*P*=0.3190, n.s.) [Figure 40B].

However, when examining this data expressed as the change in grams, there is a significant difference in between genotypes (*P*=0.0414, *) [Figure 40C] and this difference is also shown in the AUC analysis (*P*=0.0358, *) [Figure 40D]. As the rings have been shown to relax in a proportionally equivalent way [Figure 40A-B], this difference is probably due to $GS^{+/LacZ}$ mice having a slightly blunted response to the pre-constrictor PE (*P*=0.0895, n.s.) [Figure 40E].

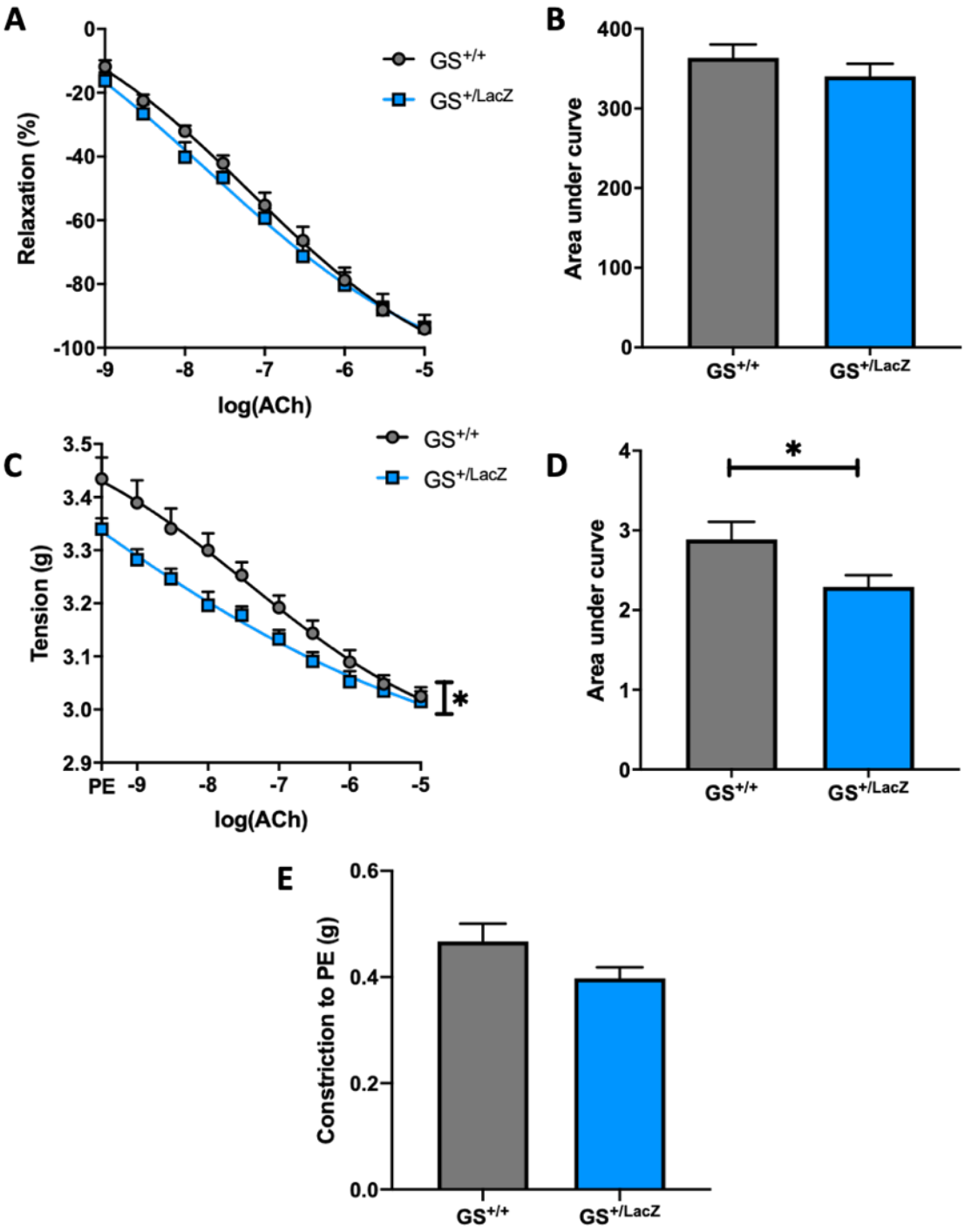

Figure 40: Endothelium-dependent vasodilation Vasomotor function was assessed using the vasodilator acetylcholine (ACh) after pre-constriction with the vasoconstrictor phenylephrine (PE) ($GS^{+/+}$: *n*=14, $GS^{+/LacZ}$: *n*=13). Vasorelaxation is expressed as a percentage of pre-constricted tension [**A**] or alternatively as the change in grams [**C**]. AUC analyses were also used to compare these curves [**B & D** respectively]. The initial PE-induced pre-constriction response of the rings was also assessed [**E**]

4.4.3 Assessment of PE-induced vasoconstriction

Although the response to the vasoconstrictor PE was already partially assessed through a single bolus of PE administered as a pre-constrictor ahead of ACh dose response testing, the vascular response to PE was fully tested in a similar accumulative dose manner. To determine whether any further blunting was due to differences in eNOS activity, the dose-response was measured both before and after incubation with the non-selective NOS inhibitor L-NMMA [Figure 41].

PE-induced vasoconstriction is significantly blunted in $GS^{+/LacZ}$ mice compared to $GS^{+/+}$ animals (P=0.0131, *) [Figure 41A] and this difference is also confirmed by AUC analysis (P=0.0100, *) [Figure 41B]. Whilst still significantly different (P=0.0379, *), this blunting effect in $GS^{+/LacZ}$ mice is partially abrogated after the use of L-NMMA versus control littermates [Figure 41C]. This is further confirmed by the AUC analysis also indicating that whilst there is still a significant difference between the genotypes (P=0.0405, *), this difference has been reduced [Figure 41D].

Furthermore, the fold increase in PE maximum effect (E_{max}) after use of L-NMMA is nominally increased in $GS^{+/LacZ}$ mice compared to $GS^{+/+}$ controls [Figure 41E] (P=0.2568, n.s.) indicating that L-NMMA has a greater effect on $GS^{+/LacZ}$ mice compared to their littermate $GS^{+/+}$ controls. Together this data suggests that there is at least a nominal difference in eNOS activity, and by extension NO bioavailability, between the genotypes.

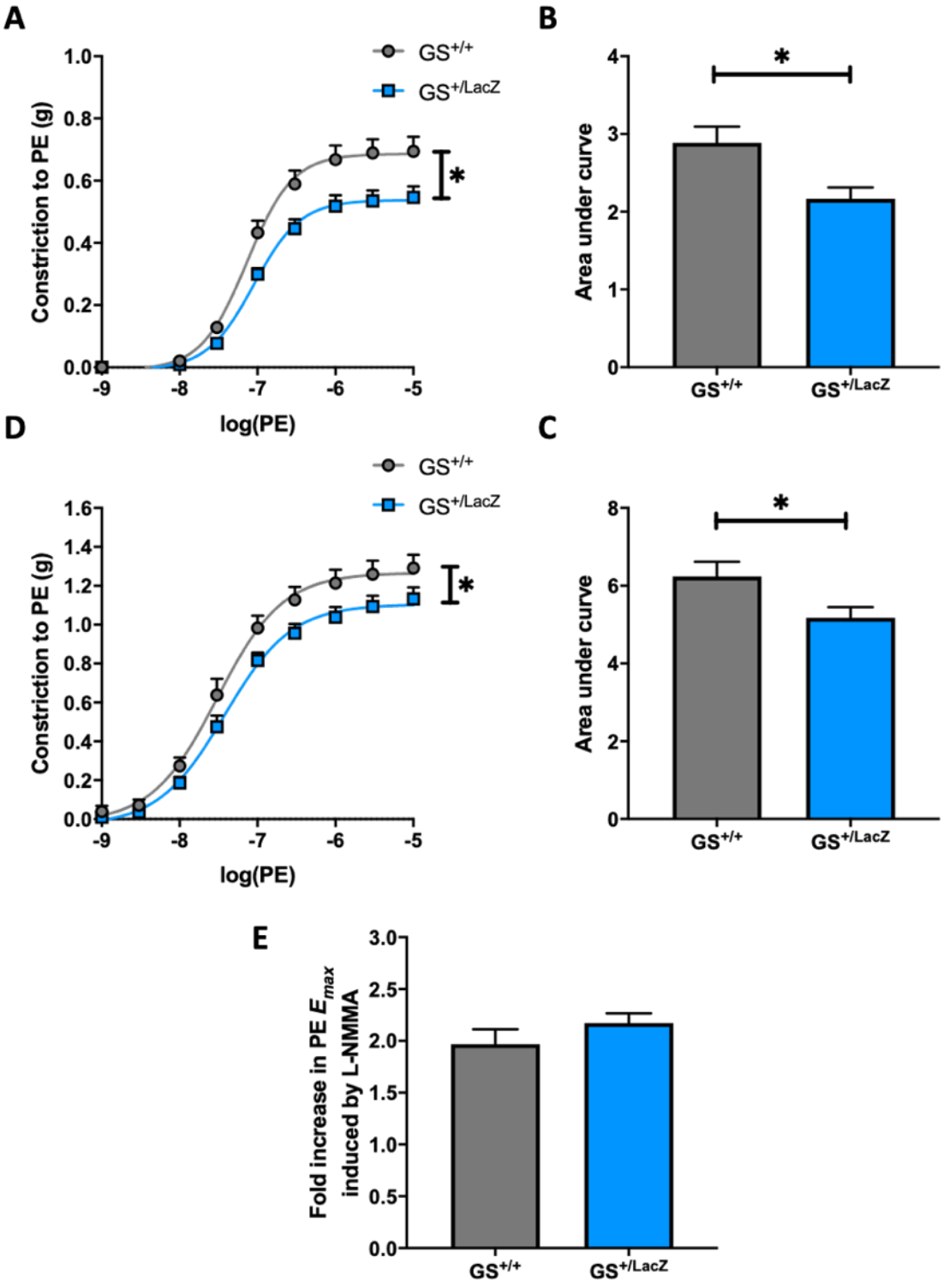

Figure 41: PE-induced vasoconstriction Vasomotor function was assessed using the vasoconstrictor phenylephrine (PE) both before [**A**] ($GS^{+/+}$: *n*=13, $GS^{+/LacZ}$: *n*=11) and after [**C**] addition of L-NMMA (*n*=9 per genotype). AUC analyses were also used to compare these curves [**B & D** respectively]. Additionally, the mean fold increase in vasoconstriction (E_{max}) induced by L-NMMA in matched samples was compared between genotypes (*n*=8 per genotype) [**E**]

4.4.4 Endothelium-independent vasodilation

Finally, to confirm that any differences measured are not due to the vascular smooth muscle cells (VSMCs) within the aortic rings being incapable of responding appropriately to NO signalling, endothelium-independent vasodilation was measured through use of the NO-donor sodium nitroprusside (NaNP) [Figure 42].

There is no difference in NaNP-induced vasorelaxation between genotypes [Figure 42A] (*P*=0.4262, n.s.) and this is confirmed by AUC analysis (*P*=0.5108, n.s.) [Figure 42B].

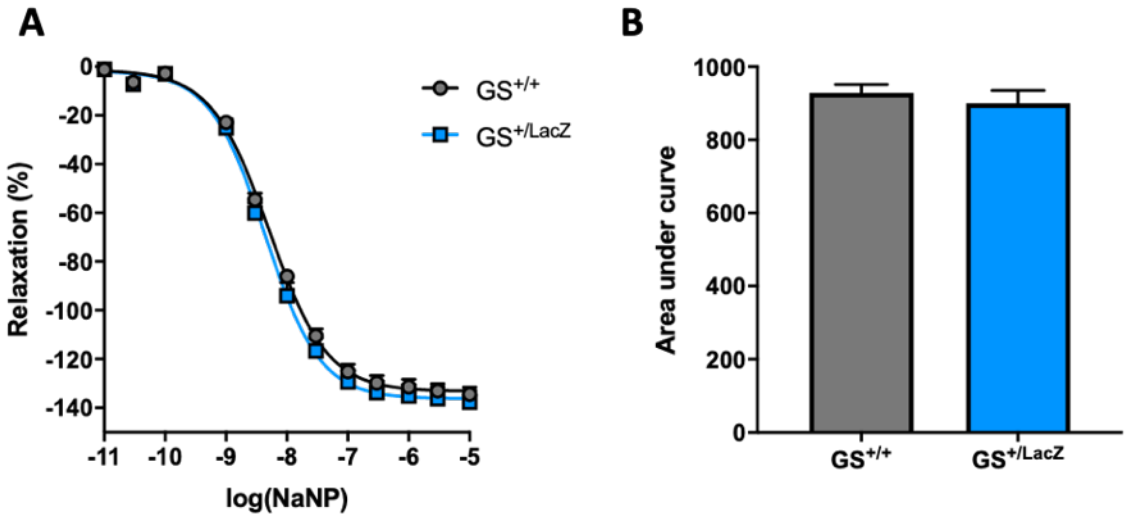

Figure 42: Endothelium-independent vasodilation Vasomotor function was assessed using the vasodilator and NO-donor sodium nitroprusside (NaNP) after pre-constriction with the vasoconstrictor PE and the NOS inhibitor L-NMMA (*n*=9 per genotype). Vasorelaxation is expressed as a percentage of pre-constricted tension [**A**] and curves were compared using AUC analyses [**B**]

4.4.5 Summary of vasomotion findings

There is no difference in stimulated vasorelaxation between the aortic rings of $GS^{+/LacZ}$ and $GS^{+/+}$ mice, whether endothelium-mediated (ACh) [Figure 40] or endothelium-independent (NaNP) [Figure 42]. By contrast, the endothelium-mediated (PE) [Figure 41A-B] vasoconstriction response is significantly blunted in $GS^{+/LacZ}$ mice. This blunted response is partially abrogated by the NOS inhibitor L-NMMA [Figure 41C-D] and is further confirmed by L-NMMA having a nominally greater effect on $GS^{+/LacZ}$ mice compared to $GS^{+/+}$ controls. Furthermore, there is no significant difference in KCl-induced endothelium independent vasoconstriction [Figure 39] suggesting diminished PE responsiveness is not likely to be a result of the VSMCs being mechanically unable to constrict.

Together these data suggest that the blunted response to the vasoconstrictor PE observed in $GS^{+/LacZ}$ mice compared to blunting seen in $GS^{+/+}$ controls is likely, at least in part, to reflect a nominal increase in NO bioavailability, and this could be due to increased basal eNOS activity.

4.5 Mechanistic studies

As stated previously, altered eNOS activity may alter NO bioavailability. As both increased and decreased NO availability can alter vascular function and precede atherogenesis, the effect of reduced GS expression on eNOS activity was examined through both the *ex vivo* assessment of aortic rings in the L-Arginine to L-Citrulline conversion assay [3.4.2], and through examining protein expression of eNOS and activating phosphorylation of eNOS at Serine-1177 (S1177) using Western blotting [3.5.3].

4.5.1 eNOS activity assay

The activity of eNOS, and by inference the bioavailability of NO, was quantified using the using the radiolabelled [^{14}C]-L-Arginine to [^{14}C]-L-Citrulline assay.

Aortas were harvested from male, 8-week-old GS$^{+/LacZ}$ mice and GS$^{+/+}$ littermate controls (n>3), split into two rings each and then weighed before being treated with [^{14}C]-L-Arginine. One aortic ring per animal was then stimulated with the endothelium-mediated vasodilator ACh in order to augment eNOS activity and subsequent conversion of [^{14}C]-L-Arginine to [^{14}C]-L-Citrulline and NO. The tissue was lysed to release the [^{14}C]-L-Citrulline which was then measured using a scintillation counter.

The scintillation counter measures the number of disintegrations in the scintillation fluid caused by the emitted radiation over a period of 5 minutes, and then produces an average number of disintegrations per minute, DPM. This DPM value is then normalised to the weight of the tissue to give a value of DPM/mg. [Figure 43A]. As such, it can be inferred that the higher the DPM/mg value, the higher the amount of [^{14}C]-L-Citrulline converted from [^{14}C]-L-Arginine and therefore, the higher the eNOS activity.

There was no significant difference between GS$^{+/LacZ}$ mice and GS$^{+/+}$ controls in the eNOS activity of aortic rings insofar as the DPM/mg value, whether unstimulated (P=0.2834, n.s.) [Figure 43A - left] or stimulated with ACh (P=0.3220, n.s.) [Figure 43A - right]. However, when examining the mean fold increase in eNOS activity, GS$^{+/LacZ}$ mice have a nominal 12% increase in basal eNOS activity (P=0.1233, n.s.) [Figure 43B] and a significantly different 22% increase in ACh-induced eNOS activity (P=0.0460, *) [Figure 43C] when compared to GS$^{+/+}$ controls. Although this finding that ACh has a significantly increased effect on the eNOS activity of GS$^{+/LacZ}$ rings when compared to those of GS$^{+/+}$ controls may seem unexpected given that aortic vasomotion studies indicated there to be no difference in ACh induced vasorelaxation [Figure 40], this is likely down to a difference in experimental conditions.

Additionally, the mean fold increase in eNOS activity induced by ACh in matched samples was compared between genotypes and again this was shown to be nominally higher in $GS^{+/LacZ}$ rings (P=0.5155, n.s.) [Figure 43D], further supporting the hypothesis that NO bioavailability is increased in $GS^{+/LacZ}$ mice.

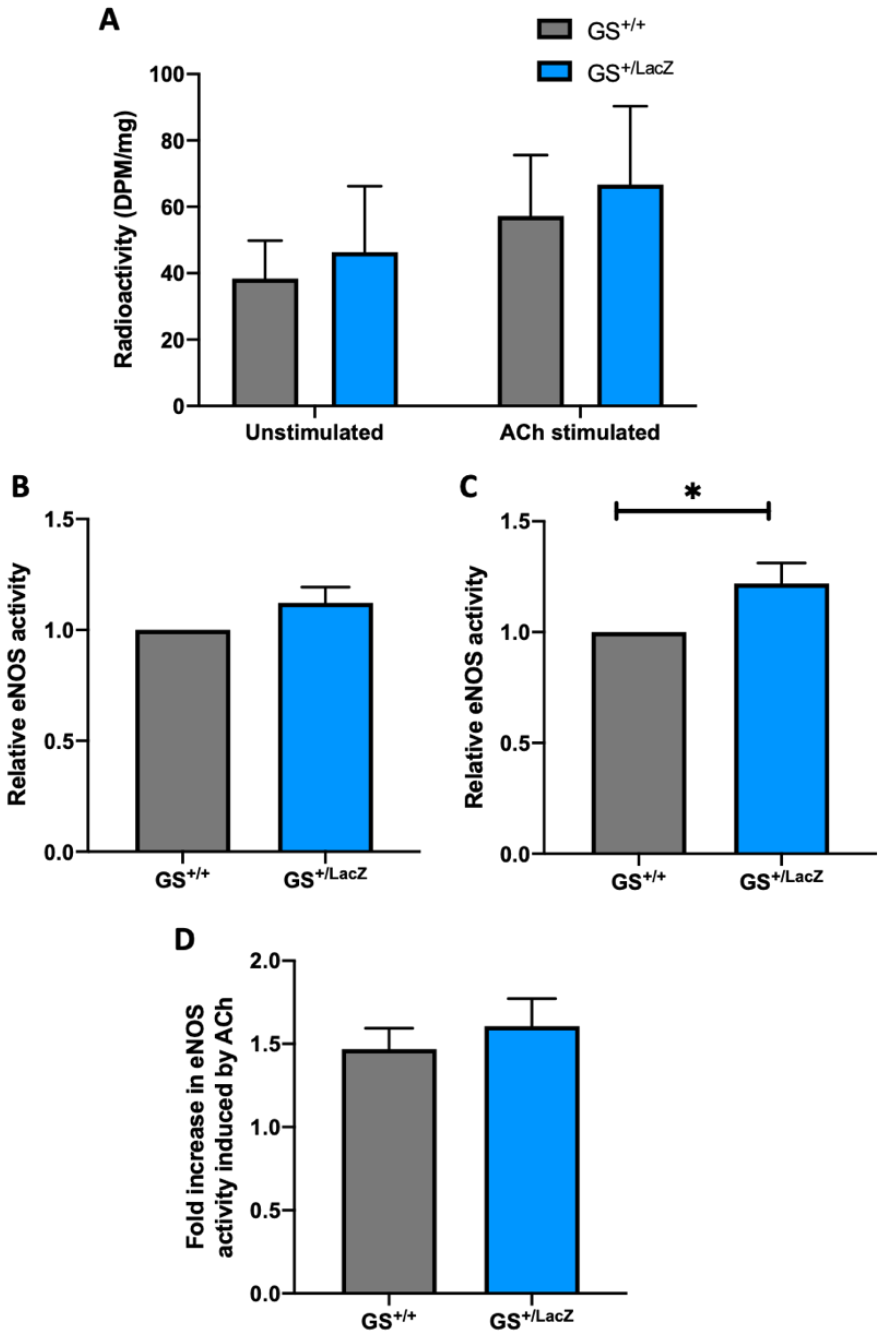

Figure 43: Quantification of eNOS activity The ability of eNOS to convert [^{14}C]-L-Arginine to [^{14}C]-L-Citrulline was assessed in unstimulated [**A -left** and **B**] and ACh-treated [**A – right** and **C**] aortic rings ($GS^{+/+}$: n=11, $GS^{+/LacZ}$: n=10). The mean fold increase in ACh stimulated eNOS activity was measured in matched samples and compared between genotypes [**D**] (n=9 per genotype)

4.5.2 Protein analysis

Previous aortic vasomotion studies showed a blunted response to the vasoconstrictor PE in $GS^{+/LacZ}$ mice compared to $GS^{+/+}$ controls which was partially abrogated by the NOS inhibitor L-NMMA suggesting an increased bioavailability of NO due to increased eNOS activity [Figure 41]. This hypothesis was further supported by the results of the [^{14}C]-L-Arginine to [^{14}C]-L-Citrulline conversion assay which indicated that compared to $GS^{+/+}$ mice, $GS^{+/LacZ}$ animals have increased basal and stimulated eNOS activity as per the increased levels of [^{14}C]-L-Citrulline detected from these samples [Figure 43]. As such, the protein expression of ß-actin, GS, eNOS, and activated eNOS phosphorylated at the S1177 residue (phospho-eNOS) was analysed by western blotting.

Whole aorta tissues were harvested from male and female, 8-week-old $GS^{+/LacZ}$ mice (n=4) and $GS^{+/+}$ littermate controls (n=6), and each tissue lysed to enable protein quantification.

As there was no difference in ß-Actin expression between genotypes (P=0.9143, n.s.), [Figure 44A], it was therefore suitable for use as a normalisation control as per previous qPCR work [4.2.1]. Additionally, as expected from previous qPCR work confirming *Glul* haploinsufficiency [Figure 14B], GS expression is significantly lower in $GS^{+/LacZ}$ mice compared to $GS^{+/+}$ control animals (P=0.0046, **) [Figure 44C].

Interestingly, despite the previous indications of a difference in eNOS activity, there is no difference between genotypes in either eNOS expression (P=0.6528, n.s.) [Figure 44D] or activated phospho-eNOS expression (P=0.9557, n.s.) [Figure 44D]. Together these data suggest that any difference in eNOS activity, and therefore NO bioavailability, is not due to a difference in total eNOS expression or activatory phosphorylation of eNOS at S1177.

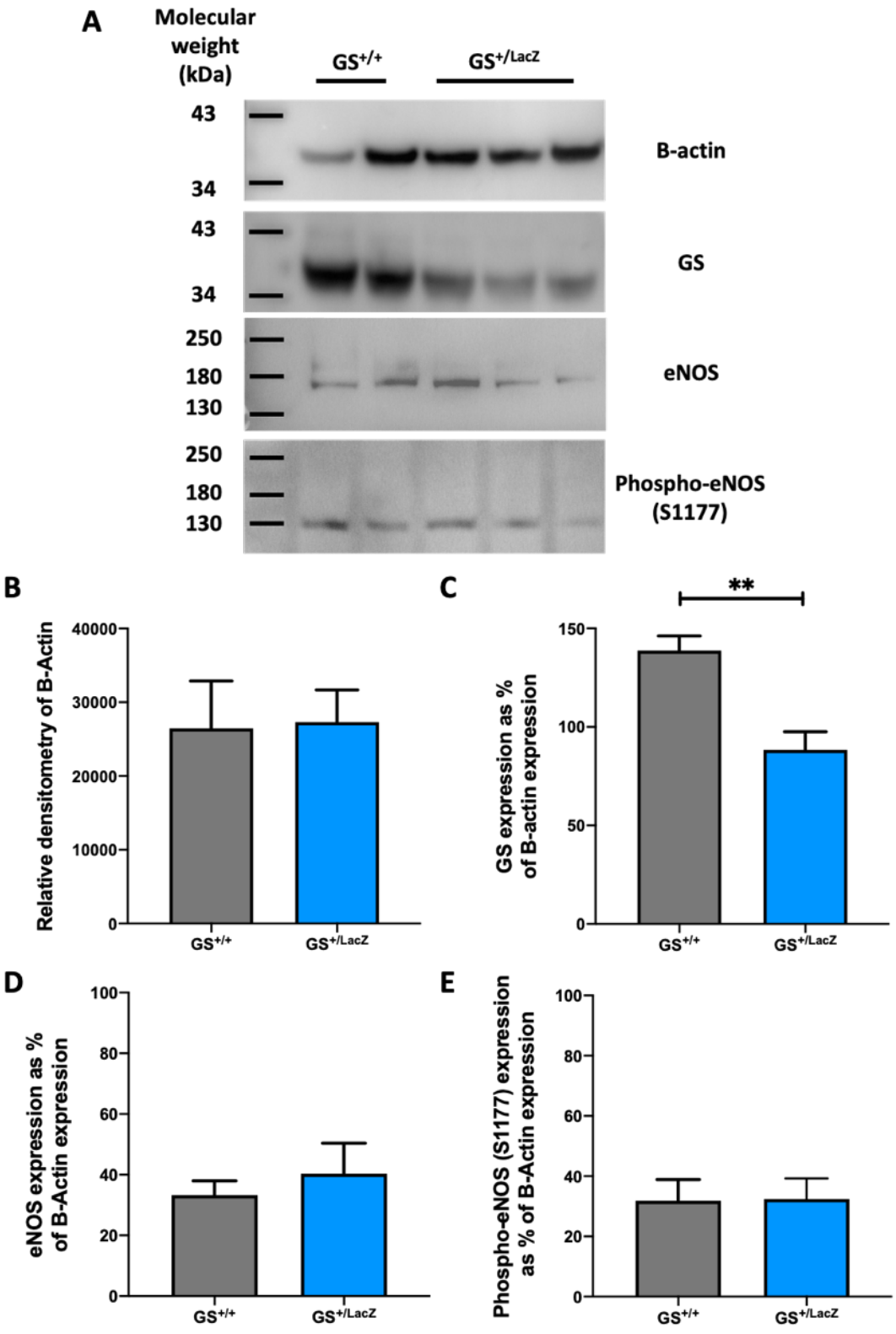

Figure 44: Quantification of protein expression Representative Western blots of ß-Actin, GS, eNOS, and phospho-eNOS (S1177) in $GS^{+/LacZ}$ mice (*n*=4) compared to $GS^{+/+}$ controls (*n*=6) [**A**]. There was no difference in ß-Actin expression between genotypes and was therefore suitable for use as a loading control [**B**]. As such, the mean expression of GS [**C**], eNOS [**D**] and phospho-eNOS [**E**] is expressed as a relative percentage of ß-Actin expression (*n*>4)

Chapter 5 Discussion

5.1 Key findings

Despite the wealth of published data on GS expression within the both the general vasculature[18,78] and within the atherosclerotic plaque microenvironment[58,87], and the identification of a novel role of GS within ECs as a modulator of RhoJ and subsequently the actin cytoskeleton[64], there is still very little knowledge of the role GS plays in arterial function or disease. This is further complicated by the seemingly contradictory findings that whilst decreased EC *GLUL* mRNA expression related to the SNP rs10911021 is linked to an increased risk of CHD in T2DM[9], increased plaque *GLUL* protein expression is a marker of plaque instability[57]. As such, this project had an overarching aim to elucidate the role of GS in atherosclerosis and vascular function.

Firstly, this project sought to establish and corroborate previous findings that GS is expressed in a cell-[18] and tissue-dependent[60–62,80] manner using the previously established $GS^{+/LacZ}$ mouse model[61]. *GLUL* expression has been shown to be differentially expressed between tissues, with aortas of both $GS^{+/+}$ and $GS^{+/LacZ}$ mice expressing substantially higher levels of *GLUL* than kidneys from the same animals, and $GS^{+/LacZ}$ mice exhibiting lower levels than $GS^{+/+}$ controls. This finding was recapitulated in the $GS^{+/LacZ}ApoE^{-/-}$ model of atherosclerosis

Next, I sought to establish whether global haploinsufficiency of GS alters the development of atherosclerosis. $GS^{+/LacZ}ApoE^{-/-}$ mice were found to have altered plaque burden and structure when compared to $GS^{+/+}ApoE^{-/-}$ littermate controls, exhibiting smaller plaques with differential fibrous cap composition and more features associated with plaque instability. Furthermore, whilst *GLUL* was shown to be expressed throughout the plaques of both $GS^{+/LacZ}ApoE^{-/-}$ and $GS^{+/+}ApoE^{-/-}$ mice, the increased relative expression of *GLUL* localised to the shoulder region of the plaque associated with unstable plaques was found to be uniquely observed in the plaques of $GS^{+/LacZ}ApoE^{-/-}$ mice. Furthermore, a striking and unique pattern of lipid deposition was observed in the plaques of $GS^{+/LacZ}ApoE^{-/-}$ mice whereby rather than lipids being sequestered within the centre of the plaque, they are instead concentrated within the thin fragmented layers of fibrous cap at the plaque surface.

Finally, as atherosclerosis is a complex multifactorial disease and given the differences in plaque morphology and burden, further work was undertaken on both the $GS^{+/LacZ}$ and $GS^{+/LacZ}ApoE^{-/-}$ models and their respective controls in order to establish whether these differences could be attributable to any of those risk factors, and in particular, altered endothelial function.

$GS^{+/LacZ}ApoE^{-/-}$ mice were found to be mildly protected against diet-induced impairments in glucose tolerance and possibly insulin tolerance when compared to $GS^{+/+}ApoE^{-/-}$ controls, which may partially contribute to the smaller plaque volume and burden in $GS^{+/LacZ}ApoE^{-/-}$ mice, but is unlikely to underpin the increased hallmarks of plaque instability.

Vascular function was assessed in the organ bath apparatus and no difference was found in stimulated vasorelaxation between the aortic rings of $GS^{+/LacZ}$ and $GS^{+/+}$ mice, whether endothelium-mediated via ACh or endothelium-independent via the NO-donor NaNP. By contrast, whilst there is no significant difference in KCl-induced endothelium independent vasoconstriction between genotypes, the PE vasoconstriction response was significantly blunted in $GS^{+/LacZ}$ mice when compared to $GS^{+/+}$ controls, and this was partially abrogated by the NOS inhibitor L-NMMA, suggesting a potential difference in NO bioavailability and this is supported by the finding that eNOS activity was increased in $GS^{+/LacZ}$ mice compared to $GS^{+/+}$ controls with a nominal increase in basal eNOS activity and a significant increase in ACh-stimulated activity.

An increase in NO bioavailability may be due to increased basal eNOS activity, and this was found to be increased in $GS^{+/LacZ}$ mice compared to $GS^{+/+}$ controls, with both basal and ACh-stimulated activity increased.

As the simplest explanation for this finding is an increase in eNOS expression and/or activating S1177 phosphorylation, total eNOS and activated eNOS aortic proteins were measured and found to be no different between $GS^{+/LacZ}$ and $GS^{+/+}$ mice. This suggests that whilst there is an increase in eNOS activity, this is due to another form of eNOS activation.

Together these data suggest that the blunted response to the vasoconstrictor PE observed in $GS^{+/LacZ}$ mice is likely, at least in part, to reflect an increase in eNOS activity and subsequent increase in NO bioavailability, which is known to be associated with reduced atherogenesis although further work is required to not only fully test this hypothesis that reduced GS increases eNOS activity and explore the underpinning mechanisms, but to also elucidate other mechanisms leading to the blunted response to PE observed in $GS^{+/LacZ}$ mice.

5.1.1 GS expression

Multiple studies have indicated that GS is expressed throughout the body in a cell- and tissue-dependent manner and Kalucka *et al* recently established that within ECs, GLUL is enriched in the arterial subset. However, as no previous study has been undertaken to establish the typical level of GS expression within the whole aorta, this project examined relative expression within the aorta versus the kidneys as these are known to express high levels of GS.

5.1.1.1 GS haploinsufficiency

The results from both qPCR and Western blotting confirmed that GS is strongly expressed within the aorta, despite the relatively high concentration of glutamine within the blood potentially negating the need for *de novo* synthesis of glutamine. This therefore further supports both the finding by Eelen *et al* of an alternative non-glutamine synthesising role of GS in ECs[64] and the work by Kalucka *et al* that GLUL is enriched in arterial ECs[18].

From the qPCR work, *GLUL* expression was also shown to be substantially higher in the aorta than in the kidney, confirming the previous findings that GS is differentially expressed throughout the body in a tissue-dependent manner. Furthermore, *GLUL* expression in $GS^{+/LacZ}$ mice was reduced in both kidneys and aortas when compared to $GS^{+/+}$ controls, with a significant reduction in aortas. This was corroborated by the results from the Western blotting, whereby GS expression is significantly lower in $GS^{+/LacZ}$ mice compared to $GS^{+/+}$ controls. Together this data supports the suitability of the $GS^{+/LacZ}$ mouse as a model of global GS haploinsufficiency.

5.1.1.2 The influence of diet on vascular GS expression

The previous finding that *GLUL* is more strongly expressed in the aorta than in the kidney has been recapitulated in both $GS^{+/LacZ}ApoE^{-/-}$ mice and $GS^{+/+}ApoE^{-/-}$ controls, and again $GS^{+/+}ApoE^{-/-}$controls were shown to have higher expression levels than $GS^{+/LacZ}ApoE^{-/-}$ mice.

Whilst there was no significant difference between genotypes in either kidney or aortic GS expression at any time, this data has unexpectedly suggested that Western diet feeding may alter GS expression. Within the kidneys, GS expression was suggested to decrease in $GS^{+/LacZ}ApoE^{-/-}$ mice and increase in $GS^{+/+}ApoE^{-/-}$controls. Within the kidneys, GS expression was suggested to decrease in $GS^{+/LacZ}ApoE^{-/-}$ mice and increase in $GS^{+/+}ApoE^{-/-}$controls. In direct contrast to this, within the aortas, Western diet feeding appears to GS expression in both genotypes, with a progressive decrease

in $GS^{+/+}ApoE^{-/-}$controls and $GS^{+/LacZ}ApoE^{-/-}$ mice plateauing at a level lower than baseline from 6 weeks to 12 weeks.

Although unexpected, this finding that Western diet reduces aortic GS expression is particularly important as it stresses the need to understand how reduced GS expression influences atherosclerosis and affects vascular tone given that diet may indeed drive these processes independently of other factors such as genetics (e.g. the SNP rs10911021). Further work is therefore required to confirm this finding in a larger sample size and to elucidate the underlying mechanisms responsible, perhaps through examining whether Western diet alters glutamine metabolism and/or the γ-glutamyl cycle, or through examining whether this change is due to the migration into and/or proliferation within the aorta of cell populations which enriched in *GLUL*.

5.1.2 GS haploinsufficiency and atherogenesis

As the atherosclerotic plaque is a complex microenvironment comprising multiple cell types including ECs, VSMCs and macrophages, amongst others, much work has been undertaken to better understand the factors influencing plaque stability and by extension the risk of plaque rupture leading to MCEs. As such, this project sought to establish whether global haploinsufficiency of GS alters the development of atherosclerosis. In order to do this, the established $GS^{+/LacZ}$ model was crossed with the well described $ApoE^{-/-}$ model of atherosclerosis to produce $GS^{+/LacZ}ApoE^{-/-}$ mice and $GS^{+/+}ApoE^{-/-}$ littermate controls capable of recapitulating pathological disease.

5.1.2.1 Plaque burden

Unsurprisingly, both the degree of stenosis and the volume of the whole plaque have been associated with increased MCE risk. This is not only because large plaques may occlude the artery, but also because larger plaques will typically have larger lipid cores and therefore be subject to increased plaque stresses such as inflammation, thinning of the cap, and endothelial erosion, and are also subject to greater pulsatile stresses from blood pressure due to the reduced lumen volume[3,39,51,54].

Upon first examination, $GS^{+/LacZ}ApoE^{-/-}$ mice were found to have significantly reduced plaque burden, within both the whole aorta and within the aortic root when compared to $GS^{+/+}ApoE^{-/-}$ controls. Further analysis of aortic root samples also indicated that there is no difference between genotypes in the number of plaques present. However, $GS^{+/LacZ}ApoE^{-/-}$ mice have a significantly lower mean plaque area and the mean size of the largest plaque is significantly reduced which underpins the difference in overall plaque burden.

This initial finding that $GS^{+/LacZ}ApoE^{-/-}$ mice have reduced plaque burden and significantly smaller plaques which do not mature to the same size as those of $GS^{+/+}ApoE^{-/-}$ mice, suggested reduced GS expression to have a protective effect. However, further histological examination of these plaques within the aortic root found that although $GS^{+/LacZ}ApoE^{-/-}$ mice have smaller plaques, these have features associated with plaque instability. Importantly, whilst plaque volume and degree of stenosis are understandably linked to MCEs, small non-obstructive plaques may still lead to acute vessel occlusion through thrombosis formation as a result of plaque instability.

5.1.2.2 Lipid deposition

Atherogenesis commences with the accumulation of lipids in the arterial sub-endothelial space, particularly low-density lipoproteins (LDLs) that undergo local oxidation, inducing a self-perpetuating feedback loop whereby they reduce the uptake of L-arginine, driving eNOS uncoupling and superoxide production and increasing oxidative stress[23,33,40–42]. As the plaque progresses, ECs and VSMCs augment inflammatory processes in response to the accumulation of ROS and oxidised lipids, attracting immune cells including monocytes[3,12,39]. These monocytes proliferate and differentiate within the developing plaque, with some eventually progressing into lipid-laden foam cells which have limited migration capacity and thus remain in the lipid-rich core[39,43]. As this self-perpetuating inflammatory cycle continues within this microenvironment, necrosis follows with the death of macrophages and VSMCs forming a necrotic core consisting of cellular debris and pooling lipids, which further accelerates the inflammatory cycle[3,39,49]. Should this thrombogenic pro-inflammatory core be exposed to the lumen, it is likely to result in a thrombus capable of occluding the arterial lumen, causing a MCE[3,39].

Histological examination of the aortic sinus with Oil red O staining also revealed plaques from $GS^{+/LacZ}ApoE^{-/-}$ mice to have altered lipid deposition when compared to controls. Whilst initial RGB colour analysis indicated there was no overall difference in colour, this analysis only provides a mean value for the whole plaque and is therefore unsuitable for differentiating between plaques with an even staining pattern and those with distinct regions of high and low intensity staining and therefore different patterns of lipid deposition. Colour thresholding identified a significant spatial difference in lipid deposition, with $GS^{+/LacZ}ApoE^{-/-}$ mice having more than double the area of red staining when compared with controls.

Furthermore, qualitative analysis of both the sections stained with Oil Red O and those stained immunofluorescently revealed a striking and unique pattern of lipid deposition in the plaques of $GS^{+/LacZ}ApoE^{-/-}$ mice. Rather than lipids being sequestered within the centre of the plaque, they were instead concentrated within the thin fragmented layers of fibrous cap at the plaque surface. Whilst further work is required to establish the mechanism by which this altered deposition is occurring, it stands to reason that this deposition could not only alter the tensile strength of the fibrous cap, but could also increase the acute occlusive risk of superficial erosions through exposure of these thrombogenic lipids to the lumen.

5.1.2.3 Plaque fibrosis

As the plaque progresses and inflammation increases, both VSMCs and macrophages differentiate and proliferate before producing collagen and elastin proteins which mature into cross-linked fibres with a higher tensile strength, and are assembled into a protective fibrous cap[50,51,88,89]. As such, features associated with plaque vulnerability and rupture risk include plaque ulceration resulting from superficial fissures being recapped, thinner caps due to either immature fibrous proteins or exposure to inflammatory proteolytic processes, and weak caps due to collagen and/or elastin incompletely maturing or fragmenting[3,39,50,51,55].

Histological examination with the Miller-van Gieson and picrosirius red stains has also shown plaques from $GS^{+/LacZ}ApoE^{-/-}$ mice to have altered fibrous composition versus controls. RGB colour analysis of plaques stained using Miller-van Gieson showed those from $GS^{+/LacZ}ApoE^{-/-}$ mice had higher mean and modal red and green intensities and lower blue intensities than controls, resulting in the plaques of $GS^{+/LacZ}ApoE^{-/-}$ mice having a purple tone, versus a yellow-beige colour of controls. As Miller-van Gieson stains elastic fibres blue to black, collagen magenta to red, and cytoplasm yellow, this difference in colour composition suggests that the plaques of $GS^{+/LacZ}ApoE^{-/-}$ mice have an altered ratio of fibrous to cytoplasmic material. This difference in composition between $GS^{+/LacZ}ApoE^{-/-}$ and controls is supported by RGB colour analysis of plaques stained using the collagen-specific stain Picrosirius red. As this is a red stain, as expected, there was no difference in mean or modal red intensities, however the plaques of $GS^{+/LacZ}ApoE^{-/-}$ animals have lower green and blue intensities than those of $GS^{+/+}ApoE^{-/-}$ controls and as a consequence, plaques of $GS^{+/LacZ}ApoE^{-/-}$ mice are both darker and more intensely red than those of controls. As Picrosirius red is a monochromatic stain, colour thresholding was used and identified a significant spatial difference in collagen deposition, with controls having less than half the area of collagen staining when compared with controls.

Qualitative assessment of cap structure using immunofluorescent staining and confocal microscopy also complements these data. The plaques of $GS^{+/LacZ}ApoE^{-/-}$ mice exhibited small, irregular, fragmented, and poorly structured caps of varying thickness with blebbing, in contrast to the smooth, thick, clearly delineated fibrous caps of $GS^{+/+}ApoE^{-/-}$ plaques. The α-SMA content and distribution is also different between the plaques, with $GS^{+/+}ApoE^{-/-}$ sections exhibiting strongest staining in the walls of the aortic root and in the smooth, thick cap, and moderate staining throughout the plaque, whereas $GS^{+/LacZ}ApoE^{-/-}$ sections only displayed strong staining in the shoulder region of the plaque, with only moderate staining within the fractured caps.

Together, these data suggest that plaque fibrosis differs between $GS^{+/LacZ}ApoE^{-/-}$ and control mice, with $GS^{+/LacZ}ApoE^{-/-}$ mice having reduced elastin deposition and increased collagen deposition, which may be related to reduced infiltration of VSMCs to provide this structure. Although not identified previously as a marker of plaque instability, it is possible that this altered fibrous cap composition increases rigidity and decreases elasticity of the cap and therefore it is reasonable to hypothesise this results in $GS^{+/LacZ}ApoE^{-/-}$ mice having a more friable and brittle cap structure vulnerable to the pulsatile stresses of blood pressure.

5.1.2.4 GS as a marker of plaque instability

Saksi *et al* demonstrated a 2.2-fold increase in *GLUL* expression in stroke associated (i.e. unstable) carotid atherosclerotic plaques versus asymptomatic plaques. They also demonstrated that GS was expressed throughout the plaque, including within the lipid core and particularly strongly in macrophages and VSMCs within the shoulder region of the plaque, a common site of plaque rupture[57]. This finding that increased plaque *GLUL* expression is associated with plaque instability has been corroborated by the work of Perisic *et al* who determined that symptomatic plaques had a 1.3-fold increase in expression compared to asymptomatic samples[59]. Whilst these particular studies were conducted on human carotid plaques, the same expression pattern has been particularly observed in the plaques of $GS^{+/LacZ}ApoE^{-/-}$ mice using immunofluorescent staining.

Unlike $GS^{+/+}ApoE^{-/-}$ plaques which have uniform GS expression, $GS^{+/LacZ}ApoE^{-/-}$ mice displayed an expectedly lower overall GS staining intensity, but the shoulder regions exhibited intense staining suggesting that these regions were predominantly composed of cells (e.g. macrophages and VSMCs) with greater GS expression. Furthermore, whilst $GS^{+/+}ApoE^{-/-}$ mice had smaller acellular (necrotic) regions and a well-structured thick fibrous cap, plaques from $GS^{+/LacZ}ApoE^{-/-}$ mice had larger acellular regions, and poorly structured caps with blebbing, potentially indicative of ulceration, mirroring those plaque instability features described by Saksi *et al* [57].

5.1.3 GS haploinsufficiency and metabolism

As atherosclerosis is a complex multifactorial disease, much work has been undertaken to better understand the factors influencing both the risk of developing atherosclerosis, and of events relating to plaque rupture, identifying obesity[4], T2DM[5], and insulin resistance[41] as increasing MCE risk. Therefore, given the differences in atherosclerosis between the $GS^{+/LacZ}ApoE^{-/-}$ mice and controls, further work assessed whether these factors were also influenced by GS haploinsufficiency.

Both $GS^{+/LacZ}ApoE^{-/-}$ and control mice were weighed prior to commencing Western diet feeding to induce atherosclerosis, and throughout the experiment, and no differences were observed.

Additionally, prior to commencing the Western diet both $GS^{+/LacZ}ApoE^{-/-}$ and control mice underwent profiling of systemic glucose homeostasis and insulin sensitivity, but no differences were found. On completion of Western diet, there was still no difference in fasting blood glucose, but $GS^{+/LacZ}ApoE^{-/-}$ mice had a significantly improved glucose tolerance and nominally increased insulin sensitivity versus controls.

Together, these data suggest that whilst reducing GS expression does not influence weight gain, it confers mild protection against diet-induced glucose intolerance, and possibly insulin resistance. Whilst this may partially explain the reduced plaque burden of $GS^{+/LacZ}ApoE^{-/-}$ mice, it is unlikely to explain the differences in plaque morphology versus controls.

5.1.4 GS haploinsufficiency and vascular tone and function

Previous work by Eelen *et al* demonstrated that GS undergoes autopalmitoylation and directly palmitoylates RHOJ, resulting in membrane localisation and altering actin remodelling within ECs, facilitating their migration during sprouting angiogenesis[64]. Coupled with work by Kondrikov *et al*, which has demonstrated that F-actin fibres not only colocalise with eNOS, but also directly promote eNOS activity by interacting with its oxygenase domain[30], it is possible that GS indirectly influences eNOS activity via this mechanism. However, whilst Kalucka *et al* showed *GLUL* expression to be enriched in arterial ECs[18], the role of GS within arteries has not yet been established. Furthermore, perturbed eNOS activity and endothelial dysfunction, leading to altered vascular tone[12,40] and hypertension[8] have also been identified as driving atherosclerosis. Evidence suggests that endothelial dysfunction precedes plaque formation[37], with production of superoxides and reactive oxygen species (ROS) causing oxidative damage to ECs[31,38]. The atherogenic process is further accelerated by eNOS dysfunction as NO has been shown to reduce immune cell recruitment and thereby retarding plaque development[3,12,39]. Together, these data suggest that GS has an important role within the arteries beyond *de novo* synthesis of glutamine and led to my hypothesis that reduced vascular GS expression increases arterial NO generation.

5.1.4.1 Vascular function

In order to investigate the effect of reduced GS on vascular function, and more specifically on NO production by eNOS, aortic vasomotion studies were undertaken on both $GS^{+/LacZ}$ mice and $GS^{+/+}$ controls using aortic rings mounted within the organ bath apparatus.

Aortic rings were treated with NaNP, a potent NO-donor, and their dilatory response measured. As there was no difference in NaNP-induced vasorelaxation between genotypes, it can be assumed that any differences in endothelial-mediated vasodilation are not due to altered VSMC responsiveness to NO.

Endothelial dependent vasodilation was tested in PE pre-constricted aortic rings via a cumulative dose response to the endothelium-dependent vasodilator ACh. ACh induces the production of NO by enabling an influx of Ca^{2+} into EC, promoting dissociation of eNOS from Cav1, and activating eNOS through the association of CaM[23,24]. When vasorelaxation was expressed as a percentage of pre-constricted tension, there was no difference in vasorelaxation between genotypes, indicating relative eNOS activation by ACh was similar in both groups. However, when ACh-induced vasodilation was expressed as absolute change in tension, this was

significantly lower in in $GS^{+/LacZ}$ mice versus controls, driven by the lower absolute starting tension achieved by a fixed pre-constricting dose of PE.

PE selectively binds to α_1-adrenoreceptors on VSMCs, inducing a Ca^{2+} influx into these cells, depolarising them and inducing vasoconstriction[90]. The finding that, compared to controls, $GS^{+/LacZ}$ aortic rings have a blunted constriction response to PE was further confirmed by specific assessment of the cumulative dose response, possibly suggesting increased endogenous generation of an opposing vasorelaxation factor, such as NO.

In order to test the specific hypothesis that $GS^{+/LacZ}$ mice have a blunted PE response due to increased NO bioavailability resulting from increased eNOS activity, PE responses were reassessed after incubation with the non-selective NOS inhibitor L-NMMA and this partially abrogated the blunted PE response of $GS^{+/LacZ}$ rings. This is bolstered by the finding that whilst vasoconstriction was increased in both genotypes after incubation with L-NMMA, the fold increase in PE maximum effect (E_{max}) was nominally increased in $GS^{+/LacZ}$ mice versus controls, indicating L-NMMA had a greater effect.

Finally, as KCl induces vasoconstriction through the depolarisation of VSMCs in a receptor- and endothelial-independent manner[91], the vasoconstriction response of $GS^{+/LacZ}$ mice and controls was measured to see whether differences in endothelium-mediated responses were associated with VSMCs being mechanically unable to constrict. As there was no difference between genotypes, this supported the hypothesis that diminished PE responsiveness was contributed to by NO bioavailability.

5.1.4.2 eNOS activity and expression

As stated previously, altered eNOS activity is one mechanism that influences NO bioavailability. Decreased NO availability can impair vascular function and precede atherogenesis. As previous findings have indicated that NO bioavailability is increased in $GS^{+/LacZ}$ mice, eNOS activity in their aortic rings was also investigated.

In the production of NO, eNOS converts L-Arginine to L-Citrulline. As NO is rapidly degraded and difficult to measure, the production of L-Citrulline can be measured as a proxy of eNOS activity[23,24,29,37,40,41]. This was defined by exposing aortic rings to radiolabelled [^{14}C]-L-Arginine and separating off the resultant [^{14}C]-L-Citrulline, which was quantified by measuring the radiation emitted, with higher radioactivity implying higher the eNOS activity.

Although not significantly different, a clear trend can be seen whereby basal eNOS activity was nominally increased in $GS^{+/LacZ}$ mice compared to $GS^{+/+}$ controls, whilst

ACh-stimulated activity was significantly increased. This is further supported by the finding that the mean fold increase in ACh-induced eNOS activity was also nominally higher in $GS^{+/LacZ}$ rings. As stated previously [**Error! Reference source not found.**], this finding that ACh has a significantly increased effect on the eNOS activity of $GS^{+/LacZ}$ rings when compared to those of $GS^{+/+}$ controls may seem unexpected given that aortic vasomotion studies indicated there to be no difference in ACh induced vasorelaxation [Figure 40], but this is likely down to a difference in experimental conditions. Within the organ bath, the aortic rings are held under tension and whilst this has been documented to alter responses[92,93], it is more likely that as the effect of ACh is measured as a change in tension and there is a limit to how relaxed the vessel can become around the triangular wires before the transducers fail to record further changes, it is therefore plausible that the higher doses of ACh may continue to further stimulate eNOS and increase NO bioavailability without this being seen in the resultant experimental data.

As an increase in eNOS activity may be attributed to increased eNOS expression and/or increased activation of eNOS, this was examined through measuring total aortic eNOS protein and its phosphorylation at S1177 as a proxy of activation. There was no difference between genotypes in either total eNOS or phospho-eNOS-S1177, suggesting that whilst there is an increase in eNOS activity, this is due to another mechanism, such as via F-actin binding of eNOS.

5.2 Study limitations

5.2.1 Use of murine models

The first and most obvious limitation of this study is that it consists of *ex vivo* and *in vivo* work from murine models rather than human samples or *in vitro* work utilising human cells, and yet relates the findings within these models to the human condition. The use of murine models of disease is widespread given they confer a number of benefits when compared to human sampling, not least practical aspects with regards to cost and ease of sampling, the possibility of genetic manipulation, and that providing the same inbred strain is used, e.g. C57BL/6, the background influence of other genes is mitigated. Furthermore, the average lifespan of a mouse is only 2 years, enabling longitudinal studies to take place in a relatively short time frame[94]. There are also clear ethical barriers to performing my project in humans.

Given this widespread use, a plethora of information is available, and genomic sequencing has indeed proven that the common house mouse *Mus musculus* and its derivative strains have a 99% sequence homology with humans[94]. However, whilst intragenic sequence homology is high, there are still substantial genetic differences, particularly within supposed non-coding intergenic regions. Indeed, the SNP rs10911021, previously linked to increased CHD risk in patients with T2DM and shown to reduce endothelial GS expression[9], has no murine homologue. Whilst the $GS^{+/LacZ}$ mouse model was originally developed as a reporter strain[61], this study has shown it can be repurposed for studying the role of GS in vascular biology and disease.

Given the wealth of knowledge available on mouse models, it is unsurprising that they are currently the most commonly utilised *in vivo* model for atherosclerosis studies[95]. However, the use of murine models for atherosclerosis studies is not without its controversies. One major limitation of the use of murine models is that as mice have substantially different lipid profiles to humans and as such are relatively resistant to the development of atherosclerosis. Therefore, genetic modification, such as $ApoE^{-/-}$, must be used in combination with a high-fat and/or high cholesterol diet to successfully drive atherosclerosis[96].

5.2.2 Plaque architecture

As discussed previously, murine models of atherosclerosis, whilst commonly employed due to their inherent advantages, are not without their faults. The ApoE$^{-/-}$ model of atherosclerosis employed within this study is well characterised and recapitulates many of the features of human atherosclerosis. However one major limitation is that whilst fulminant plaque rupture and subsequent lumenal thrombus formation preceding death has been described in the ApoE$^{-/-}$ atherosclerosis model[97], the relevancy of this is still under much debate given that the vast majority of murine plaques do not rupture. Therefore, hallmarks of plaque structure expected to lead to this outcome, which have been explicitly defined in humans, may be present in mice , but can only be inferred to confer altered risk of plaque rupture and MCE[98].

Whilst ideally, a human study would be undertaken in order to translate the findings of this study to the human disease state, the vast majority of human atherosclerotic plaque histological examination is conducted on samples obtained via carotid endarterectomy. Carotid endarterectomy is usually employed to reduce the risk of stroke when patients have either a moderate degree of stenosis (50-79%) with symptoms, such as prior stroke, or are asymptomatic with a high degree of stenosis (>80%)[99]. Given the findings of this study that reduced GS expression reduces not only plaque burden but individual plaque size, it is possible that this could bias sampling insofar as plaques of patients with a reduced GS phenotype never reaching these size criteria.

One approach to overcoming this limitation would be to repeat much of this work using a new murine model of tamoxifen-inducible knockdown of *GLUL* on an ApoE$^{-/}$ background whereby *GLUL* is reduced after inducing atherosclerosis. This would enable examination of the impact of reduced *GLUL* expression on established plaques of similar size to those of controls.

5.2.3 Limitations of the aortic vasomotion study

Use of organ bath apparatus enables the examination of aortic vasomotion in a highly controlled environment without the influence of other external factors such as hormones. In order to achieve this, aortic rings are placed under wire tension, which alters their ability to regulate vascular tone[92,93]. Previous work by de Moudt *et al* has indicated that should pathophysiological tension be applied to aortic rings, VSMCs are depolarised through Ca^{2+} offloading, reducing contractility, resulting in extreme sensitivity to exogenous NO[92]. Whilst this is certainly worthy of consideration, the previous findings of this study that there is no difference between $GS^{+/+}$ and $GS^{+/LacZ}$ mice in both voltage-dependent (endothelium independent) vasoconstriction by KCl and exogenous-NO induced (NaNP) vasodilation indicates that tension was applied optimally to the aortic rings but underlines the need for careful equilibration of the aortic rings.

Furthermore, whilst the use of Krebs-Henseleit buffer and supplementary oxygen in combination with a maintained temperature of 37ºC mimics normal physiological conditions, it is limited insofar as Krebs-Henseleit buffer does not provide any of the other nutrients present in blood which are required for normal vascular homeostasis, such as the amino acids glutamine and L-arginine. As such, this lack of essential amino acids may well contribute to altered physiological responses by the vessels, for example the activity of eNOS may be rate limited by the lack of available substrate, as indicated by the previous work of MacKenzie and Wadsworth[100].

One approach to overcoming these limitations would be to measure the blood pressure of $GS^{+/+}$ and $GS^{+/LacZ}$ mice as this would enable examining whether $GS^{+/LacZ}$ mice have reduced blood pressure commensurate with the reduction in vascular tone indicated by the organ bath experiments and has the inherent advantages of not only being *in vivo* and therefore not requiring an exogenous supply of amino acids, but also vessels are maintained under normal physiological flow conditions. This approach could also be applied to the atherosclerotic models utilised within this study, allowing us to see whether a reduction in vascular tone is maintained within the $GS^{+/LacZ}ApoE^{-/-}$ mice in comparison to $GS^{+/+}ApoE^{-/-}$ controls.

5.3 Future directions

5.3.1 GS as a novel regulator of vascular tone

As discussed previously, whilst the organ bath provides a controlled environment to examine vascular function, it lacks a supply of exogenous essential amino acids. For example, a lack of exogenous L-arginine may rate-limit eNOS and contribute to altered physiological responses[100]. One approach would be to repeat this work with physiological concentrations of L-arginine added to the Krebs buffering solution. This may unmask differences between genotypes related to a lack of substrate for more active eNOS of $GS^{+/LacZ}$ but could also plausibly diminish differences; in either way this may help to decipher the mechanism by which GS is modulating aortic tone.

The finding that eNOS activity is increased in the aortic rings of $GS^{+/LacZ}$ mice coupled with the finding that L-NMMA only partially abrogates the blunted vasoconstriction response to PE suggests this may be the result of an additional NO-independent mechanism. One possibility is that this is due to increased levels of the endothelium-derived hyperpolarising factor hydrogen peroxide (H_2O_2). This is supported by the recent work of Pipino *et al*, which found lowered GS expression in ECs to be linked to γ-glutamyl cycle defects indicative of reduced glutathione generation[72] and the work by Song *et al* that showed glutathione to protect ECs from hydrogen peroxide (H_2O_2) induced stress[101]. This hypothesis could be tested by repeating the organ bath experiments with the addition of catalase, an enzyme which catalyses the decomposition of hydrogen peroxide to oxygen and water, before examining whether L-NMMA is now able to fully abrogate the blunting effect seen in $GS^{+/LacZ}$ mice.

Another approach to understanding the role of GS within arterial function, and therefore the impact of reducing GS expression, would be to examine this in resistance arteries and arterioles, particularly as H_2O_2 has been shown to be responsible for flow-mediated vasodilation in these vessels[102–104]. Although the organ bath would be suitable for examining the vasoconstriction response of these vessels to PE and therefore determining whether smaller arteries from $GS^{+/LacZ}$ mice exhibit the same blunted response as the aortic rings, use of a pressure myograph would enable a constant lumenal flow to be sustained, greater mimicking the *in vivo* physiological conditions and would also allow for exploration of how changes in flow alters vasomotion responses to both PE and ACh[105].

Furthermore, in discovering the novel actin cytoskeleton remodelling role of GS within ECs, Eelen *et al* determined that although a minor role in comparison, endothelial GS is capable of producing glutamine, and will do so in response to severely reduced extracellular glutamine availability[64]. Given that the Krebs-Henseleit buffer lacks

glutamine, it is not implausible that endothelial GS was driven towards glutamine production, as opposed to actin remodelling. Whilst experiments have suggested the blunted response to PE in $GS^{+/LacZ}$ mice to be at least partially attributable to an increase in eNOS activity, the addition of physiological concentrations of glutamine to the buffering solution may therefore drive GS activity towards actin remodelling and in doing so enhance the blunted response to PE if increased eNOS activity in $GS^{+/LacZ}$ is promoted by augmented actin-eNOS interaction.

Although it is possible that the increase in eNOS activity and commensurate decrease in vascular tone seen in $GS^{+/LacZ}$ mice is due to increased F-actin fibres as a result of decreased GS, as indicated by the works of Eelen *et al* [64] and Kondrikov *et al* [30], further work is required to test this hypothesis. This may be undertaken in a number of ways such as further immunofluorescent staining to confirm co-localisation of these proteins, or alternatively to use co-immunoprecipitation on whole aorta lysates with the aim of directly targeting ß-Actin to indirectly target eNOS, confirming the protein-protein interaction, particularly within samples from $GS^{+/LacZ}$ mice. Another option would be to repeat the organ bath experiment and/or eNOS activity assay with inhibition of the ß-Actin-eNOS interaction, for example using a cell-permeable synthetic peptide capable of binding to actin and inhibiting this interaction previously described by Kondrikov *et al* [30].

Finally, it is also worth noting that these experiments have focussed on genetic reduction of GS. In order to confirm that the responses detailed in this study are driven by a reduction of GS catalytic activity, it may be worthwhile to repeat these experiments using wild-type $GS^{+/+}$ aortic rings and expose half to the GS inhibitor MSO and the remainder to vehicle control.

5.3.2 Plaque stability

As the atherosclerotic plaque is a complex microenvironment consisting of not only ECs but also VSMCs, macrophages – foamy and non-foamy, fibroblasts, T-lymphocytes, mast cells, monocytes, and platelets, the role of GS in ECs and other lineages need to be established in order to elucidate the mechanism(s) underpinning the differences in plaque morphology observed in $GS^{+/LacZ}ApoE^{-/-}$ mice.

Regional GS staining in the atherosclerotic plaques of the murine models I studied corresponds well with the previous work in humans by Saksi *et al* [57]. My data also reveal that GS is expressed throughout the plaque, including within the lipid core, and frequently co-localises with macrophages and VSMCs within the shoulder region of the plaque, a common site of plaque rupture[57]. However, this and the relatively intense GS expression in the shoulder region of $GS^{+/LacZ}ApoE^{-/-}$ mice raises new questions. These findings suggest upregulation of *GLUL* may be due to a higher concentration of *GLUL*-expressing cells within that area, as suggested by scRNA-seq studies indicating that subsets of cells differentially express genes according to their specialist function[18,106]. An alternative possibility could be that upregulation of *GLUL* this is indicative an adaptive response by the VSMCs, macrophages and ECs within this region[78,106,107]. One such mechanism encompassing both of these possibilities may be that *GLUL*-enriched VSMCs and macrophages within that region are differentiating and proliferating thus increasing the number of GLUL-enriched cells in this region as an adaptive response, for example to assemble new fibrous cap at this point of weakness; however, further work is required to establish this.

The plaques of $GS^{+/LacZ}ApoE^{-/-}$ mice also displayed a striking pattern of α-SMA and lipid staining, suggestive of lipid sequestration within the fibrous cap (as opposed to the typical fous in the necrotic core), together reduced α-SMA staining; further work is required to establish the mechanism of this unusual phenotype.

Whilst previous work by Eelen *et al* established that within the endothelium, GS predominantly influences cytoskeletal remodelling via RhoJ[64], this role has not been tested in either VSMCs or macrophages; RhoJ is expressed in aortic VSMCs[76] and to a lesser extent in leukocytes[108]. Should this mechanism be demonstrated as active within these cell types, this may go some way to explaining the unique plaque morphology of this study. For example, Eelen *et al* determined that reducing GS reduces cell migration through negatively affecting the remodelling of the actin cytoskeleton reducing both the number of filopodia and the lamellipodial area. VSMCs are actin-rich, with cell motility again reliant on filopodial and lamellipodial projections through cytoskeletal remodelling[109] and therefore it stands to reason that GS may also regulate this process in VSMCs, a hypothesis supported by the finding that whilst $GS^{+/+}ApoE^{-/-}$

plaques display strong α-SMA staining within the fibrous cap, $GS^{+/LacZ}ApoE^{-/-}$ plaques have a substantially reduced α-SMA content and altered distribution suggestive of reduced VSMC motility. With regards to macrophages, previous work by Palmieri *et al* has shown that reducing GS activity, whether through genetic reduction of GS expression or alternatively through inhibition of its enzymatic activity using MSO, indirectly reduces EC migration and angiogenesis, albeit within the tumour microenvironment as opposed to atherosclerotic plaque[44]. Again, whilst altered EC motility was established within this study, macrophage motility was not examined. However, if this is also the case with macrophages, then this could contribute to the presence of lipid-laden cells in the caps of $GS^{+/LacZ}ApoE^{-/-}$ mice. One approach to examine this could be to conduct further immunofluorescent co-staining to not only stain for lipid deposition using LipidTOX, but to simultaneously stain for macrophages, either using IB4 again or through use of an antibody against a macrophage-specific cell marker.

In addition to decreased α-SMA and increased lipid deposition within the fibrous cap of $GS^{+/LacZ}ApoE^{-/-}$ plaques, these plaques also displayed overall reduced elastin and increased collagen staining and thinner, fractured, unstructured caps when compared to those of controls. Previous work by Krettek *et al* has indicated that within plaques, elastogenesis is a continuous process mediated by not only VSMCs but also by macrophages. However, it has been suggested that this macrophage-mediated elastogenesis is often ineffective and dysfunctional, producing disordered, immature elastin fibres, in contrast to the mature cross-linked elastin fibres of fibrous caps produced by VSMCs[50]. Furthermore, previous work by Douglas *et al* has also determined that these disordered fibres may in themselves lead to plaque rupture at the shoulder region of the plaque due to increased shear stress between disorganised fibres when compared to those with the same orientation and dispersion[52]. Examining whether this fibre disorganisation is enhanced in $GS^{+/LacZ}ApoE^{-/-}$ plaques when compared to controls is worth pursuing given that samples have previously been stained with Picrosirius red which in addition to staining collagen red, also enhances collagen birefringence enabling examination of both fibre orientation and fibre thickness when viewed under polarised light conditions[85,86].

One approach to understanding how the global reduction of GS influences plaque phenotype would be to repeat much of this work using the new murine model of tamoxifen-inducible knockdown of *GLUL* on an $ApoE^{-/}$ background mentioned previously. Knocking down *GLUL* expression in some animals after commencing the Western diet would enable us to examine whether this model recapitulates the unique plaque morphology observed in $GS^{+/LacZ}ApoE^{-/-}$ mice and whether untreated mice mimic the plaque morphology of the $GS^{+/+}ApoE^{-/-}$ controls, and if so, would not only

validate this new model, but also confirm the influence of GS on plaque morphology, independent of plaque development *per se*.

In addition to the global *GLUL* knockdown models, both the $GS^{+/LacZ}ApoE^{-/-}$ developed for this project and the inducible global model described above, another complementary approach would be to repeat much of this work utilising lineage-specific *GLUL* knockdown models, each on an $ApoE^{-/-}$ background for the purpose of studying atherogenesis. This could include separate VSMC- and macrophage-specific, and a combination VSMC-and-macrophage-specific *GLUL* knockdown model. Tamoxifen-inducible models may prove to be more versatile for this work as early knockdown prior to commencing the Western diet would allow us to examine how plaque morphology is affected by each of these knockdowns and examine their contribution to the specific features described of $GS^{+/LacZ}ApoE^{-/-}$ plaques such as the altered lipid deposition and fibrous architecture, whilst later induction after commencing the Western diet would enable us to examine how plaque development diverges in plaques of equal size, potentially revealing new pathways involved in plaque maturation.

Together, these findings of a shift in plaque architecture support the hypothesis that the lack of cap fibre maturation and lipid deposition within these fibres seen in $GS^{+/LacZ}ApoE^{-/-}$ plaques is potentially due to macrophage and/or VSMC dysfunction and supports the need to establish the role of GS within these cells and the impact of reduced GS on the production of the important scaffolding proteins elastin and collagen.

5.3.3 Reduced GS expression and Type 2 Diabetes Mellitus

People with T2DM are 2-3 times more likely to have a cardiovascular event and these events occur approximately 15 years earlier when compared to age-matched healthy controls. Additionally, the risk of death after these events is approximately doubled in people with diabetes and, despite advances in diabetes management, post-acute myocardial infarction mortality rates remain increased[6,7,110]. Multiple risk factors have been identified as contributing to this increased risk of cardiovascular disease including obesity, inflammation, hyperglycaemia, dyslipidaemia, insulin resistance, increased vascular tone and hypertension, and endothelial dysfunction, and the clustering and subsequent exacerbation of these pro-atherogenic risk factors has led to the term metabolic syndrome[4,5,41].

With diabetes now affecting over 400 million people globally and type 2 accounting for over 90% of these cases[111,112], much work has been undertaken to elucidate possible genetic links underpinning the significantly increased risk of atherosclerosis related major cardiovascular events seen in patients with T2DM. Qi *et al* directly implicated *GLUL* expression in CHD risk in patients with T2DM[57] and the specific finding that the SNP rs10911021 risk allele reduces GS expression and confers a substantially increased risk of MCEs in patients with T2DM is in stark contrast to the finding that no risk was conferred to non-diabetics[57].Further work by this group has suggested that this may be due to perturbed levels of γ-glutamyl cycle intermediates resulting in increased oxidative damage[72]. Whilst it remains plausible that metabolic perturbation contributes to the association between *GLUL* and cardiovascular risk in T2DM, for example through altered glutathione recycling, the novel role of GS identified in ECs by Eelen *et al* [64] may also be relevant and warrants future exploration.

My thesis has successfully demonstrated that reducing GS reduces plaque size, which may be at least partially explained by increased NO bioavailability. However, my work has also indicated that these plaques have multiple hallmarks of instability. Given that this was established within non-diabetic models, we cannot assume the same will apply in diabetic models, given the reported divergent associations of rs10911021 risk alleles with cardiovascular outcomes in diabetic and non-diabetic populations. What remains unanswered is how diabetes combines with the reduced GS phenotype to drive up the CHD risk and this question is sufficient to justify further murine studies investigating the mechanism underpinning this relationship.

When taken together with the previous studies discussed here, the results of my thesis point towards a new hypothesis that disrupted glucose homeostasis provides the molecular switch to drive atherosclerotic plaques from a small and possibly less stable

phenotype, to a more unstable phenotype with clinical events due to increased plaque rupture.

As discussed previously, the SNP rs10911021 is unable to be directly replicated in murine models, and whilst the models utilised within this project allow assessment of globally reduced GS expression, they do not recapitulate key elements of diabetes. This could be addressed in future studies by using genetically or chemically induced diabetes in my established models[113,114]. Although it may be possible to produce a new genetic model through inter-strain breeding, it is technically challenging, costly, not in line with the current 3Rs approach of “replacement, refinement and reduction”. As such, chemically inducing diabetes through the use of the drug streptozotocin (STZ), a well-documented model, seems most appropriate. Originally discovered as an antibiotic, it has since been determined to be a cytotoxic glucose analogue capable of destroying pancreatic ß-cells. The use of STZ is generally regarded to be a model of type 1 diabetes mellitus (T1DM), owing to high doses being capable of fully destroying the ß-cells, mimicking the ß-cell destruction of T1DM. However, the use of continuous low doses of STZ to partially destroy ß-cells effectively mimics the ß-cell exhaustion of late-stage T2DM, particularly as the remaining cells must compensate for the loss of those targeted by the drug[113] and the diet induced insulin resistance.

5.4 Conclusions

Atherosclerosis is a complex multifactorial disease and much work has been undertaken to better understand the factors influencing both the risk of developing atherosclerosis, and of events relating to plaque rupture leading to myocardial infarction and stroke. Increased localised expression of *GLUL* within atherosclerotic plaques has been repeatedly identified as a marker of plaque instability and yet, directly contrasting with this, decreased *GLUL* expression has been linked to both a pro-inflammatory skewing in macrophages and an increased risk of CHD in T2DM. Furthermore, new work on EC biology indicates *GLUL* has not only an important role in atherosclerosis, but an important role in vascular function, with GLUL expression having been shown to be enriched in arterial ECs, and a novel role for GS having been identified within ECs with regards to altered actin remodelling during angiogenesis.

Despite this recent wealth of information on the expression and roles of GS, very little was known about the role of GS in atherogenesis and plaque morphology, and how reducing *GLUL* may impact upon these processes. Similarly, as the previous work uncovering the novel role of GS focussed on angiogenesis, no work had yet been done exploring whether decreasing GS expression could affect arterial endothelial function, nor has work been conducted on the possibility that GS may be involved in the function of other plaque-resident cells such as VSMCs and macrophages.

In order to answer these questions, the pre-existing murine model $GS^{+/LacZ}$, originally developed as a GS reporter strain, was repurposed as a model of GS haploinsufficiency for the purpose of studying vascular tone and function. The $GS^{+/LacZ}$ model was then crossed with the well characterised $ApoE^{-/-}$ mouse model to produce a new model, the $GS^{+/LacZ}ApoE^{-/-}$ mouse model for the purpose of determining the previously undiscovered roles of GS in atherogenesis.

Work examining atherosclerosis within the $GS^{+/LacZ}ApoE^{-/-}$ model has indicated that the reduced GS phenotype reduces plaque burden overall and produces smaller plaques with multiple hallmarks of plaque instability including proportionally larger necrotic cores, altered plaque architecture likely to contribute to an increase in friability due to reduced elastin and increased collagen, and thin fractured fibrous caps with reduced VSMC infiltration and a unique and striking pattern of lipid deposition within these caps. My work was conducted within non-diabetic models, and their smaller (i.e. lower risk) plaques with other high risk features may partially explain why SNP rs10911021 does not confer altered risk in non-diabetic people, but increases risk in people with T2DM, which could tip the balance toward plaque rupture risk. It is also notable that the unstable plaques of $GS^{+/LacZ}ApoE^{-/-}$ mice were also shown to have increased relative *GLUL* expression within the shoulder region of the plaque, consistent with previously

published histological analysis of the unstable plaque. Effectively, these findings may marry together the previously stated controversy within the literature – genetically reduced GS expression produces smaller but higher-risk plaques with a localised increase in GLUL expression at the most vulnerable shoulder region of the atherosclerotic microenvironment. When these findings are taken together with other previously published studies and the recently identified alternative role for GS, this points towards the possibility of VSMC and/or macrophage dysfunction and whilst other mechanisms are likely to also be involved, such as inflammatory macrophage skewing, it is possible that altered actin remodelling reducing cell migration is a contributory factor, although this requires formal proof.

This finding of Eelen *et al* that decreasing endothelial GS results in increased F-actin stress fibres[64] is also complemented by previous work demonstrating that eNOS colocalises with F-actin, with this interaction promoting its activity[30], and led me to hypothesise that reduced GS impacts eNOS activity. Data from the $GS^{+/LacZ}$ model has shown that reducing GS does indeed alter vascular tone, as supported by organ bath and eNOS activity assays. This was not associated with altered expression of either total eNOS or phospho-eNOS-S1177, suggesting an alternate mechanism of eNOS activation. Although further proof is required, it is plausible that increased interaction of ß-actin and eNOS could underpin this finding.

In summary, the work in this project adds to the existing literature on GS by adding to our understanding of GS as a regulator eNOS activity, vascular tone, atherogenesis, and plaque morphology. Many questions remain about the key cellular players and the molecular mechanisms within these, along with how diabetes adversely interacts with such phenomena. As a result of this thesis, it is hoped that ultimately a better understanding of the molecular mechanisms underpinning atherosclerosis may provide new strategies for managing cardiovascular risk, perhaps through stratifying patients, both with and without diabetes, according to GS expression and/or rupture risk.

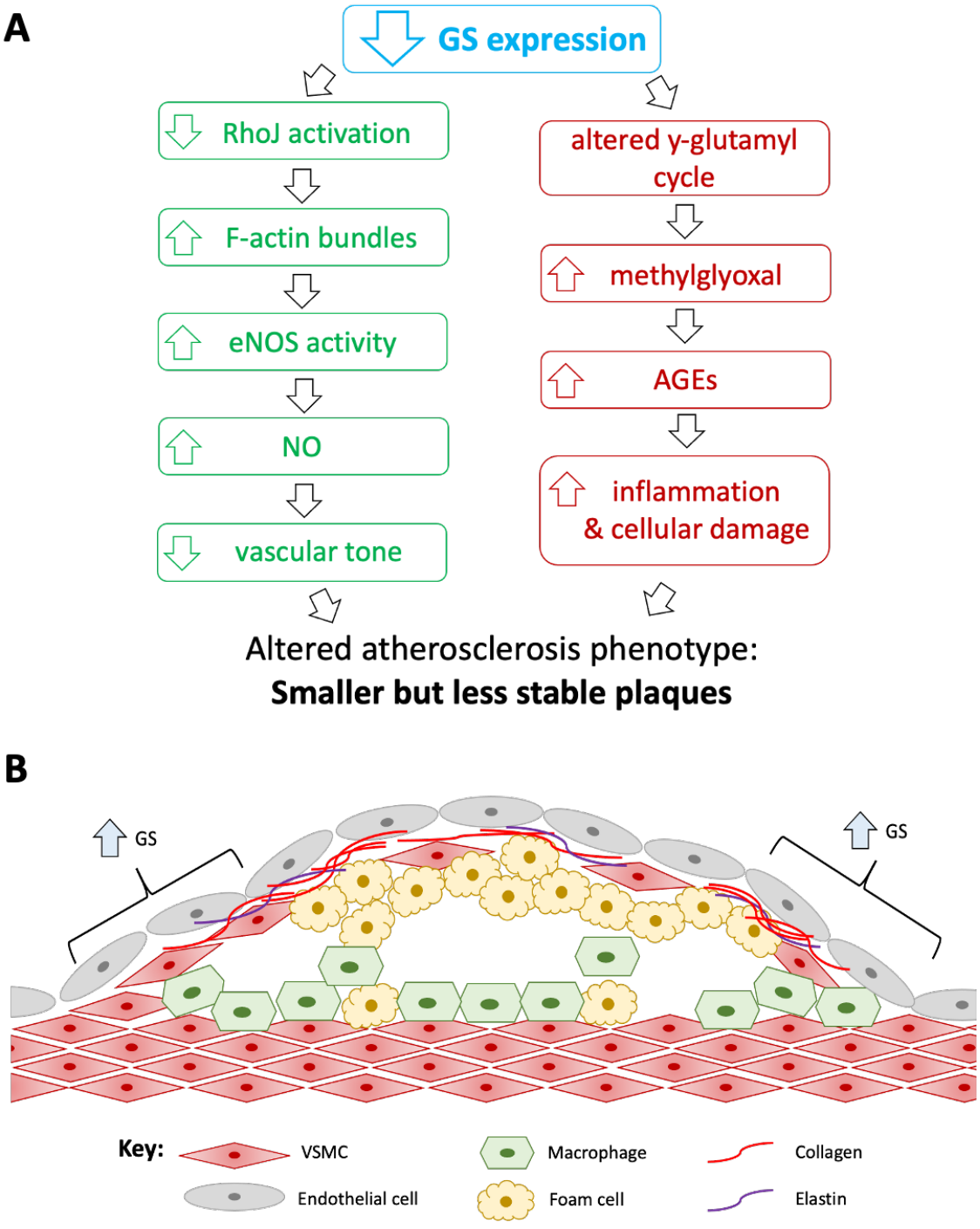

Figure 45: Summary diagram of the proposed effects of reduced GS expression
The flowchart represents two mechanisms likely to contribute towards changes in vascular function and atherogenesis [**A**]. The atherosclerotic plaque schematic indicates a number of features of these plaques identified as unique to the reduced GS genotype. This includes large acellular regions relative to the size of the plaque, shoulder regions which have increased GS expression, an irregular border, a thin, weak, and fractured fibrous cap containing a higher ratio of collagen to elastin, and a high proportion of lipid-laden cells, which are most likely to be foam cells, within the cap region of the plaque [**B**]

References

1. World Health Organization. Fact sheets: Cardiovascular diseases (CVDs). *World Health Organization* (2017). Available at: https://www.who.int/en/news-room/fact-sheets/detail/cardiovascular-diseases-(cvds). (Accessed: 14th December 2020)

2. British Heart Foundation. *UK Cardiovascular Disease Factsheet*. *British Heart Foundation* (2020).

3. Insull, W. The pathology of atherosclerosis: plaque development and plaque responses to medical treatment. *Am. J. Med.* **122**, S3–S14 (2009).

4. Hubert, H. B., Feinleib, M., McNamara, P. M. & Castelli, W. P. Obesity as an independent risk factor for cardiovascular disease: a 26-year follow-up of participants in the Framingham Heart Study. *Circulation* **67**, 968–77 (1983).

5. Mercer, B. N., Morais, S., Cubbon, R. M. & Kearney, M. T. Diabetes mellitus and the heart. *Int. J. Clin. Pract.* **66**, 640–647 (2012).

6. Almdal, T., Scharling, H., Jensen, J. S. & Vestergaard, H. The Independent Effect of Type 2 Diabetes Mellitus on Ischemic Heart Disease, Stroke, and Death. *Arch. Intern. Med.* **164**, 1422 (2004).

7. Booth, G. L., Kapral, M. K., Fung, K. & Tu, J. V. Relation between age and cardiovascular disease in men and women with diabetes compared with non-diabetic people: a population-based retrospective cohort study. *Lancet* **368**, 29–36 (2006).

8. Weycker, D. *et al.* Risk-Factor Clustering and Cardiovascular Disease Risk in Hypertensive Patients. *Am. J. Hypertens.* **20**, 599–607 (2007).

9. Qi, L. *et al.* Association between a genetic variant related to glutamic acid metabolism and coronary heart disease in individuals with type 2 diabetes. *JAMA - J. Am. Med. Assoc.* **310**, 821–828 (2013).

10. Eckel, R. H., Alberti, K., Grundy, S. M. & Zimmet, P. Z. The metabolic syndrome. *Lancet* **375**, 181–183 (2010).

11. Tennant, M. & McGeachie, J. K. BLOOD VESSEL STRUCTURE AND FUNCTION: A BRIEF UPDATE ON RECENT ADVANCES. *Aust. N. Z. J. Surg.* **60**, 747–753 (1990).

12. Sandoo, A., Veldhuijzen van Zanten, J. J. C. S., Metsios, G. S., Carroll, D. & Kitas, G. D. The Endothelium and Its Role in Regulating Vascular Tone. *Open*

Cardiovasc. Med. J. **4**, 302–312 (2015).

13. Boulanger, C. M. Endothelium. *Arterioscler. Thromb. Vasc. Biol.* **36**, (2016).

14. Augustin, H. G. & Koh, G. Y. Organotypic vasculature: From descriptive heterogeneity to functional pathophysiology. *Science (80-.).* **357**, eaal2379 (2017).

15. Mayers, J. R. & Vander Heiden, M. G. Famine versus feast: understanding the metabolism of tumors in vivo. *Trends Biochem. Sci.* **40**, 130–140 (2015).

16. Van Geemen, D. *et al.* F-actin-anchored focal adhesions distinguish endothelial phenotypes of human arteries and veins. *Arterioscler. Thromb. Vasc. Biol.* **34**, 2059–2067 (2014).

17. Schaum, N. *et al.* Single-cell transcriptomics of 20 mouse organs creates a Tabula Muris. *Nature* **562**, 367–372 (2018).

18. Kalucka, J. *et al.* Single-Cell Transcriptome Atlas of Murine Endothelial Cells. *Cell* **180**, 764-779.e20 (2020).

19. Paik, D. T. *et al.* Single-Cell RNA Sequencing Unveils Unique Transcriptomic Signatures of Organ-Specific Endothelial Cells. *Circulation* **142**, 1848–1862 (2020).

20. Kalluri, A. S. *et al.* Single-Cell Analysis of the Normal Mouse Aorta Reveals Functionally Distinct Endothelial Cell Populations. *Circulation* **140**, 147–163 (2019).

21. Han, X. *et al.* Construction of a human cell landscape at single-cell level. *Nature* **581**, 303–309 (2020).

22. He, S. *et al.* Single-cell transcriptome profiling of an adult human cell atlas of 15 major organs. *Genome Biol.* **21**, 294 (2020).

23. Vanhoutte, P. M., Zhao, Y., Xu, A. & Leung, S. W. S. Thirty Years of Saying NO. *Circ. Res.* **119**, 375–396 (2016).

24. Vanhoutte, P. M., Shimokawa, H., Feletou, M. & Tang, E. H. C. Endothelial dysfunction and vascular disease – a 30th anniversary update. *Acta Physiol.* **219**, 22–96 (2017).

25. Alderton, W. K., Cooper, C. E. & Knowles, R. G. *Nitric oxide synthases : structure, function and inhibition*. *Biochem. J* **357**, (2001).

26. WU, K. K. Regulation of Endothelial Nitric Oxide Synthase Activity and Gene Expression. *Ann. N. Y. Acad. Sci.* **962**, 122–130 (2002).

27. Feron, O. & Balligand, J. L. Caveolins and the regulation of endothelial nitric oxide synthase in the heart. *Cardiovascular Research* **69**, 788–797 (2006).

28. Kolluru, G. K., Siamwala, J. H. & Chatterjee, S. ENOS phosphorylation in health and disease. *Biochimie* **92**, 1186–1198 (2010).

29. Wheatcroft, S. B. *et al.* Preserved glucoregulation but attenuation of the vascular actions of insulin in mice heterozygous for knockout of the insulin receptor. *Diabetes* **53**, 2645–52 (2004).

30. Kondrikov, D. *et al.* β-actin association with endothelial nitric-oxide synthase modulates nitric oxide and superoxide generation from the enzyme. *J. Biol. Chem.* **285**, 4319–4327 (2010).

31. Xu, S. & Touyz, R. M. Reactive oxygen species and vascular remodelling in hypertension: Still alive. *Canadian Journal of Cardiology* **22**, 947–951 (2006).

32. Kondrikov, D., Elms, S., Fulton, D. & Su, Y. eNOS-β-actin interaction contributes to increased peroxynitrite formation during hyperoxia in pulmonary artery endothelial cells and mouse lungs. *J. Biol. Chem.* **285**, 35479–35487 (2010).

33. Vergnani, L. *et al.* Effect of Native and Oxidized Low-Density Lipoprotein on Endothelial Nitric Oxide and Superoxide Production. *Circulation* **101**, 1261–1266 (2000).

34. Su, Y., Edwards-Bennett, S., Bubb, M. R. & Block, E. R. Regulation of endothelial nitric oxide synthase by the actin cytoskeleton. *Am. J. Physiol. - Cell Physiol.* **284**, (2003).

35. Su, Y., Kondrikov, D. & Block, E. R. Cytoskeletal regulation of nitric oxide synthase. *Cell Biochemistry and Biophysics* **43**, 439–449 (2005).

36. Pircher, A., Treps, L., Bodrug, N. & Carmeliet, P. Endothelial cell metabolism: A novel player in atherosclerosis? Basic principles and therapeutic opportunities. *Atherosclerosis* **253**, 247–257 (2016).

37. Gage, M. C. *et al.* Endothelium-specific insulin resistance leads to accelerated atherosclerosis in areas with disturbed flow patterns: A role for reactive oxygen species. *Atherosclerosis* **230**, 131–139 (2013).

38. Thum, T. *et al.* Endothelial nitric oxide synthase uncoupling impairs endothelial progenitor cell mobilization and function in diabetes. *Diabetes* **56**, 666–674 (2007).

39. Gisterå, A. & Hansson, G. K. The immunology of atherosclerosis. *Nature Reviews Nephrology* **13**, 368–380 (2017).

40. Gimbrone, M. A. & García-Cardeña, G. Endothelial Cell Dysfunction and the Pathobiology of Atherosclerosis. *Circ. Res.* **118**, 620–36 (2016).

41. Cersosimo, E. & DeFronzo, R. A. Insulin resistance and endothelial dysfunction: the road map to cardiovascular diseases. *Diabetes. Metab. Res. Rev.* **22**, 423–436 (2006).

42. Kattoor, A. J., Pothineni, N. V. K., Palagiri, D. & Mehta, J. L. Oxidative Stress in Atherosclerosis. *Current Atherosclerosis Reports* **19**, 1–11 (2017).

43. Tabas, I. & Bornfeldt, K. E. Macrophage Phenotype and Function in Different Stages of Atherosclerosis. *Circ. Res.* **118**, 653–667 (2016).

44. Palmieri, E. M. *et al.* Pharmacologic or Genetic Targeting of Glutamine Synthetase Skews Macrophages toward an M1-like Phenotype and Inhibits Tumor Metastasis. *Cell Rep.* **20**, 1654–1666 (2017).

45. Martinez, F. O. & Gordon, S. The M1 and M2 paradigm of macrophage activation: time for reassessment. *F1000Prime Rep.* **6**, (2014).

46. Cochain, C. *et al.* Single-cell RNA-seq reveals the transcriptional landscape and heterogeneity of aortic macrophages in murine atherosclerosis. *Circ. Res.* **122**, 1661–1674 (2018).

47. Kim, K. *et al.* Transcriptome analysis reveals nonfoamy rather than foamy plaque macrophages are proinflammatory in atherosclerotic murine models. *Circ. Res.* **123**, 1127–1142 (2018).

48. Depuydt, M. A. C. *et al.* Microanatomy of the Human Atherosclerotic Plaque by Single-Cell Transcriptomics. *Circ. Res.* **127**, 1437–1455 (2020).

49. Tabas, I., Tall, A. & Accili, D. The Impact of Macrophage Insulin Resistance on Advanced Atherosclerotic Plaque Progression. *Circ. Res.* **106**, 58–67 (2010).

50. Krettek, A., Sukhova, G. K. & Libby, P. Elastogenesis in human arterial disease: A role for macrophages in disordered elastin synthesis. *Arterioscler. Thromb. Vasc. Biol.* **23**, 582–587 (2003).

51. Katsuda, S. *et al. Collagens in Human Atherosclerosis Immunohistochemical Analysis Using Collagen Type-Specific Antibodies*. (1992).

52. Douglas, G. R. *et al.* Impact of Fiber Structure on the Material Stability and Rupture Mechanisms of Coronary Atherosclerotic Plaques. *Ann. Biomed. Eng.* **45**, 1462–1474 (2017).

53. Pasterkamp, G., Galis, Z. S. & de Kleijn, D. P. V. Expansive Arterial Remodeling: Location, Location, Location. *Arterioscler. Thromb. Vasc. Biol.* **24**,

650–657 (2004).

54. Alexopoulos, N. & Raggi, P. Calcification in atherosclerosis. *Nature Reviews Cardiology* **6**, 681–688 (2009).

55. Van der Donckt, C. *et al.* Elastin fragmentation in atherosclerotic mice leads to intraplaque neovascularization, plaque rupture, myocardial infarction, stroke, and sudden death. *Eur. Heart J.* **36**, 1049–1058 (2015).

56. Costopoulos, C. *et al.* Plaque Rupture in Coronary Atherosclerosis Is Associated With Increased Plaque Structural Stress. *JACC Cardiovasc. Imaging* **10**, 1472–1483 (2017).

57. Saksi, J. *et al.* Gene expression differences between stroke-associated and asymptomatic carotid plaques. *J. Mol. Med.* **89**, 1015–1026 (2011).

58. Wang, H., Liu, D. & Zhang, H. Investigation of the Underlying Genes and Mechanism of Macrophage-Enriched Ruptured Atherosclerotic Plaques Using Bioinformatics Method. *J. Atheroscler. Thromb.* **26**, 636–658 (2019).

59. Perisic, L. *et al.* Profiling of atherosclerotic lesions by gene and tissue microarrays reveals pcsk6 as a novel protease in unstable carotid atherosclerosis. *Arterioscler. Thromb. Vasc. Biol.* **33**, 2432–2443 (2013).

60. Lee, H.-W. *et al.* Proximal tubule-specific glutamine synthetase deletion alters basal and acidosis-stimulated ammonia metabolism. *Am. J. Physiol. Physiol.* **310**, F1229–F1242 (2016).

61. He, Y. *et al.* Glutamine synthetase deficiency in murine astrocytes results in neonatal death. *Glia* **58**, 741–754 (2010).

62. Qvartskhava, N. *et al.* Hyperammonemia in gene-targeted mice lacking functional hepatic glutamine synthetase. *Proc. Natl. Acad. Sci.* **112**, 5521–5526 (2015).

63. Brosnan, M. E. & Brosnan, J. T. Hepatic glutamate metabolism: a tale of 2 hepatocytes. *Am. J. Clin. Nutr.* **90**, 857S-861S (2009).

64. Eelen, G. *et al.* Role of glutamine synthetase in angiogenesis beyond glutamine synthesis. *Nature* **561**, 63–69 (2018).

65. Kim, B., Li, J., Jang, C. & Arany, Z. Glutamine fuels proliferation but not migration of endothelial cells. *EMBO J.* **36**, 2321–2333 (2017).

66. Tomlinson, C., Rafii, M., Ball, R. O. & Pencharz, P. Arginine synthesis from enteral glutamine in healthy adults in the fed state. *Am. J. Physiol. Metab.* **301**, E267–E273 (2011).

67. Huang, H. *et al.* Role of glutamine and interlinked asparagine metabolism in vessel formation. *EMBO J.* **36**, 2334–2352 (2017).

68. Fu, S. *et al.* Glutamine Synthetase Promotes Radiation Resistance via Facilitating Nucleotide Metabolism and Subsequent DNA Damage Repair. *Cell Rep.* **28**, 1136-1143.e4 (2019).

69. The Look AHEAD Research Group. Prospective association of GLUL rs10911021 with cardiovascular morbidity and mortality among individuals with type 2 diabetes: The Look AHEAD Study. *Diabetes* db150890 (2015). doi:10.2337/db15-0890

70. Beaney, K. E. *et al.* Variant rs10911021 that associates with coronary heart disease in type 2 diabetes, is associated with lower concentrations of circulating HDL cholesterol and large HDL particles but not with amino acids. *Cardiovasc. Diabetol.* **15**, 115 (2016).

71. Wilson, P. W. F., Abbott, R. D. & Castelli, W. P. High density lipoprotein cholesterol and mortality. The Framingham heart study. *Arteriosclerosis* **8**, 737–741 (1988).

72. Pipino, C. *et al.* Association of the 1q25 diabetes-specific coronary heart disease locus with alterations of the γ-glutamyl cycle and increased methylglyoxal levels in endothelial cells. *Diabetes* **69**, 2206–2216 (2020).

73. Kilhovd, B. K. *et al.* Increased serum levels of methylglyoxal-derived hydroimidazolone-AGE are associated with increased cardiovascular disease mortality in nondiabetic women. *Atherosclerosis* **205**, 590–594 (2009).

74. Hanssen, N. M. J. *et al.* Higher plasma methylglyoxal levels are associated with incident cardiovascular disease and mortality in individuals with type 2 diabetes. *Diabetes Care* **41**, 1689–1695 (2018).

75. Hall, A. Rho GTPases and the Actin Cytoskeleton. *Science (80-.).* **279**, 509–514 (1998).

76. Yuan, L. *et al.* RhoJ is an endothelial cell-restricted Rho GTPase that mediates vascular morphogenesis and is regulated by the transcription factor ERG. *Blood* **118**, 1145–1153 (2011).

77. Kaur, S. *et al.* RhoJ/TCL regulates endothelial motility and tube formation and modulates actomyosin contractility and focal adhesion numbers. *Arterioscler. Thromb. Vasc. Biol.* **31**, 657–664 (2011).

78. Rohlenova, K. *et al.* Single-Cell RNA Sequencing Maps Endothelial Metabolic Plasticity in Pathological Angiogenesis. *Cell Metab.* **31**, 862-877.e14 (2020).

79. Dumas, S. J., García-Caballero, M. & Carmeliet, P. Metabolic Signatures of Distinct Endothelial Phenotypes. *Trends in Endocrinology and Metabolism* **31**, 580–595 (2020).

80. He, Y., Hakvoort, T. B. M., Vermeulen, J. L. M., Lamers, W. H. & Van Roon, M. A. Glutamine synthetase is essential in early mouse embryogenesis. *Dev. Dyn.* **236**, 1865–1875 (2007).

81. Refsnes Data. Colors: RGB Calculator (w3schools.com). *w3schools.com - Colors: RGB Calculator* Available at: https://www.w3schools.com/colors/colors_rgb.asp.

82. Ellis, R. IHC World: Miller's Elastic Staining Protocol. *IHC World* Available at: https://www.ihcworld.com/_protocols/special_stains/miller's_elastic_ellis.htm.

83. Ellis, R. IHC World: van Gieson Staining Protocol. *IHC World* Available at: http://www.ihcworld.com/_protocols/special_stains/van_gieson_ellis.htm.

84. Percival, K. & Radi, Z. Comparison of five elastin histochemical stains to identify pulmonary small vasculature. *J. Histotechnol.* **40**, 73–78 (2017).

85. Coelho, P. G. B., Souza, M. V. de, Conceição, L. G., Viloria, M. I. V. & Bedoya, S. A. O. Evaluation of dermal collagen stained with picrosirius red and examined under polarized light microscopy. *An. Bras. Dermatol.* **93**, 415–418 (2018).

86. Vogel, B., Siebert, H., Hofmann, U. & Frantz, S. Determination of collagen content within picrosirius red stained paraffin-embedded tissue sections using fluorescence microscopy. *MethodsX* **2**, 124–134 (2015).

87. Winkels, H. *et al.* Atlas of the immune cell repertoire in mouse atherosclerosis defined by single-cell RNA-sequencing and mass cytometry. *Circ. Res.* **122**, 1675–1688 (2018).

88. Ploeger, D. T. *et al.* Cell plasticity in wound healing: Paracrine factors of M1/ M2 polarized macrophages influence the phenotypical state of dermal fibroblasts. *Cell Commun. Signal.* **11**, 29 (2013).

89. Bennett, M. R., Sinha, S. & Owens, G. K. Vascular Smooth Muscle Cells in Atherosclerosis. *Circ. Res.* **118**, 692–702 (2016).

90. Gericke, A. *et al.* Functional Role of α 1 -Adrenoceptor Subtypes in Murine Ophthalmic Arteries. *Investig. Opthalmology Vis. Sci.* **52**, 4795 (2011).

91. Brinton, M., Mandel, Y., Schachar, I. & Palanker, D. Mechanisms of electrical vasoconstriction. *J. Neuroeng. Rehabil.* **15**, 43 (2018).

92. De Moudt, S., Leloup, A., Van Hove, C., De Meyer, G. & Fransen, P. Isometric

Stretch Alters Vascular Reactivity of Mouse Aortic Segments. *Front. Physiol.* **8**, 157 (2017).

93. Franchi-Micheli, S. *et al.* Mechanical stretch reveals different components of endothelial-mediated vascular tone in rat aortic strips. *Br. J. Pharmacol.* **131**, 1355–62 (2000).

94. Vandamme, T. F. Use of rodents as models of human diseases. *J. Pharm. Bioallied Sci.* **6**, 2–9 (2014).

95. Getz, G. S. & Reardon, C. A. Animal models of atherosclerosis. *Arterioscler. Thromb. Vasc. Biol.* **32**, 1104–15 (2012).

96. Emini Veseli, B. *et al.* Animal models of atherosclerosis. *Eur. J. Pharmacol.* **816**, 3–13 (2017).

97. Johnson, J. L. & Jackson, C. L. Atherosclerotic plaque rupture in the apolipoprotein E knockout mouse. *Atherosclerosis* **154**, 399–406 (2001).

98. Schwartz, S. M., Galis, Z. S., Rosenfeld, M. E. & Falk, E. Plaque Rupture in Humans and Mice. *Arterioscler. Thromb. Vasc. Biol.* **27**, 705–713 (2007).

99. Pounds, L. C. Carotid Endarterectomy | Society for Vascular Surgery. *Society for Vascular Surgery* Available at: https://vascular.org/patient-resources/vascular-treatments/carotid-endarterectomy. (Accessed: 30th March 2021)

100. MacKenzie, A. & Wadsworth, R. M. Extracellular L-arginine is required for optimal NO synthesis by eNOS and iNOS in the rat mesenteric artery wall. *Br. J. Pharmacol.* **139**, 1487–97 (2003).

101. Song, J. *et al.* Glutathione protects brain endothelial cells from hydrogen peroxide-induced oxidative stress by increasing nrf2 expression. *Exp. Neurobiol.* **23**, 93–103 (2014).

102. CAI, H. Hydrogen peroxide regulation of endothelial function: Origins, mechanisms, and consequences. *Cardiovasc. Res.* **68**, 26–36 (2005).

103. Bretón-Romero, R. & Lamas, S. Hydrogen peroxide signaling in vascular endothelial cells. *Redox Biol.* **2**, 529–534 (2014).

104. Martinez-Lemus, L. A. The dynamic structure of arterioles. *Basic Clin. Pharmacol. Toxicol.* **110**, 5–11 (2012).

105. Jadeja, R. N., Rachakonda, V., Bagi, Z. & Khurana, S. Assessing Myogenic Response and Vasoactivity In Resistance Mesenteric Arteries Using Pressure Myography. *J. Vis. Exp.* e50997 (2015). doi:10.3791/50997

106. Fernandez, D. M. *et al.* Single-cell immune landscape of human atherosclerotic

plaques. *Nat. Med.* **25**, 1576–1588 (2019).

107. Dobnikar, L. *et al.* Disease-relevant transcriptional signatures identified in individual smooth muscle cells from healthy mouse vessels. *Nat. Commun.* **9**, 1–17 (2018).

108. Düzen, I. *et al.* Investigation of leukocyte RHO/ROCK gene expressions in patients with non-valvular atrial fibrillation. *Exp. Ther. Med.* (2019). doi:10.3892/etm.2019.7929

109. Afewerki, T., Ahmed, S. & Warren, D. Emerging regulators of vascular smooth muscle cell migration. *J. Muscle Res. Cell Motil.* **40**, 185–196 (2019).

110. Cubbon, R. M. *et al.* Temporal trends in mortality of patients with diabetes mellitus suffering acute myocardial infarction: a comparison of over 3000 patients between 1995 and 2003. *Eur. Heart J.* **28**, 540–545 (2006).

111. Chatterjee, S., Khunti, K. & Davies, M. J. Type 2 diabetes. *Lancet* **389**, 2239–2251 (2017).

112. World Health Organisation. *GLOBAL REPORT ON DIABETES*. (World Health Organisation, 2016).

113. Kleinert, M. *et al.* Animal models of obesity and diabetes mellitus. *Nat. Rev. Endocrinol.* **14**, 140–162 (2018).

114. King, A. J. The use of animal models in diabetes research. *Br. J. Pharmacol.* **166**, 877–894 (2012).

1. World Health Organization. Fact sheets: Cardiovascular diseases (CVDs). *World Health Organization* (2017). Available at: https://www.who.int/en/news-room/fact-sheets/detail/cardiovascular-diseases-(cvds). (Accessed: 14th December 2020)

2. British Heart Foundation. *UK Cardiovascular Disease Factsheet*. *British Heart Foundation* (2020).

3. Insull, W. The pathology of atherosclerosis: plaque development and plaque responses to medical treatment. *Am. J. Med.* **122**, S3–S14 (2009).

4. Hubert, H. B., Feinleib, M., McNamara, P. M. & Castelli, W. P. Obesity as an independent risk factor for cardiovascular disease: a 26-year follow-up of participants in the Framingham Heart Study. *Circulation* **67**, 968–77 (1983).

5. Mercer, B. N., Morais, S., Cubbon, R. M. & Kearney, M. T. Diabetes mellitus and the heart. *Int. J. Clin. Pract.* **66**, 640–647 (2012).

6. Almdal, T., Scharling, H., Jensen, J. S. & Vestergaard, H. The Independent

Effect of Type 2 Diabetes Mellitus on Ischemic Heart Disease, Stroke, and Death. *Arch. Intern. Med.* **164**, 1422 (2004).

7. Booth, G. L., Kapral, M. K., Fung, K. & Tu, J. V. Relation between age and cardiovascular disease in men and women with diabetes compared with non-diabetic people: a population-based retrospective cohort study. *Lancet* **368**, 29–36 (2006).

8. Weycker, D. *et al.* Risk-Factor Clustering and Cardiovascular Disease Risk in Hypertensive Patients. *Am. J. Hypertens.* **20**, 599–607 (2007).

9. Qi, L. *et al.* Association between a genetic variant related to glutamic acid metabolism and coronary heart disease in individuals with type 2 diabetes. *JAMA - J. Am. Med. Assoc.* **310**, 821–828 (2013).

10. Eckel, R. H., Alberti, K., Grundy, S. M. & Zimmet, P. Z. The metabolic syndrome. *Lancet* **375**, 181–183 (2010).

11. Tennant, M. & McGeachie, J. K. BLOOD VESSEL STRUCTURE AND FUNCTION: A BRIEF UPDATE ON RECENT ADVANCES. *Aust. N. Z. J. Surg.* **60**, 747–753 (1990).

12. Sandoo, A., Veldhuijzen van Zanten, J. J. C. S., Metsios, G. S., Carroll, D. & Kitas, G. D. The Endothelium and Its Role in Regulating Vascular Tone. *Open Cardiovasc. Med. J.* **4**, 302–312 (2015).

13. Boulanger, C. M. Endothelium. *Arterioscler. Thromb. Vasc. Biol.* **36**, (2016).

14. Augustin, H. G. & Koh, G. Y. Organotypic vasculature: From descriptive heterogeneity to functional pathophysiology. *Science (80-.).* **357**, eaal2379 (2017).

15. Mayers, J. R. & Vander Heiden, M. G. Famine versus feast: understanding the metabolism of tumors in vivo. *Trends Biochem. Sci.* **40**, 130–140 (2015).

16. Van Geemen, D. *et al.* F-actin-anchored focal adhesions distinguish endothelial phenotypes of human arteries and veins. *Arterioscler. Thromb. Vasc. Biol.* **34**, 2059–2067 (2014).

17. Schaum, N. *et al.* Single-cell transcriptomics of 20 mouse organs creates a Tabula Muris. *Nature* **562**, 367–372 (2018).

18. Kalucka, J. *et al.* Single-Cell Transcriptome Atlas of Murine Endothelial Cells. *Cell* **180**, 764-779.e20 (2020).

19. Paik, D. T. *et al.* Single-Cell RNA Sequencing Unveils Unique Transcriptomic Signatures of Organ-Specific Endothelial Cells. *Circulation* **142**, 1848–1862

(2020).

20. Kalluri, A. S. *et al.* Single-Cell Analysis of the Normal Mouse Aorta Reveals Functionally Distinct Endothelial Cell Populations. *Circulation* **140**, 147–163 (2019).

21. Han, X. *et al.* Construction of a human cell landscape at single-cell level. *Nature* **581**, 303–309 (2020).

22. He, S. *et al.* Single-cell transcriptome profiling of an adult human cell atlas of 15 major organs. *Genome Biol.* **21**, 294 (2020).

23. Vanhoutte, P. M., Zhao, Y., Xu, A. & Leung, S. W. S. Thirty Years of Saying NO. *Circ. Res.* **119**, 375–396 (2016).

24. Vanhoutte, P. M., Shimokawa, H., Feletou, M. & Tang, E. H. C. Endothelial dysfunction and vascular disease – a 30th anniversary update. *Acta Physiol.* **219**, 22–96 (2017).

25. Alderton, W. K., Cooper, C. E. & Knowles, R. G. *Nitric oxide synthases : structure, function and inhibition*. *Biochem. J* **357**, (2001).

26. WU, K. K. Regulation of Endothelial Nitric Oxide Synthase Activity and Gene Expression. *Ann. N. Y. Acad. Sci.* **962**, 122–130 (2002).

27. Feron, O. & Balligand, J. L. Caveolins and the regulation of endothelial nitric oxide synthase in the heart. *Cardiovascular Research* **69**, 788–797 (2006).

28. Kolluru, G. K., Siamwala, J. H. & Chatterjee, S. ENOS phosphorylation in health and disease. *Biochimie* **92**, 1186–1198 (2010).

29. Wheatcroft, S. B. *et al.* Preserved glucoregulation but attenuation of the vascular actions of insulin in mice heterozygous for knockout of the insulin receptor. *Diabetes* **53**, 2645–52 (2004).

30. Kondrikov, D. *et al.* β-actin association with endothelial nitric-oxide synthase modulates nitric oxide and superoxide generation from the enzyme. *J. Biol. Chem.* **285**, 4319–4327 (2010).

31. Xu, S. & Touyz, R. M. Reactive oxygen species and vascular remodelling in hypertension: Still alive. *Canadian Journal of Cardiology* **22**, 947–951 (2006).

32. Kondrikov, D., Elms, S., Fulton, D. & Su, Y. eNOS-β-actin interaction contributes to increased peroxynitrite formation during hyperoxia in pulmonary artery endothelial cells and mouse lungs. *J. Biol. Chem.* **285**, 35479–35487 (2010).

33. Vergnani, L. *et al.* Effect of Native and Oxidized Low-Density Lipoprotein on Endothelial Nitric Oxide and Superoxide Production. *Circulation* **101**, 1261–1266

(2000).

34. Su, Y., Edwards-Bennett, S., Bubb, M. R. & Block, E. R. Regulation of endothelial nitric oxide synthase by the actin cytoskeleton. *Am. J. Physiol. - Cell Physiol.* **284**, (2003).

35. Su, Y., Kondrikov, D. & Block, E. R. Cytoskeletal regulation of nitric oxide synthase. *Cell Biochemistry and Biophysics* **43**, 439–449 (2005).

36. Pircher, A., Treps, L., Bodrug, N. & Carmeliet, P. Endothelial cell metabolism: A novel player in atherosclerosis? Basic principles and therapeutic opportunities. *Atherosclerosis* **253**, 247–257 (2016).

37. Gage, M. C. *et al.* Endothelium-specific insulin resistance leads to accelerated atherosclerosis in areas with disturbed flow patterns: A role for reactive oxygen species. *Atherosclerosis* **230**, 131–139 (2013).

38. Thum, T. *et al.* Endothelial nitric oxide synthase uncoupling impairs endothelial progenitor cell mobilization and function in diabetes. *Diabetes* **56**, 666–674 (2007).

39. Gisterå, A. & Hansson, G. K. The immunology of atherosclerosis. *Nature Reviews Nephrology* **13**, 368–380 (2017).

40. Gimbrone, M. A. & García-Cardeña, G. Endothelial Cell Dysfunction and the Pathobiology of Atherosclerosis. *Circ. Res.* **118**, 620–36 (2016).

41. Cersosimo, E. & DeFronzo, R. A. Insulin resistance and endothelial dysfunction: the road map to cardiovascular diseases. *Diabetes. Metab. Res. Rev.* **22**, 423–436 (2006).

42. Kattoor, A. J., Pothineni, N. V. K., Palagiri, D. & Mehta, J. L. Oxidative Stress in Atherosclerosis. *Current Atherosclerosis Reports* **19**, 1–11 (2017).

43. Tabas, I. & Bornfeldt, K. E. Macrophage Phenotype and Function in Different Stages of Atherosclerosis. *Circ. Res.* **118**, 653–667 (2016).

44. Palmieri, E. M. *et al.* Pharmacologic or Genetic Targeting of Glutamine Synthetase Skews Macrophages toward an M1-like Phenotype and Inhibits Tumor Metastasis. *Cell Rep.* **20**, 1654–1666 (2017).

45. Martinez, F. O. & Gordon, S. The M1 and M2 paradigm of macrophage activation: time for reassessment. *F1000Prime Rep.* **6**, (2014).

46. Cochain, C. *et al.* Single-cell RNA-seq reveals the transcriptional landscape and heterogeneity of aortic macrophages in murine atherosclerosis. *Circ. Res.* **122**, 1661–1674 (2018).

47. Kim, K. *et al.* Transcriptome analysis reveals nonfoamy rather than foamy plaque macrophages are proinflammatory in atherosclerotic murine models. *Circ. Res.* **123**, 1127–1142 (2018).

48. Depuydt, M. A. C. *et al.* Microanatomy of the Human Atherosclerotic Plaque by Single-Cell Transcriptomics. *Circ. Res.* **127**, 1437–1455 (2020).

49. Tabas, I., Tall, A. & Accili, D. The Impact of Macrophage Insulin Resistance on Advanced Atherosclerotic Plaque Progression. *Circ. Res.* **106**, 58–67 (2010).

50. Krettek, A., Sukhova, G. K. & Libby, P. Elastogenesis in human arterial disease: A role for macrophages in disordered elastin synthesis. *Arterioscler. Thromb. Vasc. Biol.* **23**, 582–587 (2003).

51. Katsuda, S. *et al. Collagens in Human Atherosclerosis Immunohistochemical Analysis Using Collagen Type-Specific Antibodies*. (1992).

52. Douglas, G. R. *et al.* Impact of Fiber Structure on the Material Stability and Rupture Mechanisms of Coronary Atherosclerotic Plaques. *Ann. Biomed. Eng.* **45**, 1462–1474 (2017).

53. Pasterkamp, G., Galis, Z. S. & de Kleijn, D. P. V. Expansive Arterial Remodeling: Location, Location, Location. *Arterioscler. Thromb. Vasc. Biol.* **24**, 650–657 (2004).

54. Alexopoulos, N. & Raggi, P. Calcification in atherosclerosis. *Nature Reviews Cardiology* **6**, 681–688 (2009).

55. Van der Donckt, C. *et al.* Elastin fragmentation in atherosclerotic mice leads to intraplaque neovascularization, plaque rupture, myocardial infarction, stroke, and sudden death. *Eur. Heart J.* **36**, 1049–1058 (2015).

56. Costopoulos, C. *et al.* Plaque Rupture in Coronary Atherosclerosis Is Associated With Increased Plaque Structural Stress. *JACC Cardiovasc. Imaging* **10**, 1472–1483 (2017).

57. Saksi, J. *et al.* Gene expression differences between stroke-associated and asymptomatic carotid plaques. *J. Mol. Med.* **89**, 1015–1026 (2011).

58. Wang, H., Liu, D. & Zhang, H. Investigation of the Underlying Genes and Mechanism of Macrophage-Enriched Ruptured Atherosclerotic Plaques Using Bioinformatics Method. *J. Atheroscler. Thromb.* **26**, 636–658 (2019).

59. Perisic, L. *et al.* Profiling of atherosclerotic lesions by gene and tissue microarrays reveals pcsk6 as a novel protease in unstable carotid atherosclerosis. *Arterioscler. Thromb. Vasc. Biol.* **33**, 2432–2443 (2013).

60. Lee, H.-W. *et al.* Proximal tubule-specific glutamine synthetase deletion alters basal and acidosis-stimulated ammonia metabolism. *Am. J. Physiol. Physiol.* **310**, F1229–F1242 (2016).

61. He, Y. *et al.* Glutamine synthetase deficiency in murine astrocytes results in neonatal death. *Glia* **58**, 741–754 (2010).

62. Qvartskhava, N. *et al.* Hyperammonemia in gene-targeted mice lacking functional hepatic glutamine synthetase. *Proc. Natl. Acad. Sci.* **112**, 5521–5526 (2015).

63. Brosnan, M. E. & Brosnan, J. T. Hepatic glutamate metabolism: a tale of 2 hepatocytes. *Am. J. Clin. Nutr.* **90**, 857S-861S (2009).

64. Eelen, G. *et al.* Role of glutamine synthetase in angiogenesis beyond glutamine synthesis. *Nature* **561**, 63–69 (2018).

65. Kim, B., Li, J., Jang, C. & Arany, Z. Glutamine fuels proliferation but not migration of endothelial cells. *EMBO J.* **36**, 2321–2333 (2017).

66. Tomlinson, C., Rafii, M., Ball, R. O. & Pencharz, P. Arginine synthesis from enteral glutamine in healthy adults in the fed state. *Am. J. Physiol. Metab.* **301**, E267–E273 (2011).

67. Huang, H. *et al.* Role of glutamine and interlinked asparagine metabolism in vessel formation. *EMBO J.* **36**, 2334–2352 (2017).

68. Fu, S. *et al.* Glutamine Synthetase Promotes Radiation Resistance via Facilitating Nucleotide Metabolism and Subsequent DNA Damage Repair. *Cell Rep.* **28**, 1136-1143.e4 (2019).

69. The Look AHEAD Research Group. Prospective association of GLUL rs10911021 with cardiovascular morbidity and mortality among individuals with type 2 diabetes: The Look AHEAD Study. *Diabetes* db150890 (2015). doi:10.2337/db15-0890

70. Beaney, K. E. *et al.* Variant rs10911021 that associates with coronary heart disease in type 2 diabetes, is associated with lower concentrations of circulating HDL cholesterol and large HDL particles but not with amino acids. *Cardiovasc. Diabetol.* **15**, 115 (2016).

71. Wilson, P. W. F., Abbott, R. D. & Castelli, W. P. High density lipoprotein cholesterol and mortality. The Framingham heart study. *Arteriosclerosis* **8**, 737–741 (1988).

72. Pipino, C. *et al.* Association of the 1q25 diabetes-specific coronary heart disease

locus with alterations of the γ-glutamyl cycle and increased methylglyoxal levels in endothelial cells. *Diabetes* **69**, 2206–2216 (2020).

73. Kilhovd, B. K. *et al.* Increased serum levels of methylglyoxal-derived hydroimidazolone-AGE are associated with increased cardiovascular disease mortality in nondiabetic women. *Atherosclerosis* **205**, 590–594 (2009).

74. Hanssen, N. M. J. *et al.* Higher plasma methylglyoxal levels are associated with incident cardiovascular disease and mortality in individuals with type 2 diabetes. *Diabetes Care* **41**, 1689–1695 (2018).

75. Hall, A. Rho GTPases and the Actin Cytoskeleton. *Science (80-.).* **279**, 509–514 (1998).

76. Yuan, L. *et al.* RhoJ is an endothelial cell-restricted Rho GTPase that mediates vascular morphogenesis and is regulated by the transcription factor ERG. *Blood* **118**, 1145–1153 (2011).

77. Kaur, S. *et al.* RhoJ/TCL regulates endothelial motility and tube formation and modulates actomyosin contractility and focal adhesion numbers. *Arterioscler. Thromb. Vasc. Biol.* **31**, 657–664 (2011).

78. Rohlenova, K. *et al.* Single-Cell RNA Sequencing Maps Endothelial Metabolic Plasticity in Pathological Angiogenesis. *Cell Metab.* **31**, 862-877.e14 (2020).

79. Dumas, S. J., García-Caballero, M. & Carmeliet, P. Metabolic Signatures of Distinct Endothelial Phenotypes. *Trends in Endocrinology and Metabolism* **31**, 580–595 (2020).

80. He, Y., Hakvoort, T. B. M., Vermeulen, J. L. M., Lamers, W. H. & Van Roon, M. A. Glutamine synthetase is essential in early mouse embryogenesis. *Dev. Dyn.* **236**, 1865–1875 (2007).

81. Refsnes Data. Colors: RGB Calculator (w3schools.com). *w3schools.com - Colors: RGB Calculator* Available at: https://www.w3schools.com/colors/colors_rgb.asp.

82. Ellis, R. IHC World: Miller's Elastic Staining Protocol. *IHC World* Available at: https://www.ihcworld.com/_protocols/special_stains/miller's_elastic_ellis.htm.

83. Ellis, R. IHC World: van Gieson Staining Protocol. *IHC World* Available at: http://www.ihcworld.com/_protocols/special_stains/van_gieson_ellis.htm.

84. Percival, K. & Radi, Z. Comparison of five elastin histochemical stains to identify pulmonary small vasculature. *J. Histotechnol.* **40**, 73–78 (2017).

85. Coelho, P. G. B., Souza, M. V. de, Conceição, L. G., Viloria, M. I. V. & Bedoya,

S. A. O. Evaluation of dermal collagen stained with picrosirius red and examined under polarized light microscopy. *An. Bras. Dermatol.* **93**, 415–418 (2018).

86. Vogel, B., Siebert, H., Hofmann, U. & Frantz, S. Determination of collagen content within picrosirius red stained paraffin-embedded tissue sections using fluorescence microscopy. *MethodsX* **2**, 124–134 (2015).

87. Winkels, H. *et al.* Atlas of the immune cell repertoire in mouse atherosclerosis defined by single-cell RNA-sequencing and mass cytometry. *Circ. Res.* **122**, 1675–1688 (2018).

88. Ploeger, D. T. *et al.* Cell plasticity in wound healing: Paracrine factors of M1/ M2 polarized macrophages influence the phenotypical state of dermal fibroblasts. *Cell Commun. Signal.* **11**, 29 (2013).

89. Bennett, M. R., Sinha, S. & Owens, G. K. Vascular Smooth Muscle Cells in Atherosclerosis. *Circ. Res.* **118**, 692–702 (2016).

90. Gericke, A. *et al.* Functional Role of α 1 -Adrenoceptor Subtypes in Murine Ophthalmic Arteries. *Investig. Opthalmology Vis. Sci.* **52**, 4795 (2011).

91. Brinton, M., Mandel, Y., Schachar, I. & Palanker, D. Mechanisms of electrical vasoconstriction. *J. Neuroeng. Rehabil.* **15**, 43 (2018).

92. De Moudt, S., Leloup, A., Van Hove, C., De Meyer, G. & Fransen, P. Isometric Stretch Alters Vascular Reactivity of Mouse Aortic Segments. *Front. Physiol.* **8**, 157 (2017).

93. Franchi-Micheli, S. *et al.* Mechanical stretch reveals different components of endothelial-mediated vascular tone in rat aortic strips. *Br. J. Pharmacol.* **131**, 1355–62 (2000).

94. Vandamme, T. F. Use of rodents as models of human diseases. *J. Pharm. Bioallied Sci.* **6**, 2–9 (2014).

95. Getz, G. S. & Reardon, C. A. Animal models of atherosclerosis. *Arterioscler. Thromb. Vasc. Biol.* **32**, 1104–15 (2012).

96. Emini Veseli, B. *et al.* Animal models of atherosclerosis. *Eur. J. Pharmacol.* **816**, 3–13 (2017).

97. Johnson, J. L. & Jackson, C. L. Atherosclerotic plaque rupture in the apolipoprotein E knockout mouse. *Atherosclerosis* **154**, 399–406 (2001).

98. Schwartz, S. M., Galis, Z. S., Rosenfeld, M. E. & Falk, E. Plaque Rupture in Humans and Mice. *Arterioscler. Thromb. Vasc. Biol.* **27**, 705–713 (2007).

99. Pounds, L. C. Carotid Endarterectomy | Society for Vascular Surgery. *Society for*

Vascular Surgery Available at: https://vascular.org/patient-resources/vascular-treatments/carotid-endarterectomy. (Accessed: 30th March 2021)

100. MacKenzie, A. & Wadsworth, R. M. Extracellular L-arginine is required for optimal NO synthesis by eNOS and iNOS in the rat mesenteric artery wall. *Br. J. Pharmacol.* **139**, 1487–97 (2003).

101. Song, J. *et al.* Glutathione protects brain endothelial cells from hydrogen peroxide-induced oxidative stress by increasing nrf2 expression. *Exp. Neurobiol.* **23**, 93–103 (2014).

102. CAI, H. Hydrogen peroxide regulation of endothelial function: Origins, mechanisms, and consequences. *Cardiovasc. Res.* **68**, 26–36 (2005).

103. Bretón-Romero, R. & Lamas, S. Hydrogen peroxide signaling in vascular endothelial cells. *Redox Biol.* **2**, 529–534 (2014).

104. Martinez-Lemus, L. A. The dynamic structure of arterioles. *Basic Clin. Pharmacol. Toxicol.* **110**, 5–11 (2012).

105. Jadeja, R. N., Rachakonda, V., Bagi, Z. & Khurana, S. Assessing Myogenic Response and Vasoactivity In Resistance Mesenteric Arteries Using Pressure Myography. *J. Vis. Exp.* e50997 (2015). doi:10.3791/50997

106. Fernandez, D. M. *et al.* Single-cell immune landscape of human atherosclerotic plaques. *Nat. Med.* **25**, 1576–1588 (2019).

107. Dobnikar, L. *et al.* Disease-relevant transcriptional signatures identified in individual smooth muscle cells from healthy mouse vessels. *Nat. Commun.* **9**, 1–17 (2018).

108. Düzen, I. *et al.* Investigation of leukocyte RHO/ROCK gene expressions in patients with non-valvular atrial fibrillation. *Exp. Ther. Med.* (2019). doi:10.3892/etm.2019.7929

109. Afewerki, T., Ahmed, S. & Warren, D. Emerging regulators of vascular smooth muscle cell migration. *J. Muscle Res. Cell Motil.* **40**, 185–196 (2019).

110. Cubbon, R. M. *et al.* Temporal trends in mortality of patients with diabetes mellitus suffering acute myocardial infarction: a comparison of over 3000 patients between 1995 and 2003. *Eur. Heart J.* **28**, 540–545 (2006).

111. Chatterjee, S., Khunti, K. & Davies, M. J. Type 2 diabetes. *Lancet* **389**, 2239–2251 (2017).

112. World Health Organisation. *GLOBAL REPORT ON DIABETES*. (World Health Organisation, 2016).

113. Kleinert, M. *et al.* Animal models of obesity and diabetes mellitus. *Nat. Rev. Endocrinol.* **14**, 140–162 (2018).

114. King, A. J. The use of animal models in diabetes research. *Br. J. Pharmacol.* **166**, 877–894 (2012).